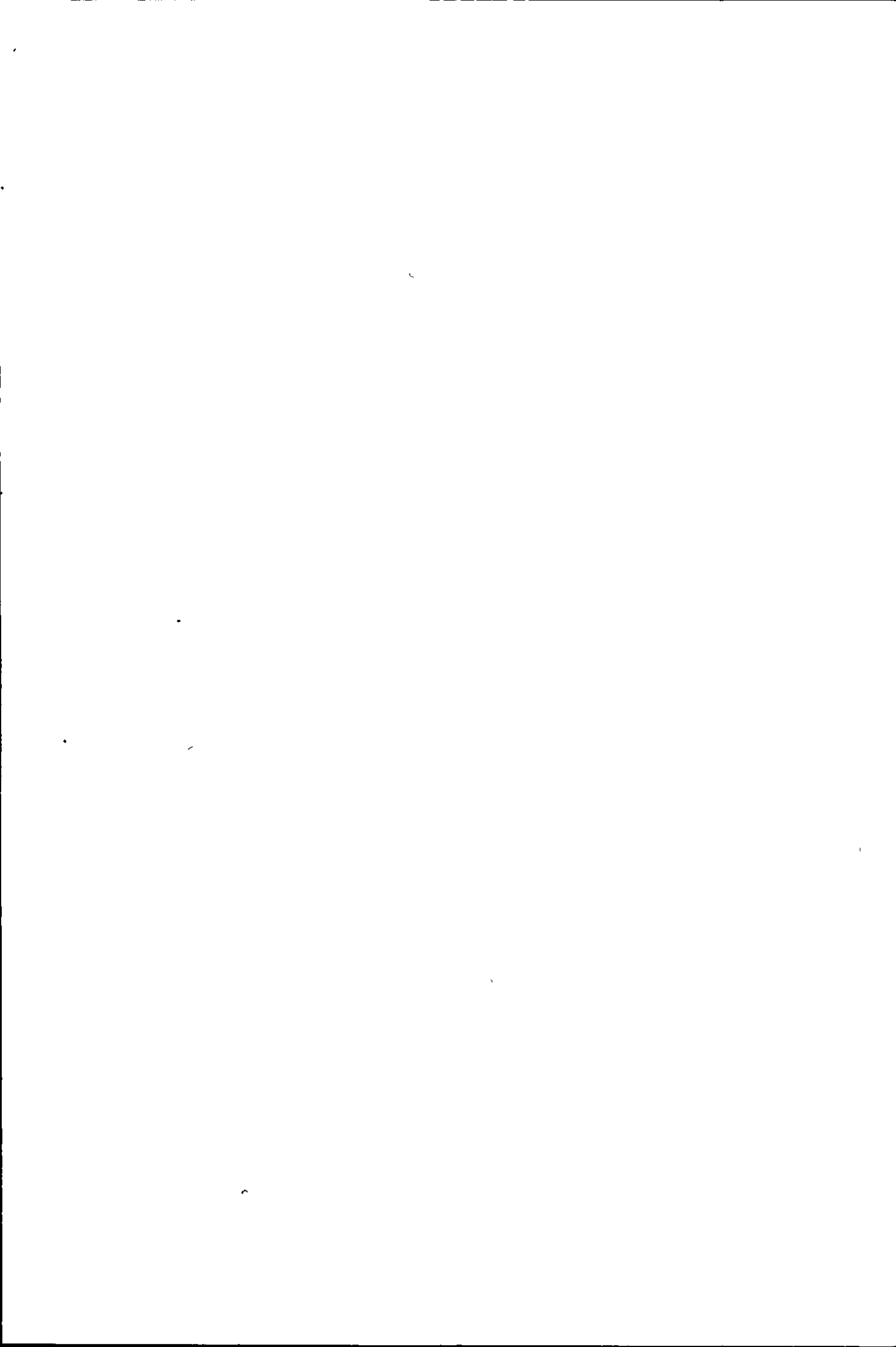


**LOUGHBOROUGH  
UNIVERSITY OF TECHNOLOGY  
LIBRARY**

<b>AUTHOR/FILING TITLE</b>		
<u>MAKH, S S</u>		
<b>ACCESSION/COPY NO</b>		
<u>102848/02</u>		
<b>VOL. NO.</b>	<b>CLASS MARK</b>	
<del>2 JUL 1982</del>	<del>3 JUL 1992</del>	<b>27 JUN 1997</b>
<del>1 JUL 1983</del>	<del>2 JUL 1993</del>	<b>27 JUN 1997</b>
<del>6 JUL 1984</del>	<del>1 JUL 1994</del>	<b>15 MAR 1999</b>
<del>30 JUN 1985</del>	<del>30 JUN 1995</del>	<del>5 APR 2000</del>
<del>4 JUL 1986</del>	<b>30 JUN 1995</b>	<b>14 APR 2000</b>
	<b>28 JUN 1996</b>	<b>12 MAY 2000</b>

010 2848 02





THE DEVELOPMENT OF SURFACE  
MORPHOLOGY DURING ION ETCHING.

BY

S.S. MAKH, B.Sc.

*A Doctoral Thesis submitted in partial  
fulfilment of the requirements for the  
award of Doctor of Philosophy of the  
Loughborough University of Technology.*

Supervisors: Dr. R. Smith,  
Department of Mathematics.

Dr. J.M. Walls,  
Department of Physics.

Loughborough University of Technology Library	
Date	Dec 81
Class	
Acc. No.	102848/02

To my parents.

## ABSTRACT

This thesis investigates the changes in surface shape which occur when solid surfaces are subjected to bombardment and erosion by energetic ion beams. The aspects which are studied lay particular emphasis on the type of problems encountered in the electronics industry where ion etching is used for the production of microrelief on many commercial devices. Ion etching is also used extensively in surface analysis using techniques such as Auger Electron Spectroscopy, X-ray Photoelectron Spectroscopy and Secondary Ion Mass Spectroscopy both for surface cleaning and composition-depth profiling.

This thesis investigates the development of surface shape due to the dependence of the sputtering yield  $S$ , on the angle of ion incidence  $\theta$ , using the method of characteristics. This is a mathematical technique which reduces the partial differential equation describing the erosion of a surface to a set of ordinary differential 'characteristic' equations. The technique has several advantages over existing methods including its suitability for numerical manipulation, its extension to three dimensions, its use with non-uniform ion current distributions and its extension to investigate the build-up of surfaces due to redeposition. Its use is illustrated by comparing the ion induced topography of surfaces obtained using one and two ion beams.

A theoretical model has been developed for the redeposition of sputtered material using the method of characteristics. The model enables the evolution of surface shape to be determined as a function of sputtering time. The effects of changes in ion energy and of different aspect ratios is investigated as a function of erosion depth.

Other factors also influence the evolution of surface shape under ion bombardment. Diffusion of surface atoms away from the bombardment zone leads to development of surface shape and this is treated using a linearised theory of surface diffusion. Finally, other secondary and tertiary effects such as local flux enhancement due to ion reflection off steep profiles and volume diffusion are discussed qualitatively.

## C O N T E N T S

	<u>PAGE NO.</u>
Abstract.	
Contents.	
Introduction.	1
<u>CHAPTER 1: Theory of surface erosion by ion bombardment.</u>	8
1.1 Experimental evidence for the formation of surface topography during ion etching.	8
1.2 Previous theories for the erosion of surfaces.	11
1.3 The method of characteristics.	29
<u>CHAPTER 2: Applications of ion etching in surface analysis.</u>	36
2.1 Introduction.	36
2.2 Surface analysis techniques.	38
2.2.1 Auger Electron Spectroscopy (AES).	38
2.2.2 X-ray Photoelectron Spectroscopy (XPS).	40
2.2.3 Secondary Ion Mass Spectroscopy (SIMS).	41
2.2.4 Composition-depth profiling.	42
2.3 The development of surface shape during sputter-depth profiling in AES.	43
2.3.1 Analysis.	44
2.3.1.1 The development of surface shape.	44
2.3.1.2 Computer simulation.	46
2.3.1.3 Depth resolution.	47
2.3.2 Results.	49
2.3.2.1 The development of surface shape.	49
2.3.2.2 Depth resolution.	50



2.3.3	Discussion.	51
2.4	The development of surface topography using two ion beams.	52
2.4.1	Theoretical model.	53
2.4.2	Computer simulation.	59
2.4.3	Results and Discussion.	61

CHAPTER 3: A theoretical model for the redeposition of sputtered material. 66

3.1	Introduction.	66
3.2	Experimental evidence for the redeposition of sputtered material.	69
3.3	Previous theories for the redeposition of sputtered material.	74
3.4	A model for redeposition using the method of characteristics.	84
3.4.1	Modelling of different distributions for the sputtered particles.	85
3.4.2	Derivation of differential equations describing the build-up due to redeposition.	86
3.4.2.1	Intermediate energy.	86
3.4.2.2	High energy.	93
3.4.2.3	Low energy.	95
3.5	Results of computer simulation.	96
3.6	Discussion.	98

CHAPTER 4: Tertiary effects. 101

4.1	Introduction.	
4.2	Development of surface topography due to surface diffusion and erosion.	103
4.2.1	Previous theories.	103
4.2.2	A new theoretical model.	109

4.2.3	Computer simulation.	113
4.2.4	Results.	114
4.3	Volume diffusion/mixing.	116
4.4	Ion reflection.	121
4.5	Discussion.	126

CHAPTER 5: Conclusions and suggestions for future work. 128

5.1	Surface analysis.	128
5.2	Redeposition of sputtered material.	131
5.3	Surface diffusion and erosion.	132
5.4	Future work.	133

REFERENCES 136

APPENDIX 1 145

ACKNOWLEDGEMENTS

## INTRODUCTION

When a beam of energetic particles is projected at a target under suitable conditions, well defined surface topographical features are observed to develop on the surface of the bombarded material. The incident particles impart their energy to the solid in slowing down, causing ejection of surface atoms, which results in the development of surface morphology. The basic mechanism involves a transfer of the incident momentum carried by the ions so that target atoms are ejected from the surface over a wide range of angles. The process of atomic ejection during bombardment is known as 'sputtering' and a sputtering coefficient  $S$  is defined as the number of atoms liberated per incident particle (Carter and Colligon (1969)).

One of the earliest attempts at postulating a mechanism to describe the sputtering process was presented by Thomson (1921) who proposed that radiation was released as the ion struck the target surface and that this in turn caused atomic ejection. Bush and Smith (1922) envisaged a situation where the gas adsorbed by the material expanded, and hence, caused a minor explosion producing sputtered atoms. However these early theories were replaced by a concept known as the 'Hot-Spot Theory'. This theory was presented by Hippel (1926) and envisaged a situation where the energy dissipated by the ion in slowing down was sufficient to raise the temperature of a small hemispherical region of atomic dimensions so that target atoms were evaporated. However experimental investigation of the ejection patterns from single crystals showed that there were preferred directions for ejection (Nelson and Thompson (1962), Kaminsky (1966)). These preferred ejection directions completely contradicted any suggestion of a thermal evaporation mechanism. Clearly,

the theory for sputtering must be based on a momentum transfer process between the ion and target atoms to explain the anisotropic ejection found in single crystal studies.

The first attempt at such a theory was made by Lamar and Compton (1934) who proposed that ions may penetrate the target material, be reflected from a lower atomic layer and recoil to strike a surface atom in an outward direction. Contemporary theories are based on this mechanism, but usually consider that many more internal collisions occur before an atom is finally ejected. A treatment on these lines has been developed by Keywell (1952) who applied the analogy of the cooling of neutrons by the atoms of a moderator to the sputtering sequence. An incoming ion was presumed to penetrate the surface and strike a target atom. This atom was not itself sputtered but, in its turn, collided with neighbouring atoms producing secondary displacements. The overall effect on the atomic array was similar to a diffusion process or 'random walk' of mobile atoms, some of which reached the surface with sufficient energy to collide with and liberate surface atoms. Subsequent theoretical models have included the effects of focused collision chains in the ejection process and the role of channeling and transparency in the anisotropy of the sputtering yield of single crystals (Thompson (1961), Harrison et al (1966), Onderdelinden (1966), Olson and Smith (1967)).

Thus on the atomic scale, each incident ion will create a cascade of recoil atoms and energy will be deposited with a geometric distribution about the point of impact (Sigmund (1969), (1973), Carter et al (1977)). Final ejection of surface atoms will occur with a radial probability distribution about the point of impact. This distribution will depend on ion mass, ion energy, target material, crystalline structure and direction of ion incidence to the solid. If the effects of many ion

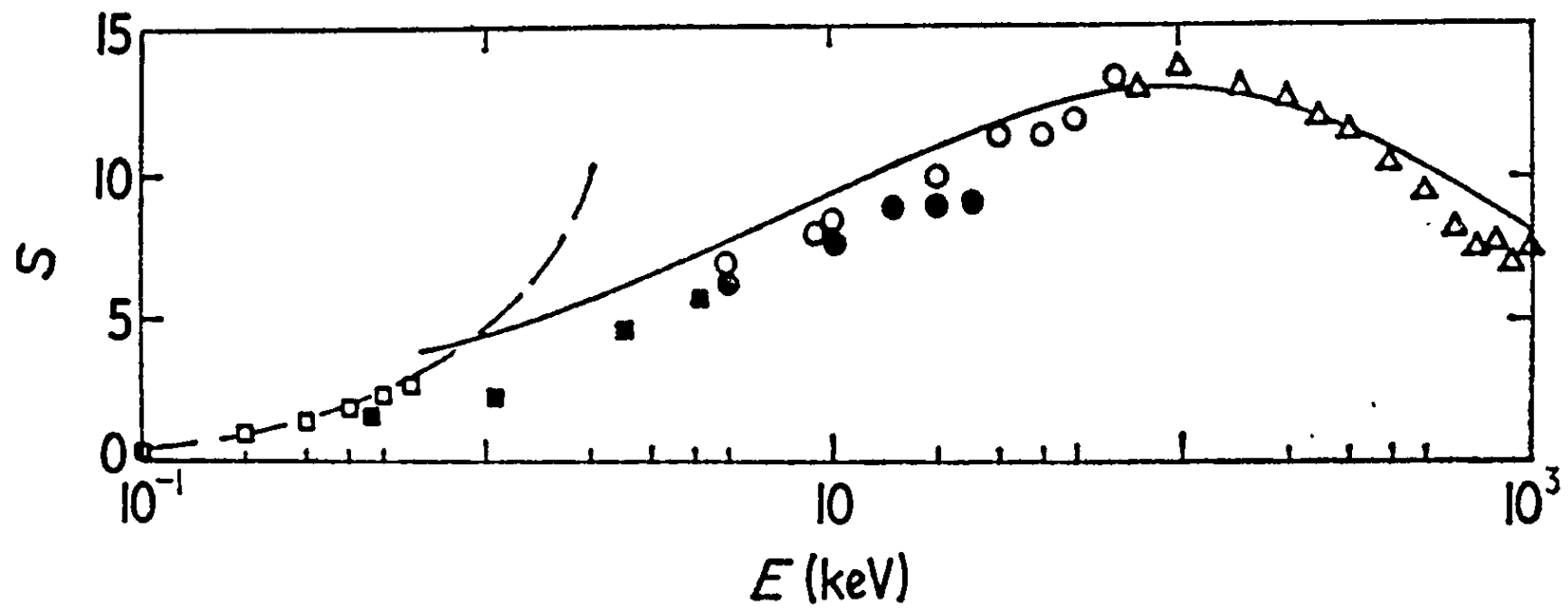
impacts over an area much larger than the collision cascade dimensions (10-1000Å for ions in the 1-100keV energy range) is considered, then the individual events sum to give a mean sputtering yield of ejected atoms per incident ion,  $S$ , which leads to macroscopic erosion of the solid.

The variation of sputtering coefficient with incident ion energy follows the general pattern shown in figure I.1 for  $\text{Kr}^+$  on Cu (McCracken (1975)). At low energy there is a threshold for sputtering to occur. Above the threshold the sputtering yield rises to a maximum, and eventually at very high energies decreases again as the cross-section for interaction with surface atoms decreases and the ion energy is deposited so far into the solid that it cannot reach the surface.

The most exhaustive experiments to determine the variation of sputtering with the target material have been carried out by Wehner and his co-workers who have bombarded a number of metals with mercury and noble gas ions (Wehner (1957), Laegreid and Wehner (1961), Rosenberg and Wehner (1962)). They showed that the sputtering yield was a function of atomic number, and that the sputtering yield showed a periodicity which was closely correlated with that of the periodic table and the heat of sublimation of solids. This general pattern was demonstrated for a number of incident ion species at energies up to 600eV, see figure 1.2. Later Almén and Bruce (1961) showed that for high energy ions (typically 45keV) a very similar pattern exists.

The mean sputtering yield  $S$  is also a function of  $\theta$ , the angle between the incident ions and the surface normal. Theoretical estimates of the behaviour of  $S$  as a function of  $\theta$  suggest a relationship of the form  $S_{\theta} \propto (\cos\theta)^{-n}$ , where  $n \leq 1$  for  $0 \leq \theta \leq 70^{\circ}$  (Sigmund (1969)).

Fig. I.1. Sputtering yield of Cu under  $\text{Kr}^+$  ion bombardment (After McCracken (1975)).



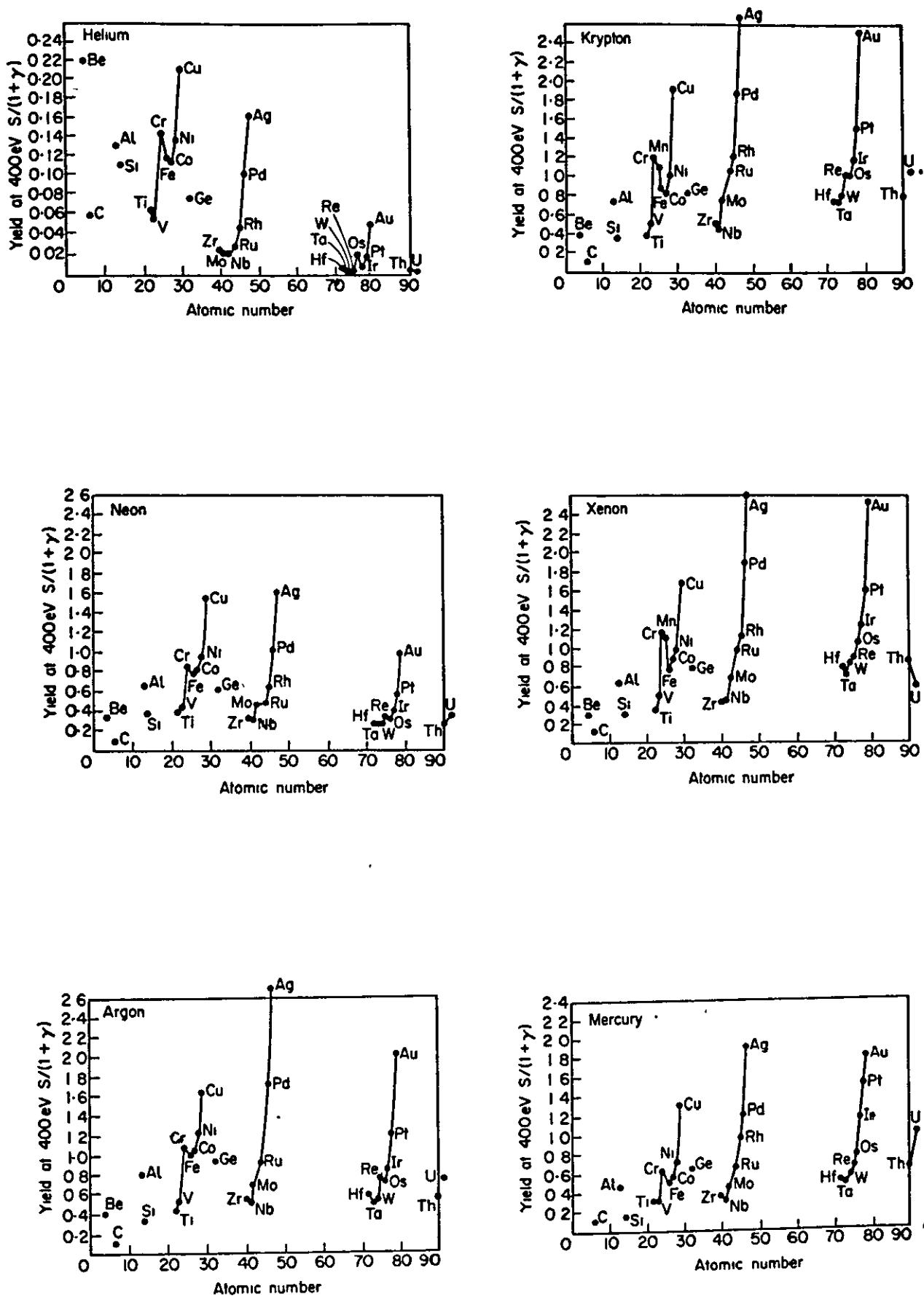


Fig. I.2. Variation of sputtering yield with atomic number of the bombarded material for bombardment by 400eV noble gas and mercury ions (After Carter and Colligon (1969)).

Experimental measurements generally confirm this relationship for many ion-solid combinations but also show that it is only true over a limited range of  $\theta$ . The more general observation is that  $S(\theta)$  increases as a  $(\cos\theta)^{-n}$  function from  $S_0$  at  $\theta = 0$ , but then departs from this function and reaches a maximum value  $S_p$  at an angle  $\theta_p$ . Thereafter  $S_\theta$  declines with increasing incidence angle until at  $\theta = \frac{\pi}{2}$   $S$  is zero, see figure I.3.

The development of surface topography during ion bombardment, due to the dependence of the sputtering yield on factors such as ion mass, ion energy, target material, target temperature, crystalline structure and direction of ion incidence, occurs at both the macroscopic and microscopic levels. Due to the importance of the process in surface analysis, not only for surface cleaning, but also for obtaining composition-depth profiles and for the production of microrelief on many commercial devices in the electronics industry, many attempts have been made to treat the development of a general surface under ion bombardment. In a first study Stewart and Thompson (1969) showed how triangular facets erode by considering the motion of intersecting semi-infinite planes. Carter and his colleagues have studied the motion of individual points on a general two-dimensional surface (Nobes et al (1969), Carter et al (1971), (1973)). These studies showed that the motion of surface points could be described by a wave equation with space-time dependant velocity. However, they did not associate this with the kinematic wave process outlined earlier by Lighthill and Whitham (1955). Barber et al (1973) have developed an apparently different approach to the problem of ion induced erosion when they adapted a theory of chemical dissolution first expounded by Frank



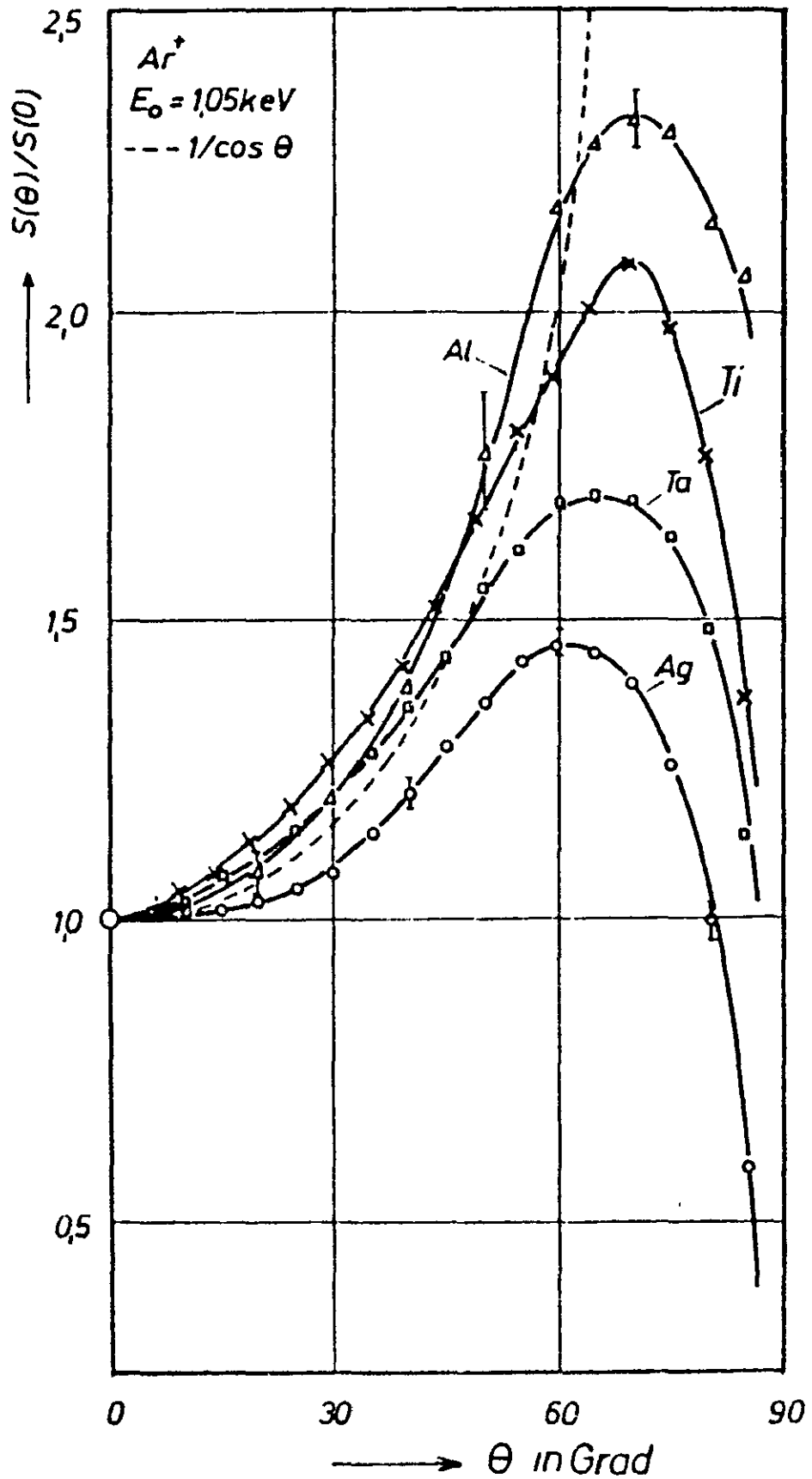


Fig. 1.3. Influence of the bombarding angle  $\theta$  on the normalized sputtering yield of different polycrystalline metals bombarded with  $Ar^+$  ions of 1.05keV (After Oechsner (1975)).

(1958), (1972). They studied the spatial and temporal motion of points of constant orientation relative to the ion flux, and showed that the loci or trajectories of these points on the real surface could be constructed through use of an 'erosion slowness curve'. The theory of chemical dissolution employed by Barber and his colleagues is based upon the motion of discrete surface steps, and has been shown by Frank to obey the equation of motion of kinematic waves studied earlier by Lighthill and Whitham (1955). At this point Carter et al (1973), recognising the similar wave nature of surface point motion in their own earlier studies and in the Lighthill and Frank basis of Barber's treatment, proposed a generalised approach to sputter erosion. They were able to show that the continuum approach of their own earlier work and the intersection plane approach of Stewart and Thompson both fall within the general framework of the Barber et al extension of the Frank theory of crystal dissolution.

However, although much progress has been made, the present analytical methods apply almost exclusively to two-dimensional surfaces and the use of a uniform ion flux, where as in many applications the surfaces undergoing ion bombardment have features whose topography is essentially three-dimensional. The existing models cannot be used to deal with three-dimensional surfaces, non-uniform ion flux or crystalline materials. Not only do the theories ignore secondary effects such as redeposition of sputtered material, surface diffusion, volume diffusion and ion reflection off steep profiles, but it also seems very difficult to modify them to incorporate these effects.

A three-dimensional theory of surface erosion has recently been developed by Smith and Walls (1979), (1980). In this theory, the

erosion of a general three-dimensional surface can be shown to be given by a non-linear first order partial differential equation of a type that occurs in geometrical optics and is sometimes known as the eikonal or Jacobi's equation. The method of solution is to determine the characteristic lines of the equation. Essentially, these are lines in space along which the partial differential equation can be reduced to a set of ordinary 'characteristic' differential equations. In principle, the solution in a whole region can be obtained by integrating these characteristic equations along the characteristics covering the region.

In this thesis, the way in which the method of characteristics can be applied to solve the problem of the erosion of three-dimensional surfaces bombarded by a uniform and non-uniform ion flux will be outlined (Smith and Walls (1980)). This theory has been further extended to include the effects of the crystalline structure of the material (Smith et al (1980), (1981)). The use of ion etching to obtain composition-depth profiles is a well established technique in surface analysis. However the formation of microtopography during ion etching causes the degradation in depth-resolution of such profiles. Thus the method of characteristics has been used to investigate this problem and the related one of the development of surface shape on the macroscopic scale (Makh et al (1980a), (1981a)). The models developed will be outlined in detail in this thesis. The theory of Smith and Walls has also been modified to investigate the build-up of surfaces due to the redeposition of backspattered material. A theoretical model has been developed which enables calculations to be made concerning shape changes due to the continuous build-up of redeposited material (Makh et al (1980b), (1981b)). This model will be outlined in detail

in this thesis. Surface diffusion is another effect which can lead to substantial changes in the development of surface topography.

These changes have been attributed to the greater influence of surface diffusion with increasing temperature. Thus a linearised theory has been developed for the simultaneous ion erosion and diffusion of surface atoms. This model will be outlined in detail in this thesis.

CHAPTER 1THEORY OF SURFACE EROSION BY ION BOMBARDMENT1.1. Experimental evidence for the formation of surface topography during ion bombardment.

The bombardment of surfaces by ions can lead to changes in the surface topography and structure due to a number of different effects. One of the most important of these is the dependence of the sputtering yield, the number of atoms emitted per incident ion, with the angle of ion incidence. If a surface is flat and free from imperfections, then during erosion of the surface by sputtering it is expected on preliminary considerations that the surface should remain flat. However, if the surface is not perfectly flat, i.e. there is initial surface roughness, the variation in sputtering coefficient with angle of ion incidence will cause the surface to be eroded at different rates. This occurs at both the microscopic and macroscopic level. To show the effects of the variation of sputtering yield on the development of surface topography at the macroscopic level Wehner (1969) and Meckel et al (1975) have bombarded spheres and fibres with circular cross-sections. Under the influence of bombardment the geometry changes from initially circular to a conical form, see figures 1.1 and 1.2.

Surface topography also develops at the microscopic level due to variations in  $S(\theta)$ . However here the presence of impurities is a greater factor in the development of surface shape. Impurities in the surface can give rise to regions having a different sputtering coefficient than the bulk material, which leads to non-uniform etching of the surface.

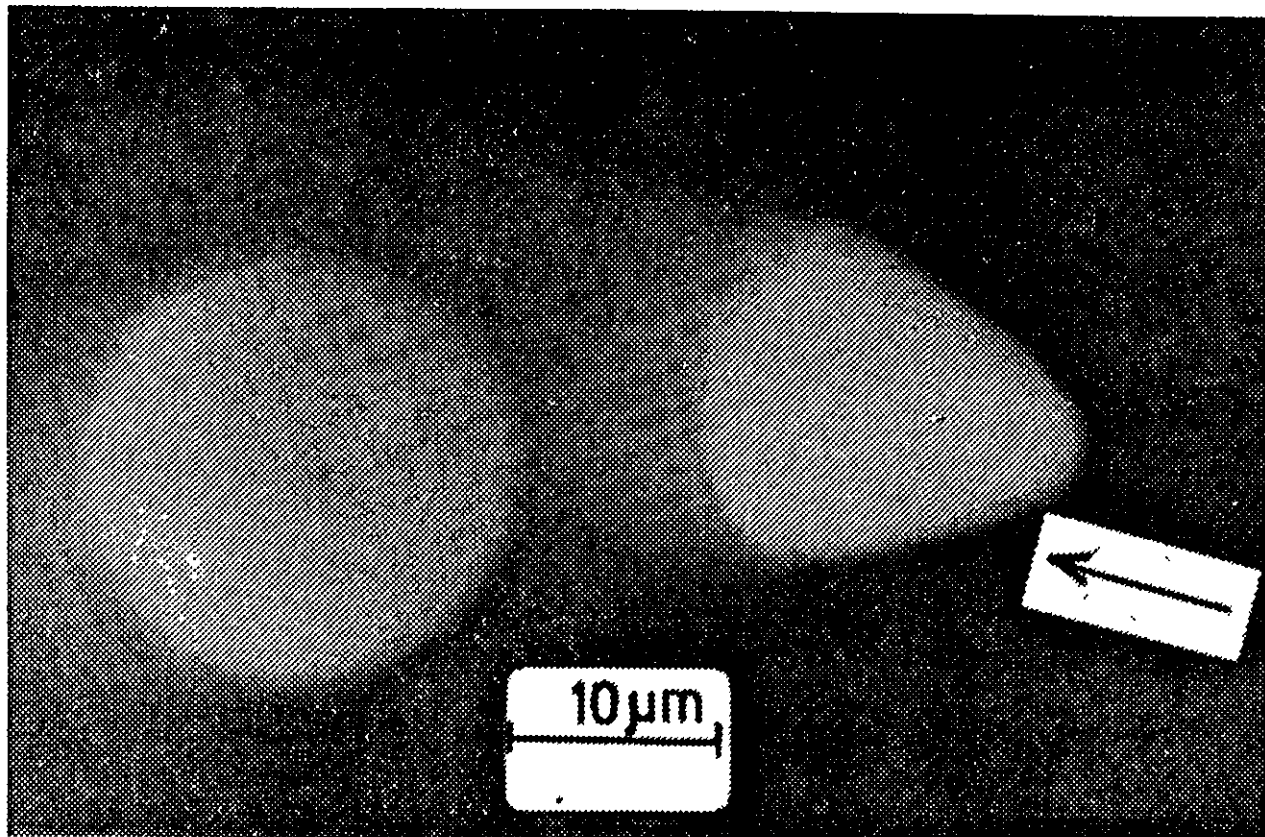


Fig. 1.1. Two silica fibre profiles; one unspattered, the other sputtered with 6 keV Ar<sup>+</sup> ions. (After Meckel et al (1975)).

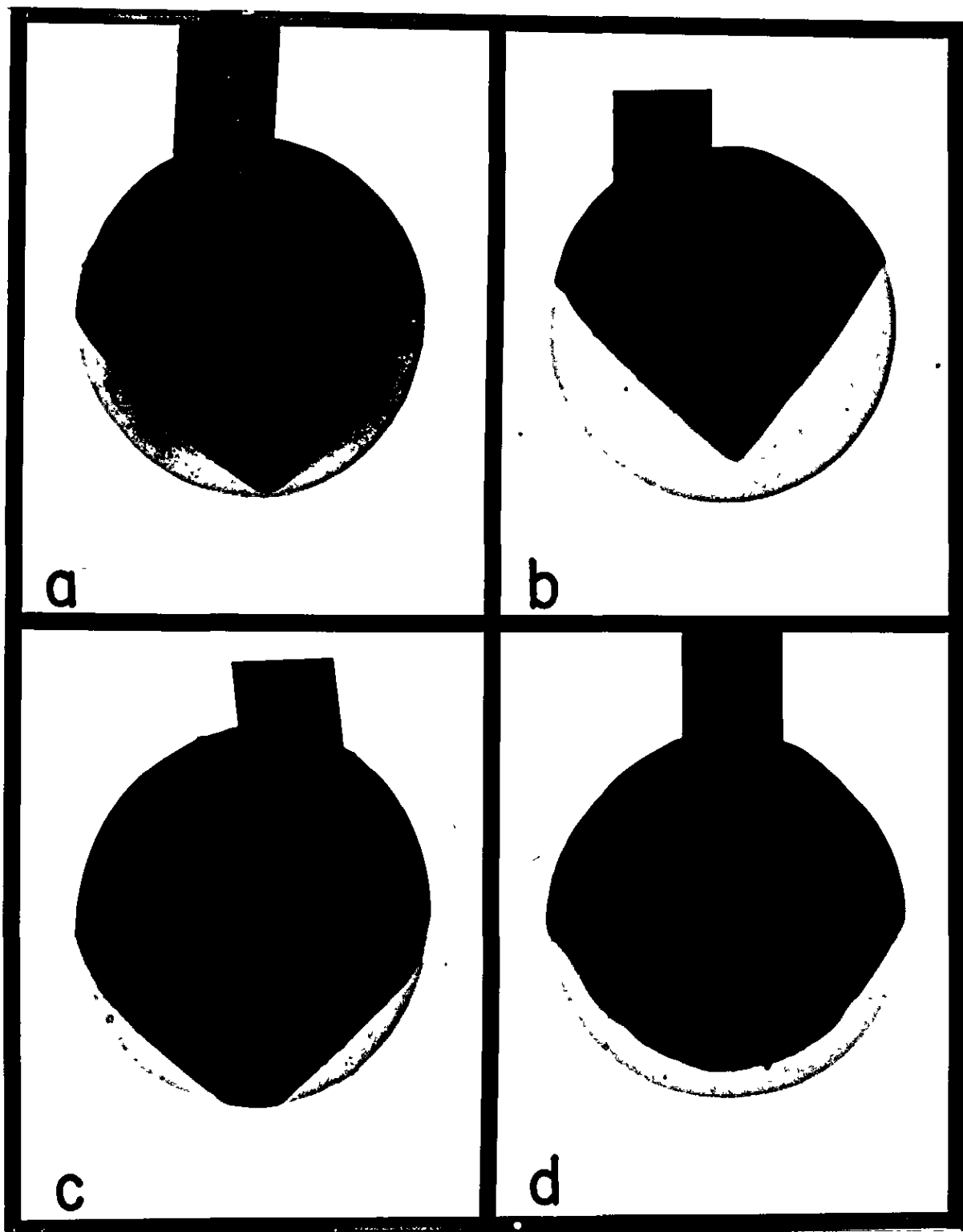


Fig. 1.2. (a) Shadow micrograph of iron sphere sputtered for 500 hr with 200 eV  $\text{Hg}^+$  ions.  
(b) Iron sphere sputtered for 168 hr with 400 eV  $\text{Hg}^+$  ions.  
(c) Tantalum sphere sputtered for 500 hr with 200 eV  $\text{Hg}^+$  ions.  
(d) Nickel sphere sputtered for 168 hr with 400 eV  $\text{Hg}^+$  ions  
(Courtesy of Professor G.K. Wehner).

Once the topography is nucleated, it is further modified since the erosion rate at each point on the surface is a sensitive function of ion incidence angle. A good example of the type of structure to which this can lead is shown in figure 1.3.

Another possibility for the production of surface structure has been discussed by Mazey et al (1968) and more recently by Hermanne (1973). When a surface is bombarded by ions, radiation damage can cause the growth of extensive defects such as dislocations. As the surface is eroded, these defects are in time exposed and lead to variations of sputtering yield across the surface, which then act as nuclei for the growth of larger-scale surface structure. Such effects can therefore give rise to structure even on an initially perfect surface.

Another effect which can give rise to changes in surface structure is radiation blistering. This was first observed by Primak (1963) and then by Kaminsky (1964) but little further work has been done on the subject until recently, when its potential importance in the erosion of the walls of controlled thermonuclear reactors was recognized. Some typical blistering behaviour is shown in figure 1.4.

The blistering of surfaces occurs after large doses of light ions, principally hydrogen and helium, are implanted in them. Under helium bombardment the blisters actually appear quite suddenly at critical doses  $\sim 5 \times 10^{17}$  ions  $\text{cm}^{-2}$  in a wide range of materials and a wide range of ion energies. They are most easily observed with light ions because their projected range is large compared with the depth of erosion occurring during the implantation of the critical dose, and it is therefore possible to build up high concentrations in the surface before the gas is released by erosion.



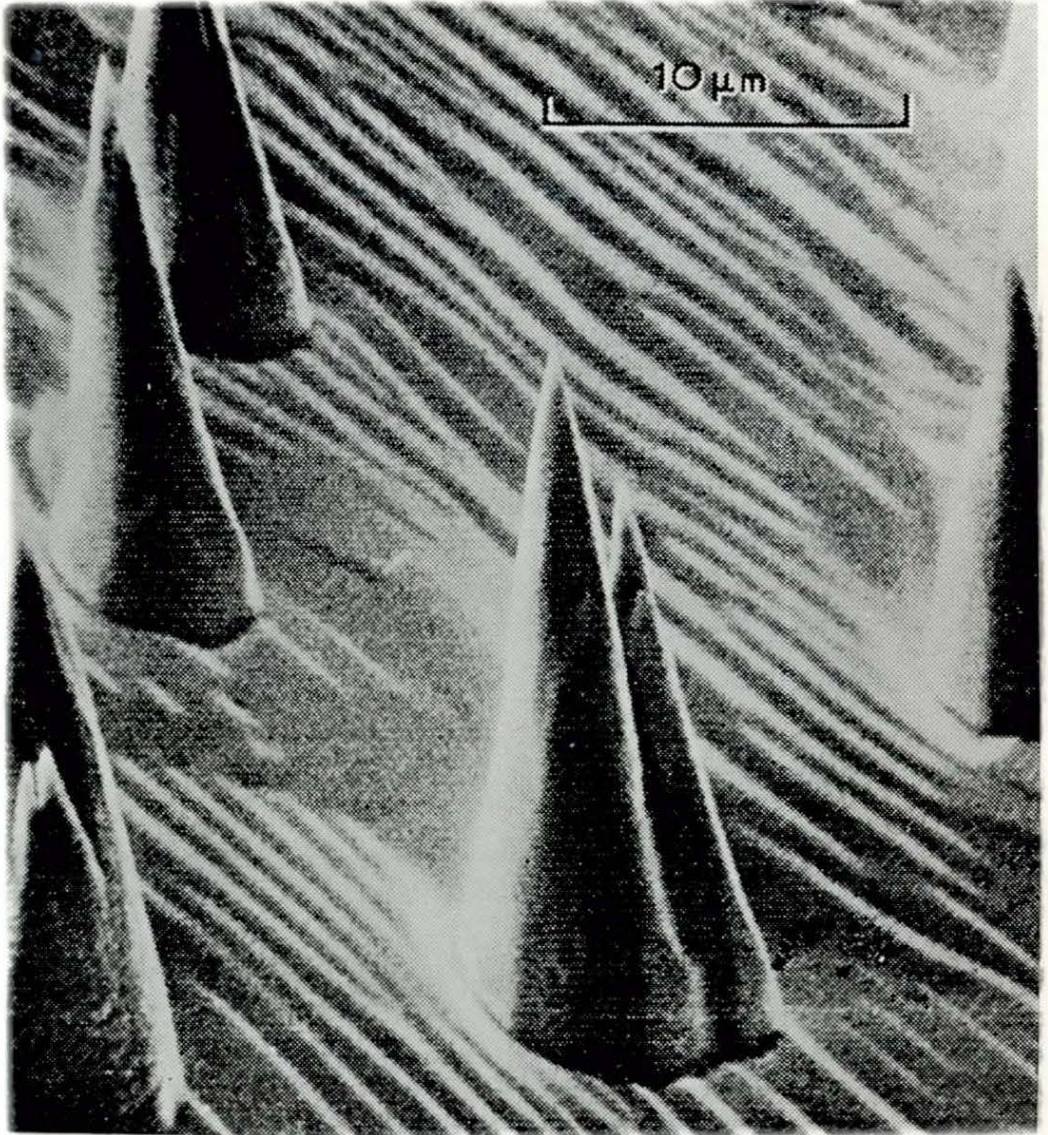


Fig. 1.3. The surface of a tin crystal following bombardment with 5 keV  $\text{Ar}^+$  ions (After Stewart and Thompson (1969)).

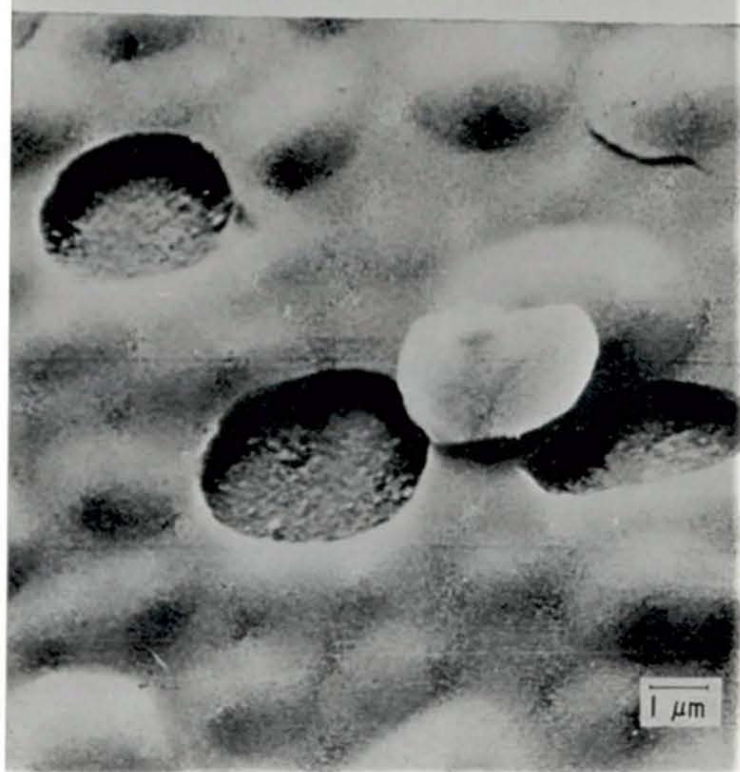
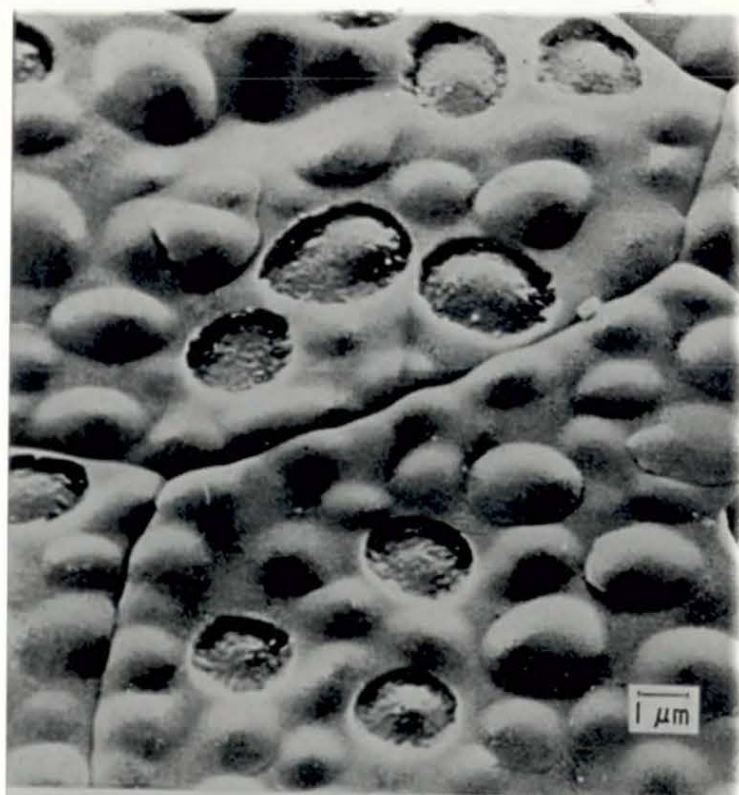


Fig. 1.4. Blistering of a molybdenum surface after bombardment with helium ions of different energies (a) 50 keV, (b) 80 keV (After Erents and McCracken (1973)).

Thus it can be seen that the development of surface topography on ion bombarded surfaces can be caused by a number of mechanisms. In the applications of ion bombardment, e.g. thinning specimens for transmission electron microscopy, surface cleaning and depth profiling in surface analysis, it is important to know how surfaces and certain surface shapes erode under ion bombardment. Therefore in the next two sections of this chapter a number of theories which attempt to explain the erosion of surfaces are outlined.



## 1.2. Previous theories for the erosion of surfaces.

Many attempts have been made to treat theoretically the development of surface topography under ion bombardment. It has been recognised that one of the most important parameters in the development of surface shape is the dependence of the sputtering yield  $S$  on the angle of ion incidence  $\theta$ . The generally observed functional relationship between  $S$  and  $\theta$  for an amorphous target material in the range  $0 \leq \theta \leq \frac{\pi}{2}$  is that  $S(\theta)$  has a minimum value  $S(0)$  at  $\theta = 0$ , rising to a maximum and then decreasing to zero at  $\theta = \frac{\pi}{2}$ , see figure 1.5. The reason for the behaviour at large angles shown in figure 1.5 is considered to be due to the increasing probability of reflection of incident ions with increasing incidence angle, leading to reduced penetration, less energy deposition per ion and hence a lower sputtering yield (Stewart and Thompson (1969)). This  $S$ - $\theta$  dependence has been the subject of a number of analytical studies.

Stewart and Thompson (1969) were one of the first to try and explain theoretically the formation of cones on ion bombarded surfaces. Their method is based on the erosion of intersecting planes. Figure 1.6 shows a surface consisting of two inclined planes A and B on which bombarding ions are incident at angles  $\alpha$  and  $\beta$  respectively. Then, following Stewart and Thompson (1969), during erosion the planes move to positions A' and B' and the line of intersection from O to O'. The angle  $\delta$  is made between the direction of ion incidence and the path OO'. The distances advanced by the planes are a and b, that advanced by the intersection is c and the sideways movement of the intersection, transverse to the direction of incidence is d. The flux of ions crossing unit area of surface normal to their direction is  $\phi$  in the

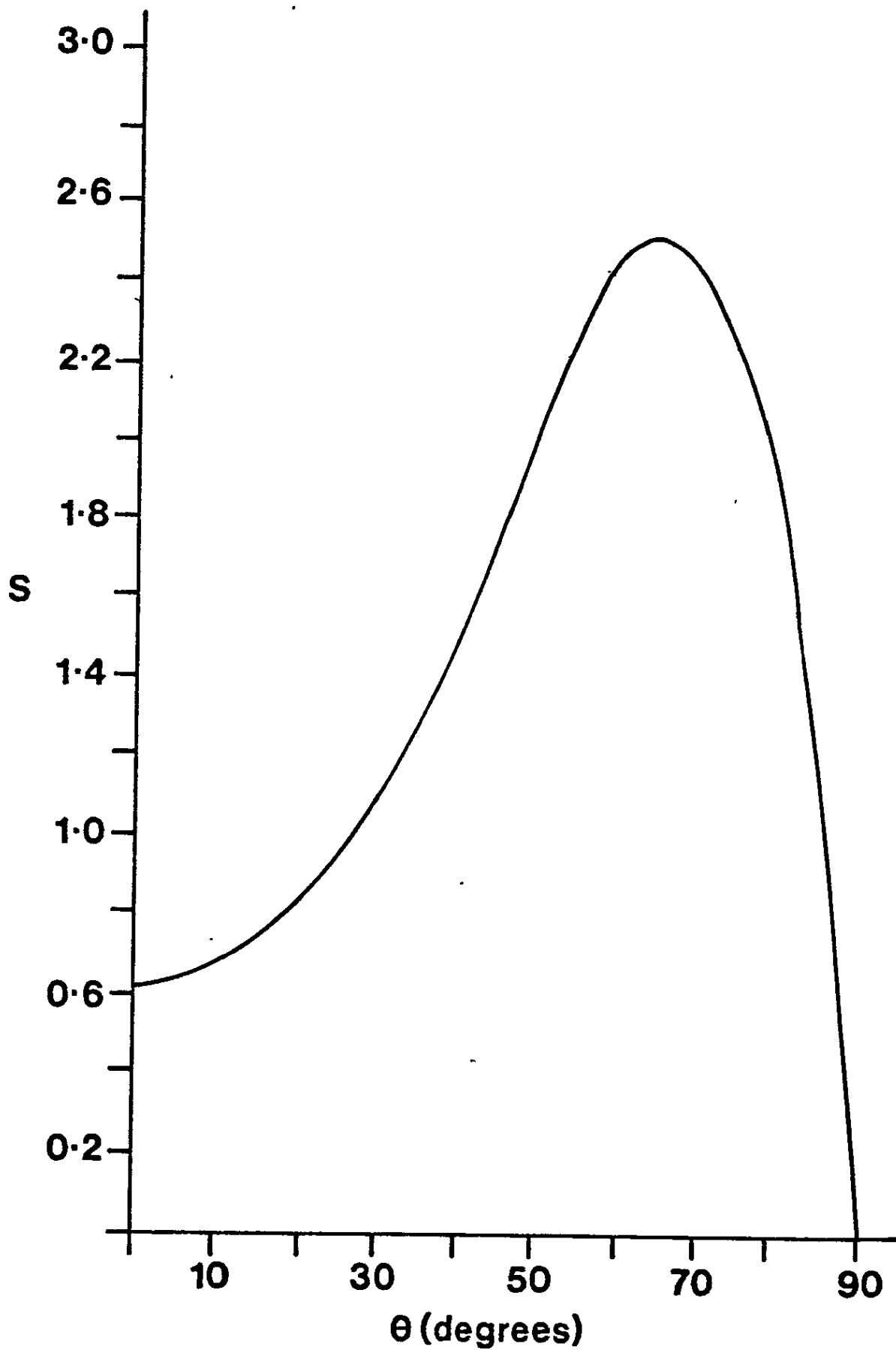


Fig 1.5. Generally observed relationship between  $S(\theta)$  and  $\theta$  for an amorphous material.

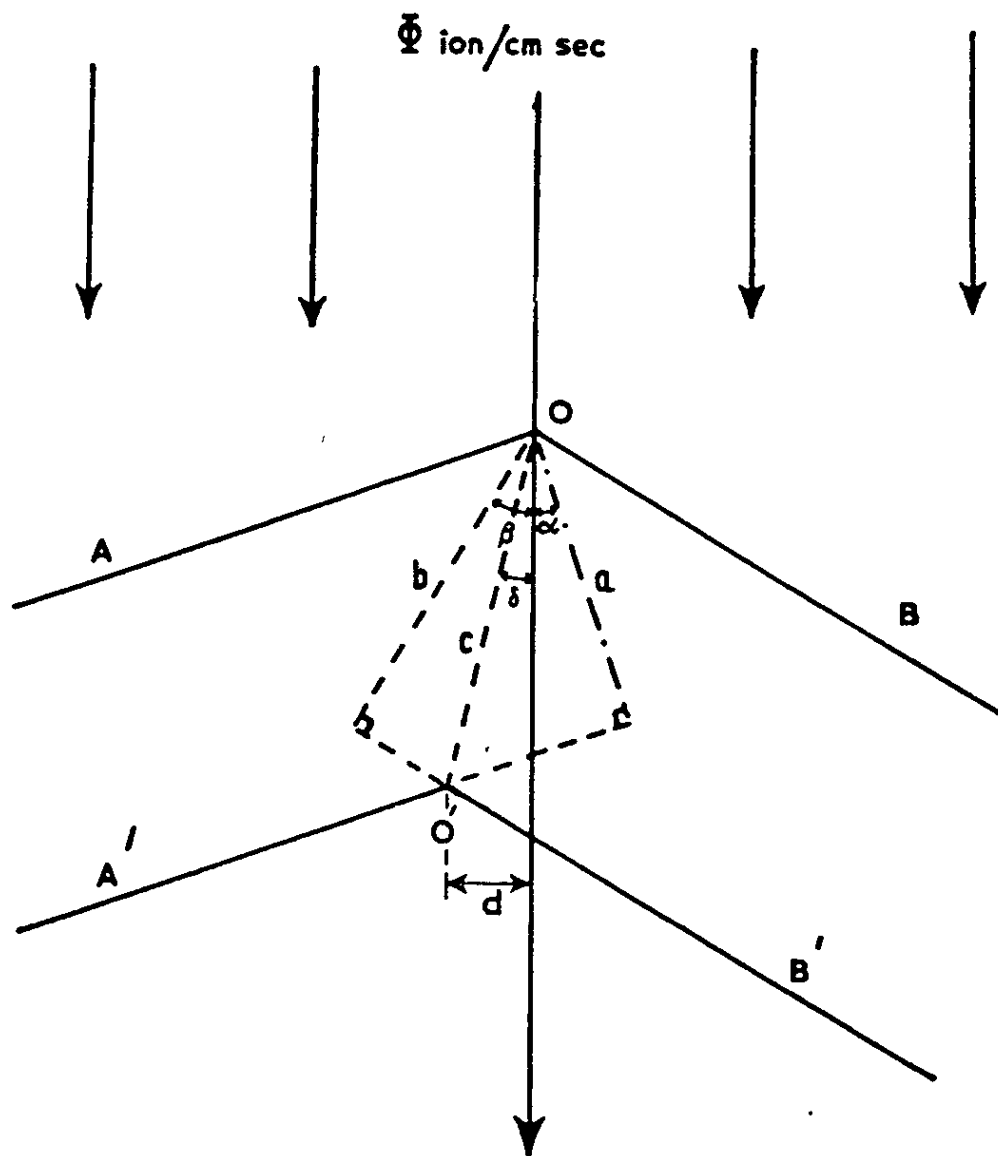


Fig. 1.6. The motion of the intersection between two plane surfaces during erosion (After Stewart and Thompson (1969)).

course of the erosion. On unit areas of the two planes the respective fluxes are  $\phi \cos \alpha$  and  $\phi \cos \beta$  and the distances advanced are

$$\left. \begin{aligned} a &= \frac{1}{n} \phi \cos \alpha S(\alpha) \\ b &= \frac{1}{n} \phi \cos \beta S(\beta) \end{aligned} \right\} \quad (1.1)$$

where  $n$  is the atomic density per unit volume.

From the geometry of the system,

$$\left. \begin{aligned} a &= c \cos(\alpha + \delta) \\ b &= c \cos(\beta - \delta) \end{aligned} \right\} \quad (1.2)$$

The above equations can be used to calculate the ratio  $d/a$  which relates the sideways movement of the intersection to the distance by which plane A advances,

$$\text{as } c = \frac{d}{\sin \delta} = \frac{a}{\cos(\alpha + \delta)}$$

$$\text{Thus } \frac{d}{a} = \frac{S(\beta) - S(\alpha)}{S(\alpha) \cos \alpha (\tan \alpha + \tan \beta)} \quad (1.3)$$

Equation (1.3) provides the means of deciding whether the intersection line  $O$  moves towards A or towards B during erosion (i.e. whether  $d$  is positive or negative). There are obviously three cases,

- (i) If  $S(\alpha) = S(\beta)$ ,  $d = 0$  and  $O$  does not move laterally;
- (ii) If  $S(\alpha) > S(\beta)$ ,  $d < 0$  and  $O$  moves towards B;
- (iii) If  $S(\alpha) < S(\beta)$ ,  $d > 0$  and  $O$  moves towards A.

If the angle between the planes had been acute, viewed from above, rather than obtuse the directions of motion would have been reversed. Thus the crest of a ridge will move towards the side for which  $S(\theta)$  is least. The foot of a valley will move towards the side for which

$S(\theta)$  is greatest. The movement of the crest illustrates the importance of the  $S(\theta)$  function. In the special case where  $\alpha = 0$  and the ions are incident normally on plane A, equation (1.3) reduces to

$$\frac{d}{a} = \frac{S(\beta) - S(0)}{S(0) \tan \beta} \quad (1.4)$$

and if  $\beta$  corresponds to the angle at which maximum sputtering occurs, consideration of figure 1.5 shows that  $d/a$  is of order unity. Therefore such a ridge should move sideways at about the same rate as it moves downwards.

Thus the model of Stewart and Thompson (1969) provides a qualitative explanation for 'cone' formation in two dimensions. However their model does not take into account processes such as surface diffusion enhanced by ion bombardment, redeposition of sputtered material, the variation in ion current density or even the erosion of a profile whose gradient is continuously changing. Cases undoubtedly occur when this would not be justified and if diffusion were the dominant mechanism, surface-faceting of crystal planes might then result.

Nobes, Colligon and Carter (1969) studied the motion of individual points on a general two dimensional surface initially requiring end points to the contour. However this restriction was later removed (Carter, Colligon and Nobes (1971)). These studies showed that the motion of surface points could be described by a wave equation with space-time dependant velocity. This theory has subsequently been shown to have general applicability and will therefore be described in some detail here.

In describing the general treatment of erosion of a continuous curve Carter et al (1971) have assumed that sputter induced erosion only



is responsible for morphological development. Consider a beam of  $\Phi$  ions/sec striking an area  $A$  of a surface at an angle  $\theta$  to the normal and let  $N$  be the atomic density of the target. In a time  $\delta t$ , let the surface erode by a distance  $\delta r$ , in a direction perpendicular to the surface. Then the number of atoms ejected is  $NA\delta r$  and the number of atoms incident is  $\Phi\delta t$ . Now the sputtering coefficient  $S$ , is defined as the number of atoms of a solid ejected per incident ion. Thus

$$S = \frac{NA\delta r}{\Phi\delta t} = \frac{NA\cos\theta\delta r}{\Phi\cos\theta\delta t} = \frac{N\delta r}{\phi\cos\theta\delta t}$$

where  $\phi$  is the incident flux density. Therefore

$$\frac{\delta r}{\delta t} = \frac{\phi}{N} S(\theta) \cos\theta \quad (1.5)$$

Now consider the erosion of a surface generator lying in the  $x$ - $y$  plane, with the beam of ions incident in the negative  $y$  direction. Let  $A$  and  $B$  be two adjacent points on an eroding surface with centre of curvature at  $P$ , which erode to  $A'$ ,  $B'$  where  $AA'$  and  $BB'$  are perpendicular to the tangents at  $A$  and  $B$ , see figure 1.7. At  $A$  the angle made by the ion beam with the normal is  $\theta$  and at  $B$  is  $(\theta + \frac{\partial\theta}{\partial x}\delta x)$ . Then using equation (1.5)

$$\left. \begin{aligned} AA' &= \frac{\phi}{N} S(\theta) \cos\theta \delta t \\ \text{and} \\ BB' &= \frac{\phi}{N} S\left(\theta + \frac{\partial\theta}{\partial x}\delta x\right) \cos\left(\theta + \frac{\partial\theta}{\partial x}\delta x\right) \delta t \end{aligned} \right\} \quad (1.6)$$

Equation (1.6) can be expanded using Taylors theorem. If  $A'C$  is drawn parallel to  $AB$ , then to first order

$$CB' = BB' - AA' = \frac{\phi}{N} \frac{d}{d\theta} \{S(\theta) \cos\theta\} \frac{\partial\theta}{\partial x} \delta x \delta t$$

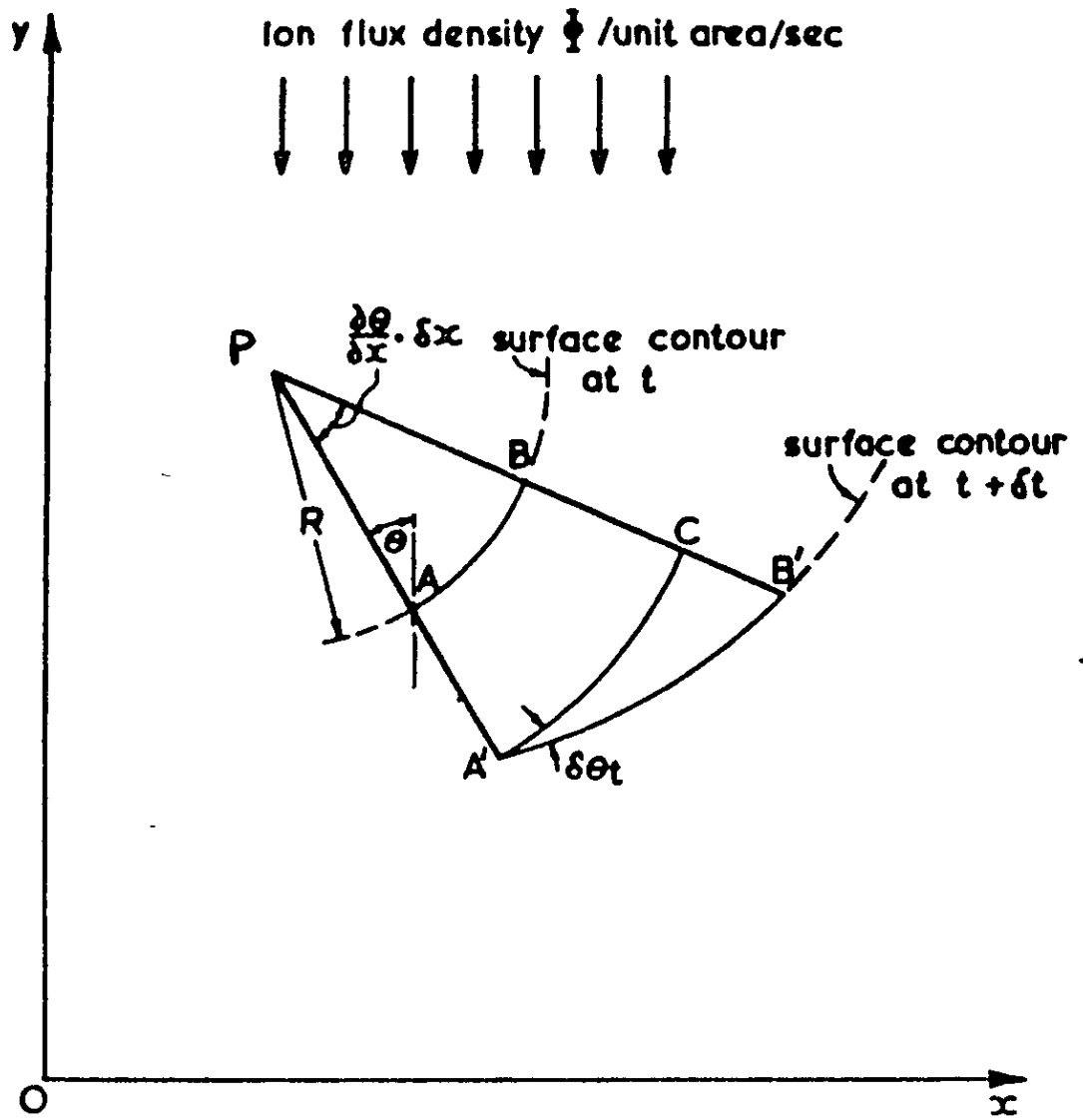


Fig. 1.7. Erosion of a surface generator by an ion flux (After Carter et al (1971)).

and

$$A'C = R \frac{\partial \theta}{\partial x} \delta x$$

If  $\delta \theta_t$  is the change in tangential angle from A to A' in time  $\delta t$ , then

$$- \delta \theta_t = \frac{CB'}{A'C} = \frac{\phi}{NR} \frac{d}{d\theta} \{S(\theta) \cos \theta\} \delta t$$

i.e.

$$\frac{\delta \theta_t}{\delta t} = - \frac{\phi}{NR} \frac{d}{d\theta} \{S(\theta) \cos \theta\} \quad (1.7)$$

This expresses the rate of change of tangential angle in the direction of the surface normal. Now consider  $\theta$  to be a function only of  $x$  and time. Then

$$\delta \theta = \left( \frac{\partial \theta}{\partial x} \right)_t \delta x + \left( \frac{\partial \theta}{\partial t} \right)_x \delta t$$

$$\therefore \frac{\delta \theta}{\delta t} \text{ in any direction} = \left( \frac{\partial \theta}{\partial x} \right)_t \frac{\delta x}{\delta t} + \left( \frac{\partial \theta}{\partial t} \right)_x$$

The above equation expresses the rate of change of  $\theta$  in any direction.

If the direction is chosen to be the normal direction  $n$  then using

(1.7) gives

$$\frac{\phi}{NR} \frac{d}{d\theta} \{S(\theta) \cos \theta\} = \left( \frac{\partial \theta}{\partial x} \right)_t \left( \frac{\partial x}{\partial t} \right)_n + \left( \frac{\partial \theta}{\partial t} \right)_x$$

As  $\left( \frac{\partial \theta}{\partial x} \right)_t = \frac{1}{R \cos \theta}$ , and from equation (1.5) the rate of change in the

$x$  co-ordinate of the point A is given by  $\frac{\phi}{N} S \cos \theta \sin \theta$ , it can be shown

that

$$\left( \frac{\partial \theta}{\partial t} \right)_x \bigg/ \left( \frac{\partial \theta}{\partial x} \right)_t = - \frac{\phi}{N} \cos^2 \theta \frac{dS}{d\theta} \quad (1.8)$$

Conversely, if  $\theta$  is a function only of  $y$  and time, then

$$\frac{\delta\theta}{\delta t} = \left(\frac{\partial\theta}{\partial y}\right)_t \frac{\delta y}{\delta t} + \left(\frac{\partial\theta}{\partial t}\right)_y$$

where 
$$\left(\frac{\partial\theta}{\partial y}\right)_t = -\frac{1}{R\sin\theta}$$

and using equation (1.7) it can be shown that

$$\left(\frac{\partial\theta}{\partial t}\right)_y / \left(\frac{\partial\theta}{\partial y}\right)_t = -\frac{\phi}{N} \left\{ \sin\theta\cos\theta \frac{dS}{d\theta} - S \right\} \quad (1.9)$$

Carter et al (1971) recognised that equations (1.8) and (1.9) defined a wave nature for variations of  $\theta$  with  $x$  and  $t$  and  $y$  and  $t$  respectively, but did not associate this with the kinematic wave process outlined by Lighthill and Whitham (1955). The connection was made after the paper by Barber, Frank, Moss, Steeds and Tsong (1973). These authors developed an apparently different approach to the problem of ion induced erosion when they adapted a theory of chemical dissolution first expounded by Frank (1958), (1972). They studied the spatial and temporal motion of points of constant orientation relative to the ion flux and showed that the loci or trajectories of these points on the real surface could be constructed through use of an 'erosion slowness curve', which is a polar plot of  $1/S(\theta)\cos\theta$  as a function of  $\theta$ . The theory of chemical dissolution employed by Barber et al (1973) is based upon the motion of discrete surface steps, and was shown by Frank (1958), (1972) to obey the equation of motion of kinematic waves studied earlier by Lighthill and Whitham (1955). The theory of Barber et al (1973) will now be outlined here.

Consider a crystal growth or dissolution process, described as a progression of unit steps, each of height  $h$ , across an appropriate reference face of a crystal, figure 1.8 (Frank (1958)). The speed with which steps move depends, among other things, on the proximity of other steps. It has been assumed that this can be expressed as a dependence of speed on density of steps only. The methods used by Frank are precisely those employed by Lighthill and Whitham (1955) to problems of road traffic and river floods, in which also the flow (cars, or gallons, per minute) may often be assumed to depend only on the linear density (cars, or gallons, per mile).

Let  $k$  be the step density i.e. the number of steps per unit length in the neighborhood of a particular point, and let  $q$  be the step flux i.e. the number of steps passing that point in unit time. Then in two dimensions, the slope of the surface at any fixed time is

$$hk = \frac{\partial y}{\partial x} \quad (1.10a)$$

and the dissolution rate normal to the reference surface is

$$hq = - \frac{\partial y}{\partial t} \quad (1.10b)$$

From the basic postulate that  $q = q(k)$  two important velocities are given by

$$v(k) = \frac{q}{k} ; \quad c(k) = \frac{dq}{dk} \quad (1.11)$$

The first is the speed of an individual step; the second is called by Lighthill the "kinematic wave velocity". From the continuity equation (conservation of steps),

$$\frac{\partial q}{\partial x} + \frac{\partial k}{\partial t} = 0$$

we have

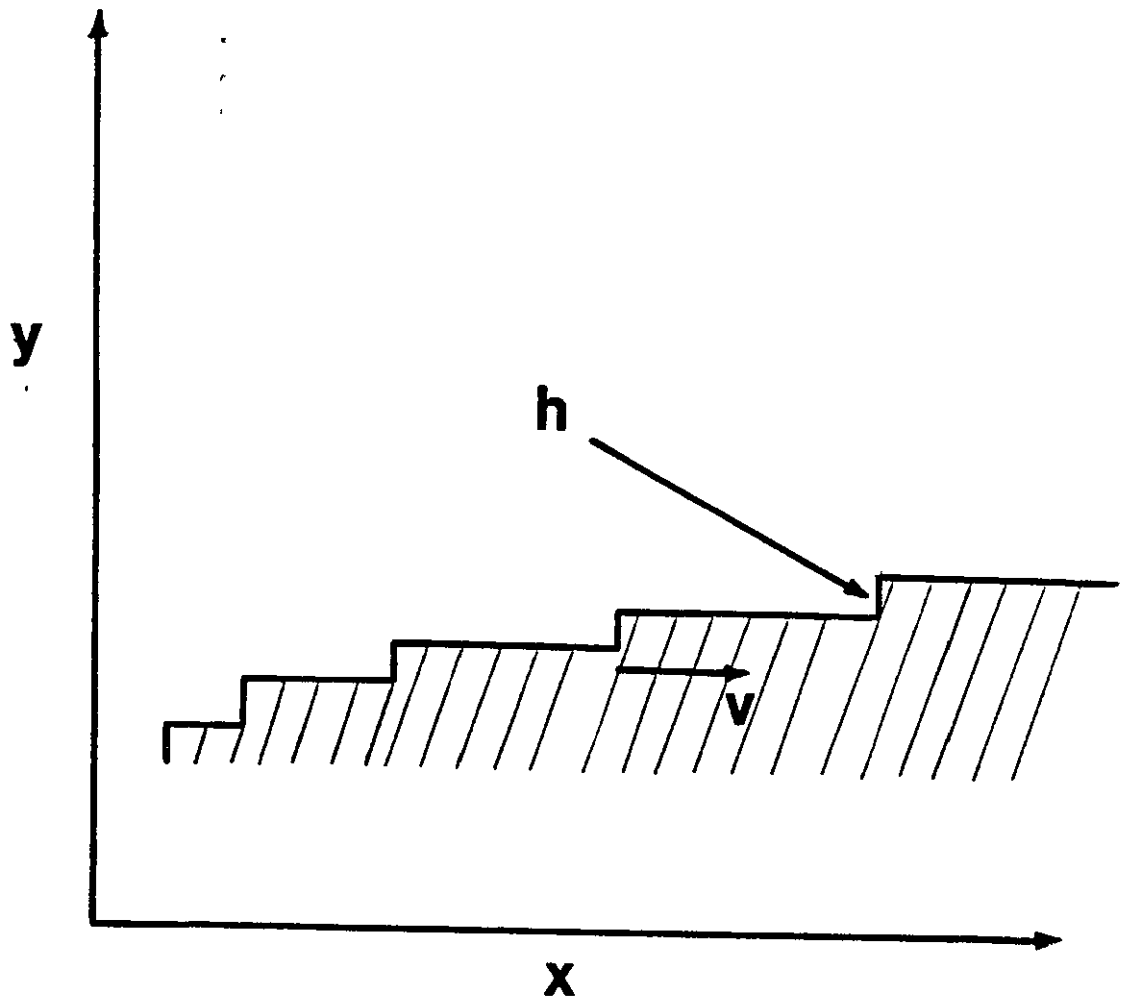


Fig. 1.8. Steps on a crystal face, in the case of dissolution. For the case of growth  $h$  (or  $v$ ) is negative. (After Frank (1958)).

$$\frac{dq}{dk} \cdot \frac{\partial k}{\partial x} + \frac{\partial k}{\partial t} = 0$$

i.e. -

$$c(k) \cdot \frac{\partial k}{\partial x} + \frac{\partial k}{\partial t} = 0 \quad (1.12)$$

This equation implies that in the  $(x,t)$  plane, along a line slope

$$\frac{dx}{dt} = c(k) = \frac{dq}{dk} \quad (1.13)$$

$k$  is constant and therefore  $q$  is constant also. Such a line is called a 'characteristic' and this will be discussed in more detail later in this chapter. Geometrically, the sequence of crystal profiles  $y = y(x)$  at a sequence of times  $t$  defines a surface  $y = y(x,t)$ . The characteristics correspond to lines on this surface, which have just been shown to have straight line projections on the  $(x,t)$  plane. Consider now the projection on the  $(x,y)$  plane. For this

$$\frac{dy}{dx} = \frac{\partial y}{\partial x} + \frac{\partial y}{\partial t} \cdot \frac{dt}{dx}$$

Using equation (1.10) we have

$$\frac{dy}{dx} = h(k - \frac{q}{c}) \quad (1.14)$$

which is constant. The characteristics therefore project as straight lines on the  $(x,y)$  plane also. It follows that they are straight lines on the  $y(x,t)$  surface. The most direct interpretation of equation (1.14) is that points of a given orientation have straight line trajectories. A simple geometric construction from the graph of  $q$  against  $k$  gives the direction of the trajectory of a point of given orientation in accordance with equation (1.14). It is readily shown that a discontinuity in slope, with densities  $k_1$  and  $k_2$  for which the corresponding fluxes are  $q_1$  and  $q_2$ , follows a trajectory in the  $(x,t)$  plane of slope

$$\frac{dx}{dt} = \frac{q_2^{-q_1}}{k_2^{-k_1}}$$

while the trajectory in the (x,y) plane has a slope

$$\frac{dy}{dx} = h \left[ k_1^{-q_1} \cdot \frac{k_2^{-k_1}}{q_2^{-q_1}} \right] = h \left[ k_2^{-q_2} \cdot \frac{k_2^{-k_1}}{q_2^{-q_1}} \right] \quad (1.15)$$

These edge-trajectories are not necessarily straight. Frank also reformulated the above results in vector notation to obtain another useful theorem. Redefine the dissolution rate as measured normal to the actual surface of the crystal (rather than normal to a particular crystallographic plane) and form the polar diagram of the reciprocal of this velocity. Then the trajectory of a point of given orientation on the crystal surface may be shown to be parallel to a normal to the polar diagram at the point of corresponding orientation. The dissolution rate measured normal to the actual macroscopic surface is  $q(1+h^2k^2)^{-\frac{1}{2}}$ . The vector whose magnitude is the reciprocal of this rate, and whose direction is normal to the macroscopic surface, is

$$\begin{aligned} \underline{d} &= q^{-1}(1+h^2k^2)^{\frac{1}{2}} \cdot (h\underline{k}\underline{i}-\underline{j}) \cdot (1+h^2k^2)^{-\frac{1}{2}} \\ &= q^{-1}(h\underline{k}\underline{i}-\underline{j}) \end{aligned} \quad (1.16)$$

where  $\underline{i}$  and  $\underline{j}$  are unit vectors in the x and y directions. The tangent to the polar diagram of  $\underline{d}$  has the same direction as

$$\begin{aligned} \underline{e} &= \frac{d\underline{d}}{dk} = -q^{-2} \left( \frac{dq}{dk} \right) (h\underline{k}\underline{i}-\underline{j}) + q^{-1}h\underline{i} \\ &= -cq^{-2} \{h(k-q/c)\underline{i} - \underline{j}\} \end{aligned} \quad (1.17)$$

The orientation trajectory according to equation (1.14) has the direction of the vector



$$\underline{F} = \underline{i} + h(k - q/c)\underline{j} \quad (1.18)$$

The vectors  $\underline{e}$  and  $\underline{F}$  are orthogonal as  $\underline{e} \cdot \underline{F} = 0$ . This establishes the fact that the orientation trajectory is parallel to a normal, at the point of corresponding orientation, to the polar diagram of reciprocal velocity of dissolution. Frank enunciated these results in several theorems as follows:-

1. The locus of a point on the crystal surface with a given orientation is a straight line called a dissolution trajectory (Equations (1.12) and (1.14)).
2. If the reciprocal of the dissolution rate normal to the surface is plotted in polar form as a function of surface orientation, then the trajectory of a point on the crystal surface of a given orientation is parallel to the normal to the polar diagram at the point of corresponding orientation (Equations (1.16), (1.17) and (1.18)).

A corollary to these theorems is that at a discontinuity (an edge) the dissolution trajectory is parallel to the normal to the chord in the polar diagram joining the points corresponding to the orientations of points at either side of the edge (this follows from equation (1.15)).

Barber et al (1973) saw that the similarity between sputtering and chemical etching lies in the fact that the erosion rate of a given element of specimen surface due to sputtering also depends on the orientation of that element, which is usually expressed as the variation of sputtering yield with the angle of incidence of the ion beam. As Frank's theorems have been successfully applied to interpret experimental results on the dissolution of crystals (Frank and Ives (1960),

Ives (1961)) Barber et al demonstrated that they are equally applicable to the erosion of surfaces by ion bombardment.

Barber et al assumed that the depth  $d$  sputtered from a plane surface is given by (c.f. equation (1.5))

$$d = \frac{\phi t}{N} S(\theta) \cos\theta \quad (1.19)$$

where  $\phi$  is the number of ions per second striking unit area of surface normal to their direction,  $N$  is the number of atoms per unit volume of target material,  $t$  is the time of bombardment,  $S$  the sputtering yield and  $\theta$  the angle between the ion beam and the target normal. The parameter of interest is the thickness of material removed by sputtering rather than the number of atoms ejected from the surface at any given time. Therefore it is convenient to plot  $S(\theta)\cos\theta/S(0)$  against  $\theta$ . Figure 1.9 shows such a plot for the case of a silica glass surface bombarded by  $\text{Ar}^+$  ions. The data is taken from Bach (1970). Silica glass was chosen since it is single-phase and non-crystalline and thus the assumption that the amount of surface eroded is entirely dependent on the inclination of the ion beam to the surface can be made.

From the data of figure 1.9, they plotted the reciprocals of the sputtering ratio  $S(\theta)\cos\theta/S(0)$  in accordance with the second theorem of Frank. This they call the "erosion slowness" polar diagram and it is shown in figure 1.10. Given a particular starting surface shape they were able to deduce the successive sputtered topographies for silica glass. They considered the case of a glass sphere which is represented in two dimensions by a circle on polar graph paper, which is superimposed on the erosion slowness curve of figure 1.10. The next step is to draw the orientation trajectories which obey the

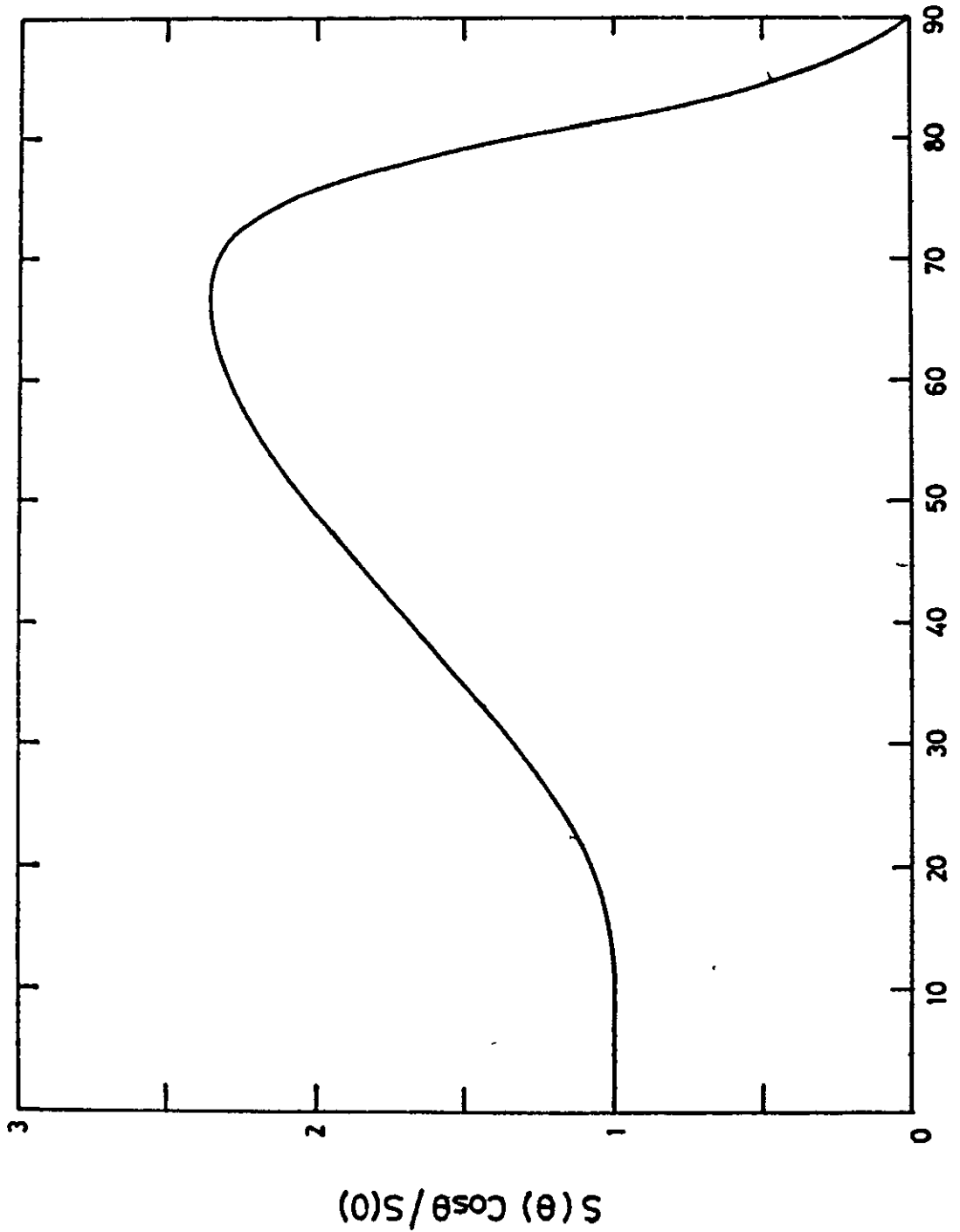


Fig. 1.9. Variation of sputtering ratio with angle of incidence for  $\text{Ar}^+$  ions on silica glass, derived from experimental results of Bach (1970).

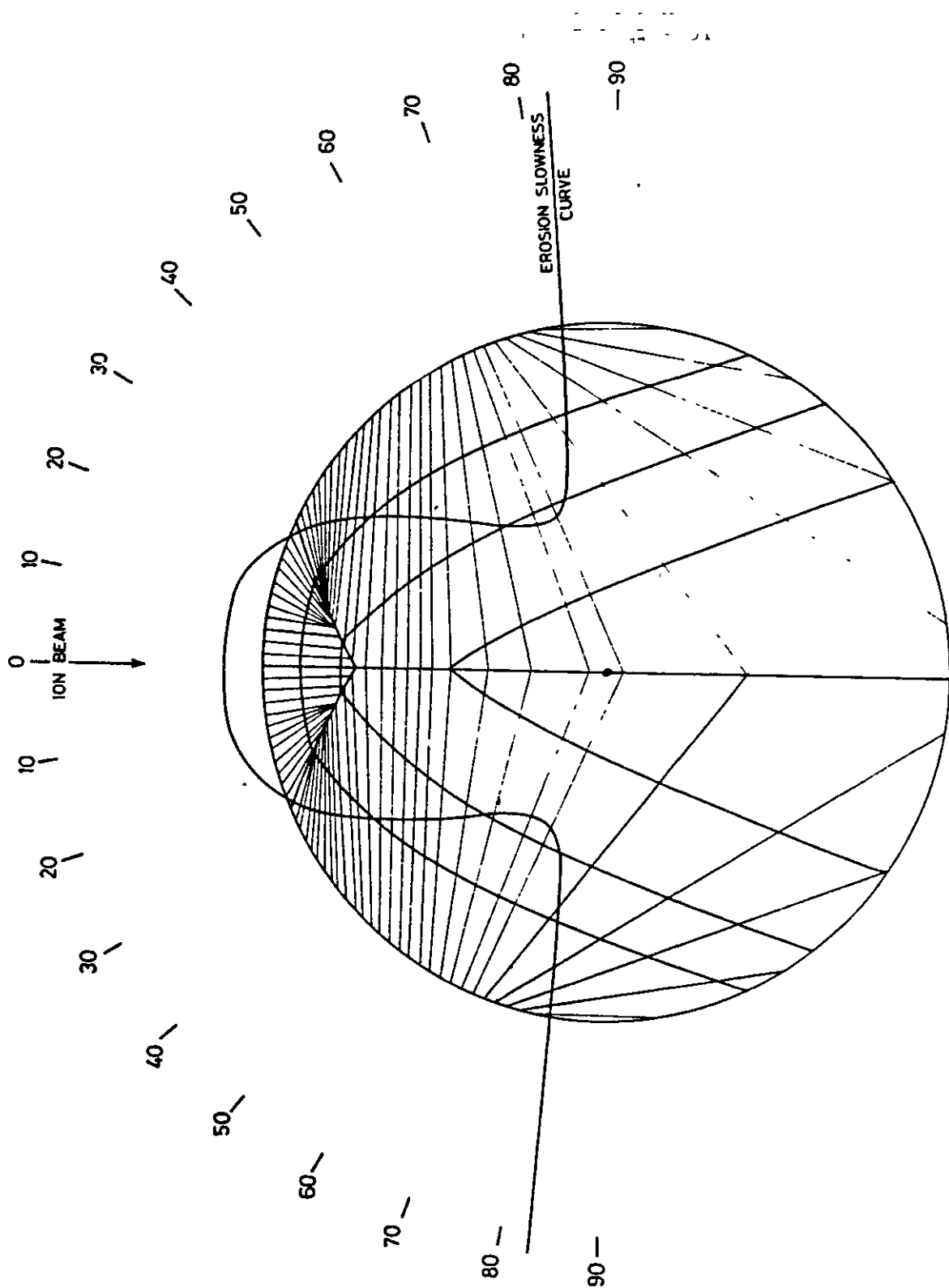


Fig. 1.10. Polar diagram of the reciprocal sputtering ratio for silica (erosion slowness curve) and the 'dissolution' trajectories and derived profiles for the sputtering of a silica glass sphere (After Barber et al (1973)).

dissolution theorems. These trajectories are parallel to the direction of the normals to the erosion slowness curve at corresponding orientations. They are drawn inwards towards the inside of the circle because of erosion due to ion bombardment. The final step is to derive resultant topographies at any given time during bombardment from the trajectory array constructed. Three resultant shapes of the bombarded surface are shown in figure 1.10. The first corresponds to the shape after a short time of bombardment and the second and third correspond to longer periods. These shapes agree quite well with the experimental observations on ion bombarded metal spheres by Wehner (1959). The isotropic theory is presumably applicable on account of the small grain size of the material. Differences are probably due to the effects of the impurities at the cone tips.

Barber et al went on to apply the erosion slowness curve to a hemispherical trough and a sinusoidal surface. They showed that the sputtering of a deep trough will turn it into a shaft-like depression with vertical walls and a flat bottom whereas sputtering of a shallower trough results in the widening of the trough and a decrease in the slope of the sidewalls. The evolution of a sinusoidal surface ( $y = \sin x$ ,  $0 \leq x \leq \pi$ ) indicates a polishing process i.e. the initial convex topography ( $0 \leq x \leq \frac{\pi}{2}$ ) in the direction of the ion beam progresses towards flatness as does the trough for  $\frac{\pi}{2} \leq x \leq \pi$ . This is a more accurate description of what actually goes on during the bombardment of a sinusoidal surface than that reported by Catana et al (1972) whose computer simulation predicts an equilibrium topography of a sharp peak and a plateau. The difference is not a consequence of the exact form of the sputtering curve but rather a spurious result arising in the computational procedure used by Catana et al (1972).

Ishitani, Kato and Shimizu (1974) have modified the programme of Catana et al and have shown that the final equilibrium shape is indeed a featureless plane as predicted by Barber et al (1973). The method of Barber et al (1973) has been further applied by Witcomb (1975) to predict the apex angles of conical structures produced by ion bombardment.

Thus the theory of Barber et al (1973) has been shown to give results which agree well with experimental results. However the use of erosion slowness curves has its limitations. The slowness curves are convenient since they enable the development of a geometrical construction, but these are not easily extended into three dimensions. Erosion slowness curves are restricted to use with a uniform flux, since a family of curves are required for a non uniform flux. It is also difficult to see how the erosion slowness curves could be modified to include the effects of redeposition, ion reflection and surface diffusion.

At this point Carter, Colligon and Nobes (1973) recognising the similar wave nature of surface point motion in their own earlier studies (Nobes et al (1969), Carter et al (1971)) and in the Lighthill and Frank basis of Barber et al's treatment, proposed a generalised approach to sputter erosion. They were able to show that the continuum approach of their own earlier work and the intersection plane approach of Stewart and Thompson (1969) both fall within the general framework of Barber et al's extension of the Frank theory of crystal dissolution. The generalised theory proposed by Carter et al (1973) has been shown to have general applicability and it is easier to compute solutions with this theory than the erosion slowness curve approach. The same approach cannot be used to extend the theory into three dimensions.

However recently Carter, Nobes, Arshak, Webb, Evanson, Eghawary and Williamson (1979) have considered the influence of a non-uniform incident flux upon the surface erosion process in two dimensions, but this treatment has its limitations and these will be discussed later. Also the theory does not take into account the effects of redeposition of sputtered material and ion reflection, and its extension to include these effects is not clear. It must however be pointed out that Frank (1972) has given a three dimensional theory for the case of crystal dissolution but its application to the sputtering case is not entirely clear.

Ducommun, Cantagrel and Marchal (1974) and Ducommun, Cantagrel and Moulin (1975) have obtained similar results by treating a general surface contour as an envelope of linear segments and investigating the time dependent behaviour of this envelope during erosion. These authors paid particular attention to the behaviour of edges or discontinuities on a surface which form as the local radius of curvature becomes zero and have extended the earlier work of Barber et al (1973) in this respect. The treatment of Ducommun et al (1974) will now be outlined here.

Ducommun et al considered the erosion of a surface contour (C) lying in the x-y plane and represented by the equation  $y = f(x,0)$ . As with other theoretical treatments before them, secondary effects such as defects introduced by ion bombardment, redeposition of sputtered material and diffusion are ignored. They considered (C),  $y = f(x,0)$  to be the envelope of a family of straight lines (D) described by:

$$y - xf'(x_i) + x_i f'(x_i) - f(x_i) = 0 \quad (1.20)$$

where  $x_i, y_i = f(x_i)$  is an arbitrary point of C. The family of straight lines (D') transformed from the family (D) by ion beam erosion is

$$y - xf'(x_i) + x_i f'(x_i) - f(x_i) + A(x_i) = 0 \quad (1.21)$$

where  $A(x_i)$  is the displacement of a straight line (D) parallel to itself.  $A(x_i)$  can be represented as a function of the parameters that govern the ion beam erosion process. Thus

$$A(x_i) = A[\theta(x_i)] = \frac{\phi}{N} t S(\theta) \quad (1.22)$$

where  $\tan\theta = f'(x_i)$  for  $-\frac{\pi}{2} < \theta < +\frac{\pi}{2}$  and  $\phi$  is the ion flux in the negative y direction, N the atomic density of the target, t is time in seconds and S is the sputtering yield. The new surface contour (C') is the envelope of (D') and is given by the solution of the system of equations

$$y - xf'(x_i) + x_i f'(x_i) - f(x_i) + A(x_i) = 0 \quad (1.23)$$

$$-xf''(x_i) + x_i f''(x_i) + \frac{\delta A(x_i)}{\delta x_i} = 0 \quad (1.24)$$

Equation (1.24) is equivalent to

$$x = x_i + \frac{1}{f''(x_i)} \frac{\delta A(x_i)}{\delta x_i} \quad (1.25)$$

Substituting  $\tan\theta = f'(x_i)$  and equation (1.22) into (1.25) and (1.23) gives

$$x = x_i + \frac{\phi t}{N} \cos^2 \theta \frac{dS(\theta)}{d\theta} \quad (1.26)$$



$$y = f(x_i) + \frac{\phi t}{N} \left\{ \sin\theta \cos\theta \frac{dS(\theta)}{d\theta} - S(\theta) \right\} \quad (1.27)$$

as obtained previously by other authors. According to equations (1.26) and (1.27), for any point  $(x_i, y_i)$  of  $C$  there is a corresponding point on  $(C')$ . In the mathematical treatment the angles  $\theta$  measured on  $(C)$  are preserved on  $(C')$ . However, physically some points  $(x, y)$  of the transformed curve disappear. This is because the translations along  $x$  and  $y$ , as defined by equations (1.26) and (1.27), occur simultaneously. Thus the authors followed the development of the surface contour and derived expressions for cusps and double points. Cusps, when existing are given by

$$\frac{dx}{dx_i} = 1 + \frac{d}{dx_i} (\Delta x(x_i)) = 0 \quad (1.28)$$

$$\frac{dy}{dx_i} = f'(x_i) + \frac{d}{dx_i} (\Delta y(x_i)) = 0 \quad (1.29)$$

Equations (1.28) and (1.29) are interdependent and lead to

$$\frac{\phi t}{N} \left[ \cos^2\theta \frac{d^2S(\theta)}{d\theta^2} - 2\sin\theta\cos\theta \frac{dS(\theta)}{d\theta} \right] \cos^2\theta f''(x_i) = -1$$

This is equivalent to

$$\frac{\phi t}{N} \left[ 2\sin\theta \frac{dS(\theta)}{d\theta} - \cos\theta \frac{d^2S(\theta)}{d\theta^2} \right] \frac{f''(x_i)}{|f''(x_i)|} = R(x_i, 0) \quad (1.30)$$

where  $R(x_i, 0)$  is the radius of curvature of  $(C)$ . Equation (1.30) will be verified if  $R(x_i, 0)$  and

$$Z(x_i, t) = \frac{\phi t}{N} \left[ 2\sin\theta \frac{dS(\theta)}{d\theta} - \cos\theta \frac{d^2S(\theta)}{d\theta^2} \right] \frac{f''(x_i)}{|f''(x_i)|}$$

are secant. The authors then designated

$$Z^*(\theta) = 2\sin\theta \frac{dS(\theta)}{d\theta} - \cos\theta \frac{d^2S(\theta)}{d\theta^2}$$

with  $-\frac{\pi}{2} < \theta < \frac{\pi}{2}$  and  $S$  being defined in the same interval. They then analysed the function  $Z^*(\theta)$  when  $S(\theta)$  was a prescribed function of  $\theta$  given by (Catana et al (1972))

$$S(\theta) = 3.2696\cos\theta + 13.1059\cos^2\theta - 15.3755\cos^4\theta \quad (1.31)$$

They showed that the cusps, when they exist, can be associated in pairs and occur when  $R(x_i, 0) = 0$ . Each pair of cusps gives rise to a double point. However, the mathematical analysis of double points and cusps predicted more features than were expected. A physical interpretation of these points showed that the extra features disappear when a time parameter is introduced into the analysis. They devised a computer programme to solve equations (1.26) and (1.27) which allowed the curve (C') to be drawn from (C) using a non-iterative method. Figure 1.11 shows the results when the curve (C) is represented by  $y = 0.1 \sin x$ . As can be seen one double point and two cusps have appeared.

The part of the curve (C') which contains the cusps over the double point has no physical significance, so the points (x,y) of this part of (C') vanish. The same phenomena occurs when the double point is not on the symmetry axis. So the physical contour (C') will exhibit corners instead of double points of the mathematical contour.

Thus the computer programme was modified to search for cusps, calculate the double points and to strike out the points that have no physical significance. The completed programme was applied to the curve  $y = a \sin x$ ,  $a = 0.1, 1.0$  and  $5.0$ , see figure 1.12.  $N$  is an

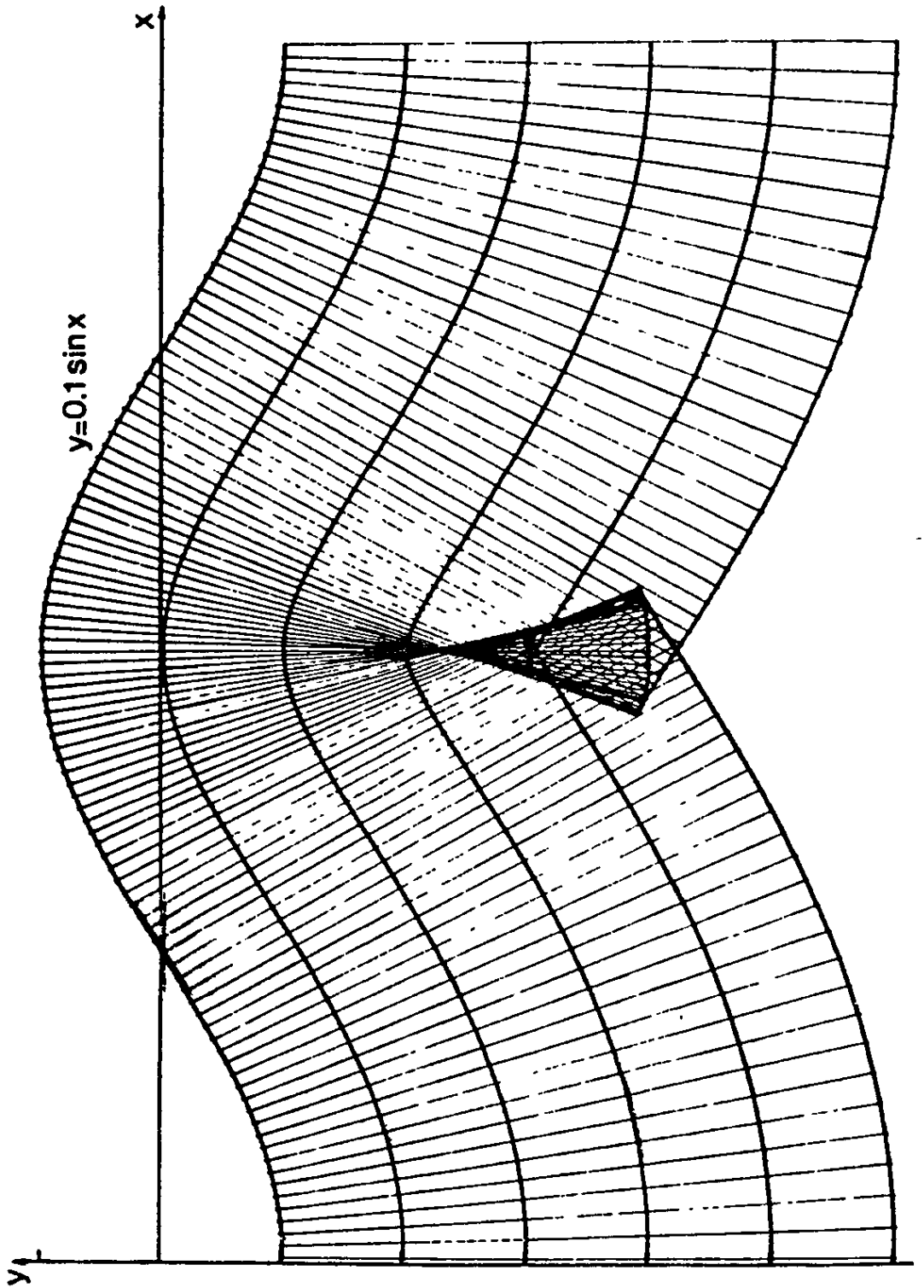


Fig. 1.11. Mathematical evolution of a profile defined by the function  $y = 0.1 \sin x$ . (After Ducommun et al (1974)).

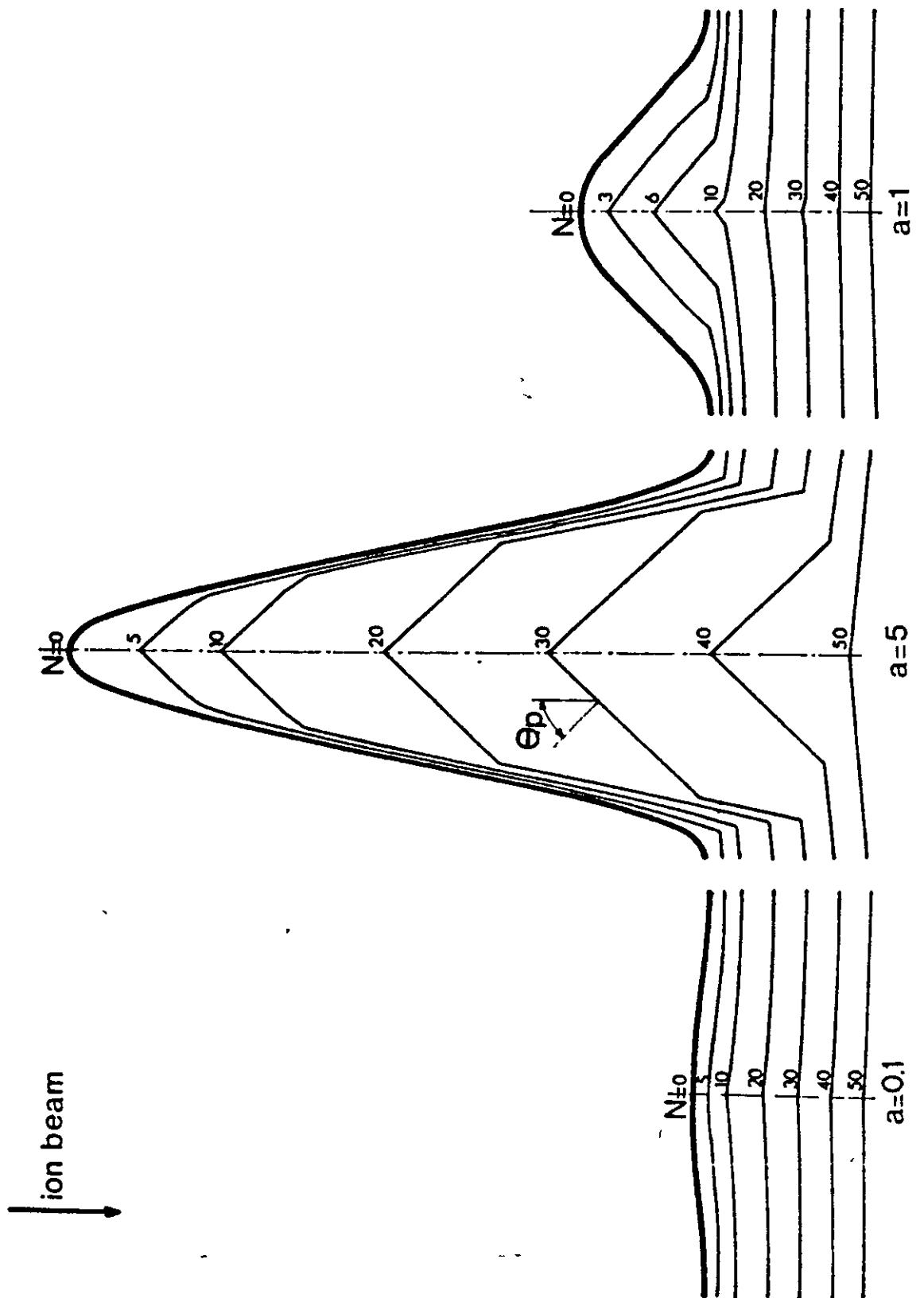


Fig. 1.12. Evolution of profiles defined by the function  $y = a \sin x$  (After Ducommun et al (1974)).

integer in the programme related to time. The general tendency of a sinusoidal contour is to progressively transform into a horizontal straight line. This result is in agreement with that of Barber et al (1973) who also predict a horizontal surface as the final equilibrium topography for a sinusoidal contour.

Thus the theory of Ducommun et al (1974), (1975) can predict the formation of edges or discontinuities on a surface which form as the local radius of curvature becomes zero. They have also devised a non-iterative method for predicting the shape of ion eroded profiles. Their method of treating a general surface contour as an envelope of linear segments has been shown to lead to the same results as the theories of Carter et al (1973) and Barber et al (1973).

In summary, in the preceding pages previous theories used to describe the erosion of surfaces have been outlined. The advantages and disadvantages of each theory have been discussed. It can be seen that all the models suffer from the same limitations viz. they are difficult to extend into three dimensions, to deal with a non-uniform ion flux and to deal with crystalline materials. The crystal dissolution theory as originally outlined by Frank (1958), (1972) was presented in two and three dimensions but the way in which it could be applied to the sputtering case, in three dimensions, was not clear. Not only do the theories ignore secondary effects such as redeposition of sputtered material, surface diffusion, ion reflection off steep profiles and volume diffusion, but it also seems very difficult to modify them to incorporate these effects. In this context it should be noted that Carter (1976) has treated surface and volume diffusion, in two dimensions, using the differential erosion theory. However, the analysis presented by Carter (1976) is not strictly correct and this will be discussed in more detail in a later chapter.

A three dimensional theory of surface erosion has recently been presented which can also be used to deal with a non-uniform ion flux, in three dimensions (Smith and Walls (1979),(1980)). This theory has subsequently been extended to include the effects of the crystalline structure of the material (Smith, Makh and Walls (1980), Smith, Valkering and Walls (1981)) and, in two dimensions, the effects of redeposition of sputtered material (Makh, Smith and Walls (1980b)). This theory, the method of characteristics, will now be outlined.

### 1.3. The method of characteristics.

Consider a surface whose equation at time  $t$  is  $A(\underline{r},t) = 0$ , where  $\underline{r}$  is the position vector of a point on the surface. Let the surface be subjected to an ion bombardment of incident ion flux  $\phi$  (ions.cm<sup>-2</sup>sec<sup>-1</sup>) in the  $z$  direction defined by a unit vector  $\underline{k}$  and let the atomic density of the target be  $N$ . Here the spatial variation in  $\phi$  is described by the function  $\phi = \phi(x,y)$  where  $x$  and  $y$  are the cartesian co-ordinates perpendicular to  $z$ . Thus the rate of erosion of the target in the surface normal direction is  $\frac{\phi}{N} S \underline{k} \cdot \underline{n}$ , where  $\underline{n}$  is the unit normal to the surface. Let the angle between the normal and the  $z$ -direction be  $\theta$ . It is assumed that  $S$  depends only on  $\theta$  so that the differential equation describing erosion in the normal direction is

$$\frac{\partial r_n}{\partial t} = - \frac{\phi}{N} S(\theta) \cos \theta \quad (1.32)$$

where  $r_n$  is distance in the normal direction. Smith and Walls (1979), (1980) then showed that as  $\delta t \rightarrow 0$  the equation describing the motion of the surface can be written as

$$\frac{\partial A}{\partial t} - \frac{\phi}{N} S(\theta) \cos\theta |\nabla A| = 0 \quad (1.33)$$

This is a non-linear first order partial differential equation of a type that occurs in geometrical optics and is sometimes known as the eikonal or Jacobi's equation (Whitham (1974)). In the further construction of the solution it is convenient to specify the surface  $A(\underline{r}, t) = 0$  in a form where  $t$  is given explicitly as a function of  $\underline{r}$ , i.e.

$$A(\underline{r}, t) = t - \sigma(\underline{r}) = 0 \quad (1.34)$$

The family of surfaces  $\sigma(\underline{r}) = \text{constant}$  gives the successive positions of the surface as it erodes with time. Smith and Walls then showed that equation (1.33) can be written in the standard form (Whitham (1974))

$$H(\underline{r}, \underline{p}, \sigma) = 1 - \frac{\phi^2}{N^2} S^2 \sigma_z^2 = 0 \quad (1.35)$$

for which a standard method of analysis exists. Here subscripts denote partial derivatives. In equation (1.35)  $\underline{p} = (\sigma_x, \sigma_y, \sigma_z)$ . The method of solution is to determine the characteristic lines of equation (1.35). Essentially these are lines in space along which the partial differential equation (1.35) can be reduced to a set of ordinary 'characteristic' differential equations. In principle, the solution in a whole region can be obtained by integrating these characteristic equations along the characteristics covering the region.

Let a characteristic curve be given in parametric form by  $\underline{r} = \underline{r}(\lambda)$  for some parameter  $\lambda$ . Then such curves are the lines defined by (Whitham (1974))

$$\frac{dx}{d\lambda} = \frac{\partial H}{\partial \sigma_x}; \quad \frac{dy}{d\lambda} = \frac{\partial H}{\partial \sigma_y}; \quad \frac{dz}{d\lambda} = \frac{\partial H}{\partial \sigma_z}; \quad (1.36)$$

with corresponding characteristic equations

$$\left. \begin{aligned} \frac{d\sigma_x}{d\lambda} &= -\sigma_x \frac{\partial H}{\partial \sigma} - \frac{\partial H}{\partial x} \\ \frac{d\sigma_y}{d\lambda} &= -\sigma_y \frac{\partial H}{\partial \sigma} - \frac{\partial H}{\partial y} \\ \frac{d\sigma_z}{d\lambda} &= -\sigma_z \frac{\partial H}{\partial \sigma} - \frac{\partial H}{\partial z} \end{aligned} \right\} \quad (1.37)$$

and where  $t$  is related to  $\lambda$  by

$$\frac{dt}{d\lambda} = \sigma_x \frac{\partial H}{\partial \sigma_x} + \sigma_y \frac{\partial H}{\partial \sigma_y} + \sigma_z \frac{\partial H}{\partial \sigma_z} \quad (1.38)$$

Thus Smith and Walls (1979), (1980) determined the characteristic lines to be given by the equations

$$\frac{dx}{dt} = -\frac{S'}{S} \cos^2 \theta \frac{\sigma_x}{\sigma_z (\sigma_x^2 + \sigma_y^2)^{\frac{1}{2}}} \quad (1.39)$$

$$\frac{dy}{dt} = -\frac{S'}{S} \cos^2 \theta \frac{\sigma_y}{\sigma_z (\sigma_x^2 + \sigma_y^2)^{\frac{1}{2}}} \quad (1.40)$$

$$\frac{dz}{dt} = \frac{1}{\sigma_z} + \frac{S'}{S} \frac{(\sigma_x^2 + \sigma_y^2)^{\frac{1}{2}}}{\sigma_x^2 + \sigma_y^2 + \sigma_z^2} \quad (1.41)$$

with the characteristic differential equations reducing to

$$\frac{\phi_x}{\phi} = \frac{d\sigma_x}{dt}; \quad \frac{\phi_y}{\phi} = \frac{d\sigma_y}{dt}; \quad \frac{d\sigma_z}{dt} = 0 \quad (1.42)$$

(The way in which the method of characteristics can be used to derive the equations of the characteristic lines, in two dimensions, is shown in Appendix 1).



In the case of a uniform beam ( $\phi = \text{constant}$ ) these characteristics are the trajectories of constant surface orientation, since the right hand sides of equation (1.42) are constant. Since  $(\sigma_x, \sigma_y, \sigma_z)$  is a constant vector along the characteristics the right hand sides of equations (1.39) - (1.41) are also constant and thus the characteristics are straight lines. In the general non-uniform case this will not be so and the characteristics will be curved. Smith and Walls in particular emphasised the fact that, although the trajectories of constant surface orientation have been used in both geometrical and numerical calculations, the equivalence of these lines with the 'rays' of geometrical optics and the general physical significance of the characteristics have not previously been recognised. This analogy is useful since it enables the visualisation of an eroding surface as an advancing wave front.

Smith and Walls then carried out numerical calculations to follow the erosion of an elliptical hummock in three dimensions bombarded by a uniform and non-uniform beam. For a uniform beam ( $\phi = \text{constant}$ ), the vector  $(\sigma_x, \sigma_y, \sigma_z)$  is a constant and after a time  $t_1$  the new surface is the envelope of the points  $(x'_i, y'_i, z'_i)$  where

$$\left. \begin{aligned} x'_i &= x_i - \frac{S'}{S} \cos^2 \theta \frac{\sigma_x}{\sigma_z (\sigma_x^2 + \sigma_y^2)^{\frac{1}{2}}} t_1 \\ y'_i &= y_i - \frac{S'}{S} \cos^2 \theta \frac{\sigma_y}{\sigma_z (\sigma_x^2 + \sigma_y^2)^{\frac{1}{2}}} t_1 \\ z'_i &= z_i + \left\{ \frac{1}{\sigma_z} + \frac{S'}{S} \frac{(\sigma_x^2 + \sigma_y^2)^{\frac{1}{2}}}{\sigma_x^2 + \sigma_y^2 + \sigma_z^2} \right\} t_1 \end{aligned} \right\} \quad (1.43)$$

since the right hand sides of equations (1.39) - (1.41) are then constant. It is possible to obtain physically unrealistic solutions when the characteristic lines intersect. It is important that such spurious points are removed since they are physically unrealistic. When the folded part of the surface is removed the surface normal changes discontinuously and edges are formed. The results of a typical sequence of simulations are shown in figure 1.13. All the simulations were obtained using a two point perspective view at an azimuth altitude of  $45^\circ$ . The particular form of  $S(\theta)$  curve was that used previously by Ducommun et al (1975) and is given by

$$S(\theta) = 18.73845\cos\theta - 64.65996\cos^2\theta + 145.19902\cos^3\theta \\ - 206.04493\cos^4\theta + 147.31778\cos^5\theta - 39.89993\cos^6\theta.$$

This form corresponds to experimental results obtained for silicon whose surface is amorphous under ion bombardment, but the application of the method to more complex cases including crystalline surfaces is straightforward providing the appropriate  $S(\theta)$  dependence is known.

The particular shape of the hummock is shown in figure 1.13(a) while the way in which the shape develops under the influence of equal doses of spatially uniform ion flux is shown in figures 1.13(b), 1.13(c) and 1.13(d).

When the beam is not uniform then equations (1.39) - (1.41) and equation (1.42) must be solved numerically. In this case a closed form solution for  $(x'_1, y'_1, z'_1)$  cannot be written down as in equation (1.43). The ion flux distribution was assumed to be Gaussian and described by

$$\phi = \phi_0 \exp \left[ -\frac{x^2 + y^2}{\rho^2} \right]$$

with  $\rho = \frac{1}{\sqrt{3}}$

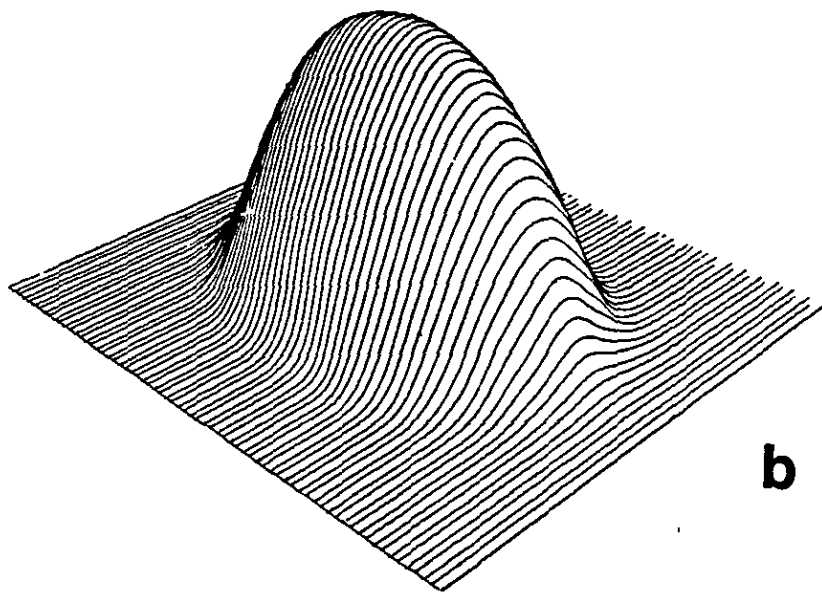
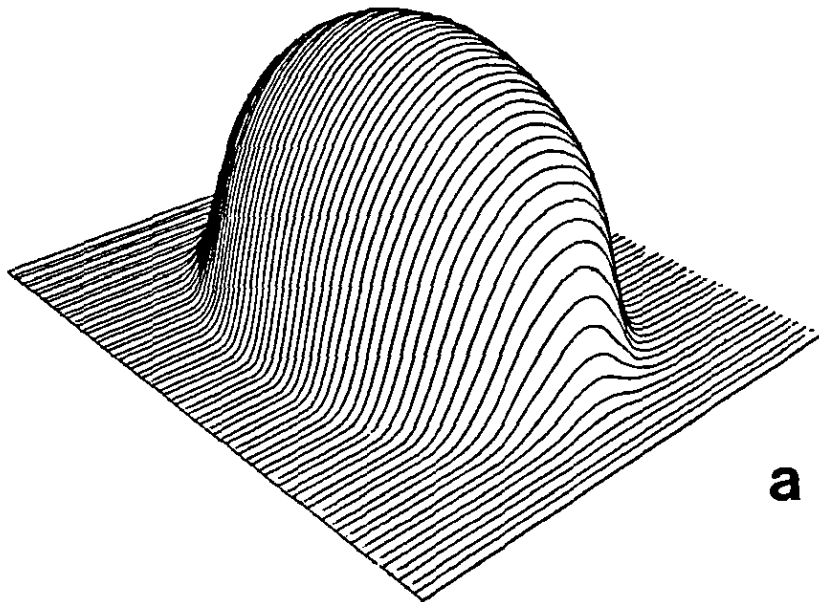
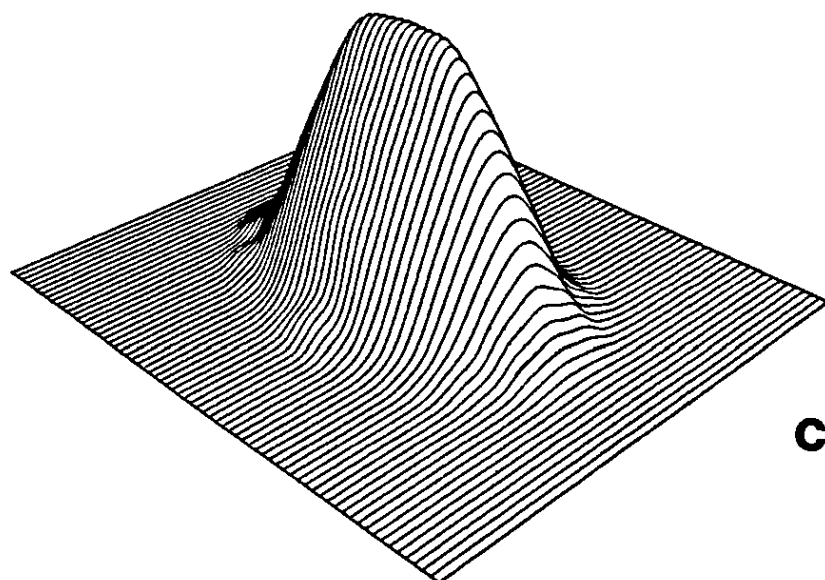
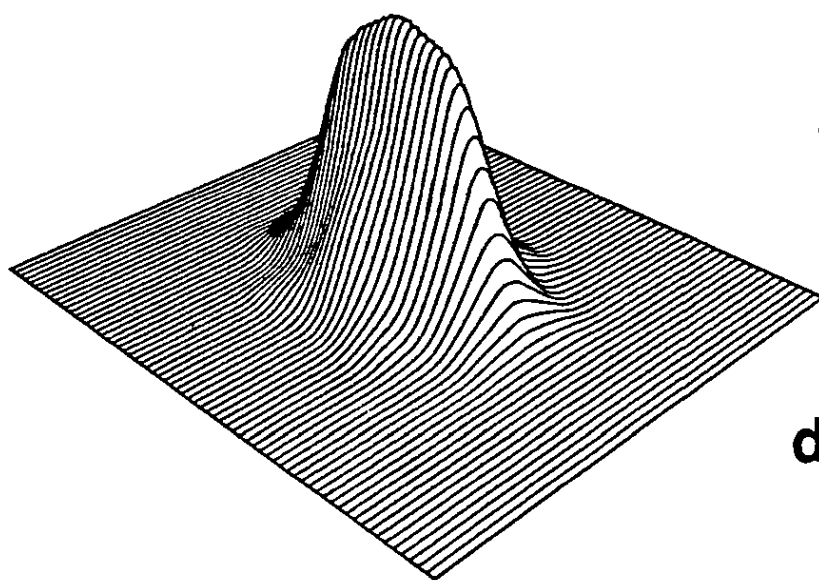


Fig. 1.13. Two point perspective view of an amorphous elliptical hummock, subject to bombardment by a uniform ion beam (a) before ion bombardment  $\phi t/N = 0$  (b)  $\phi t/N = 0.2$  (c)  $\phi t/N = 0.4$  (d)  $\phi t/N = 0.6$  (After Smith and Walls (1980)).



**c**



**d**

This value of  $\rho$  was chosen so that the effective ion beam width and the hummock size were of the same order magnitude. The results of ion bombardment following equal increments of ion dose are shown in figures 1.14(a), 1.14(b) and 1.14(c) and this should be compared with the original starting shape shown in figure 1.13(a).

Thus it can be seen that the characteristic line approach provides a very useful method for studying the erosion of surfaces in two or three dimensions. It can be used to follow the development of surface shape under bombardment by either a uniform or non-uniform ion flux in three dimensions. Recently, using the method of characteristics, Smith, Makh and Walls (1980), have outlined a method by which the erosion of crystalline materials could be followed and presented results showing the erosion of a crystalline surface in two dimensions. Subsequently, Smith, Valkering and Walls (1981), have presented a fully three dimensional theory for the erosion of crystalline surfaces under ion bombardment. The problem of redeposition of sputtered material has also been treated using the method of characteristics in two dimensions (Makh, Smith and Walls (1980b)) and will be outlined in a following chapter.

Thus the method of characteristics can be seen to be a very versatile theory which suffers few of the limitations of the theories of Stewart and Thompson (1969), Carter et al (1973), Barber et al (1973) and Ducommun et al (1974). One of the drawbacks to the theory, which it has in common with the other theories, is that it can predict points on an eroded profile which, although mathematically feasible, have no physical meaning. This occurs when the surface develops a fold, and then these physically unrealistic points must be removed. However the

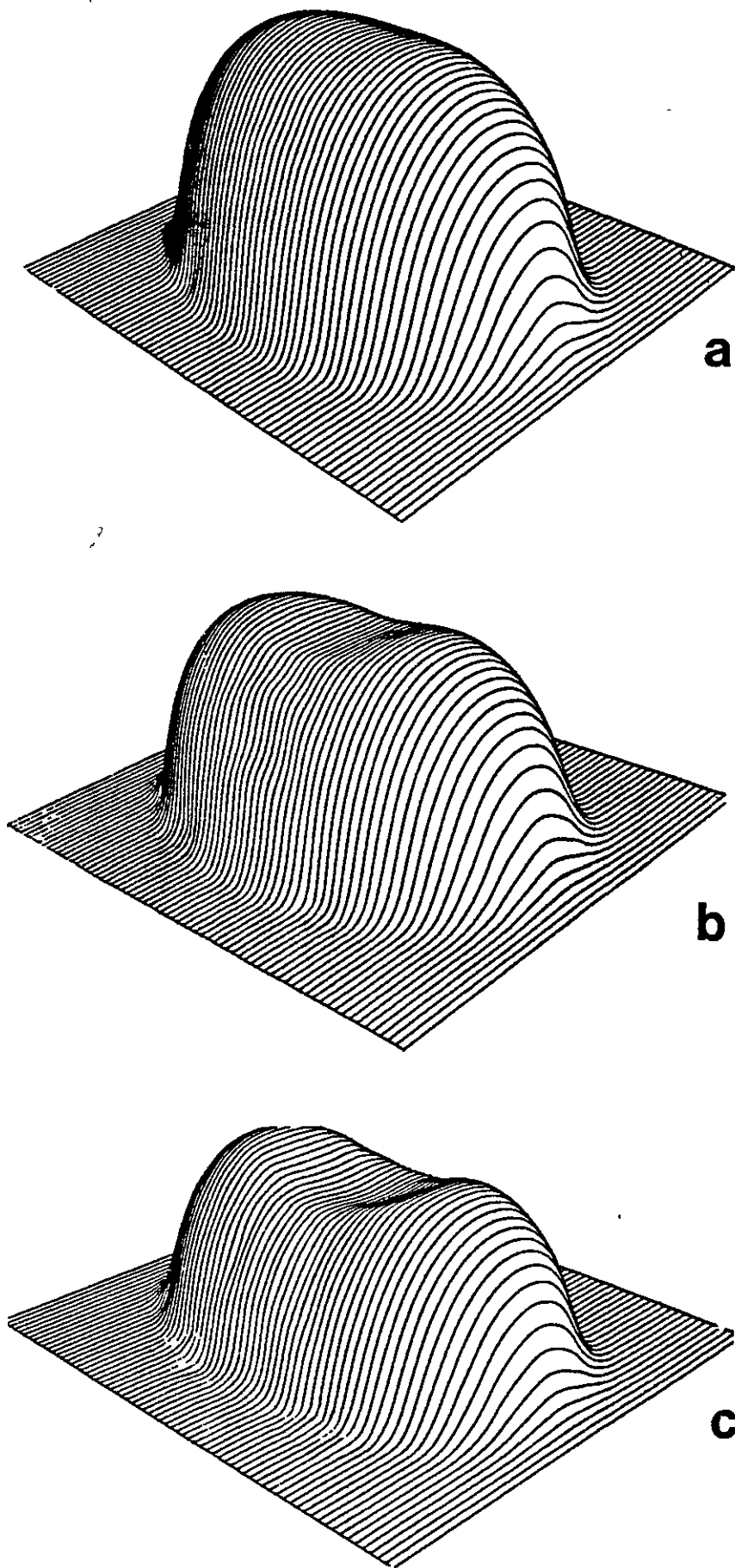


Fig. 1.14. Two point perspective view of an amorphous elliptical hummock, subject to bombardment by a non-uniform, Gaussian ion beam with  $\rho = 1/\sqrt{3}$  and with the same starting shape as figure 1.13 (a)  $\phi t/N = 0.2$  (b)  $\phi t/N = 0.4$  (c)  $\phi t/N = 0.6$  (After Smith and Walls (1980)).

advantages that have been outlined above for the method of characteristics far outweigh the disadvantages. In the following chapters the method of characteristics will be used and further developed to solve some of the problems that have not been dealt with to date.

CHAPTER 2APPLICATIONS OF ION ETCHING IN SURFACE ANALYSIS2.1. Introduction.

It is well known that during ion etching of solids certain well defined features such as cones and pits can be formed (Wehner and Hajicek (1971), Wilson and Kidd (1971)). The formation of such topography is deleterious to many applications of ion etching including the micromachining of surface relief on electronic devices and in obtaining composition-depth profiles through thin films and interfaces (Smith and Walls (1979), Makh et al (1980a)).

In this chapter two separate but related problems will be considered viz the development of surface topography on the macroscopic and the microscopic scale. The calculations in the first part of this chapter are concerned particularly with the changes in the macroscopic shape of the sample. Although surface micro-roughening will also occur, this effect is dealt with in the second part of the chapter. However, it must be noted that many of the results for the development of macroscopic shape will also be relevant to the evolution of microtopography although it must be recognised that secondary effects such as surface diffusion and redeposition may then play more dominant roles.

Although the use of depth profiling is well established for initially flat surfaces and the problems associated with ion-induced artefacts such as surface topography, preferential sputtering and redeposition are well recognised, the additional problems which occur when non-flat surfaces are bombarded have been neglected. For example, depth profile analysis of rods, wires and fibres using Auger Electron Spectroscopy is now of



interest for many commercial purposes. However the erosion of such geometries is non-uniform since different angles of incidence are presented to the incoming ion beam. This non-uniform erosion is one of the mechanisms by which topography is formed on surfaces during ion etching. This can manifest itself during ion etching through the presence of impurities, implanted gas, initial surface roughness, and in the case of crystalline materials, by the formation of ion-induced crystal defects (Hermanne and Art (1970), Whitton et al (1978), Webber and Walls (1979)). Once the topography is nucleated, it is further modified since the erosion rate at each point on the surface is a sensitive function of ion incidence angle.

In principle, one way in which ion-induced topography could be minimised is by rotating the sample surface so that it subtends all angles of incidence to the ion beam. Unfortunately in many applications, and particularly those involving ultra-high vacuum, this is not practicable. However, Sykes et al (1980) have recently reported that the depth resolution of composition-depth profiles using Auger Electron Spectroscopy can be improved when two ion guns are employed each aligned symmetrically about the sample normal and both delivering the same ion current. It has been interpreted that the effect of using two ion guns is to suppress the formation of ion induced surface topography (Sykes et al (1980)). In the latter part of this chapter a theoretical analysis is presented which supports this view and which allows the mechanisms involved to be more fully understood.

However, before going on to these problems, in the next section of the thesis a number of techniques used in surface analysis will be outlined. The way in which they can be used to analyse surfaces and to obtain composition-depth profiles will also be outlined.

## 2.2. Surface analysis techniques.

A number of techniques are now available to determine the composition of surfaces. The three major techniques are Auger Electron Spectroscopy (AES), X-ray Photoelectron Spectroscopy (XPS or ESCA) and Secondary Ion Mass Spectroscopy (SIMS). Each of these techniques has the ability to measure the composition of the outermost atomic layers. The advantages and disadvantages of each technique are listed in Table 2.1. Although the techniques possess true surface sensitivity, they can also be used to determine the composition of much deeper layers by removal of the surface layers by ion bombardment and subsequent surface analysis. In this way a 'composition-depth' profile can be produced i.e. the composition of thin films and coatings can be determined as a function of depth.

### 2.2.1. Auger Electron Spectroscopy (AES).

The fundamental mechanisms involved in AES are ionization of atomic core levels by the incident electron beam, the radiationless Auger transition and the escape of the Auger electron into the vacuum where it is detected with an electron spectrometer (Joshi et al (1975)). The Auger process can be understood by considering the ionization process of an isolated atom under electron bombardment. When an incident electron with sufficient primary energy,  $E_p$  ionizes a core level, the vacancy is immediately filled by another electron, as shown by the  $L_1 \rightarrow K$  transition in figure 2.1. The energy ( $E_K - E_{L_1}$ ) from this transition can be released in the form of characteristic X-rays or be transferred to another electron e.g. in the  $L_2$  level, which is ejected from the atom as an Auger electron.

TABLE 2.1.

THE MAIN ADVANTAGES AND DISADVANTAGES OF AES, XPS AND SIMS.

ADVANTAGES		
AES	<p>High spatial resolution and visual display of the sample.</p> <p>Technique most amenable to composition-depth profiling.</p> <p>Rapid collection of data.</p> <p>Quantification to within <math>\pm 10\%</math> with standards.</p> <p>High reproducibility.</p> <p>Narrow range of sensitivities.</p>	<p>Beam damage on some insulating samples.</p> <p>Charging problems on some rough insulator surfaces.</p>
XPS	<p>Chemical information in the chemical shifts in photoelectron energies.</p> <p>Technique most amenable to delicate surfaces (no beam damage).</p> <p>Quantification to within <math>\pm 10\%</math> with standards.</p> <p>High reproducibility.</p> <p>Narrow range of sensitivities.</p>	<p>No spatial resolution .</p>
SIMS	<p>High surface sensitivity.</p> <p>High sensitivity for some elements.</p> <p>Chemical information in sputtered molecular fragments.</p>	<p>Wide range of sensitivities.</p> <p>Qualitative technique in comparatively early stage of development.</p> <p>Spatial resolution not normally obtainable.</p>

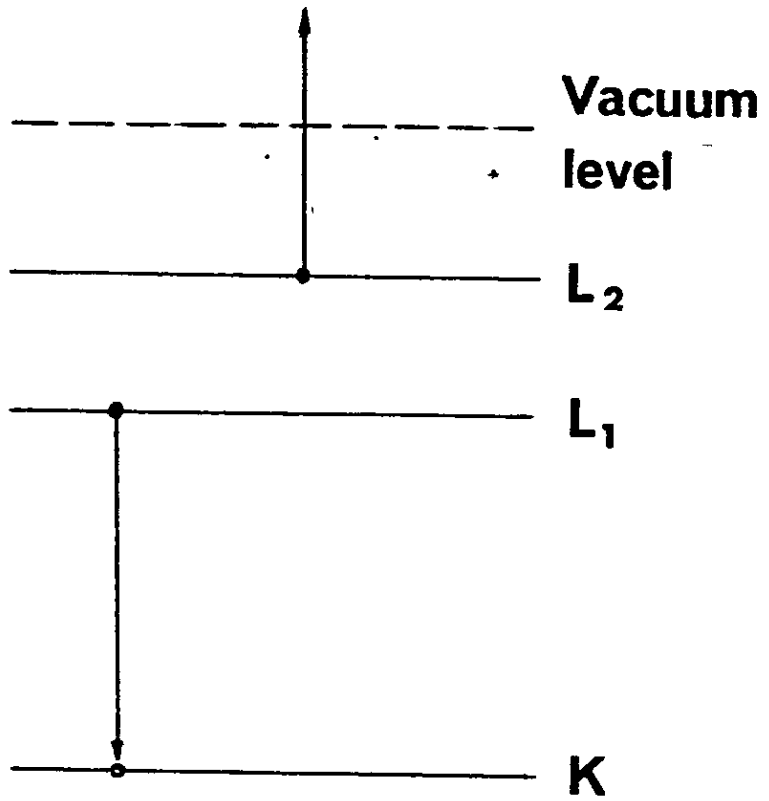


Fig.2.1. Energy level diagram depicting relaxation by an L<sub>1</sub> level electron dropping into the K level and emission of an L<sub>2</sub> electron as an Auger electron.

The measured energy of the electron is approximately equal to  $E_K - E_{L_1} - E_{L_2} - \phi_A$ , where  $\phi_A$  is the work function of the analyzer material. This ejection process is termed the  $KL_1L_2$  Auger transition. Several such transitions can occur with various transition probabilities. The Auger electron energies are characteristic of the target material and independent of the incident beam energy. Energy analysis of the ejected electrons is known as AES and results in chemical identification. The difficulty in the technique is to measure a small number of Auger electrons from the large general secondary electron emission spectrum. The Auger electrons produce a very small bump on a plot of the intensity of secondary electrons versus energy. The breakthrough in using this technique came when it was recognised that the way to make these small increments stand out was to differentiate the signal (Harris (1968)).

Although Auger electrons can be produced from as far within the solid as the original electron beam penetrates, only those which are generated within the first two or three atomic layers below the surface can escape with their original energies intact. This gives the technique its great sensitivity. The technique has become sufficiently sensitive to enable detection of as little as 0.1% of a monolayer of impurity in the surface. Only hydrogen and helium cannot be detected since these elements possess insufficient energy levels for the Auger transition to occur.

Since electron beams can be focused into fine spots (0.5 $\mu$ m diameter), scanning electron microscope techniques can be used to obtain an image of the region under analysis. This makes the technique ideal for the analysis of small surface areas and hence the appropriate one to use to determine the origin of small areas of contamination or for the

analysis of complex surfaces such as those that occur on electronic components. The technique is also best-suited to composition-depth profiling and hence for the analysis of thin films and surface coatings.

### 2.2.2. X-ray Photoelectron Spectroscopy (XPS).

X-ray photoelectron spectroscopy is a well-established technique for performing quantitative analysis of the outermost atomic layers of solid surfaces (Czanderna (1975), Briggs (1977)). The basic XPS experiment is shown schematically in figure 2.2. The incident X-ray photons, of energy  $h\nu$  ( $h$  is Planck's constant,  $\nu$  is the frequency), are absorbed by sample atoms. Each absorption event results in the emission of a photoelectron of kinetic energy  $E_k$ .  $E_k$  and  $h\nu$  are related by the Einstein relation  $E_k = h\nu - E_B$  where  $E_B$  is the binding energy of the electron in the material. The ejected photoelectrons are then analysed using an energy analyser which measures the number of photoelectrons ejected as a function of their energy.

Ejection of photoelectrons is a very direct way of obtaining information which is characteristic of atoms. Provided the exciting energy is high enough, core level spectra can be obtained for all elements of the periodic table except hydrogen and helium (since these have no core levels) and the determined binding energies of these core levels are sufficiently unique for their unambiguous assignment. For any given electron shell e.g. the K shell, the electron binding energy increases with increasing atomic number. Thus, information of the binding energies of electrons within a sample allows quantitative elemental analysis. However, electron binding energies within any one

# Photo Electrons

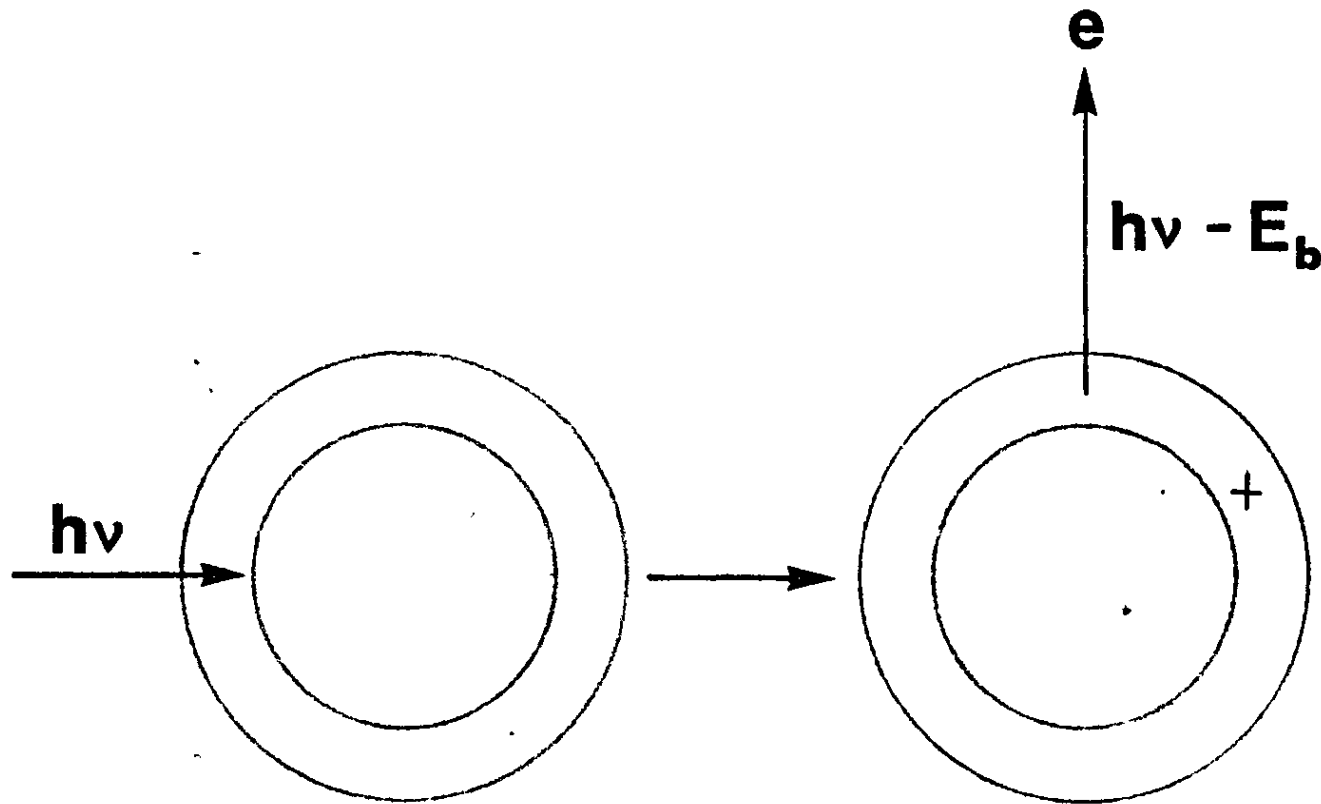


Fig. 2.2. The physical basis of XPS (ESCA).

element are far from fixed and small variations in binding energies may occur. These so called chemical shifts are caused by a decrease in electron density in the valence region around an atom in a molecule which produces an increase in the binding energy of the core level electrons.

Thus, a major advantage of the technique is that the photoelectron energy is dependant on the precise chemical configuration of the surface atoms and pronounced chemical shifts are produced in the position of the peaks in the XPS spectrum. XPS is also amenable to the widest range of sample materials since the incident X-rays do not normally cause surface damage. Hence XPS is often used to analyse surfaces such as those that occur in delicate powder materials and organic or polymeric coatings.

### 2.2.3. Secondary Ion Mass Spectroscopy (SIMS).

SIMS has been applied to a large variety of problems ranging from ion microscopy (Castaing and Slodzian (1962), Morrison and Slodzian (1975)), to surface analysis (Benninghoven (1970), (1975), Wittmaack (1979)) and depth profiling (Maul et al (1972), Hofker et al (1973), McHugh (1975), Williams (1979)). In SIMS the sample is bombarded by a probing beam of primary ions with energies ranging from several 100eV to approximately 20keV. The primary ions cause sputter erosion of the sample. Thereby atoms as well as clusters are emitted from the upper atomic layers. Most of the sputtered species leave as neutral atoms or molecules, but a small fraction is ejected as positive or negative ions.

Secondary ion emission is a complex phenomena and figure 2.3 schematically illustrates the processes that occur when an energetic ion is incident on a solid surface. The primary ion energy is dissipated among several generations of recoiling target atoms set in motion by a series of collisions. This



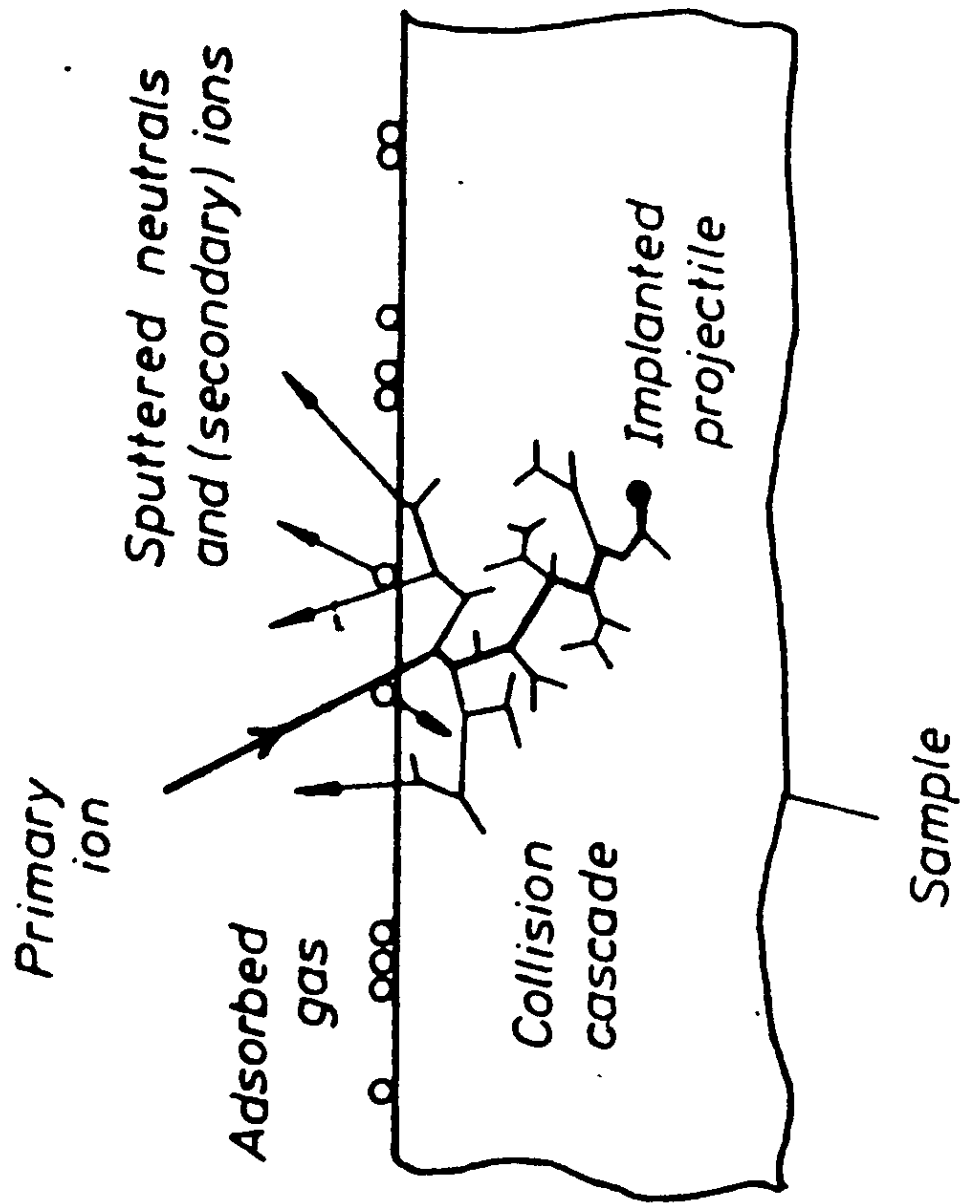


Fig. 2.3. Schematic illustration of SIMS-relevant effects introduced by impact of an energetic heavy ion on a solid (After Wittmaack (1980)).

'collision cascade' (see figure 2.3) is mostly responsible for sputter erosion in SIMS analysis. Near surface atoms of the solid sample as well as adsorbed species are emitted into vacuum if recoiled atoms end up at the solid vacuum interface with an outward directed momentum and an energy large enough to overcome the surface potential barrier. Since the energy spectrum of recoil atoms peaks at low energies (Sigmund (1969)), sputtered particles originate mostly from the topmost layer at the surface (Sigmund (1969), Wittmaack (1979)).

SIMS can be used in two modes, the static and dynamic mode. In the static mode the technique analyses the outermost atomic layers of a surface. Composition-depth profiles are obtained by increasing the primary ion beam current density e.g. by using a focussed ion beam (dynamic mode) or by combining the technique in the static mode with ion beam machining using a separate, more powerful ion source.

The technique has high surface sensitivity and high elemental sensitivity for some species and in contrast to both AES and XPS, it is able to detect the presence of hydrogen. However, the technique requires that the sputtered species are charged for analysis in the mass spectrometer and, in practise, only a small proportion emerge as ions. This leads to difficulties both in interpretation and quantification.

#### 2.2.4. Composition-depth profiling.

Composition-depth profiles are normally obtained by sequential ion beam sputtering and surface analysis using AES or XPS (Czanderna (1975), Briggs (1977), Walls (1981)). An ion gun is used to erode the surface by bombardment with low-energy inert gas ions. The electron beam used for analysis is very much smaller than the crater produced by sputtering.

Thus the composition of the surface can be measured at the bottom of the crater without taking any contribution from the crater sides.

The applications of sputter-depth profiling can be useful at two levels. On the finest scale, a depth profile through  $\leq 10\text{nm}$  enables the surface and subsurface composition to be compared. Over thicknesses up to  $1\mu\text{m}$  the technique can be used to characterise the composition of thin films or to investigate the interface between a thin film and its substrate.

The depth resolution of a sputter-depth profile should be constant and should be given simply by the escape depth. In practise it is found that the depth resolution deteriorates with increasing depth (Coburn and Kay (1974), Sykes et al (1980)). As a guide, results obtained from a multilayer  $\text{N}_1/\text{Cr}$  thin film structure suggest that the depth resolution deteriorates as a function of  $z^{\frac{1}{2}}$  where  $z$  is the depth (Hofmann (1976), (1977)).

Many mechanisms contribute to the deterioration of the depth resolution and these include non-uniform ion current distribution over the sputtered area, redeposition of material from the crater edges, radiation enhanced diffusion, misalignment of electron and ion beams and ion induced surface roughness. In the next two sections of this chapter the last two mechanisms will be investigated in more detail.

### 2.3. The development of surface shape during sputter-depth profiling in AES.

As has been mentioned above, ion bombardment is an important process in surface analysis, not only for surface cleaning, but also for obtaining composition-depth profiles through thin films and interfaces. In this section,

methods previously developed for predicting the two dimensional evolution of surfaces during ion bombardment are used to predict the changes of shape on non-flat samples which might occur in surface analysis. These predictions are then used to determine the effective depth resolution of such profiles as a function of both sample and electron and ion beam geometry.

The calculations in this section are concerned particularly with the changes in the macroscopic shape of the sample. Although surface micro-roughening will also occur during ion bombardment, this effect will be dealt with in the next section. However, it should be noted that the development of surface topography is independent of size and hence many of the results presented here will also be relevant to the evolution of microtopography.

### 2.3.1. Analysis.

#### 2.3.1.1. The development of surface shape.

Many attempts have been made to treat the development of a general surface under ion bombardment. It has been recognised that one of the most important parameters in the development of surface shape is the dependence of the sputtering yield,  $S$ , with the angle of ion incidence,  $\theta$ . Various theories have been put forward to explain the formation of surface topography during ion bombardment and these have already been outlined in Chapter 1. In this chapter the method of characteristics developed by Smith and Walls (1979), (1980) will be used but its use is restricted to two dimensions to simplify subsequent calculations.

Consider a surface under ion bombardment with a uniform ion flux incident along the negative y direction. The equation governing the time dependence of the surface angle  $\theta$  to the beam has the form in (x,t) space (Smith and Walls (1979), Carter et al (1973))

$$\left(\frac{\partial\theta}{\partial t}\right)_x = -\frac{\phi}{N} \frac{dS}{d\theta} \cos^2\theta \left(\frac{\partial\theta}{\partial x}\right)_t \quad (2.1)$$

and in (y,t) space

$$\left(\frac{\partial\theta}{\partial t}\right)_y = -\frac{\phi}{N} \left[ \sin\theta\cos\theta \frac{dS}{d\theta} - S \right] \left(\frac{\partial\theta}{\partial y}\right)_t \quad (2.2)$$

The way in which these equations are derived has already been outlined in Chapter 1. The way in which they can be derived using the method of characteristics in two dimensions, for a non-uniform ion flux, is shown in Appendix 1. In obtaining equations (2.1) and (2.2) the surface contour is represented by a curve  $y = f(x)$  and bombardment is by a uniform ion flux of  $\phi$  ions/second in the negative y - direction.  $\theta$  is the angle of incidence of the beam, with respect to the normal to any point on the target surface, S the sputtering yield, and N the atomic density of the target. In obtaining equations (2.1) and (2.2) it has been assumed that the sputtering yield is a function of the angle of ion incidence only and strictly, this applies only to amorphous materials. For crystalline materials, S is a function of  $\theta$  and the crystallographic plane being bombarded. Equations (2.1) and (2.2) are standard partial differential equations which can be solved to give the coordinates of a point (x,y) on the sputtered surface from a point  $(x_0, y_0)$  on the initial profile. Thus, we obtain

$$x = x_0 + \frac{\phi t}{N} \frac{dS}{d\theta} \cos^2 \theta \quad (2.3)$$

and

$$y = y_0 + \frac{\phi t}{N} \left( \sin \theta \cos \theta \frac{dS}{d\theta} - S \right) \quad (2.4)$$

The right hand sides of (2.3) and (2.4) are constant for a given value of  $\theta$  and thus the loci of the points  $(x,y)$  are straight lines - the characteristic lines in  $(x,y)$  space of equations (2.1) and (2.2) and the trajectories of constant surface orientation as noted by previous authors (Smith and Walls (1979), Barber et al (1973), Carter et al (1973)).

#### 2.3.1.2. Computer simulation.

In this section the development of surface topography is simulated for two different initial profiles using the analysis described in section 2.3.1.1.

The first step is to define the initial unsputtered profile in  $(x,y)$  space. The coordinates of a number of points on this profile are calculated. At each of these points the angle between the beam (incident along the negative  $y$ -axis) and the normal at the point is calculated. For a certain point the appropriate angle is taken and the coordinates of the sputtered point  $(x,y)$  calculated, for a given value of time, using equations (2.3) and (2.4). In calculating the point  $(x,y)$  the dependence of  $S$  on  $\theta$  is that one given by Ducommun et al (1975) for ion bombarded silicon, viz:

$$S(\theta) = 18.73845 \cos \theta - 64.65996 \cos^2 \theta + 145.19902 \cos^3 \theta \\ - 206.04493 \cos^4 \theta + 147.31778 \cos^5 \theta - 39.89993 \cos^6 \theta.$$

Next the coordinates of another point are calculated after time  $t$  corresponding to a period of erosion. The line joining these points is the characteristic line corresponding to that particular angle. The above procedure is carried out for all the points on the profile.

Using equations (2.3) and (2.4) it can be shown that the slope of the characteristic line in  $(x,y)$  space is given by

$$\frac{dy}{dx} = \frac{\sin\theta \cos\theta \frac{dS}{d\theta} - S}{\frac{dS}{d\theta} \cos^2\theta} \quad (2.5)$$

Thus the gradient of the characteristic line for each point on the initial surface is different. Hence some of the lines will intersect within the profile. This corresponds to the surface developing an edge. Care must be taken to ignore all points on any two characteristic lines after their point of intersection, since these points have no physical significance.

The method of characteristics described above is effectively the same computational method as used by Ducommun et al (1975) as the results for the initially sinusoidal contour, shown in figure 2.6, depict. This method lends itself more easily to computation than the methods used by Barber et al (1973), Carter et al (1977) and Ishitani et al (1974). However, direct comparison with the results presented is not possible because of the different sputtering yield data used by these authors.

#### 2.3.1.3. Depth resolution.

Many authors have considered the deterioration in depth resolution in the composition-depth profiles of flat surfaces (Palmborg (1972), Hofmann (1976),(1977), Hofmann et al (1977), Chuang and Wandelt (1978),

Wittmaack and Schulz (1978)). The degradation of such profiles is caused by the formation of microtopography during sputtering (Benninghoven (1970), Wittmaack and Schulz (1978), Webber and Walls (1979)).

In this section we consider a different but related problem viz: bombardment of macroscopically non-flat surfaces. In this case the depth resolution will be impaired because the profile will erode at different rates at different presented angles of incidence along the surface. In order to gain some perspective on the scale of this deterioration in depth resolution, computer simulations will be used to estimate the non-uniformity of erosion for some shapes commonly encountered in surface analysis. For example, consider the circular profile shown in figure 2.4. The uniform ion beam is incident along the negative y-axis. After a time  $t$ , the initial circular profile erodes to the one shown. The distance  $AA'$  is then calculated such that  $AA'$  lies along the normal at A. Similarly for a point  $B'$  on the sputtered surface the distance  $BB'$  is calculated such that  $BB'$  lies along the normal at B and similarly for  $CC'$ . Thus, if after sputtering, an electron beam of radius  $a$ , is used to examine the profile, then the depth degradation is given by

$$\left| \frac{\Delta d}{d} \right| = \left| \frac{d_1 - d_2}{d} \right| \quad (2.6)$$

where  $d_2$  is the maximum distance eroded, normal to the surface, over the area analysed and  $d_1$  is the minimum distance. The quantity  $d$  is the distance eroded at the centre of the analysing beam. This definition of  $\Delta d$  may be contrasted with that used by Hofmann (1976), (1977) and Hofmann et al (1977) where  $\Delta d$  is defined as the width of a measured concentration profile in the case of sputtering through a true rectangular profile at the sample depth  $d$ . Thus, a graph of  $\frac{\Delta d}{d}$  against  $\frac{a}{R}$  can be plotted, in normalized form, for any profile after bombardment. Therefore for given



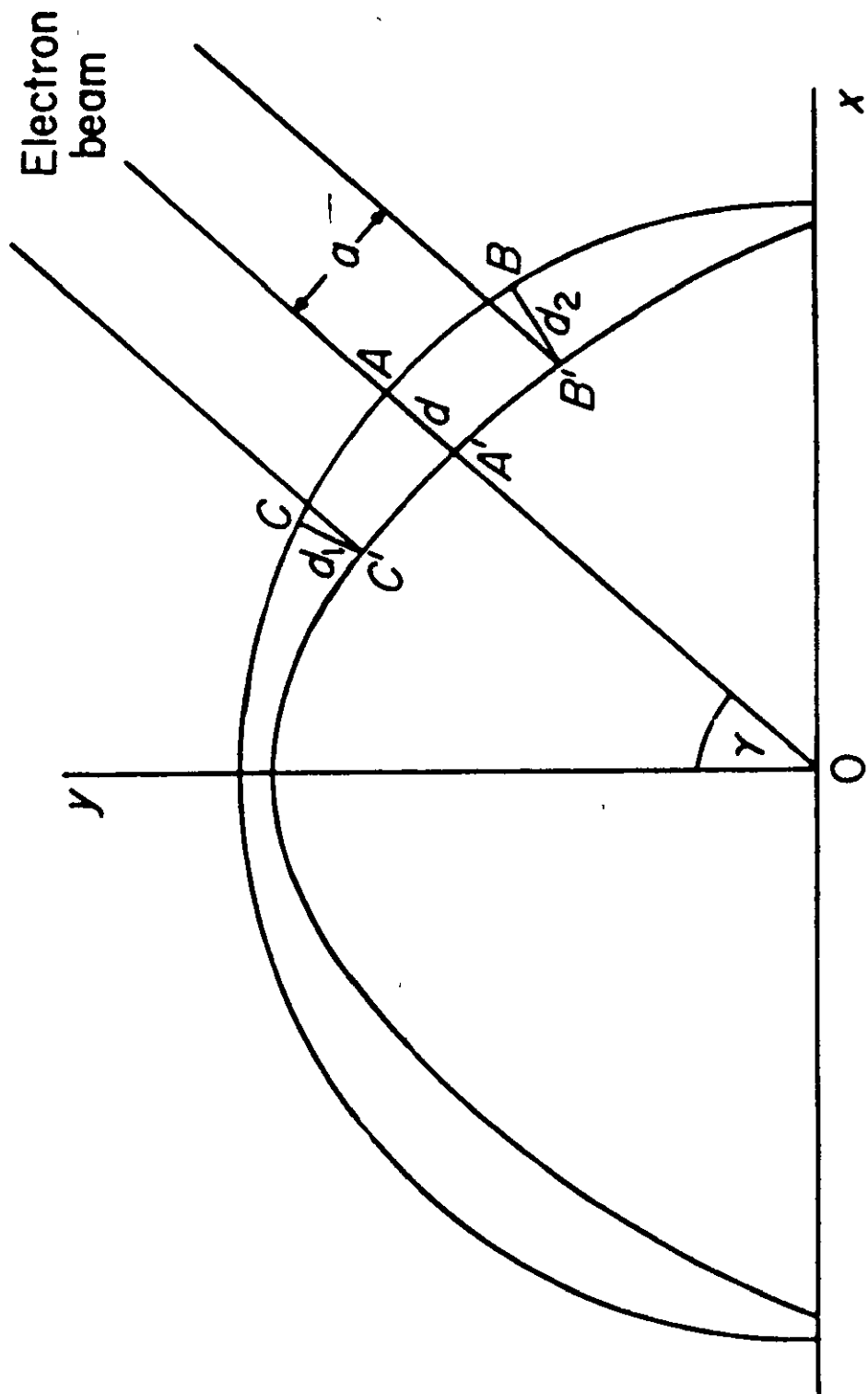


Fig. 2.4. Schematic diagram of a circular profile and the subsequent shape following ion bombardment along the negative  $y$ -axis. An electron beam of radius  $a$  is used to analyse the surface at an arbitrary point and  $d_1$  and  $d_2$  are the maximum and minimum values of eroded depth respectively.

values of  $d$  and  $a$  we can estimate the degradation of depth resolution with time.

### 2.3.2. Results.

#### 2.3.2.1. The development of surface shape.

The procedure outlined in section 2.3.1.2 has been carried out for circular and sinusoidal cross-sectional surfaces. The circular cross-section can represent a cylindrical fibre or wire, or in three dimensions a spherical particle. The sinusoidal surface is included for comparison and could represent wear tracks on a machined surface.

The way in which these profiles erode during bombardment is shown in figures 2.5 and 2.6 respectively. The characteristic lines can intersect within the material if the surface is convex in the direction of the bombarding ion beam. From figures 2.5 and 2.6 it can be seen that this has occurred in the case of the circular cross-section and that part of the curve  $y = \sin x$  for  $0 < x < \pi$ . Where the lines intersect an edge develops. The time taken for a surface discontinuity to develop from an initial well defined profile has been calculated by Ducommun et al (1974). For surfaces that are concave the characteristic lines do not intersect within the material and so the surface profile becomes shallower. This can be seen for  $y = \sin x$  for  $\pi < x < 2\pi$ .

The surface trajectories ( $K = 1, 2, 3, \dots$ ) have been calculated at equal time intervals. An estimate for the sputtering time can be obtained by a simple calculation. For example, if a current of  $10\mu\text{A}/\text{cm}^2$  is used to bombard the circular profile of silicon radius  $50\mu\text{m}$ , with  $3\text{keV Ar}^+$  ions, then the sputtering time for the  $K = 2$  profile is approximately 35 minutes.

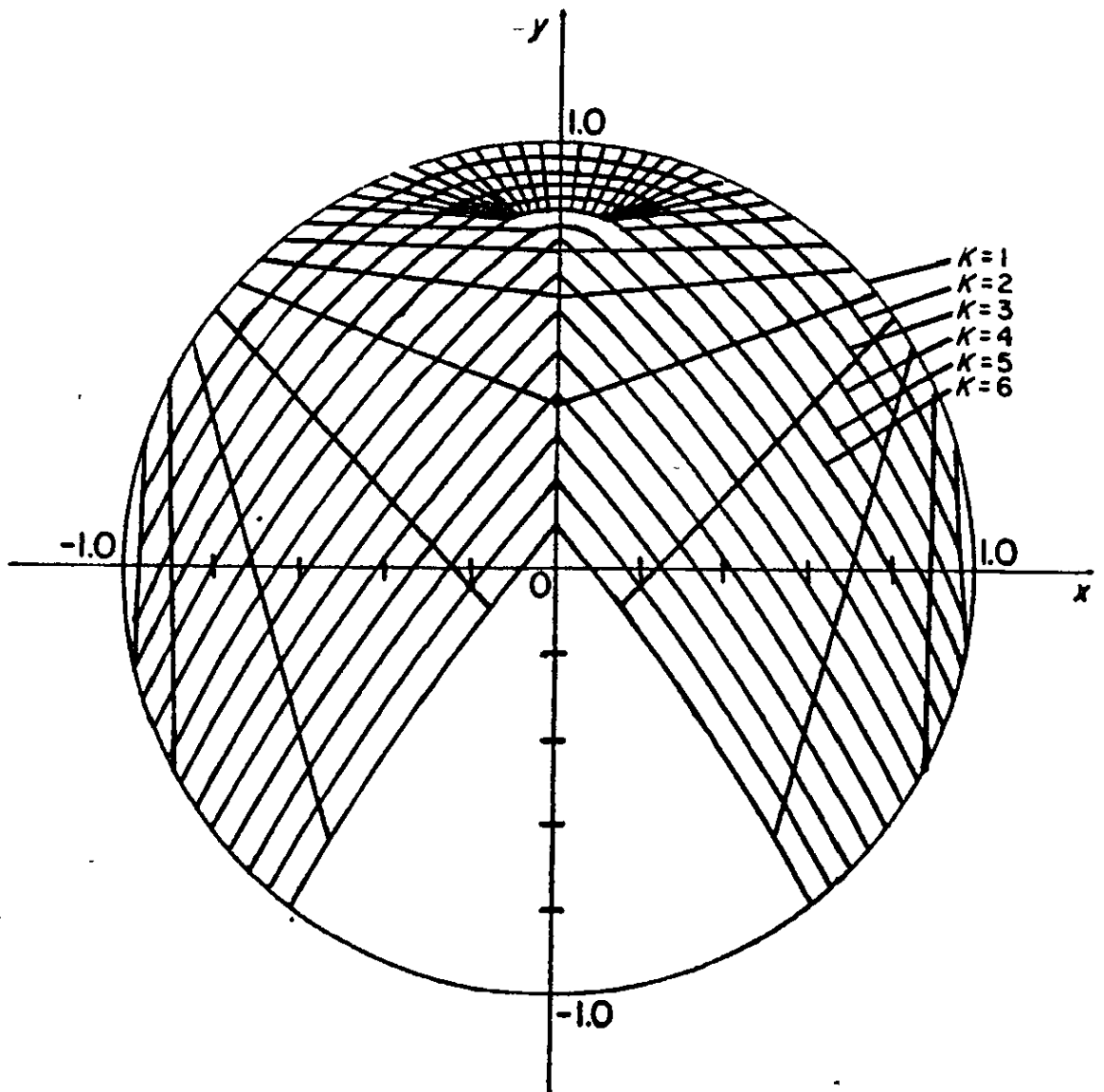


Fig. 2.5. Computer simulation showing how a circular profile ( $x^2 + y^2 = 1$ ) erodes by ion bombardment along the negative  $y$ -axis. The contour  $K = 1$  is the original surface and  $K = 2, 3$ , etc., correspond to sputtered surfaces obtained at equal increments of bombardment time.

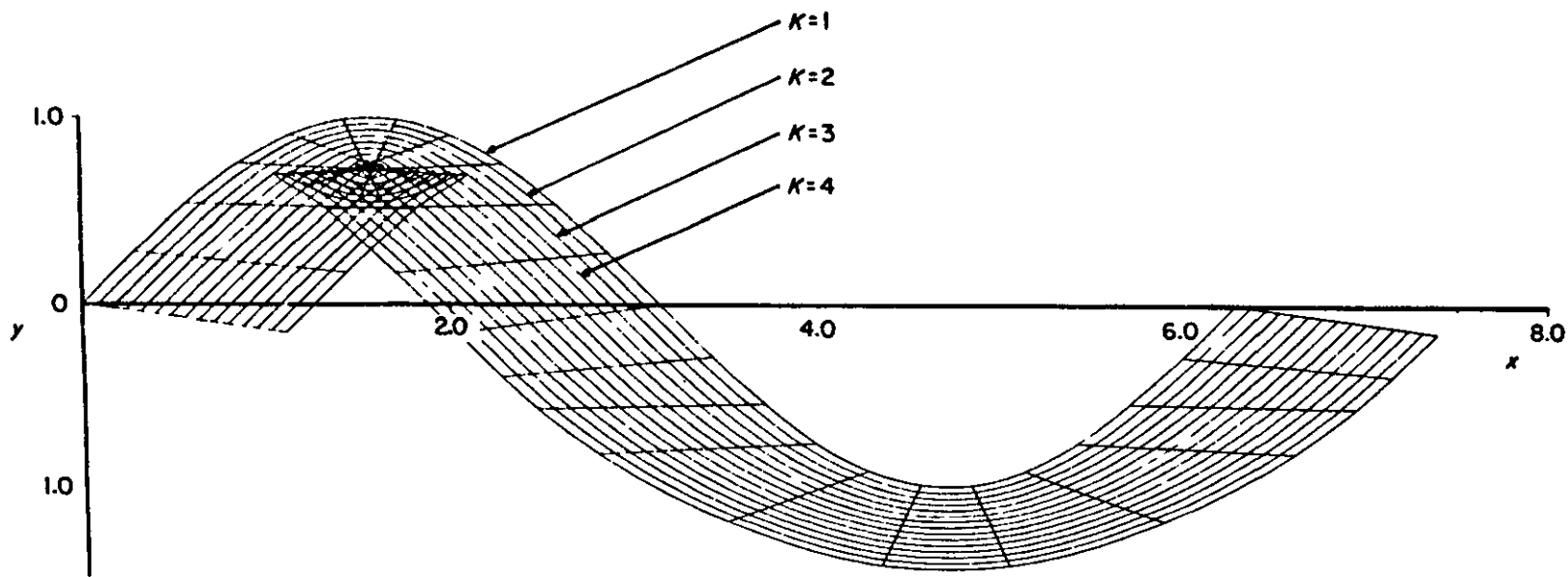


Fig. 2.6. Computer simulation showing how a sinusoidal surface ( $y = \sin x$ ) erodes by ion bombardment along the negative y-axis. The contour  $K = 1$  is the original surface and  $K = 2, 3$ , etc., correspond to sputtered surfaces obtained at equal increments of bombardment time.

### 2.3.2.2. Depth resolution.

The procedure outlined in section 2.3.1.3 was carried out for the shapes shown in figures 2.5 and 2.6 for a number of sputtered profiles. Then  $\frac{|\Delta d|}{d}$  against  $a/R$  has been plotted where  $R$  is the radius of the initial profile. The results are shown in figures 2.7 and 2.8. In both cases the electron beam used was assumed to be colinear with the ion beam and centred along the line  $x = 0$  in figure 2.5 and along  $x = \pi/2$  in figure 2.6. In these examples and the analysis which follows the incident electron beam is assumed to be incident in the direction of the unsputtered surface normal. Rotation of the electron beam would spread the beam over a larger area but this effect is not considered here.

The graphs are plotted in normalised form since the important parameter is the ratio  $a/R$ . For example, taking the sputtered profile  $K = 2$  in the circular case (figure 2.7), if the initial radius is  $50\mu\text{m}$  then  $K = 2$  corresponds to a sputtered depth of  $1.63\mu\text{m}$ . If the diameter of the electron beam  $a = 5\mu\text{m}$  then  $\frac{|\Delta d|}{d} = 0.01$  and if  $a = 0.5\mu\text{m}$  then  $\frac{|\Delta d|}{d} \ll 0.01$ . This illustrates the importance of spatial resolution in depth profiling. Similarly for  $R = 25\mu\text{m}$ , using  $a = 5\mu\text{m}$  then  $\frac{|\Delta d|}{d} = 0.05$  and if  $a = 0.5\mu\text{m}$  then  $\frac{|\Delta d|}{d} \ll 0.01$ . These examples relate to the ideal case where the ion and electron beams are co-linear.

For the object of circular cross-section shown in figure 2.4, the depth resolution varies with the region of the surface analysed. This can be seen by defining a polar angle  $\gamma$  and plotting  $\frac{|\Delta d|}{d}$  against  $a/R$  for various values of  $\gamma$ . The results shown in figure 2.9 are for the  $K = 2$  profile. In the analysis it has also been assumed that the two beams are separated by the angle  $\gamma$ , and the graphs are again plotted in normalised form. The minimum resolution degradation occurs at  $\gamma = 0^\circ$

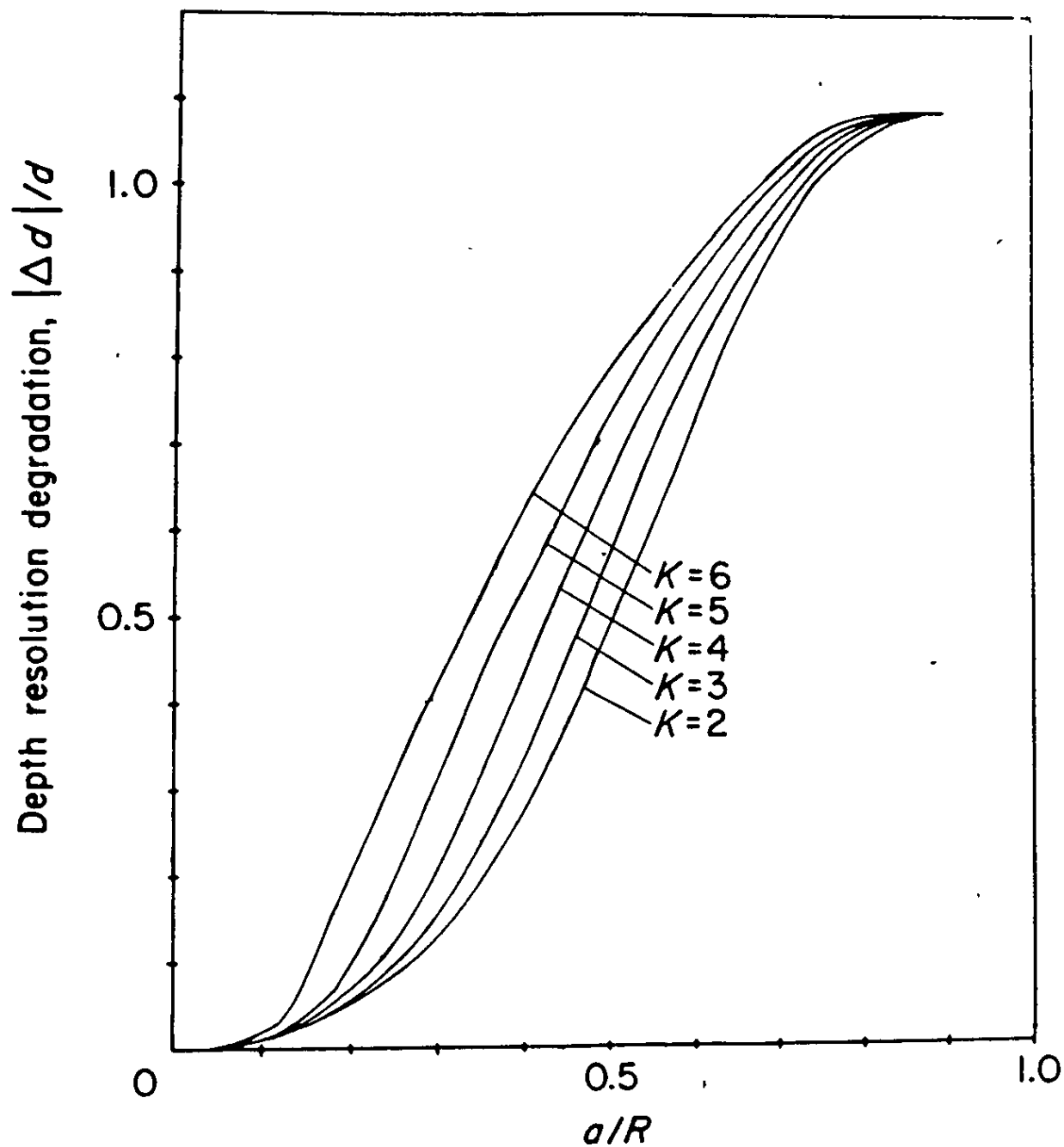


Fig. 2.7. Depth resolution degradation ( $|\Delta d|/d$ ) as a function of the ratio  $a/R$  for the various sputtered profiles of the circular surface  $K = 2, 3$ , etc., as shown in Fig. 2.5.

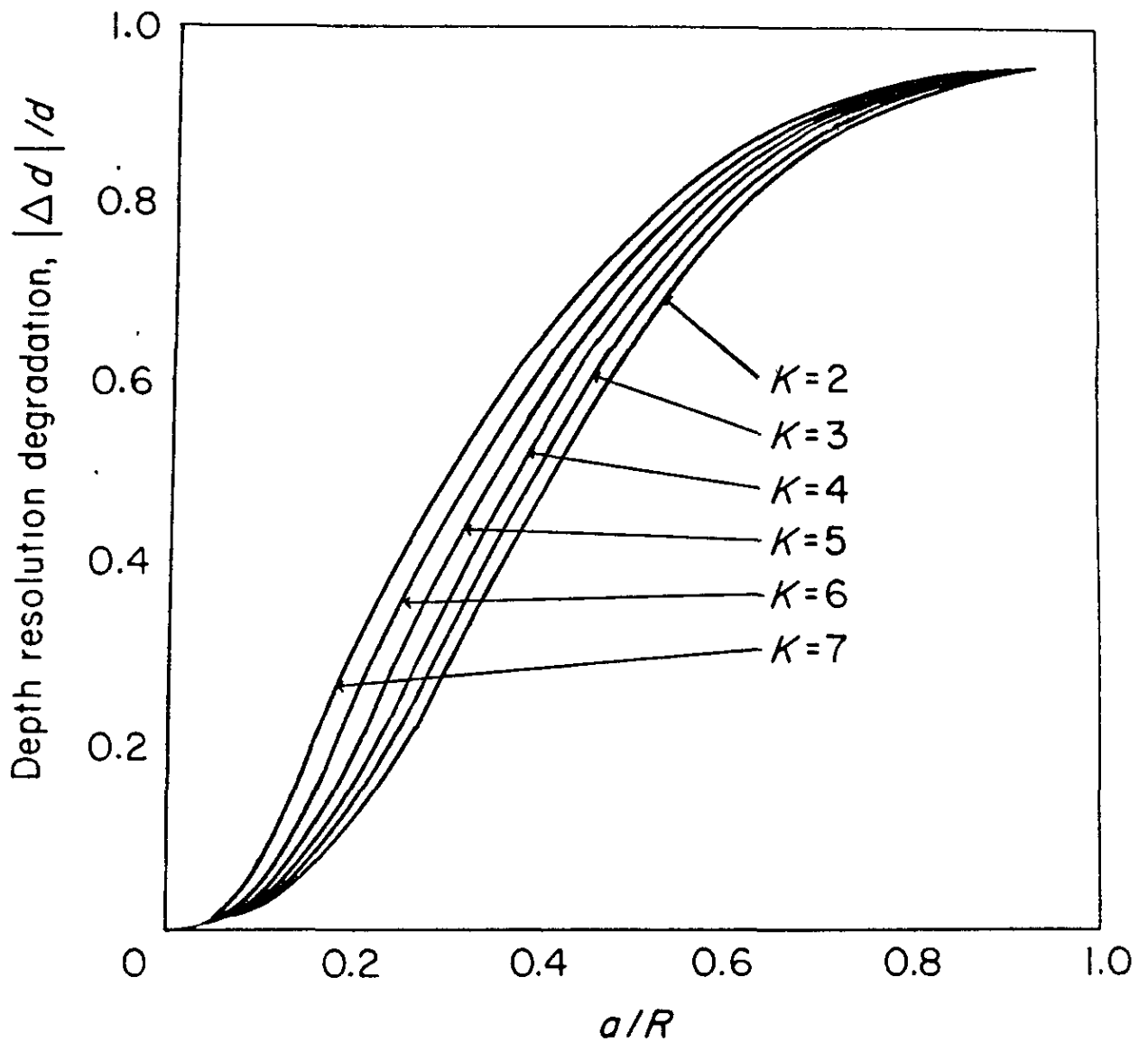


Fig. 2.8. Depth resolution degradation ( $|\Delta d|/d$ ) as a function of the ratio  $a/R$  for the various sputtered profiles of the sinusoidal surface  $K = 2, 3$ , etc., as shown in Fig. 2.6.

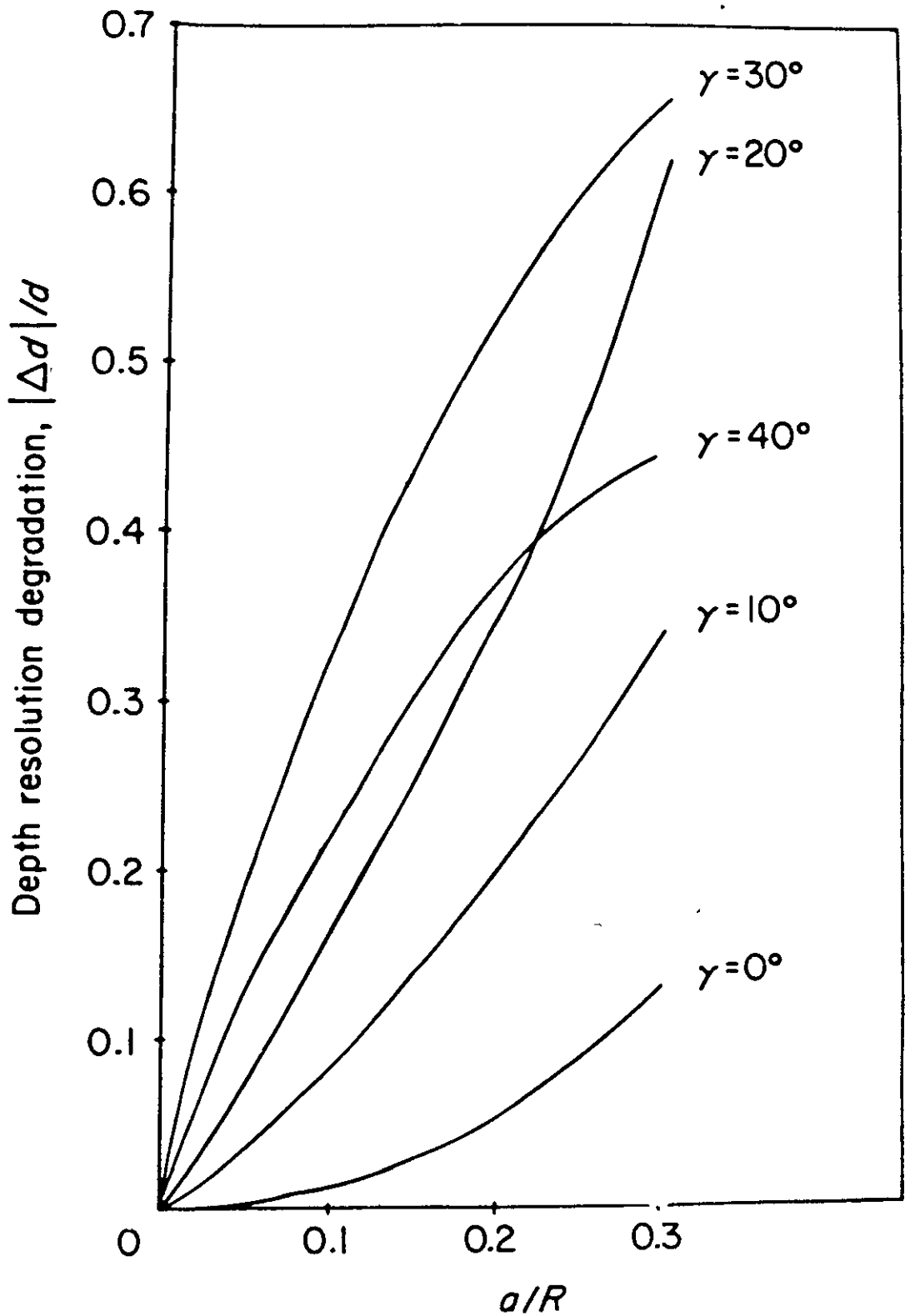


Fig. 2.9. Depth resolution degradation ( $|\Delta d|/d$ ) as a function of the ratio  $a/R$  for  $K = 2$  and various values of  $\gamma$ , the angle between the ion and analysing electron beam.



and as  $\gamma$  increases the degradation increases and then at  $\gamma = 40^\circ$  improves. At angles  $\gamma > 60^\circ$  the degradation increases once more. This behaviour is intimately connected with the dependence of the sputtering yield on ion-incident angle. For most materials this dependency shows a plateau at  $\theta = 0^\circ$  and  $\theta \sim 60^\circ$  and hence the sputter-erosion at these two values will be more uniform.

### 2.3.3. Discussion.

Computer simulation has been used to determine the way in which curved surface shapes develop during ion bombardment. It is clear from this and previous experimental work that the initial surface shape is never preserved, because the erosion rate is a sensitive function of ion-incidence angle. In general, concave surfaces tend to become shallower during ion etching while surfaces which are convex in the direction of the bombarding ion beam erode to form a conical shape. The eventual equilibrium profile in both cases is a flat plane.

In surface analysis, this non-uniform erosion leads to a deterioration in the depth resolution of composition-depth profiles of samples with curved surfaces such as rods, wires and fibres. In this section, an attempt has been made, using a model system, to estimate the extent of the problem and to determine the relative importance of the parameters involved. As a result, it has been possible to determine the likely degradation in depth resolution for given values of electron beam diameter, sample radius and the depth of eroded material. From the results it is possible to make some general conclusions:

1. The depth resolution is a sensitive function of  $a/R$  and for this reason the electron beam diameter should be as fine as possible consistent with any beam damage effects which may occur on the surface under investigation.
2. The depth resolution is optimised at a point on the surface where the ion beam is incident along the surface normal i.e.  $\gamma = 0$  in figure 2.9. For some samples this geometry may not be feasible and a local minimum in  $\frac{|\Delta d|}{d}$  occurs when the angle between the surface normal and the incident ion beam corresponds to the angle at which maximum sputtering occurs. Although this angle is different for different materials, the sputtering yield - ion incidence angle relationship used in this analysis is fairly representative where the maximum sputtering yield occurs at  $\theta \sim 60^\circ$ .

It should be noted that the effect of microroughening and other effects leading to the degradation of depth resolution have not been considered in the present analysis. However, although the analysis has been centred on the evolution of the macroscopic sample shape, the simulations presented in this study can be scaled to explain the development of surface microtopography and this will be discussed in the next section.

#### 2.4. The development of surface topography using two ion beams.

It has already been pointed out that the formation of microtopography during ion etching is deleterious to many applications of ion etching including the micromachining of surface relief on electronic devices and in sputter-depth profiling in surface analysis (Smith and Walls (1979), Makh et al (1980a)). Conventionally composition-depth profiles are obtained

by bombarding the sample with one ion beam and subsequent analysis using AES or XPS (see section 2.2.4). Recently, Sykes et al (1980) have reported that the depth resolution of composition-depth profiles using Auger Electron Spectroscopy can be improved when two ion guns are employed each aligned symmetrically about the sample normal and both delivering the same ion current. It has been interpreted that the effect of using two ion guns is to suppress the formation of ion induced surface topography (Sykes et al (1980)). In this section a theoretical analysis is presented which supports this view and which allows the mechanisms involved to be more fully understood (Makh et al (1981a)). General differential equations are derived to predict the development of surface shape during bombardment using two uniform ion beams, in two dimensions. These equations are then solved using the method of characteristics and, as an example to illustrate the method, they are used to simulate the development in shape of an initially circular cross-section during ion bombardment with two ion beams and the results are compared with a similar simulation using one ion beam.

#### 2.4.1. Theoretical model.

Consider an element of surface AB shown schematically in two dimensions in figure 2.10, exposed to two uniform fluxes of energetic ions,  $\phi_1$  and  $\phi_2$  per unit area per sec, incident at angles of  $\alpha$  and  $\beta$  to the surface normal at A. It is assumed that the erosion of this surface is controlled by the variation of sputtering yield  $S$  with the ion-incidence angles  $\alpha$  and  $\beta$  to the normal to the surface. The sputtering yield is defined as the number of atoms removed from the surface per incident ion. A typical relationship between  $S(\theta)$  and  $\theta$  for an amorphous surface

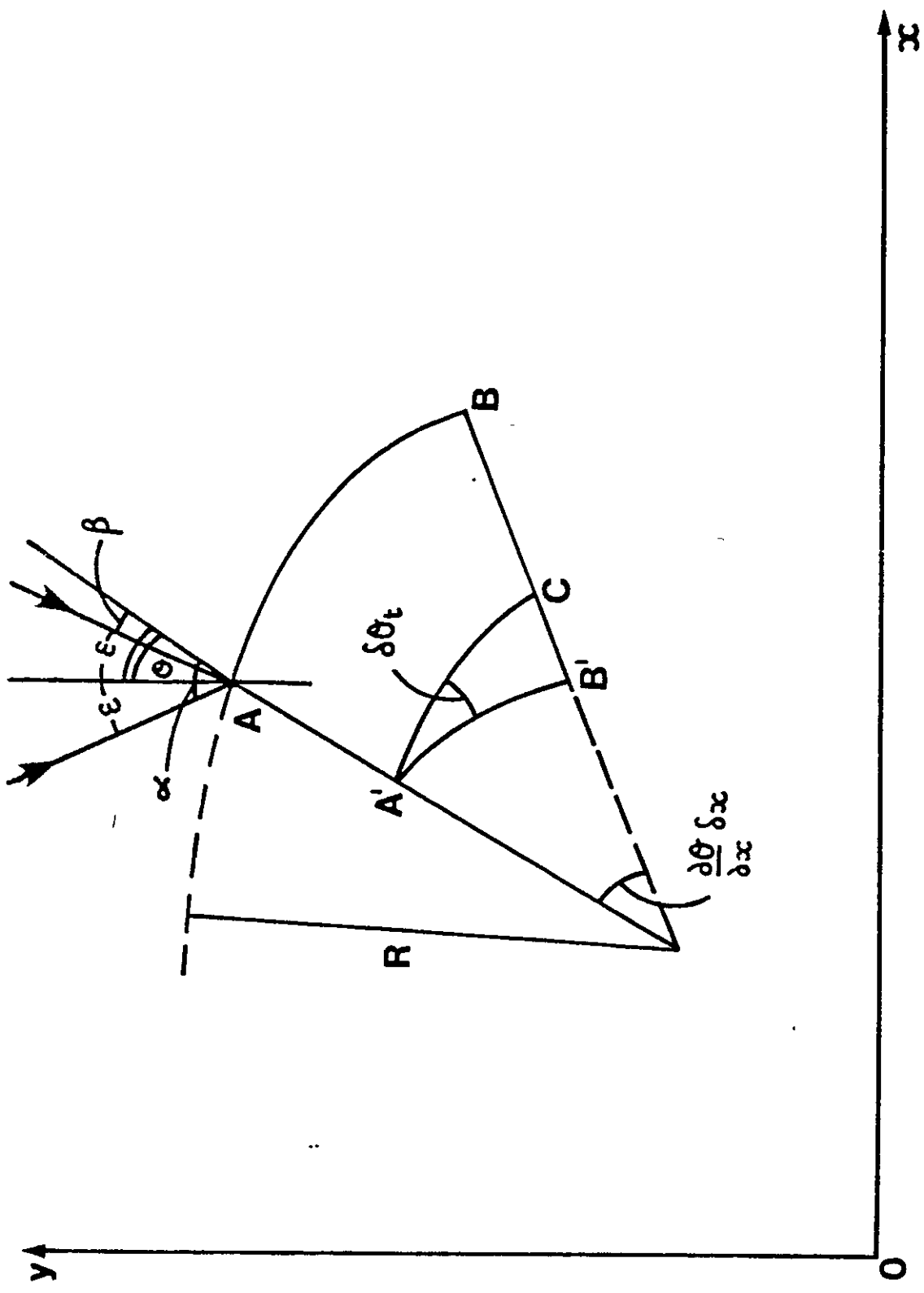


Fig. 2.10. A schematic diagram, illustrating the bombardment of the section AB at time  $t$  of a surface contour in two dimensions and its erosion to  $A'B'$  at time  $t+\delta t$ .

in the range  $0 \leq \theta \leq \frac{\pi}{2}$  is shown in figure 1.5. It can be seen that  $S(\theta)$  has a minimum value of  $S(0)$  at  $\theta = 0$ , rising to a maximum and then decreasing to zero at  $\theta = \frac{\pi}{2}$ .

Let  $S_1(\alpha)$  and  $S_2(\beta)$  respectively be the sputtering yields for the beams incident at angles  $\alpha$  and  $\beta$  to the surface normal. The y-direction is defined along the angle bisector of the beam directions so that the ion beams are placed about this line. Let the angle made by the beams to the y-direction be  $\epsilon$ . Then  $\alpha = \theta + \epsilon$  and  $\beta = \theta - \epsilon$ . In a time  $\delta t$ , the surface erodes by a distance  $\delta r$ , in a direction perpendicular to the surface. Thus

$$\frac{\partial r}{\partial t} = \frac{1}{N} \left[ \phi_1 S_1(\alpha) \cos \alpha + \phi_2 S_2(\beta) \cos \beta \right] \quad (2.7)$$

where  $N$  is the atomic density of the target. Consider now erosion in two dimensions as shown in figure 2.10. In time  $\delta t$ , A and B erode to A' and B' respectively where AA' and BB' are perpendicular to the tangents at A and B. For the element AB in figure 2.10, the tangential angles increase from  $\alpha$  and  $\beta$  at A to  $\left( \alpha + \frac{\partial \theta}{\partial x} \delta x \right)$  and  $\left( \beta + \frac{\partial \theta}{\partial x} \delta x \right)$  at B. Thus using (2.7) we have to first order

$$AA' = \frac{1}{N} \left[ \phi_1 S_1(\alpha) \cos \alpha + \phi_2 S_2(\beta) \cos \beta \right] \delta t$$

and

$$BB' = \frac{1}{N} \left[ \phi_1 S_1 \left( \alpha + \frac{\partial \theta}{\partial x} \delta x \right) \cos \left( \alpha + \frac{\partial \theta}{\partial x} \delta x \right) + \phi_2 S_2 \left( \beta + \frac{\partial \theta}{\partial x} \delta x \right) \cos \left( \beta + \frac{\partial \theta}{\partial x} \delta x \right) \right] \delta t.$$

If A'C is drawn parallel to AB, then

$$CB' = \frac{1}{N} \frac{\partial \theta}{\partial x} \delta x \frac{d}{d\theta} \left[ \phi_1 S_1 \cos \alpha + \phi_2 S_2 \cos \beta \right] \delta t$$

where  $S_1 \equiv S_1(\alpha)$  and  $S_2 \equiv S_2(\beta)$ .

Also  $A'C = R \frac{\partial \theta}{\partial x} \delta x$  where  $R$  is the radius of curvature of  $AB$ . Now  $\delta \theta_t$  is the change in tangential angle from  $A$  to  $A'$  in time  $\delta t$ , therefore

$$\frac{\delta \theta_t}{\delta x} = \frac{CB'}{A'C} = \frac{1}{NR} \frac{d}{d\theta} \left[ \phi_1 S_1 \cos \alpha + \phi_2 S_2 \cos \beta \right] \quad (2.8)$$

This expresses the rate of change of tangential angle, in the direction of the surface normal. Now consider  $\theta$  to be a function only of  $x$  and time. Then

$$\delta \theta = \left( \frac{\partial \theta}{\partial x} \right)_t \delta x + \left( \frac{\partial \theta}{\partial t} \right)_x \delta t$$

and so

$$\frac{\delta \theta}{\delta t} \text{ in any direction} = \left( \frac{\partial \theta}{\partial x} \right)_t \frac{\delta x}{\delta t} + \left( \frac{\partial \theta}{\partial t} \right)_x$$

The above equation expresses the rate of change of  $\theta$  in any one direction. If we choose this direction to be the normal direction  $n$  then, using (2.8), we have

$$\frac{1}{NR} \frac{d}{d\theta} \left[ \phi_1 S_1 \cos \alpha + \phi_2 S_2 \cos \beta \right] = \left( \frac{\partial \theta}{\partial x} \right)_t \left( \frac{\partial x}{\partial t} \right)_n + \left( \frac{\partial \theta}{\partial t} \right)_x$$

After some manipulation it can be shown that

$$\left( \frac{\partial \theta}{\partial t} \right)_x \left( \frac{\partial \theta}{\partial x} \right)_t^{-1} = \frac{1}{N} \left[ \cos \theta \left\{ \phi_1 S_1' \cos \alpha + \phi_2 S_2' \cos \beta \right\} + \left( \phi_2 S_2 - \phi_1 S_1 \right) \sin \epsilon \right] \quad (2.9)$$

where  $S_1' = \frac{dS_1(\alpha)}{d\theta}$  and  $S_2' = \frac{dS_2(\beta)}{d\theta}$ .

Conversely, if  $\theta$  is a function only of  $y$  and time, then

$$\frac{\delta\theta}{\delta t} = \left(\frac{\partial\theta}{\partial y}\right)_t \frac{\delta y}{\delta t} + \left(\frac{\partial\theta}{\partial t}\right)_y$$

and using (2.8) it can be shown that

$$\left(\frac{\partial\theta}{\partial t}\right)_y \left(\frac{\partial\theta}{\partial y}\right)_y^{-1} = -\frac{1}{N} \left[ \sin\theta \left\{ \phi_1 S_1' \cos\alpha + \phi_2 S_2' \cos\beta \right\} - (\phi_1 S_1 + \phi_2 S_2) \cos\epsilon \right] \quad (2.10)$$

Equations (2.9) and (2.10) give the rate of motion of points along a characteristic line in  $(x,t)$  and  $(y,t)$  space, respectively. Division of (2.10) by (2.9) gives the slope of the characteristic line in  $(x,y)$  space, i.e.,

$$\left(\frac{\partial y}{\partial x}\right)_\theta = - \frac{\left[ \sin\theta \left\{ \phi_1 S_1' \cos\alpha + \phi_2 S_2' \cos\beta \right\} - (\phi_1 S_1 + \phi_2 S_2) \cos\epsilon \right]}{\left[ \cos\theta \left\{ \phi_1 S_1' \cos\alpha + \phi_2 S_2' \cos\beta \right\} + (\phi_2 S_2 - \phi_1 S_1) \sin\epsilon \right]} \quad (2.11)$$

Equations (2.9) and (2.10) are standard partial differential equations which are solved by writing down their auxiliary equations. For example, (2.9) can be rewritten as

$$\left(\frac{\partial\theta}{\partial t}\right)_x - G \left(\frac{\partial\theta}{\partial x}\right)_t = 0$$

where

$$G = \frac{1}{N} \left[ \cos\theta \left\{ \phi_1 S_1' \cos\alpha + \phi_2 S_2' \cos\beta \right\} + (\phi_2 S_2 - \phi_1 S_1) \sin\epsilon \right]$$

Auxiliary equations are

$$\frac{dt}{1} = \frac{dx}{-G} = \frac{d\theta}{0}$$

Therefore along the characteristics

$$\frac{dx}{dt} = -G = -\frac{1}{N} \left[ \cos\theta \left\{ \phi_1 S_1' \cos\alpha + \phi_2 S_2' \cos\beta \right\} + (\phi_2 S_2 - \phi_1 S_1) \sin\epsilon \right]$$

and  $\theta$  is constant, as for one beam erosion.

Thus the characteristic lines are lines of constant surface orientation whose gradients in the x-y plane are given by equation (2.11). The coordinate x on the sputtered surface is related to its value  $x_0$  before bombardment by

$$x = x_0 - \frac{t}{N} \left[ \cos\theta \left\{ \phi_1 S_1' \cos\alpha + \phi_2 S_2' \cos\beta \right\} + (\phi_2 S_2 - \phi_1 S_1) \sin\epsilon \right] \quad (2.12)$$

Going through a similar procedure using equation (2.10) gives the variation of y along the characteristics,

$$y = y_0 + \frac{t}{N} \left[ \sin\theta \left\{ \phi_1 S_1' \cos\alpha + \phi_2 S_2' \cos\beta \right\} - (\phi_1 S_1 + \phi_2 S_2) \cos\epsilon \right] \quad (2.13)$$

If  $\epsilon$  is put equal to zero and  $\phi_1 = \phi_2 = \phi/2$ , then (2.12) and (2.13) reduce to the equations for a single beam of energetic ions,  $\phi$  per unit area per sec, incident along the negative y-direction. Equation (2.11) gives the direction of motion of points of constant surface orientation as the surface is sputtered. The speed of motion of such points is determined using equations (2.12) and (2.13), i.e.,

$$v^2 = \left( \frac{\partial x}{\partial t} \right)_\theta^2 + \left( \frac{\partial y}{\partial t} \right)_\theta^2$$

Hence, from equations (2.12) and (2.13)

$$v^2 = \frac{1}{N^2} \left[ \left\{ \frac{d}{d\theta} (\phi_1 S_1 \cos\alpha + \phi_2 S_2 \cos\beta) \right\}^2 + (\phi_1 S_1 \cos\alpha + \phi_2 S_2 \cos\beta)^2 \right]$$

Now the rate of erosion of the surface by sputtering along the normal direction is  $\frac{1}{N} (\phi_1 S_1 \cos\alpha + \phi_2 S_2 \cos\beta)$  from equation (2.7). Denote this normal erosion by  $\rho$ , then



$$v^2 = \left\{ \frac{\partial \rho}{\partial \theta} \right\}^2 + \rho^2 \quad (2.14)$$

as shown by Carter et al (1977) for erosion by one beam.

To determine the condition for the formation of edges, consider two points close together on the initial surface contour, with co-ordinates  $(x_o, y_o)$  and  $(x_o + \delta x_o, y_o + \delta y_o)$  and with orientations  $\theta$  and  $\theta + \delta\theta$ . Suppose after time  $t$  these have eroded to the points  $(x_t, y_t)$  and  $(x_{td}, y_{td})$ . From equation (2.12)

$$x_t = x_o - \frac{t}{N} \left[ \cos\theta \left\{ \phi_1 S_1' \cos\alpha + \phi_2 S_2' \cos\beta \right\} + (\phi_2 S_2 - \phi_1 S_1) \sin\epsilon \right] \quad (2.15)$$

and

$$x_{td} = x_o + \delta x_o - \frac{t}{N} \left[ \cos(\theta + \delta\theta) \left\{ \phi_1 S_1'(\alpha + \delta\theta) \cos(\alpha + \delta\theta) + \phi_2 S_2'(\beta + \delta\theta) \cos(\beta + \delta\theta) \right\} + \left\{ \phi_2 S_2(\beta + \delta\theta) - \phi_1 S_1(\alpha + \delta\theta) \right\} \sin\epsilon \right] \quad (2.16)$$

The radius of curvature of the initial surface at  $(x_o, y_o)$  is given by

$$\delta x_o \approx R_o \cos\theta \delta\theta \quad (2.17)$$

and after time  $t$  by

$$x_{td} - x_t \approx R_t \cos\theta \delta\theta \quad (2.18)$$

Thus subtracting equation (2.15) from equation (2.16) and expanding to first order in  $\delta\theta$  gives

$$R_t = R_o - \frac{t}{N} \left[ \phi_1 S_1'' \cos\alpha + \phi_2 S_2'' \cos\beta - 2(\phi_1 S_1 \sin\alpha + \phi_2 S_2 \sin\beta) \right] \quad (2.19)$$

where  $S_1'' = \frac{d^2 S_1(\alpha)}{d\theta^2}$  and  $S_2'' = \frac{d^2 S_2(\beta)}{d\theta^2}$

Thus  $R_t$  varies linearly with time along the characteristics.

Edges due to the intersection of the characteristics can form initially when  $R_t = 0$  on a surface at a time

$$t = \frac{NR_0}{\phi_1 S_1'' \cos\alpha + \phi_2 S_2'' \cos\beta - 2(\phi_1 S_1' \sin\alpha + \phi_2 S_2' \sin\beta)} \quad (2.20)$$

This is the same as the relationship derived by Carter et al (1977) for erosion by one beam.

#### 2.4.2. Computer simulation.

In this section the development of surface topography is simulated, for an initially circular cross-section, using the analysis described in the previous section. In the computer simulations it has been assumed that the ion flux of both beams is the same viz  $\phi_1 = \phi_2 = \phi$ .

The technique is as follows. First the initial profile,  $y = y(x)$ , is defined. The coordinates of a number of points on this profile,  $y_i = y(x_i)$   $i = 1, 2, \dots$ , are prescribed. At each of these points the angle  $\theta$ , between the  $y$ -direction and the normal is calculated. Next, the angle  $\epsilon$  between the beams and the  $y$ -direction is prescribed. Thus at each point the angles  $\alpha$  and  $\beta$  are defined. A point on the eroded surface can then be calculated, for given values of time, using equations (2.12) and (2.13). For uniform beams the locus of these points is a straight line, the characteristic line, which is a line of constant surface orientation. When a surface contour is bombarded by two beams,

the area of bombardment is not necessarily the same as with one beam even if the beams have the same radius and the same centre. For the case of beams assumed to extend to  $x = \pm \infty$ , it is possible that, depending on the angle of incidence, surface protrusions can shield other parts of the surface from the beams. In the case of the erosion of a circle, some parts of the circular contour are exposed to both beams but others are eroded only by one beam. For those parts of the surface which are undergoing bombardment by both beams simultaneously the computations are evaluated using equations (2.12) and (2.13). The shielded parts are eroded according to bombardment by one ion beam and these equations can be derived from (2.12) and (2.13) by putting  $\phi_1$  or  $\phi_2$  equal to zero. The sputtering yield  $S$ , used in the numerical calculations is that given by Ducommun et al (1975) for ion-bombarded silicon, viz.

$$S(\theta) = 18.73845\cos\theta - 64.65996\cos^2\theta + 145.19902\cos^3\theta \\ - 206.04493\cos^4\theta + 147.31778\cos^5\theta - 39.89993\cos^6\theta .$$

Equation (2.11) gives the slope of the characteristics in  $(x,y)$  space. From this it can be seen that the gradient of the characteristics will vary for each point on the initial surface. Hence some of the characteristic lines will intersect within the profile. This corresponds to the surface developing an edge. Care must be taken to ignore all points on any two characteristic lines after their point of intersection, as these points have no physical significance. In the two ion beam case, an extra edge develops at points on the surface where one of the beams becomes shielded. These edges form instantaneously unlike some edges formed by the intersection of characteristics, which form after a time given by equation (2.20).

### 2.4.3. Results and Discussion.

The procedure outlined in section 2.4.2 was carried out for circular cross-section with the two ion beams placed symmetrically about the normal at  $x = 0$ . The values of  $\epsilon$  chosen were  $0^\circ$ ,  $10^\circ$ ,  $20^\circ$ ,  $30^\circ$ ,  $45^\circ$ ,  $60^\circ$  and  $70^\circ$ , to explore fully the effects of varying the angle of ion-incidence. The erosion of an initially circular cross-section as a function of  $\epsilon$ , is shown in figures 2.11(a) - 2.11(g). The results show that the type of geometry developed varies significantly with  $\epsilon$ . For values of  $\epsilon \leq 45^\circ$  the end form is still wedge-shaped (figures 2.11(a) - 2.11(d)). However for  $\epsilon \geq 45^\circ$  a flat topped formation results (figures 2.11(a) - 2.11(g)). Also, as the angle  $\epsilon$  increases the lateral erosion of the hummocks decreases.

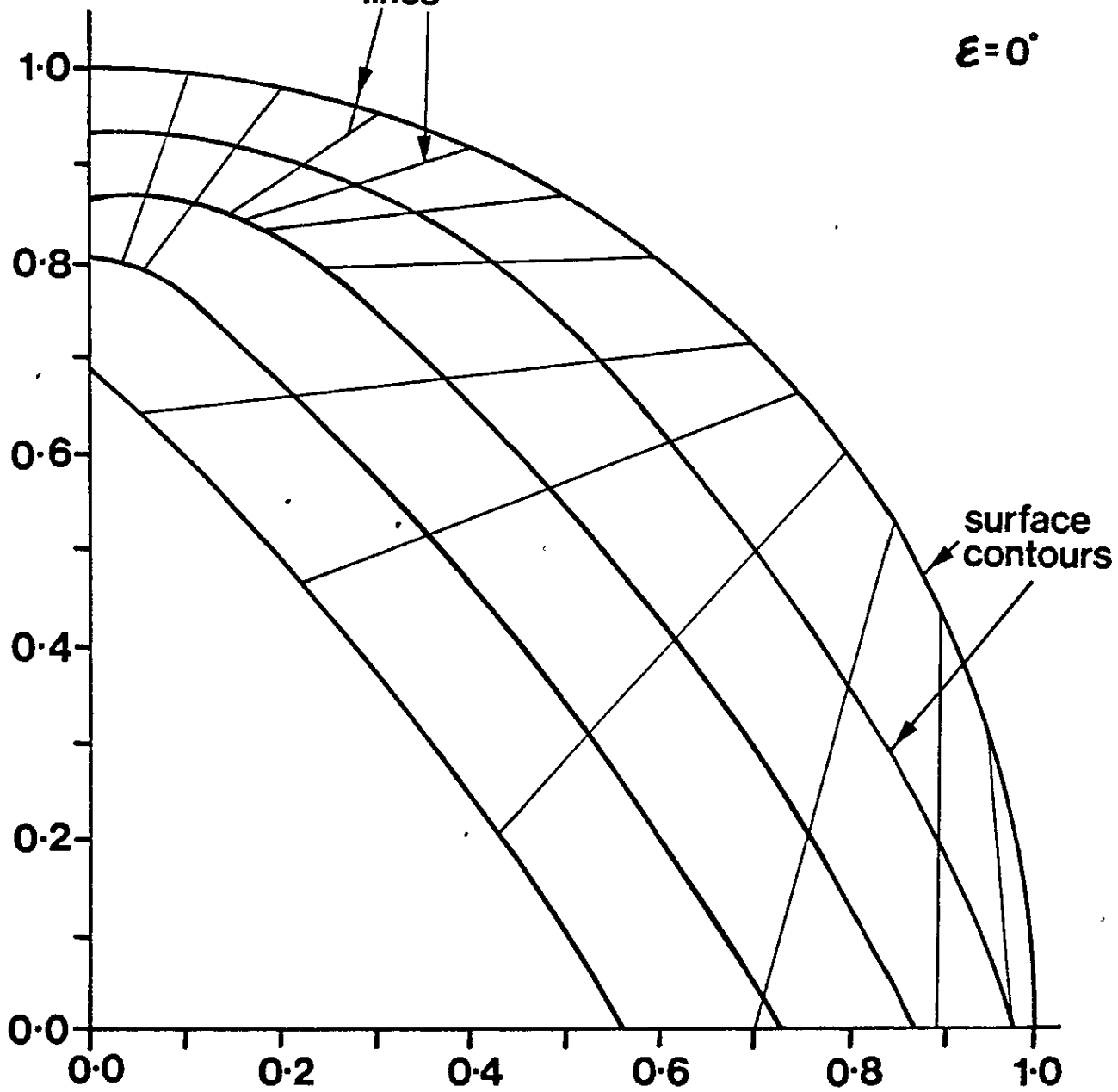
One of the most important applications of ion etching is in surface analysis and the erosion of such surfaces during depth profiling is a complex process with the constant inception of surface protrusions and pits due to impurities or intrinsic or ion-beam induced defects. Such topography is subsequently modified due to the variation of sputtering rate with ion-incidence angle. In order to determine the effects of this latter mechanism during depth profiling, a model consisting of two semicircular protrusions above a flat plane was chosen as an initial contour and the effects of bombardment by one and two beams analysed. Figures 2.12(a) - 2.12(c) show how two such adjacent protrusions from a flat surface, subject to bombardment by two beams erode for values of  $\epsilon$  of  $0^\circ$ ,  $30^\circ$  and  $60^\circ$  respectively. The distance between the centres of the hummocks is  $2.5\mu\text{m}$  and their initial height is  $1.0\mu\text{m}$ . Figure 2.12(a) is effectively the one ion beam case for normal incidence. In figure 2.12(b) the hummocks have shielded part of the intermediate flat surface from one

Fig. 2.11. The erosion of a semi-circular section by two ion beams symmetrically placed about the y-axis. The case  $\epsilon = 0^\circ$  is equivalent to erosion by one beam and illustrates the formation of a cone, but as the angular separation  $\epsilon$  of the beams increases flatter-topped structures are developed. There is no direct three-dimensional equivalent to these structures for  $\epsilon \neq 0$  since there is no rotational symmetry.

- (a)  $\epsilon = 0^\circ$
- (b)  $\epsilon = 10^\circ$
- (c)  $\epsilon = 20^\circ$
- (d)  $\epsilon = 30^\circ$
- (e)  $\epsilon = 45^\circ$
- (f)  $\epsilon = 60^\circ$
- (g)  $\epsilon = 70^\circ$

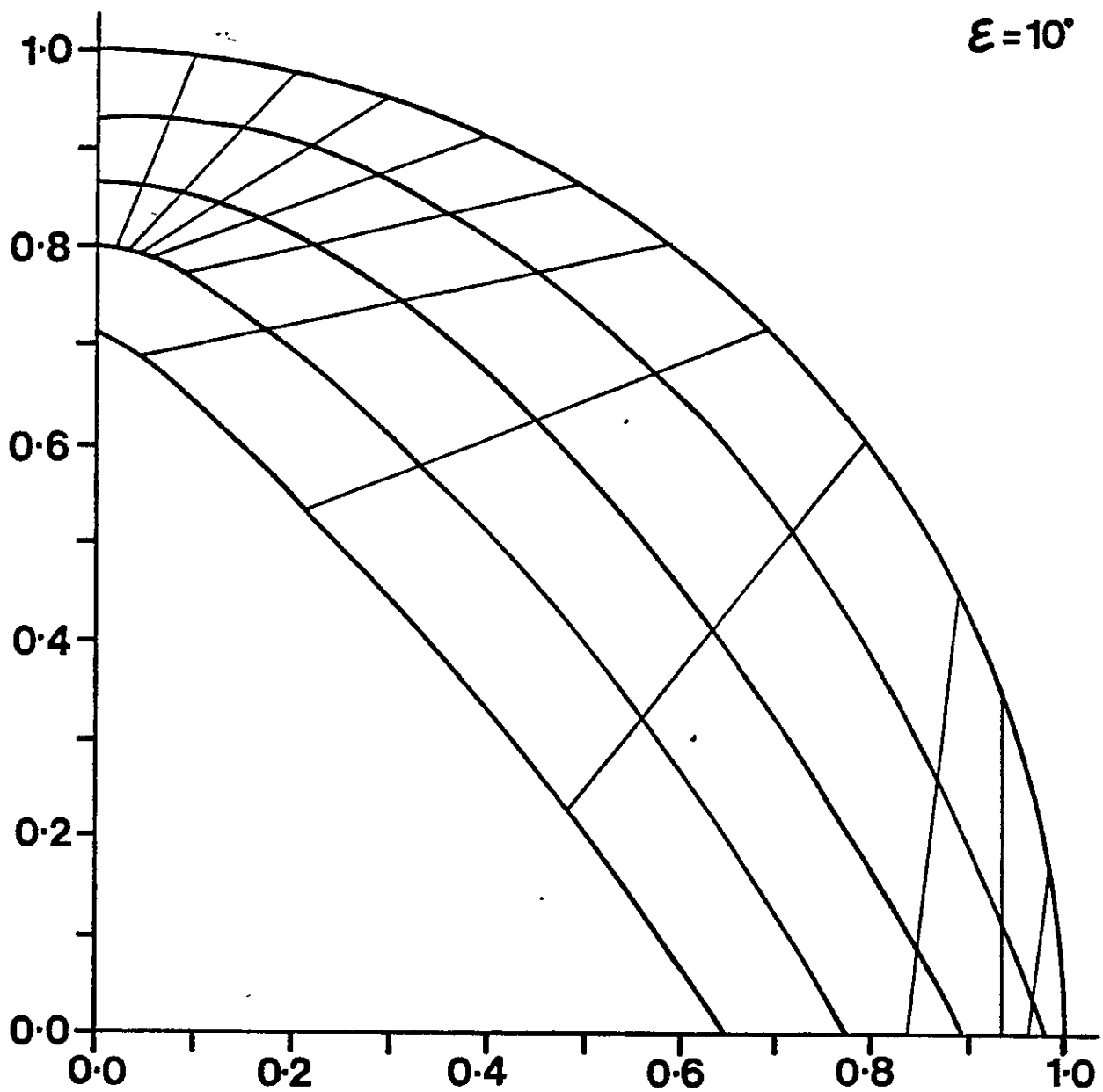
characteristic  
lines

$\epsilon = 0'$

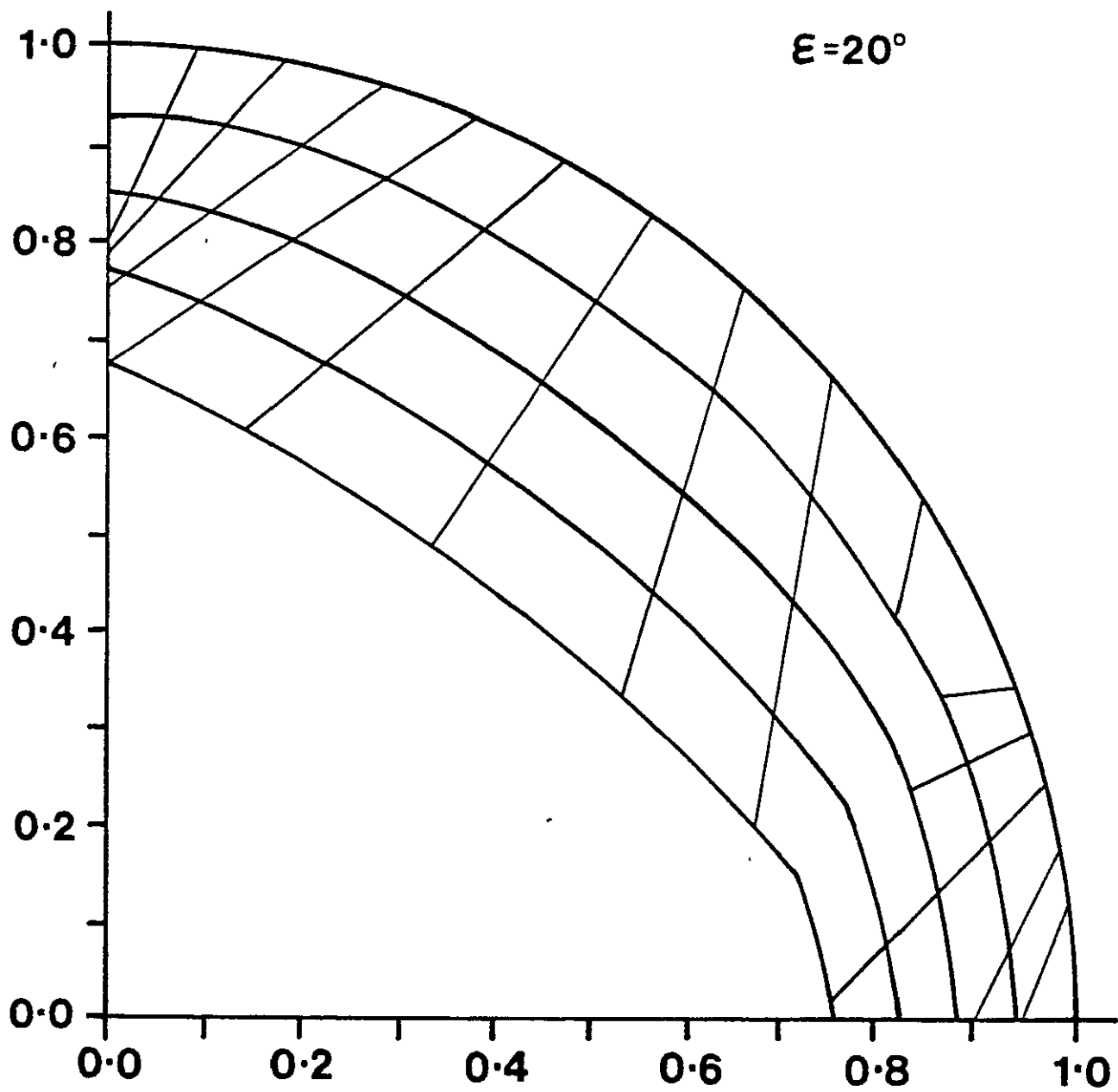


surface  
contours

a

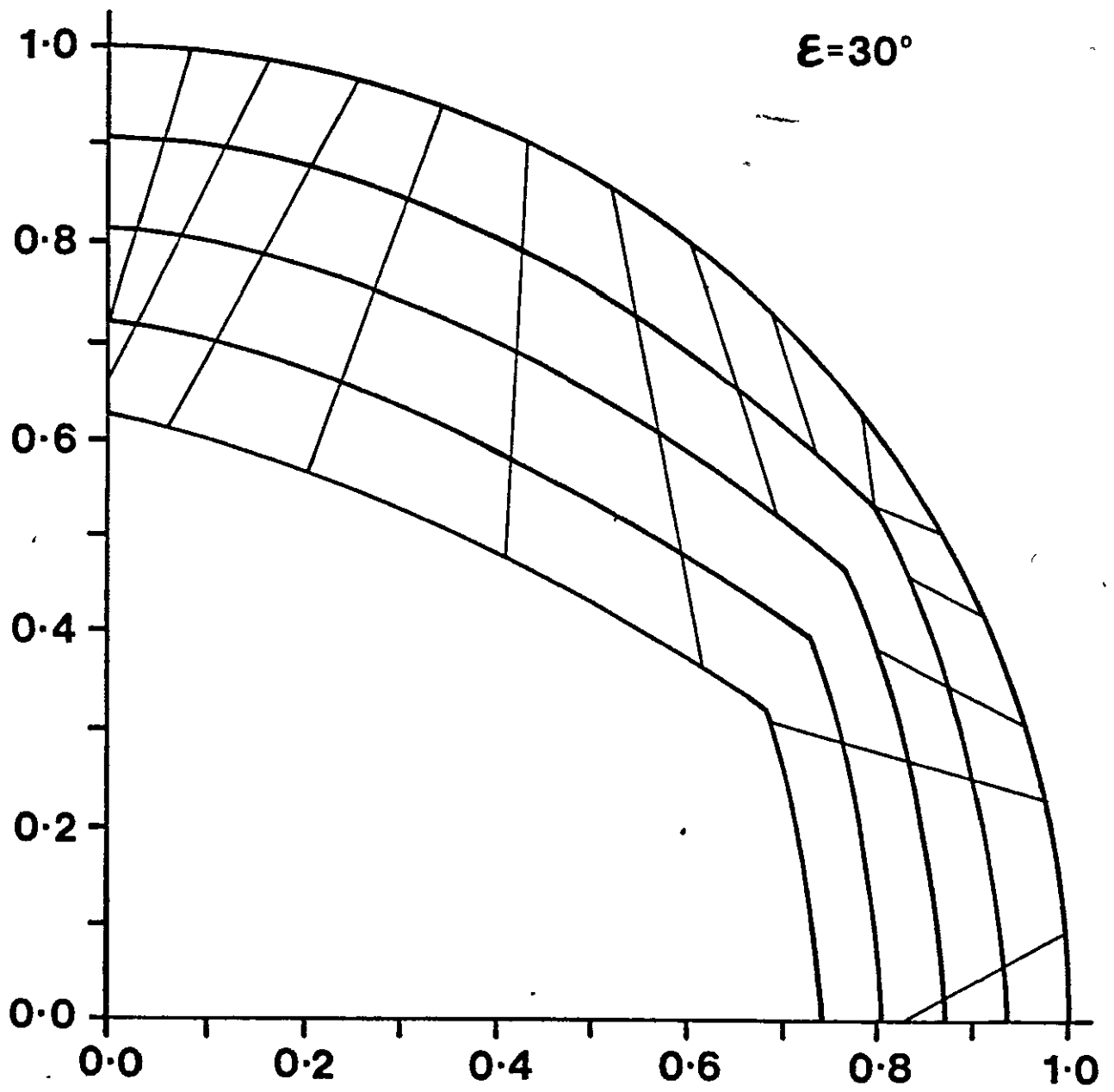


**b**



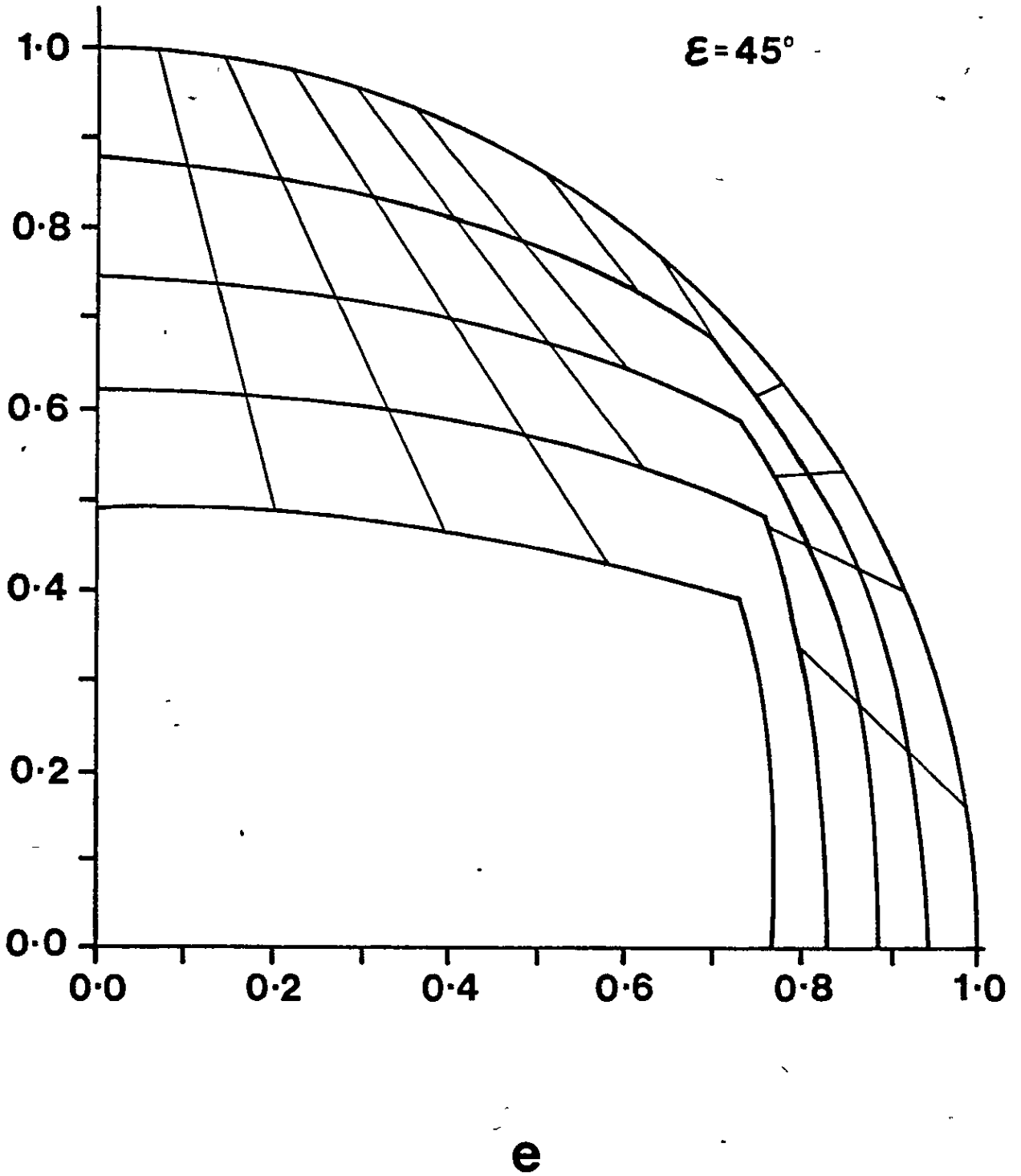
**c**

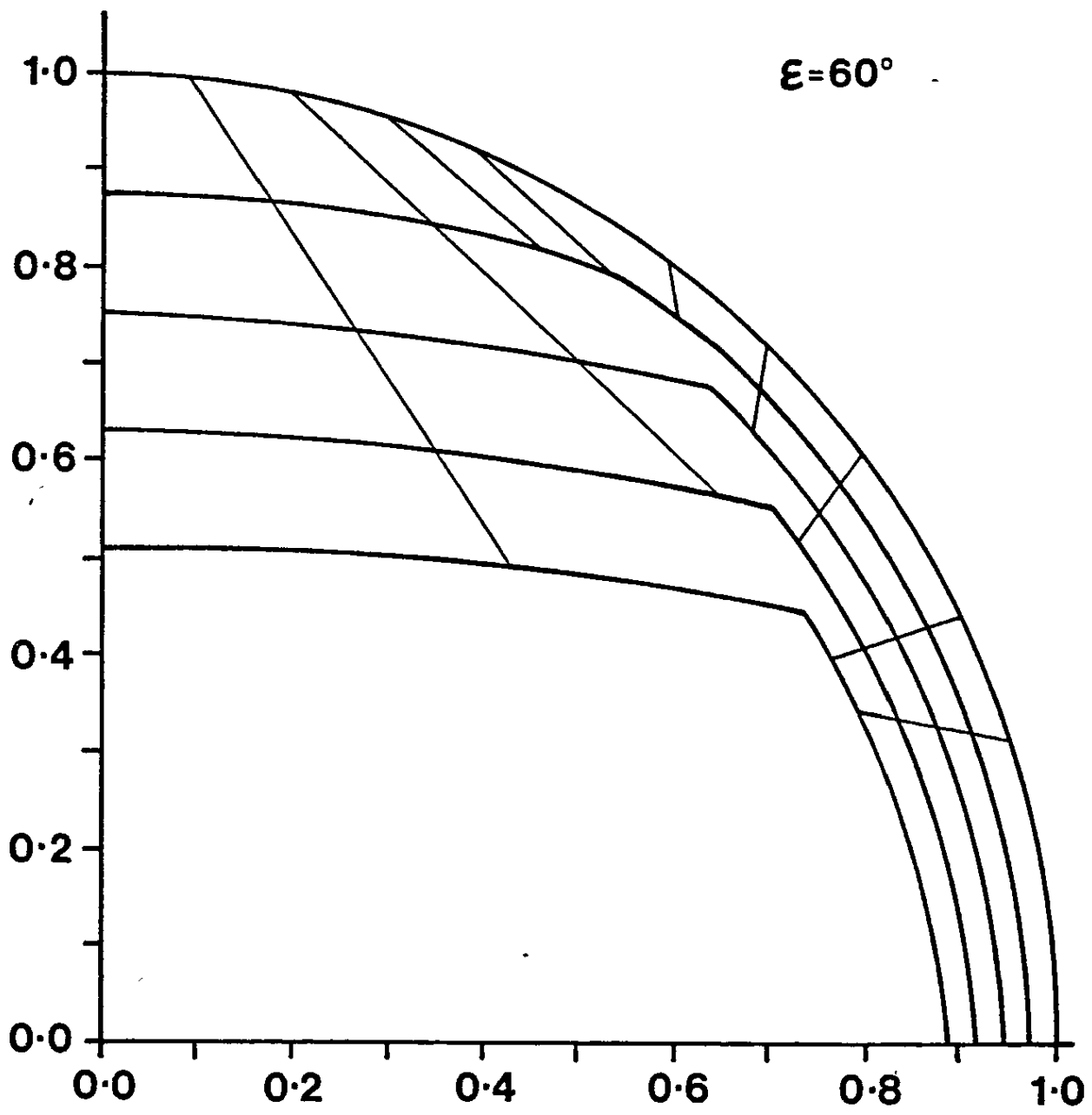




$d$

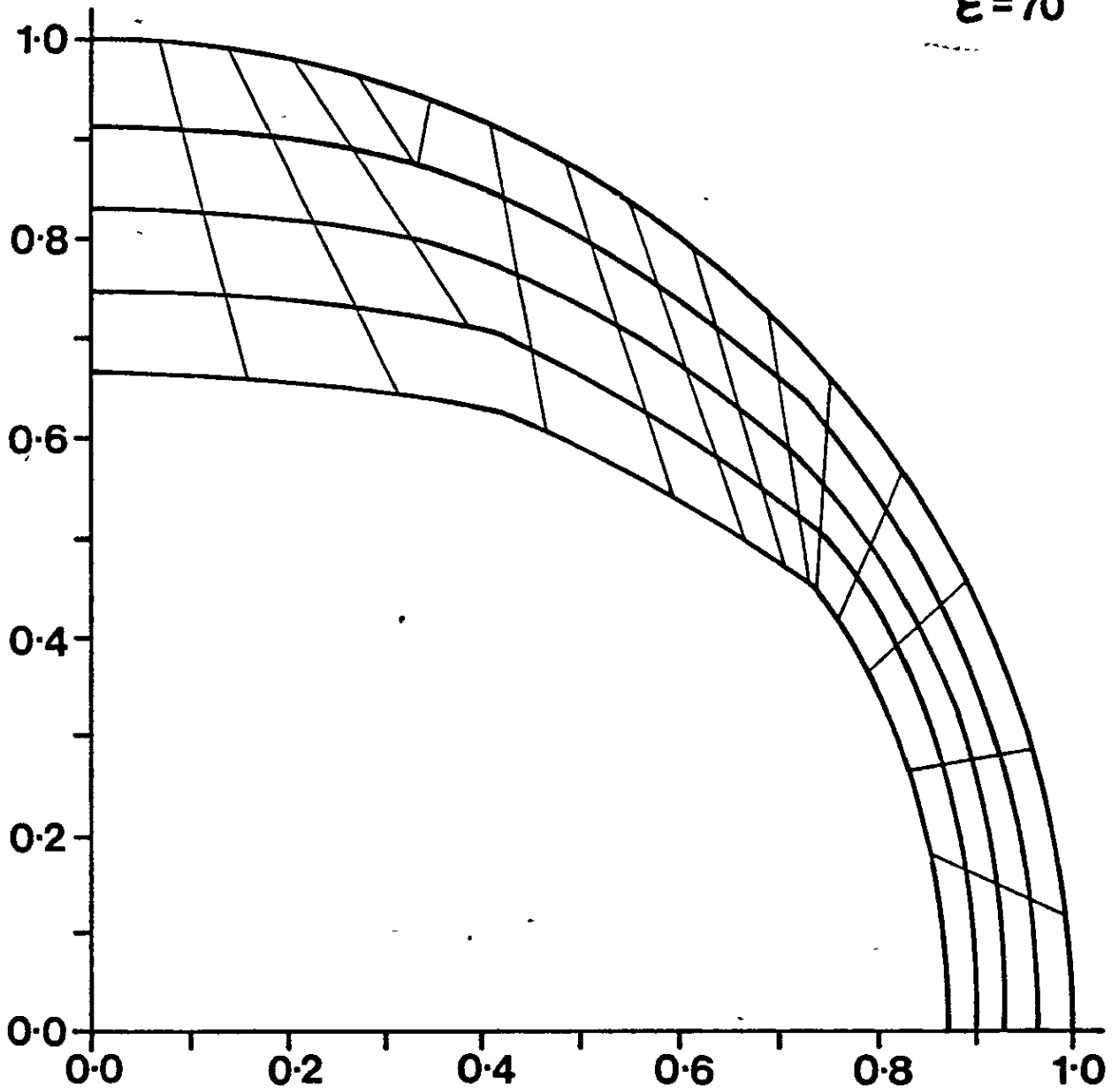
$\epsilon = 45^\circ$





**f**

$\epsilon = 70^\circ$



**g**

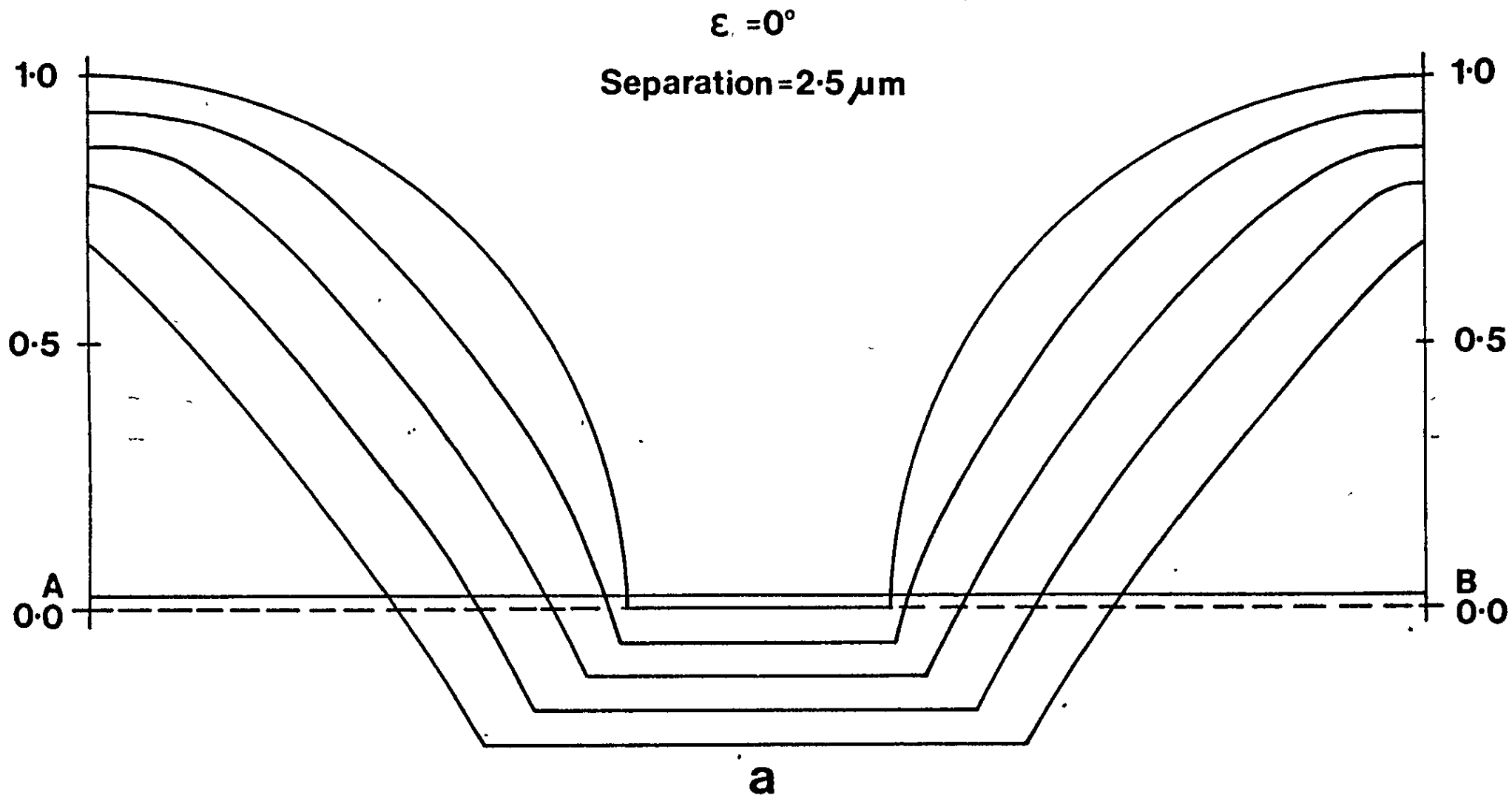
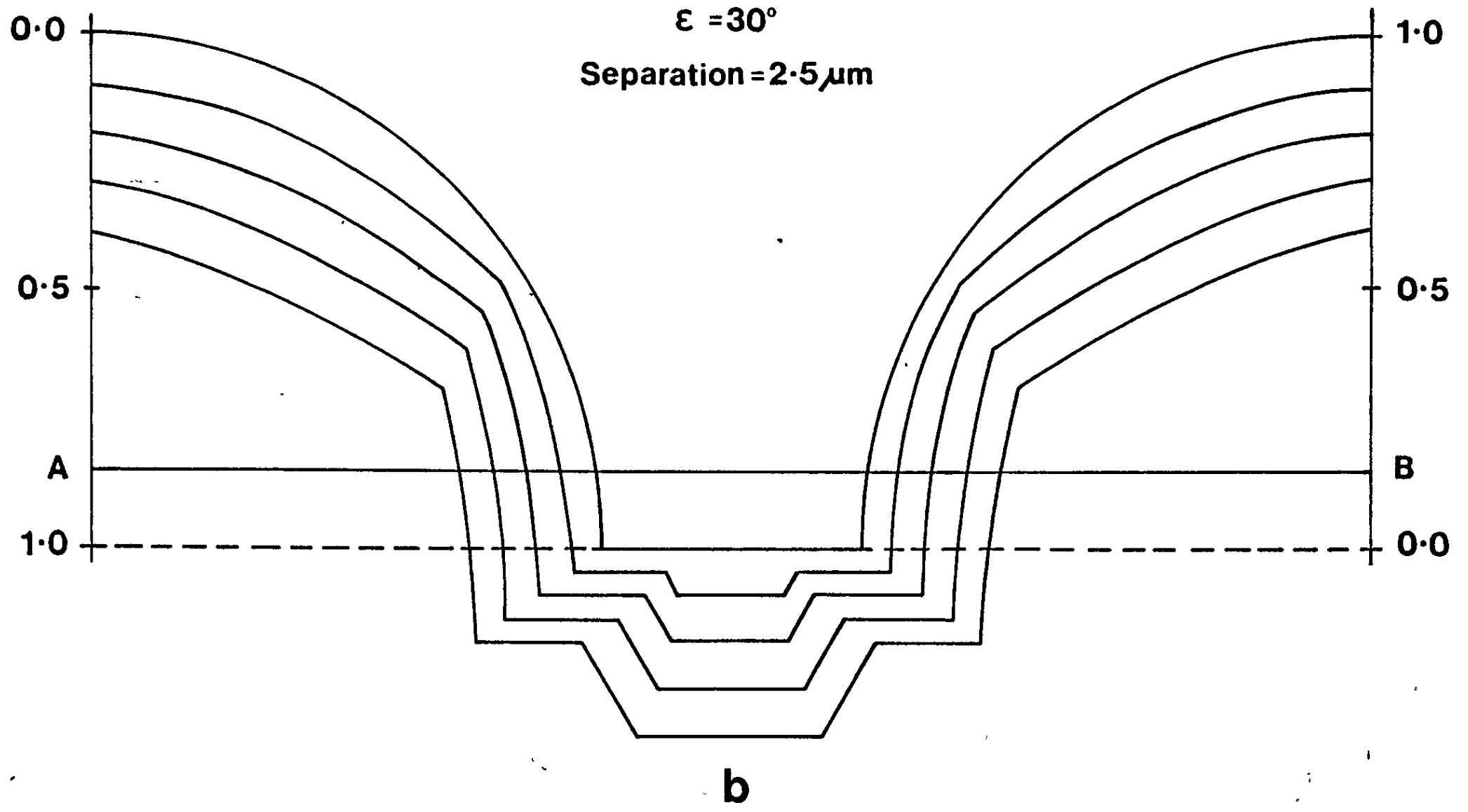
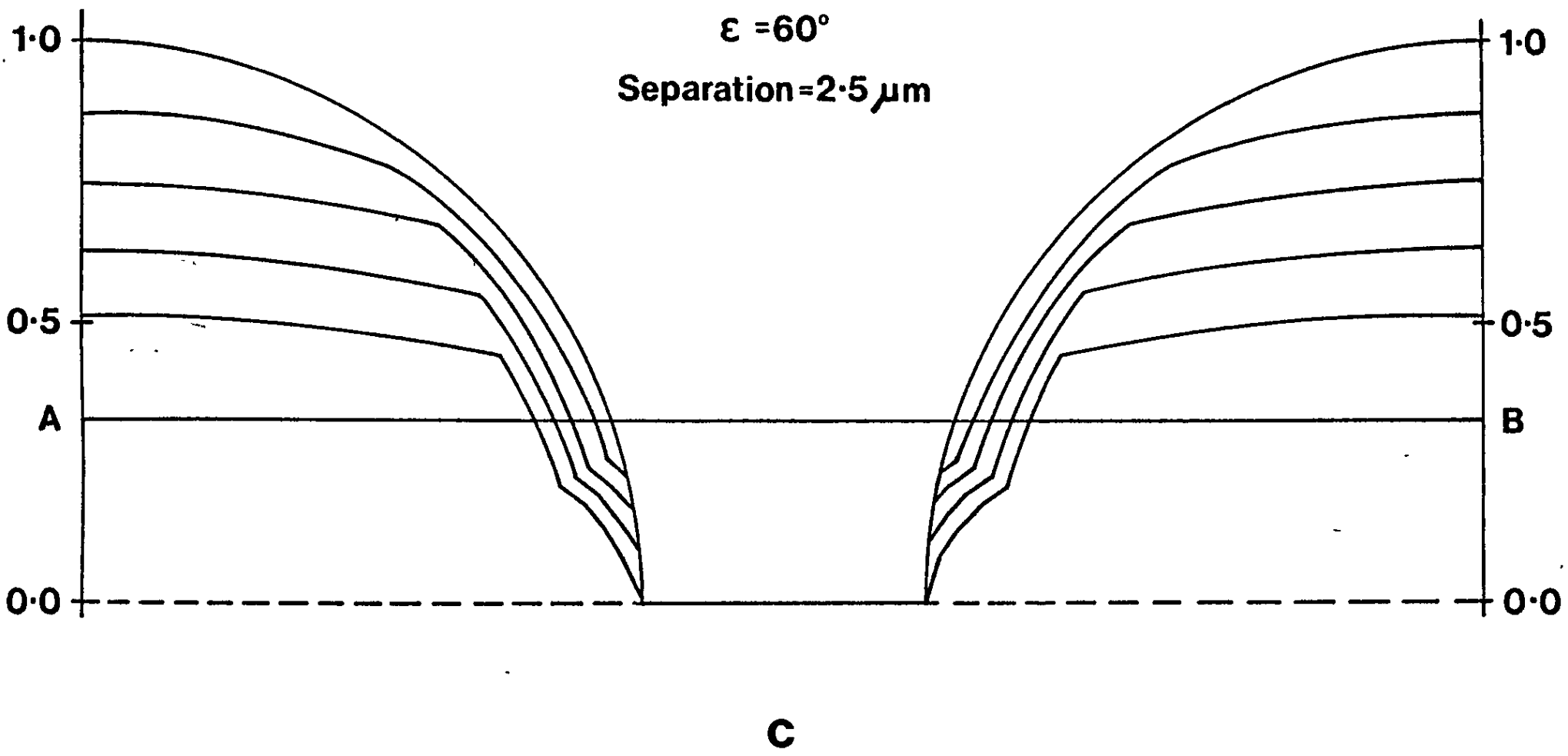


Fig. 2.12. The erosion of two adjacent semicircular structures  $1 \mu\text{m}$  radius and separated by  $2.5 \mu\text{m}$ , by two ion beams symmetrically placed about the y-axis. For  $\epsilon \neq 0$  the figures illustrate the effect of shadowing on the evolution of surface shape. Note that the gradient discontinuities at the base of the structures and those induced by shadowing in (b) and (c) would in practise be smoothed out. The line AB represents the average surface height.





of the ion beams. Due to this an initially flat surface has changed to a step-like structure, see figure 2.12(b). In figure 2.12(c) the hummocks now shield each other and the intermediate surface is subject to no erosion. Figures 2.13(a) and 2.13(b) show how the hummocks erode when the distance between centres is  $4.0\mu\text{m}$  for values of  $\epsilon$  of  $30^\circ$  and  $60^\circ$  respectively. In both these cases the hummocks are sufficiently far apart not to shield each other but part of the intermediate flat surface is shielded from the beams. This also leads to a surface with steps, similar to figure 2.12(b).

The erosion of a surface by one ion beam, for non-normal incidence, has also been considered. Thus the topography obtained with one and two beam bombardment can be compared. Figures 2.14(a) and 2.14(b) show how the circular protrusions erode when bombarded by one ion beam at angles of  $30^\circ$  and  $60^\circ$  respectively. These illustrate that for one ion beam a wedge is always formed which points in the direction of the incident ion beam.

Here it must be mentioned that recently the development of tailed cones has been observed during non-normal bombardment of surfaces using one ion beam (Auciello and Kelly (1980), (1981), Lewis et al (1980)). A number of effects have been observed such as an asymmetric pedal depression structure surrounding the cones with axes parallel to the beam and a tail or ridge like structure on the upstream side and beneath the surface projection of the cones. Lewis et al (1981) have given a simple explanation of this phenomenon using first order erosion theory (Carter et al (1977)). In this treatment a cone, pointing in the direction of the ion beam, was eroded by a uniform ion flux. The authors used an approximate form for the  $S(\theta)$  function (Ducommun et al (1975)) and from



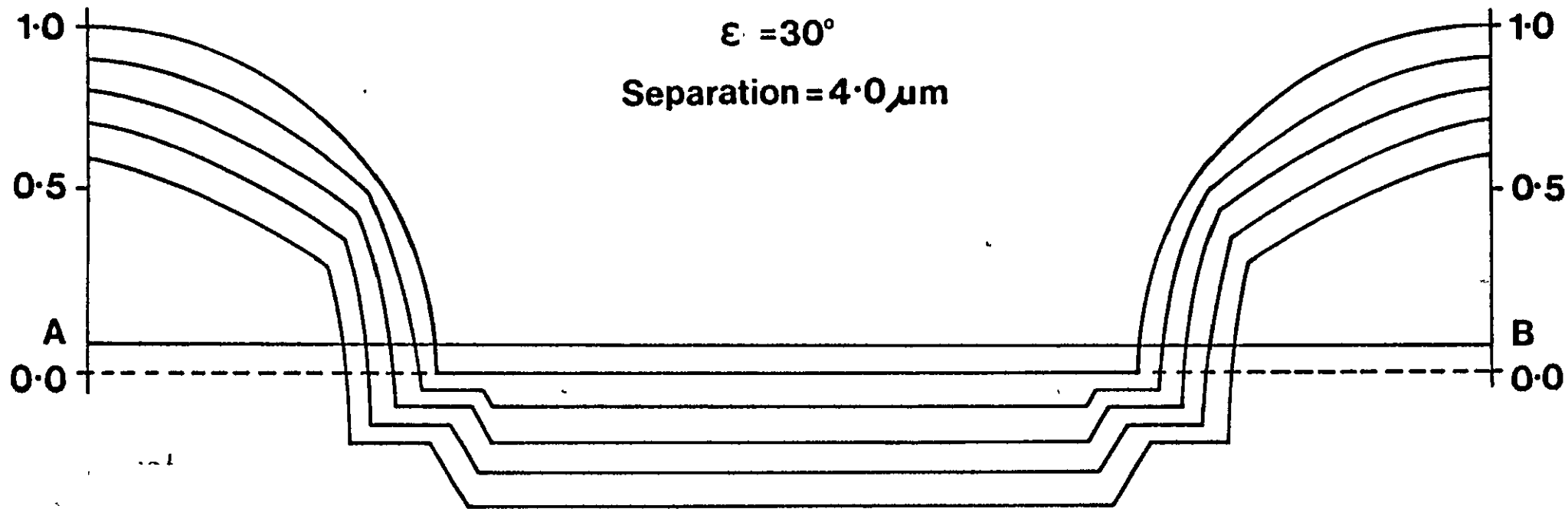
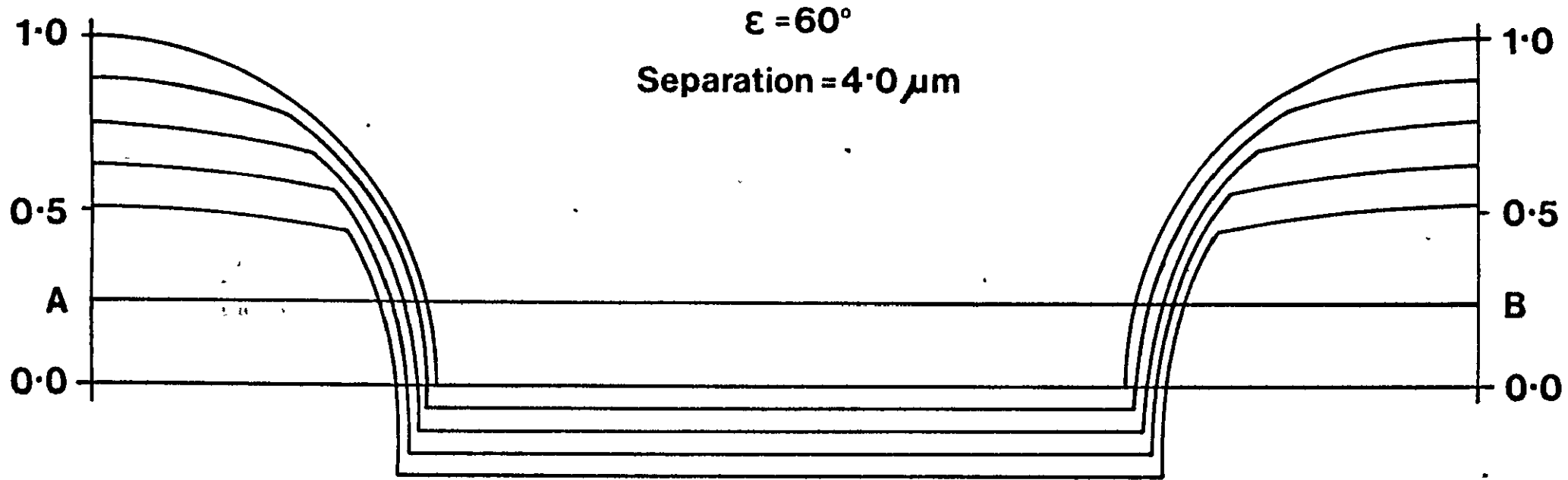


Fig. 2.13. The erosion of two adjacent semicircular structures,  $1 \mu\text{m}$  radius and separated by  $4 \mu\text{m}$ , by two ion beams symmetrically placed about the y-axis. In comparison with figure 2.12 the increased distance between the structures reduces the influence of shadowing; (a)  $\epsilon = 30^\circ$  (b)  $\epsilon = 60^\circ$ . The line AB represents the average surface height.

a



**b**

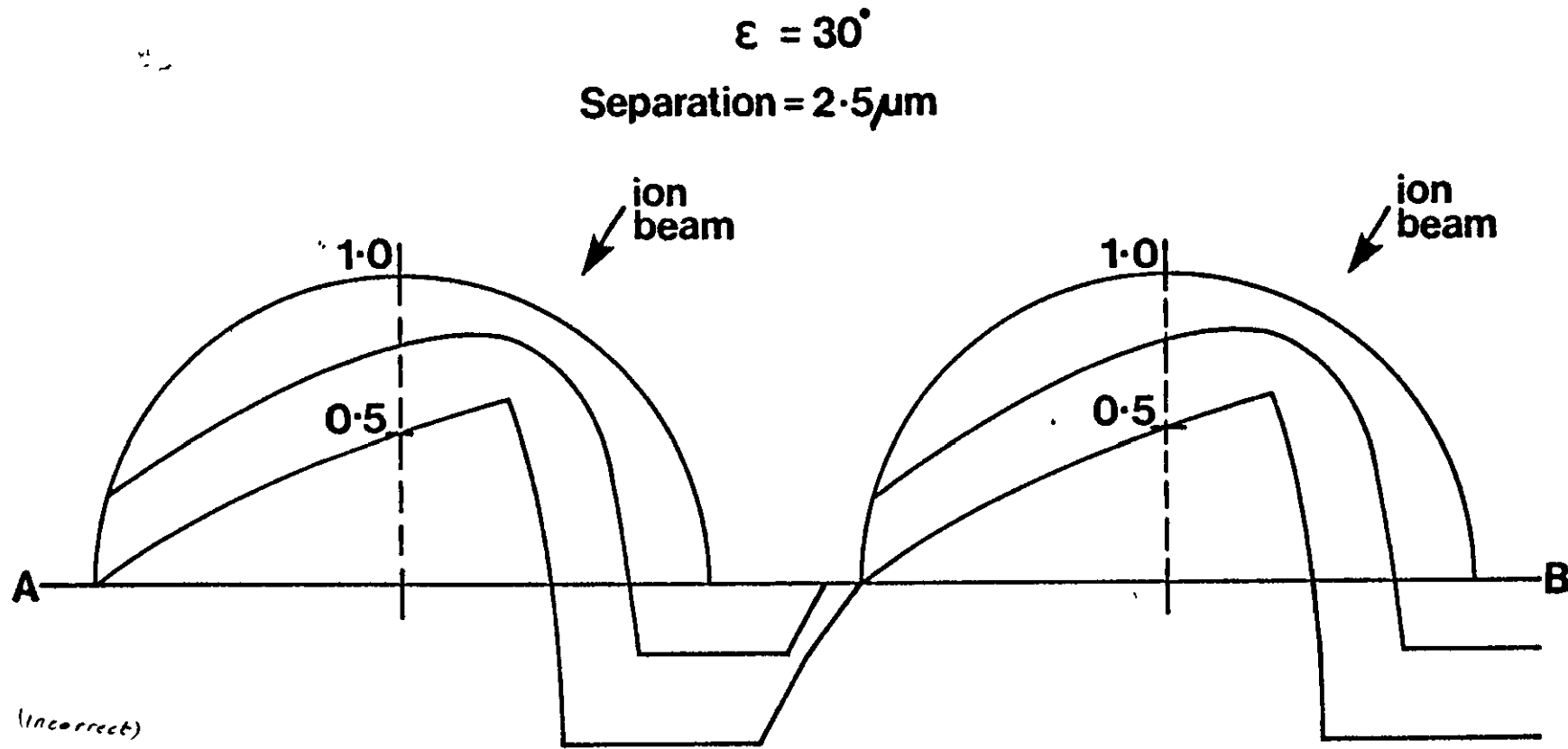
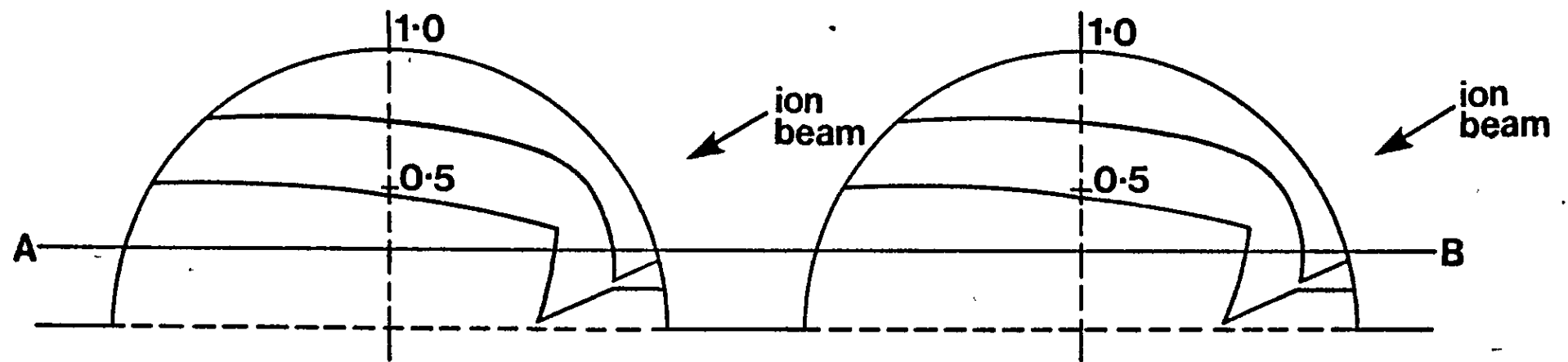


Fig. 2.14. The erosion of two adjacent semicircular structures by one ion beam at non normal incidence;  
(a)  $\epsilon = 30^\circ$  (b)  $\epsilon = 60^\circ$ . The line AB represents the average surface height.

**a**

$$\epsilon = 60^\circ$$

Separation =  $2.5 \mu\text{m}$



b

this constructed a polar diagram of velocity against surface orientation. The evolution of the cone-plane section was then determined as a function of effective ion fluence by graphically tracking the motion of a number of surface points of different initial orientations. The initial sharp edge upstream was then shown to transform into two stable edges. This behaviour of edges opening out would also occur in the diagrams shown in this section (e.g. the edges shown in figures 2.12 - 2.14). However this effect has not been incorporated into the computer programme.

Finally an attempt has been made to quantify the surface roughness obtained after bombardment of the model system by one and two beams. It has been assumed that the depth resolution can be related to the maximum deviation ( $d_{\max}$ ) about the average surface height. Thus the variation of  $d_{\max}$  under different bombardment conditions will give a measure of how the depth resolution varies. The comparison has been made after an erosion time corresponding to depth profiling  $0.26\mu\text{m}$  of a flat plane. This shows that  $d_{\max}$  is much more dependent on the angle of ion incidence than whether the surface is subjected to bombardment by one or two beams. At  $60^\circ$  incidence the value of  $d_{\max}$  is reduced by 30% of its normal value, whereas the value of  $d_{\max}$  using two beams is reduced by only about 5%, of the corresponding single beam bombardment values. Although for the model system, the results must be treated with some caution, they are consistent with the experimental evidence obtained by Sykes et al (1980) who obtained an improvement in the depth resolution using two ion guns. Figure 2.15 shows a schematic diagram illustrating the geometry of their ion bombardment arrangement. Each gun was mounted symmetrically at  $\pm 31.5^\circ$  to the sample normal. Figure 2.16(a) and (b) shows the surface topography that is obtained following ion

Fig. 2.15. A schematic diagram illustrating the geometry of the twin ion beam system used in depth profiling by Auger Electron Spectroscopy.

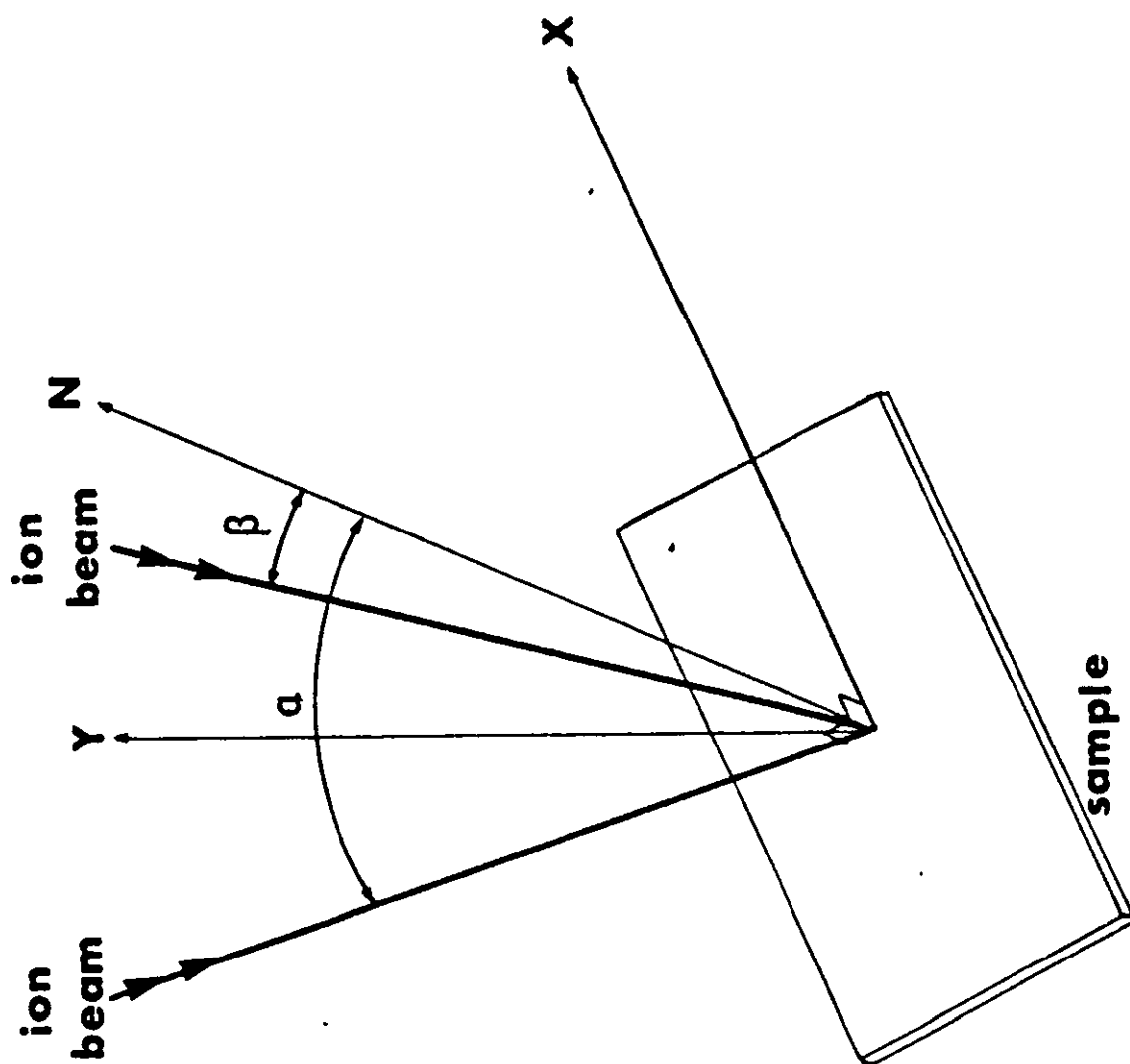
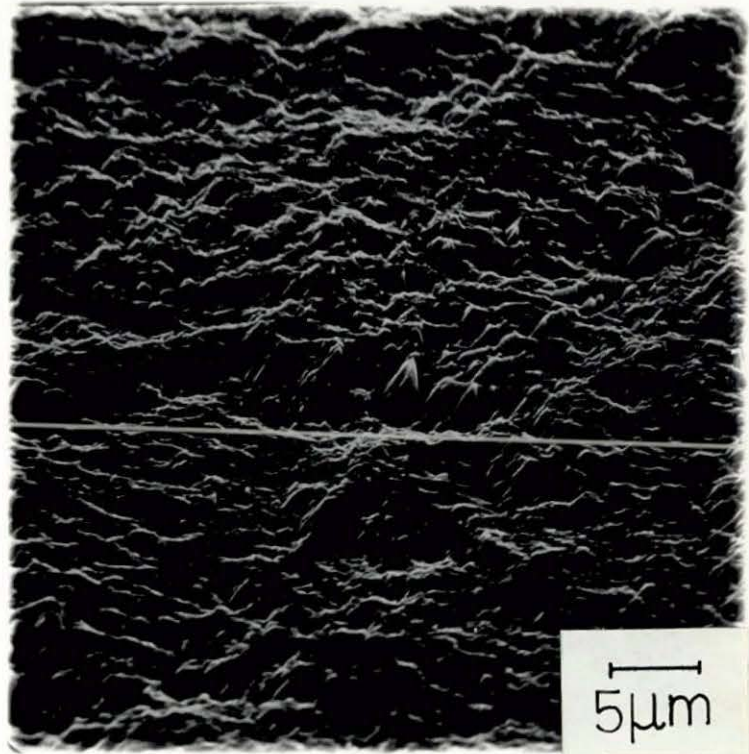




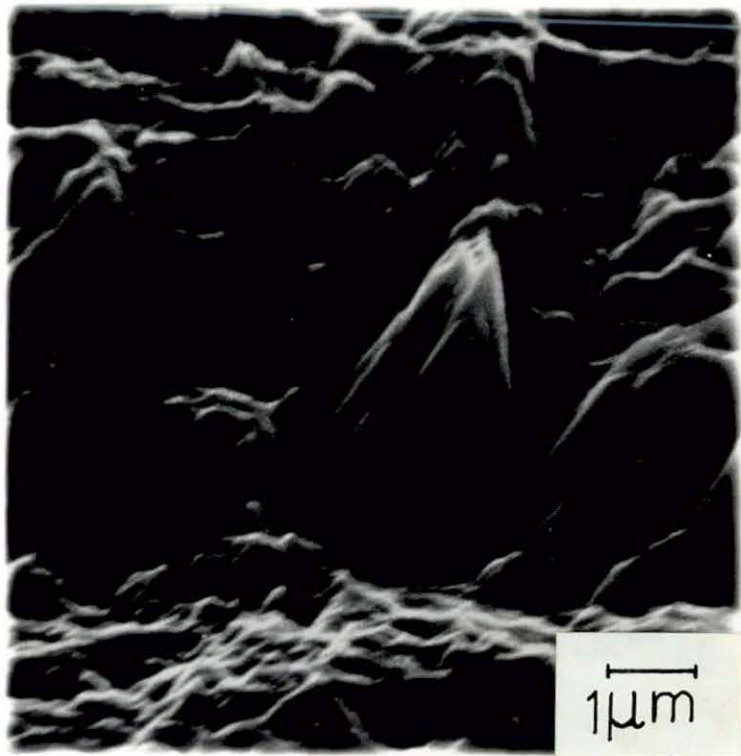
Fig. 2.16. The surface topography obtained after bombardment of a treated stainless steel surface to a depth of  $16\mu\text{m}$  with one ion gun at an angle of  $31.5^\circ$  to the surface normal. Cones orientated towards the ion beam axis are clearly evident.

- (a)  $\times$  2400
- (b)  $\times$  12000





**a**



**b**

bombardment with one ion gun at  $31.5^\circ$  to the surface normal and figure 2.17(a) and (b) the topography that is obtained when bombarding with two ion guns. In both cases a steel surface was bombarded by 3 keV  $\text{Ar}^+$  ions, current density  $0.15 \text{ mA.cm}^{-2}$ , to a depth of  $16 \mu\text{m}$ . These results illustrate the differences in surface topography when using one or two ion guns. This is reflected in the improvement usually observed in the depth resolution. This result can be partially explained by incorporating the slow lateral erosion of the hummocks for values of  $\epsilon \neq 0^\circ$  with the flattening of the tops of the hummocks and shielding effects.

In practice, massive topography on ion etched surfaces is attributed to the presence of low sputtering yield impurities or inclusions. This effect has not been considered in our model system although figures 2.11(a), 2.13 and 2.14 illustrate how their two-dimensional equivalents can form from an initially smooth hemispherical surface. Figure 2.14 shows that for non-normal incidence these structures can mask substantial portions of a surface if subjected to bombardment by one ion beam alone. However, with two ion beams, this shielding is less effective and undercutting of such conical structures will occur which will not only suppress their development but will also lead to their faster decay. This is the major reason why massive ion-induced topographical structures are not observed using two ion beams.

In conclusion, the paper has given a theoretical treatment for the erosion of surfaces during bombardment with two ion beams, and has accounted for the different types of topography observed. This modified topography can be used to explain the improved depth resolution of composition-depth profiles observed to occur with two ion beams on impurity-free surfaces. The improvements in depth resolution on surfaces which generate massive cone topography due to the presence of impurities will be due to a combination of the modified surface topography obtained

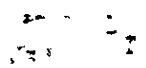
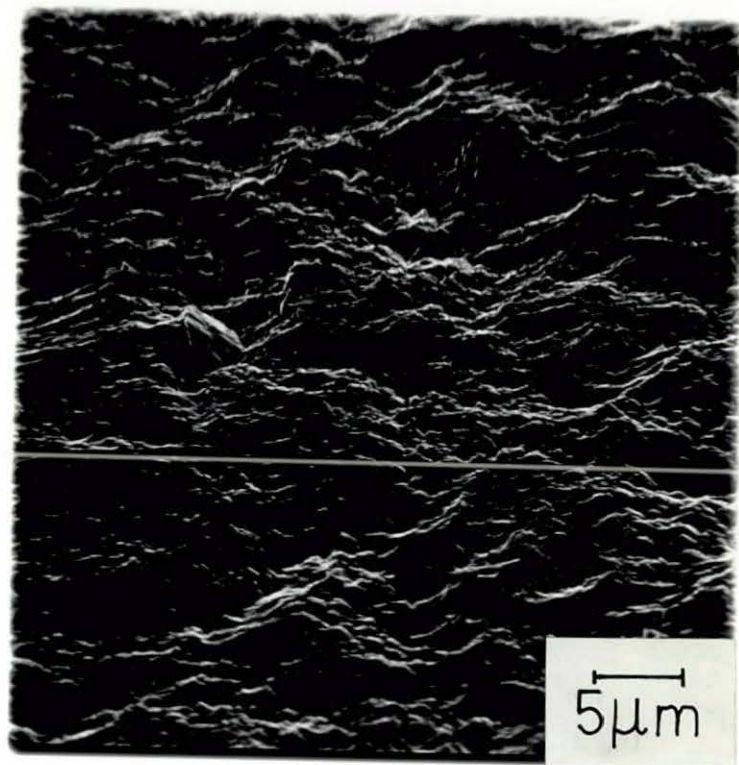


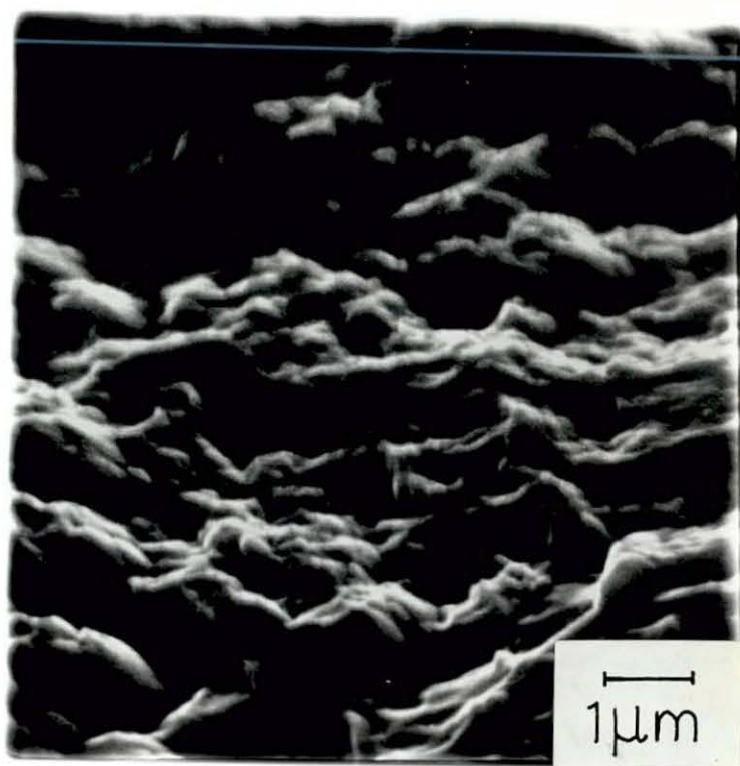
Fig. 2.17. The surface topography obtained after bombardment of a treated stainless steel surface to a depth of  $16\mu\text{m}$  with two ion guns arranged symmetrically at  $31.5^\circ$  to the surface normal. There is a complete absence of cones in this case.

(a)  $\times$  2400

(b)  $\times$  12000



**a**



**b**

using two ion beams and the undercutting of impurities preventing the extent of cone development which occurs using one ion beam.

CHAPTER 3A THEORETICAL MODEL FOR THE REDEPOSITION OF SPUTTERED MATERIAL3.1. Introduction.

The trend in the microelectronics industry, and in particular the industry concerned with the fabrication of integrated circuits, is towards circuits with increasingly high density and devices with smaller feature size (Lee (1979)). This trend has aroused interest in several new process technologies for pattern replication. Ion beam etching is one such technology which offers higher resolution, greater dimensional control and higher yield than conventional wet chemical etching.

Plasma etching (alternatively referred to as 'reactive ion etching', 'reactive sputter etching' or 'plasma ashing'), involves using a glow discharge to generate chemically reactive species from relatively inert molecular gases (Irving et al (1969)). These reactive species combine chemically with certain solid materials to form volatile compounds which are removed by the vacuum pumping system. Although the concept is relatively simple, the complexities of the glow discharge itself has impeded the development of a detailed understanding of the chemical reactions involved in the process, which in turn has impeded the implementation of plasma etching in device manufacture (Coburn and Winters (1979)). Also, with glow discharges the etching of insulators is not possible due to charging effects.

Microelectronic circuit fabrication is based on the ability to selectively remove and add material to the surface of a suitable substrate

e.g. semiconductor or garnet wafers. At present, wet chemical, plasma and sputtering methods are used to etch the required structures for integrated circuits. However, new devices and circuits (such as surface acoustic wave devices, magnetic bubble memories and gallium arsenide integrated circuits) being developed demand that materials difficult to chemically-etch be patterned down to submicron dimensions with highly accurate linewidth control. For these applications, ion-beam etching (using a well collimated and neutralized ion beam) offers several advantages. First, it is a universal etchant. Ion beams can etch any material (e.g. permalloy) or combinations of materials (such as multilayer metallizations Ti, Pt, Au) that might be difficult to etch using wet or plasma chemical techniques. Second, ion etching relies on shadow masking to expose various surfaces to the beam. Thus it does not suffer from etch penetration beneath the masking layer, which leads to mask undercut.

However, the nature of ion etching is such that several unique problems are encountered when directly applying the technique. First, the ion etch rate is strongly dependant on the angle of incidence of the ions. A typical dependance is shown in figure 1.5. The angle of maximum etch rate is important since stable facets will be formed at this angle, and these will be transferred to materials exposed to an ion beam with the facet angle corresponding to the angle of maximum etch rate for the given material (Smith et al (1973)). Another problem encountered with ion-beam etching is that backspattered material tends to redeposit around the edges of steep surface features (Dimigen and Lüthje (1975), Glöersen (1976), Smith (1976), Chapman (1977), Murray et al (1978), Johnson (1979), Castellano (1980), Dargent and Sibuet (1980)).

This phenomenon is often observed along the edges of photoresist patterns, where ridges of material are left behind when the resist pattern is removed (Smith (1976)). The redeposited material is undesirable because it could interconnect isolated regions or it might prevent complete coverage by a subsequently deposited layer.

Theoretical treatments of the build-up of material due to redeposition have been proposed by Bayly (1972), Glöersen (1976) and Belson and Wilson (1980). In these studies it has been assumed that, for an ion beam incident perpendicular to the target surface, the angular distribution of sputtered particles follows a cosine law, although Belson and Wilson (1980a,b) also considered the isotropic emission case. Also the existing models do not take into account the continuously changing geometry of the substrate caused by the redeposition of sputtered material.

Although the cosine emission distribution is a good approximation for ion energies in the range 1-10keV, the distribution is under-cosine for energies < 1keV and over-cosine for energies > 10keV. (Vossen (1979)), see figure 3.1. At oblique ion incidence sputtered angular distributions have been studied by several authors (Patterson and Tomlin (1962), Formann et al (1966), Gurmin et al (1969), Betz et al (1970), Rödelsperger et al (1974)). Typical results are shown in figure 3.2 (Oechsner (1975)). With decreasing bombarding energy  $E$  the direction of preferential emission is continuously shifted from the target normal into the region of specular reflection of the incoming ions for moderate bombarding angles  $\theta$ . The exact distribution of the sputtered particles would also be dependant on the ion species being used to bombard the surface and also on the substrate material.



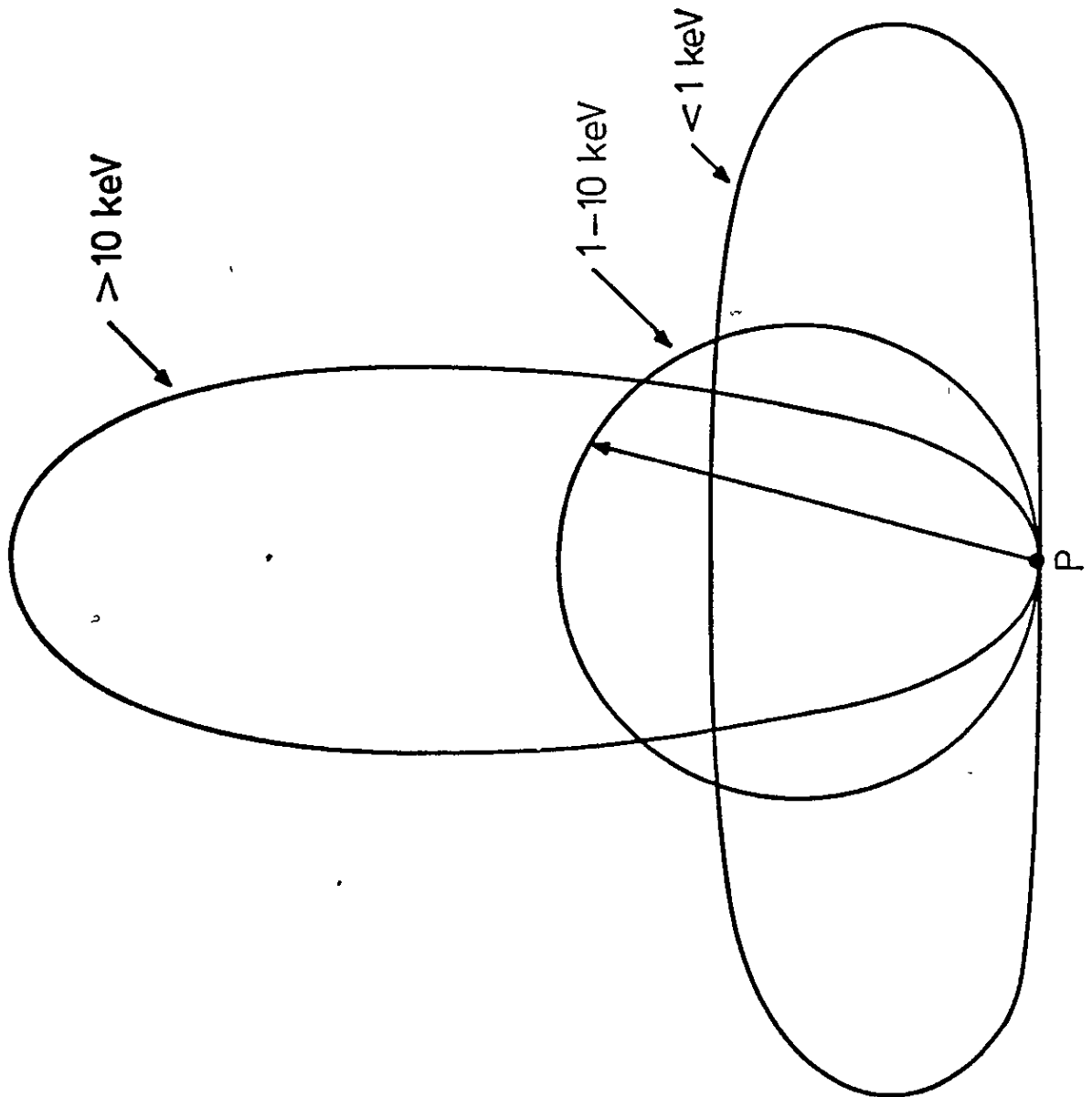


Fig. 3.1. The angular distribution of material sputtered from a point P at different energy levels. The amount of material emitted in a given direction is proportional to the length of the vector from P to the distribution curve for the particular energy level of the ion incident on the sputtered surface. (After Vossen (1979)).

$\text{Kr}^+ \rightarrow \text{W}$  polycryst. Gurmin et al 1969

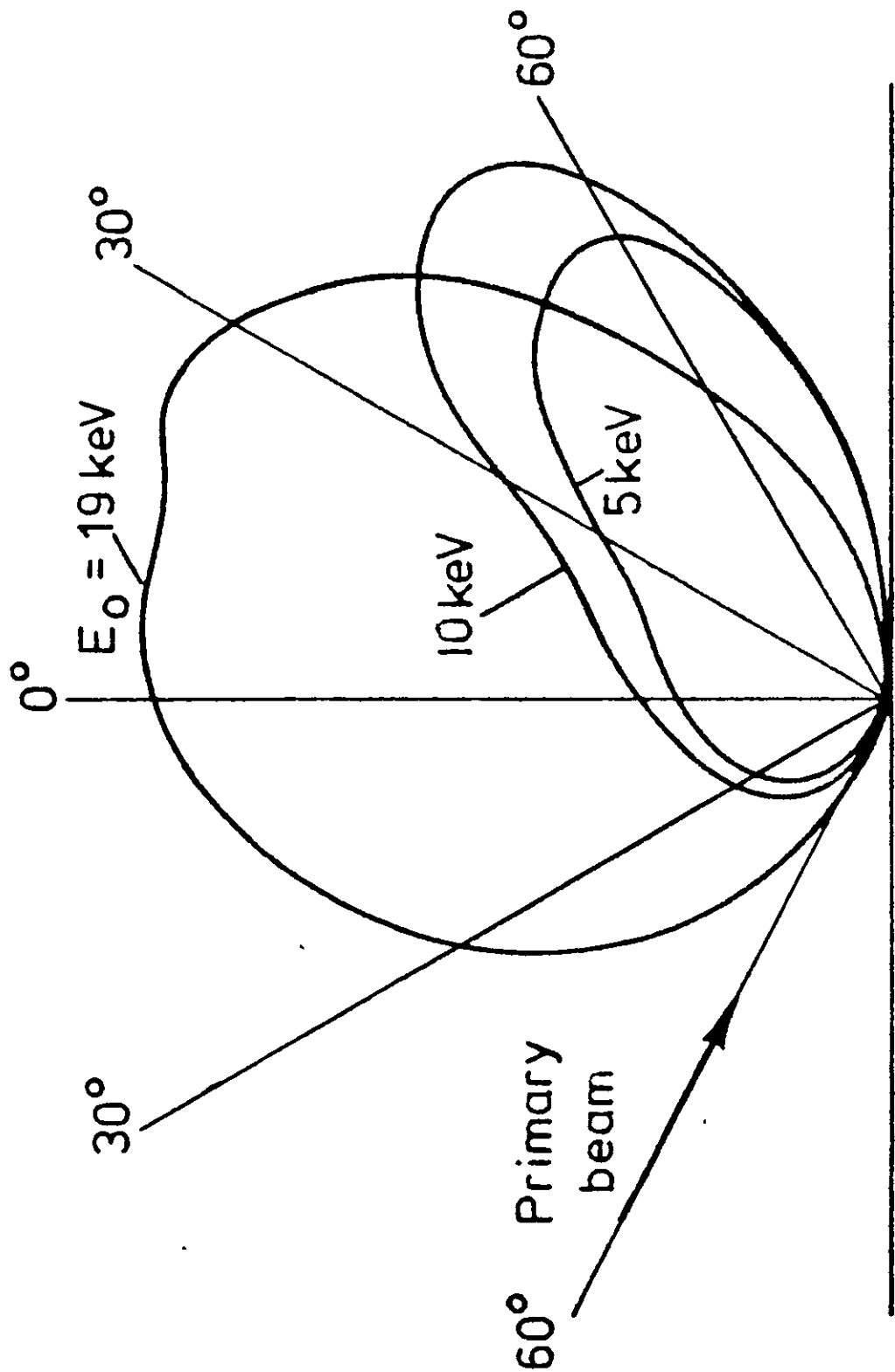


Fig. 3.2. Angular distributions of sputtered material for polycrystalline W bombarded with oblique incident  $\text{Kr}^+$  ions of different energies.

In this chapter a general two-dimensional theory is presented which not only allows for different angular distributions but also enables calculations to be made concerning shape changes due to the continuous build-up of redeposited material (Makh et al (1980b)). The theory developed here is based on the kinematic wave approach and is similar to that used by Smith and Walls (1980) to predict the surface shape of ion eroded surfaces. This approach is convenient for subsequent numerical calculations and these are used to illustrate the theory. In the latter part of this chapter, the build-up of material in initially rectangular grooves is investigated as a function of different groove widths, erosion times and different sputtered particle distributions. The simulated profiles are then compared with those obtained experimentally.

### 3.2. Experimental evidence for the redeposition of sputtered material.

In order to ion-etch a relief structure into a substrate surface, or to etch a pattern into a thin film on a substrate, the surface must first be patterned with some sort of mask. The most common type is a photoresist pattern. The etch rate of photoresist is relatively slow, and in those cases where the substrate can be cooled and gases such as oxygen can be excluded from the etching chamber, photoresist is an effective etching mask. In cases where it is not suitable, or where a greater difference between the rate of etching of the mask and the rate of etching of the exposed substrate is desired, patterns of metal films such as aluminium, titanium, chromium and vanadium are preferred (Smith (1976)). These materials have the advantage of

durability, insensitivity to heat and very low sputtering yields.

With both photoresist and metal masks, facets form at the upper corners of the sidewalls during the early stages of etching, and these etch more rapidly than surfaces normal to the direction of ion bombardment. These facets occur because the sputtering rate as a function of angle of ion incidence has a well defined maximum at some angle usually between  $40^\circ$  and  $60^\circ$ . Figure 3.3 depicts the faceting phenomena and gives a simple model for the time evolution of the profile of a mask. Clearly, if etching is continued beyond the time when the facet in the sidewall of the mask intersects the substrate surface, the pattern etched into the substrate will no longer correspond to the original mask pattern.

In addition to the limitation imposed by sidewall faceting, another important limitation to ion beam etching is redeposition of sputtered material along the sidewalls of a mask or the sidewalls of a deep groove. Gloersen (1975), (1976) studied this problem experimentally and theoretically. The author predicted a time evolution such as depicted in figure 3.4. The limitations of the analytical model will be outlined in the next section.

The definitive experiment to show the effects of faceting and redeposition of sputtered material has been carried out by Smith (1976). The results of his experiment are shown in figure 3.5. Figure 3.5(a) shows the photoresist mask on a silicon substrate and figure 3.5(b) shows the mask after ion beam etching to a depth of  $1300\text{\AA}$ . As can be seen a facet has developed at the top corners of the mask. The effects of redeposition are shown in figure 3.5(c) where the mask has been dissolved away in a solvent leaving the redeposited material.

The effects of redeposition of sputtered material have been observed by many other authors (Glöersen (1976), Chapman (1977), Murray et al (1978),

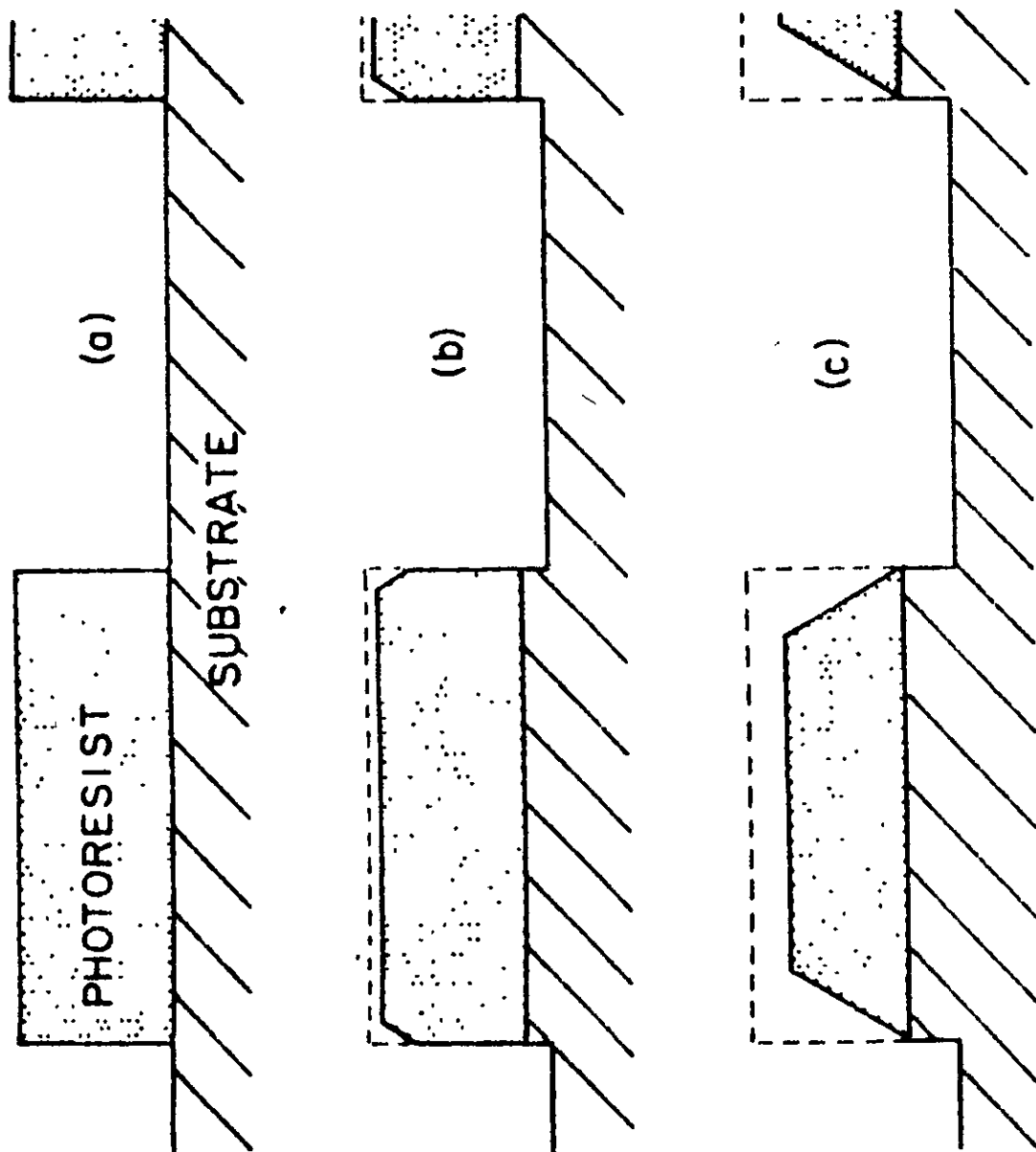


Fig. 3.3. A simple model depicting the faceting phenomenon (a) photoresist mask cross section prior to ion beam etching (b) the onset of facet formation in the photoresist mask during ion etching (c) the photoresist facet intersects the original substrate plane. If etching is continued beyond this stage, the pattern etched into the substrate will no longer correspond to the original mask pattern. (After Smith (1976)).

Fig. 3.4. Schematic illustration of the redeposition phenomenon. (a) photoresist mask prior to etching. As the etching proceeds, (b) and (c), facets are formed, and coating of the sidewalls takes place. When the remaining photoresist is lifted after etching is completed, the sidewalls may tear off (d) or may remain (e), depending on how thin and brittle the walls are. (After Gloersen (1976)).

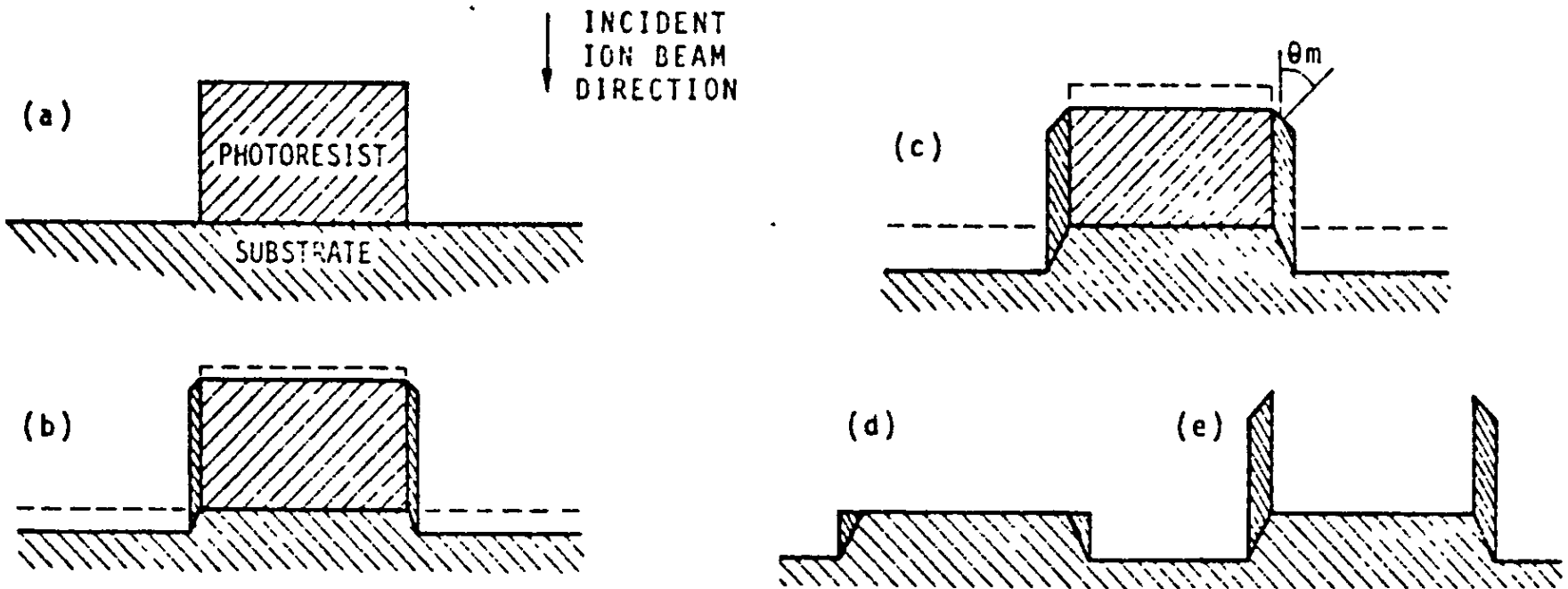


Fig. 3.5. Scanning electron micrograph illustrating the phenomena of faceting and redeposition during ion etching. (a) AZ1350 photoresist mask on silicon substrate prior to ion beam etching, (b) after ion beam etching to a depth of 1300Å, (c) the redeposited material left after dissolution of the photoresist in a solvent (Courtesy of Dr. H.I. Smith).

Castellano (1980), Dargent and Sibuet (1980), Makh et al (1980b), Brambley (1981)). Figure 3.6 shows two micrographs that illustrate the redeposition problem for etching patterns other than grooves. The pattern shown in this figure is a permalloy array for a magnetic bubble memory device. The ion beam etching conditions were: ion energy of 1keV, current density of  $0.8\text{mA}\cdot\text{cm}^{-2}$  and normal incidence. The redeposition of sputtered material can be seen quite clearly along the side walls of the pattern. Figure 3.7 shows the redeposition problem for a different pattern. The operating conditions were as follows. A  $5000\text{\AA}$  thick RF sputtered  $\text{Ni}_i\text{F}_e$  film on RF sputtered  $\text{Si}_i\text{O}_2$ . Masking was by a  $1\mu\text{m}$  thick AZ1350H photoresist and ion etching with 500eV argon ions, at an angle of  $15^\circ$  to the normal, of current density  $0.8\text{mA}\cdot\text{cm}^{-2}$ . The photoresist was then stripped off in an  $\text{O}_2$  plasma and the micrograph in figure 3.7 shows the redeposited material left after the stripping. Figure 3.8 shows a series of micrographs illustrating the redeposition effect for permalloy elements. Masking was by AZ1350J photoresist of approximately  $1\mu\text{m}$  thickness. Ion bombardment was at normal incidence using 600eV argon ions of current density  $0.6\text{mA}\cdot\text{cm}^{-2}$ . The series of micrographs show clearly the effects of redeposition along the sidewalls of the patterns after the photoresist has been removed.

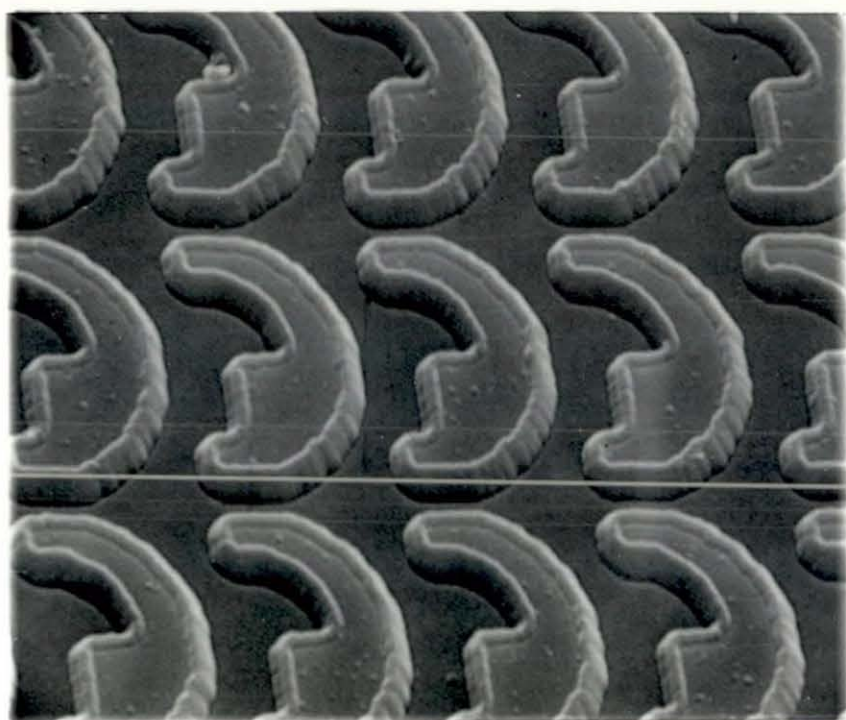
Some additional experiments have been carried out to confirm the redeposition problem and to see how it changes when the groove width is made very much greater than the groove height. The experiments have been carried out in a 'Veeco Microetch System'. Figure 3.9 shows a schematic diagram of the microetch ion beam source. Section 1, the discharge chamber, is the zone in which ions are generated. A hot tungsten cathode is used as an electron source to provide electron



Fig. 3.6. The redeposition phenomenon shown on a permalloy array for a magnetic bubble memory device. The redeposited material can be seen clearly along the sides of the pattern. Etching conditions were:- Ion energy of 1keV, current density of  $0.8\text{mA}\cdot\text{cm}^{-2}$  and normal incidence. (Courtesy of Dr. R.N. Castellano).

(a)  $\times$  2000

(b)  $\times$  10000



**a**



**b**

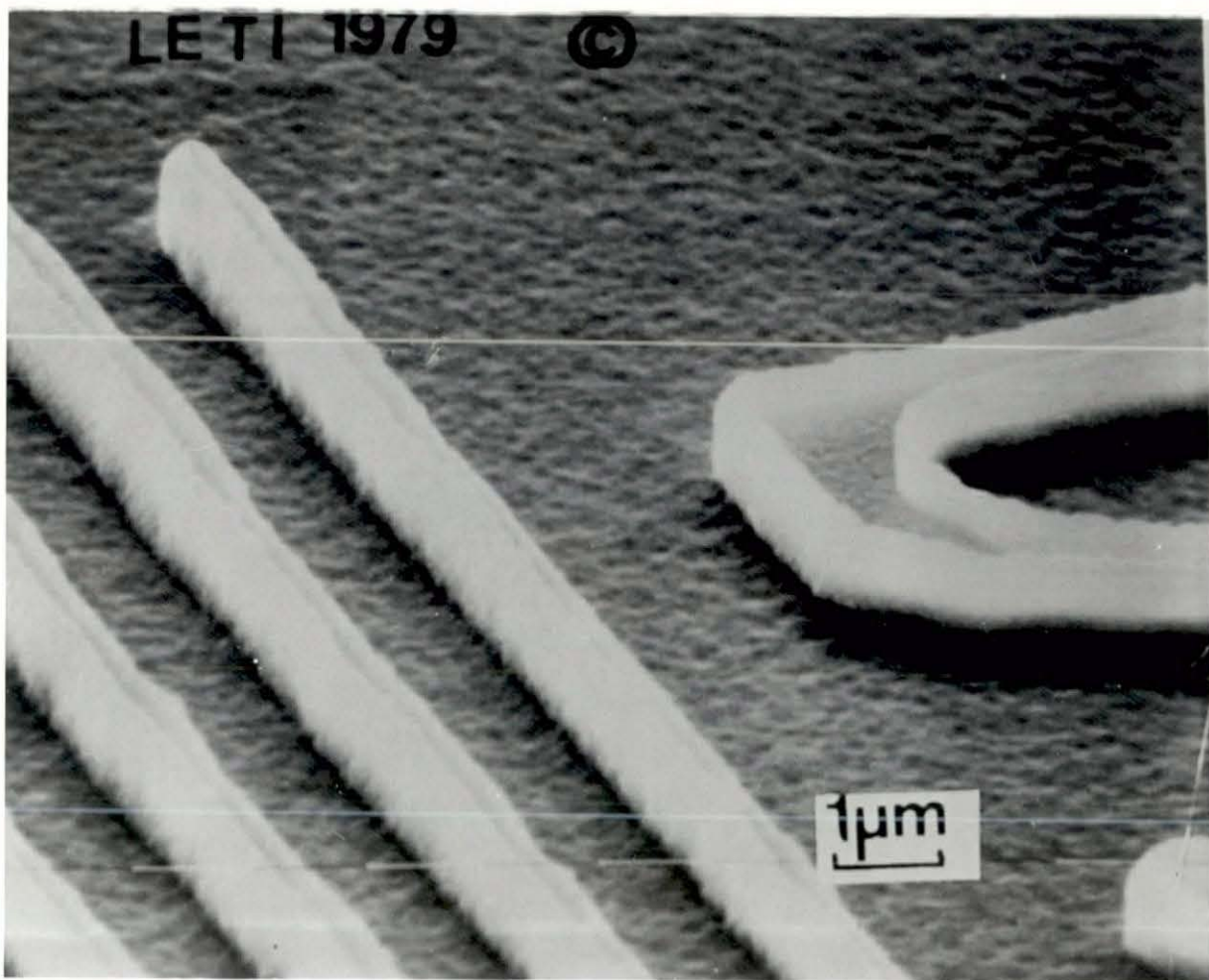


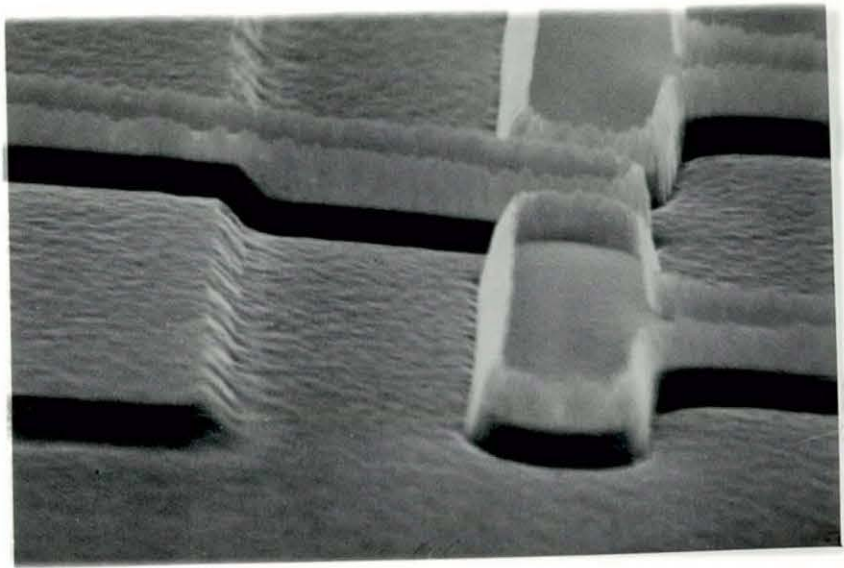
Fig. 3.7. The redeposited material left after bombardment of a photoresist mask on a RF sputtered N.F film. The mask was removed in an  $O_2$  plasma and <sup>i</sup>e the micrograph shows the redeposited <sup>2</sup> material left after the stripping. See text for details (Courtesy of Dr. B. Dargent).

Fig. 3.8. A series of micrographs illustrating the redeposition effect on permalloy elements etched using a  $1\mu\text{m}$  thick AZ1350J mask. Etching conditions were  $600\text{eV Ar}^+$  ions, current density  $0.6\text{mA}\cdot\text{cm}^{-2}$  at normal incidence. (Courtesy of Dr. D. Brambley, Plessey Research (Caswell) Ltd.).

- (a)  $\times 40000$
- (b)  $\times 14000$
- (c)  $\times 10000$
- (d)  $\times 9000$

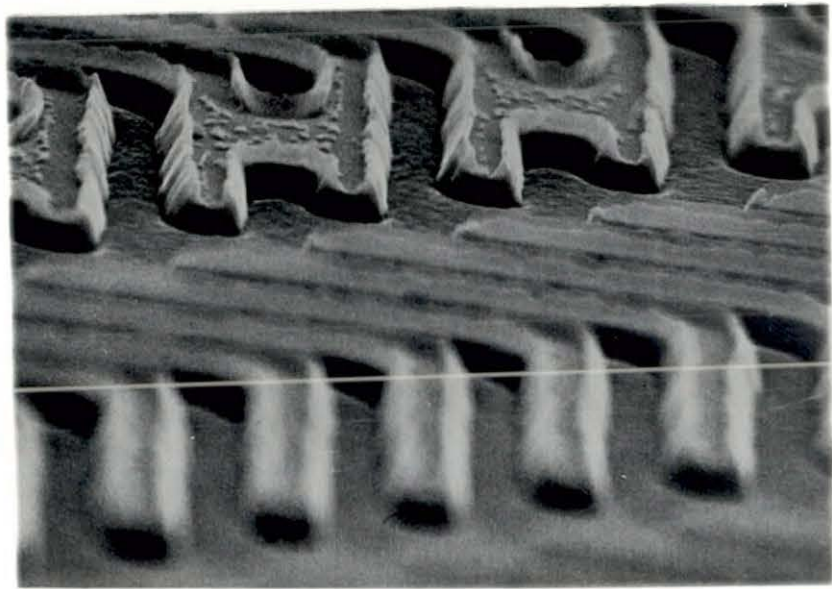


**a**

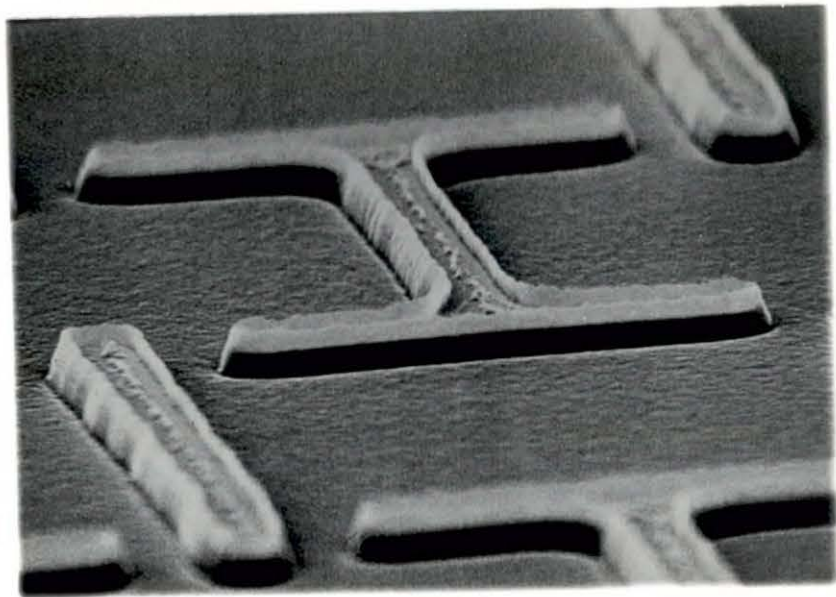


**b**



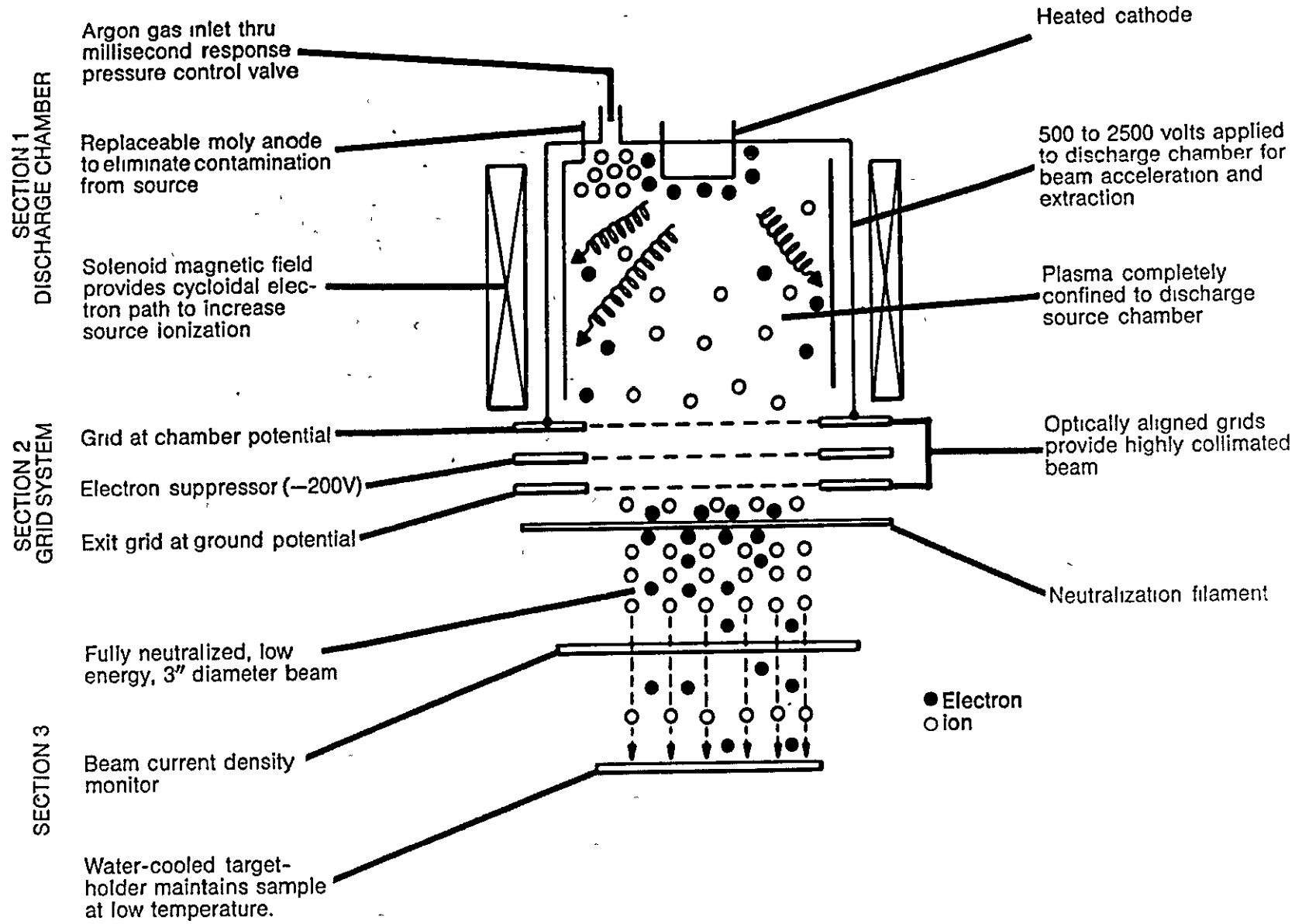


c



d

Fig. 3.9. Schematic diagram illustrating the microetch ion gun.



flow towards the chamber walls. The chamber is at the desired beam voltage (energy) and contains a dense 'plasma' consisting of  $\text{Ar}^+$  ions and electrons. This plasma is totally confined to section 1, the discharge chamber of the source. The second section consists of three optically aligned precision grids which extract and focus ions from the plasma. The second grid in section 2 acts as a screen against electron travel by being negatively biased. The third section consists of neutraliser filament, ion beam density monitor and electrically isolated, water cooled substrate platform. The neutraliser is set up by measuring ion beam density then increasing neutraliser power until this reading returns to zero. At this point ion and electron arrival rates are balanced.

The experiments to be described are in two parts. The first part consists of developing vertical walled grooves and steps on to a quartz substrate, using reactive ion beam etching, in the system described above. The procedure is as follows. The samples are coated with AZ1350J resist to a thickness of  $1.5\mu\text{m}$  and baked at  $80^\circ\text{C}$ . The patterns are defined in the resist under ultra-violet light. In order to obtain vertical steps, 'first fringe' conditions are maintained viz the gap between the top surface of the resist and the contacting surface of the mask is less than  $\frac{1}{4}$  of the wavelength of U.V. light (approximately  $1000\text{\AA}$ ). This is difficult to achieve due to a variety of reasons such as ripples in the resist surface, inclusions in the resist (e.g. dust particles) and non-flat substrate surface. Under ideal conditions reflection at the interface is very low and transmission high. Also multiple reflections are much reduced and Fresnel diffraction minimised at feature edges.



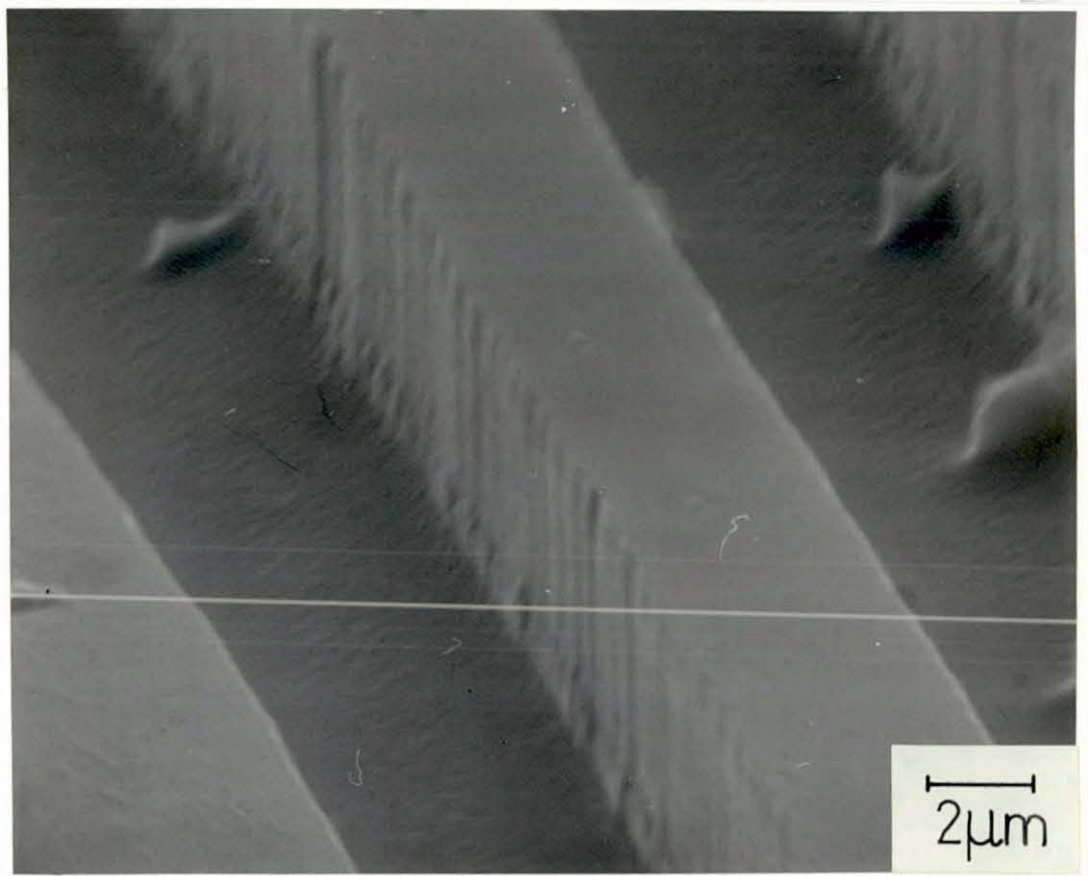
Using these vertical resist patterns the grooves were etched in the Veeco using  $\text{CHF}_3$  introduced directly into the ion gun. The resultant plasma will be partially dissociated by the hot cathode and various radicals formed including fluorine and hydrofluoric acid. These are accelerated down onto the substrate and the etching is then a combination of chemical reaction with  $\text{SiO}_2$  of the substrate and energy transfer as with the inert gas Ar.

The resist has a slow etch rate in the fluorine containing plasma and thus etch rate ratio's 7:1 can be obtained with  $\text{SiO}_2$ . As the  $\text{SiO}_2:\text{F}$  compounds are volatile, they are removed by the vacuum pumping system. Therefore redeposition is not a problem with reactive ion beam etching and hence near vertical walls can be obtained using this method. Figure 3.10 shows a series of micrographs of the vertical grooves and steps produced by reactive ion beam etching.

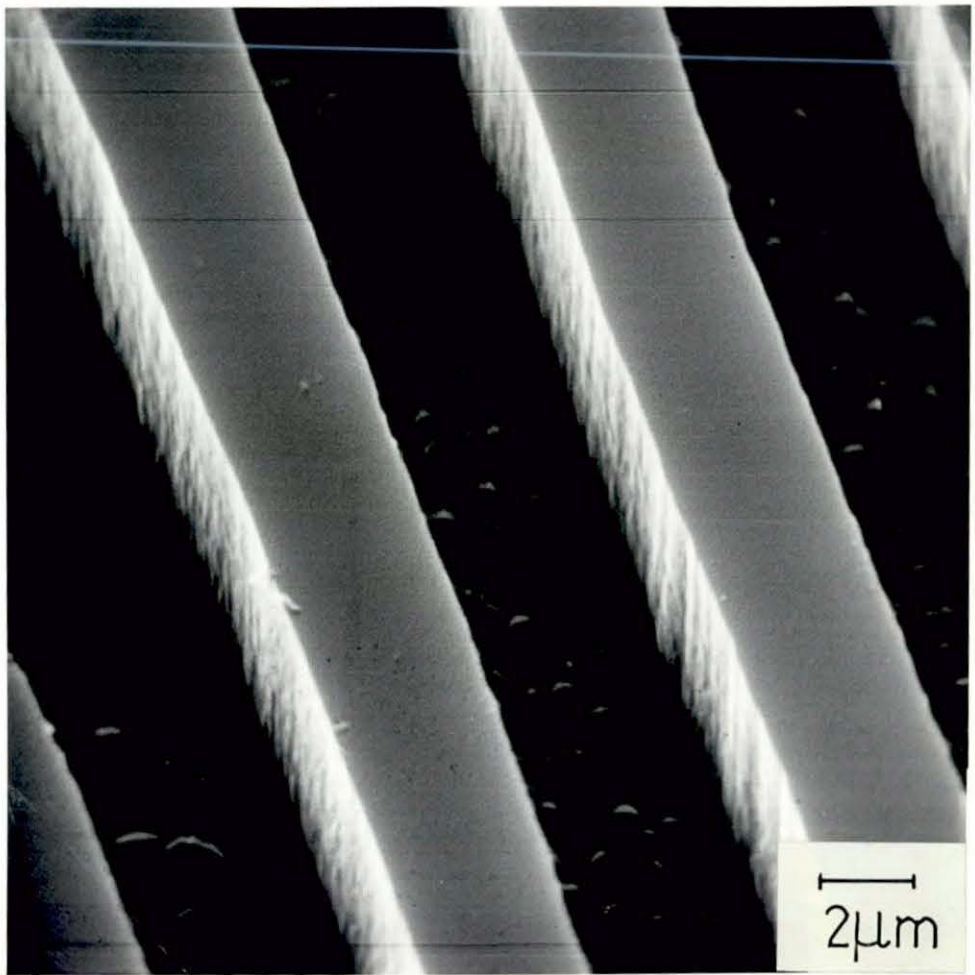
Having obtained vertical walled grooves and steps on a single crystal quartz substrate, they were subsequently bombarded with 600eV  $\text{Ar}^+$  ions with a current density of  $0.98\text{mA}\cdot\text{cm}^{-2}$ , at normal incidence, to different depths of erosion. The facets formed in this case will erode much faster than in the case considered by Smith (1976), because the grooves are made of the same material as the substrate. Figure 3.11 shows the effects of redeposition and faceting after etching to a depth of  $6000\text{\AA}$  in a groove that was originally  $4\mu\text{m}$  by  $4\mu\text{m}$ . This figure should be compared with figures 3.5(b) and (c) obtained by Smith (1976). Figure 3.12(a), (b) and (c) shows the effects of faceting and redeposition in grooves for which the width is very much greater than the height (in each case the groove width is  $0.16\text{mm}$ ). In figure 3.12(a), (b) and (c) the

Fig. 3.10 Micrographs illustrating the vertical groove walls ((a) and (b)) and steps ((c) and (d)) that are obtained after reactive ion beam etching.

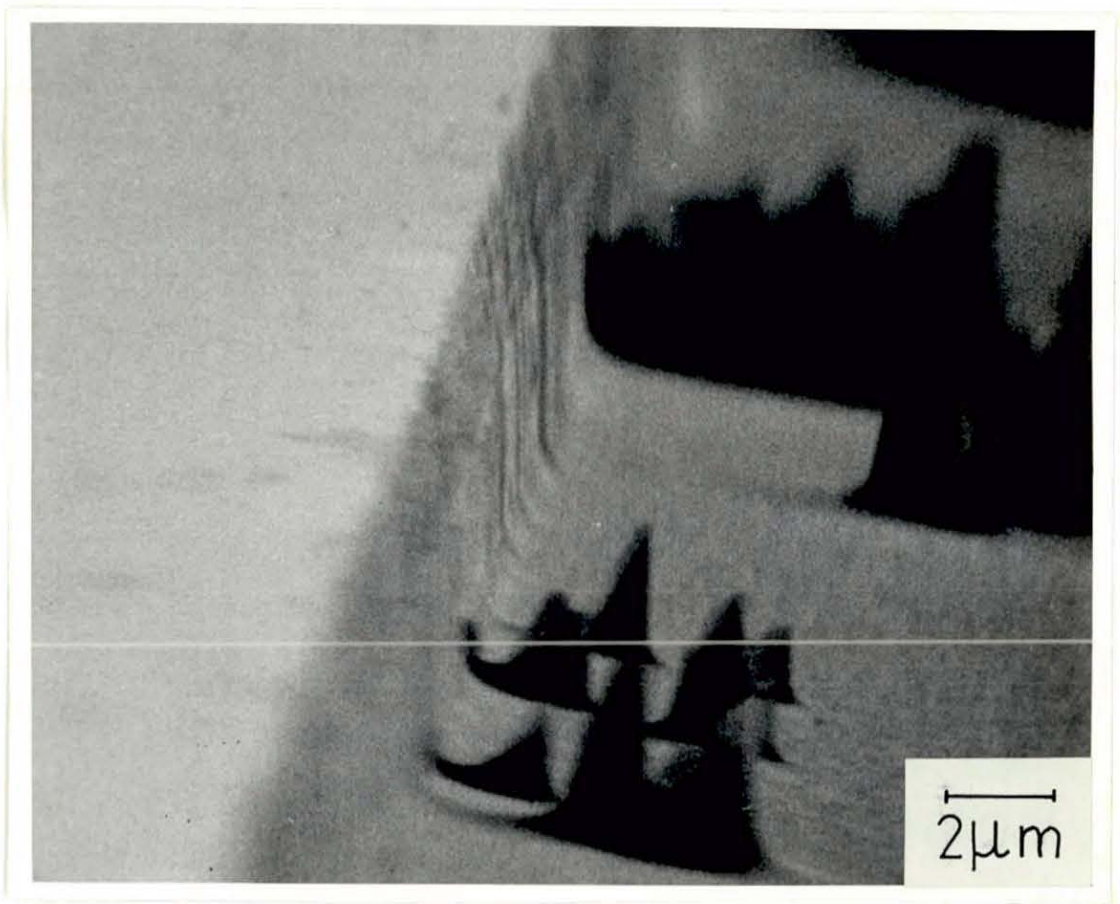
- (a) Groove height =  $4.0\mu\text{m}$ ; Groove width =  $4.0\mu\text{m}$
- (b) Groove height =  $4.9\mu\text{m}$ ; Groove width =  $4.0\mu\text{m}$
- (c) Step height =  $4.0\mu\text{m}$
- (d) Step height =  $4.9\mu\text{m}$



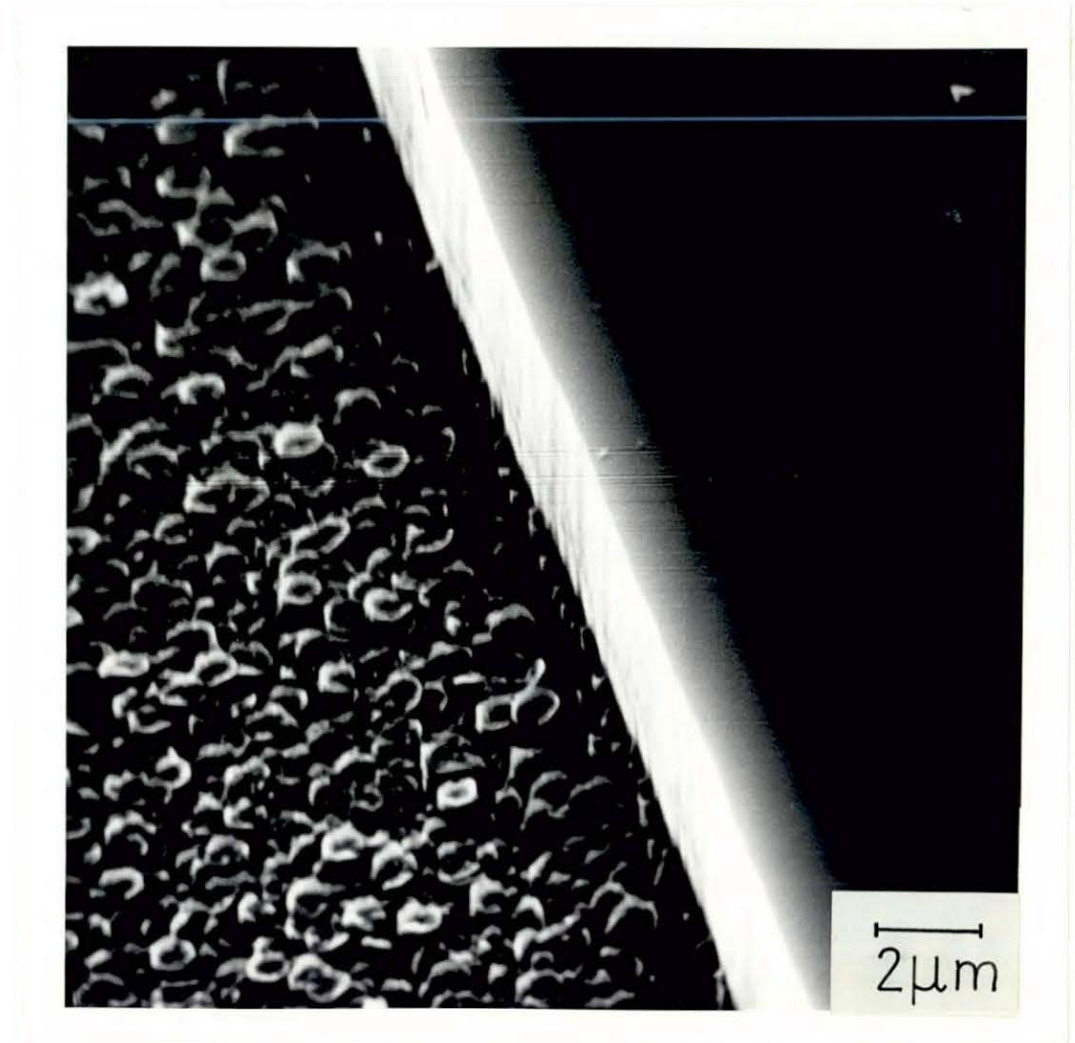
**a**



**b**



c



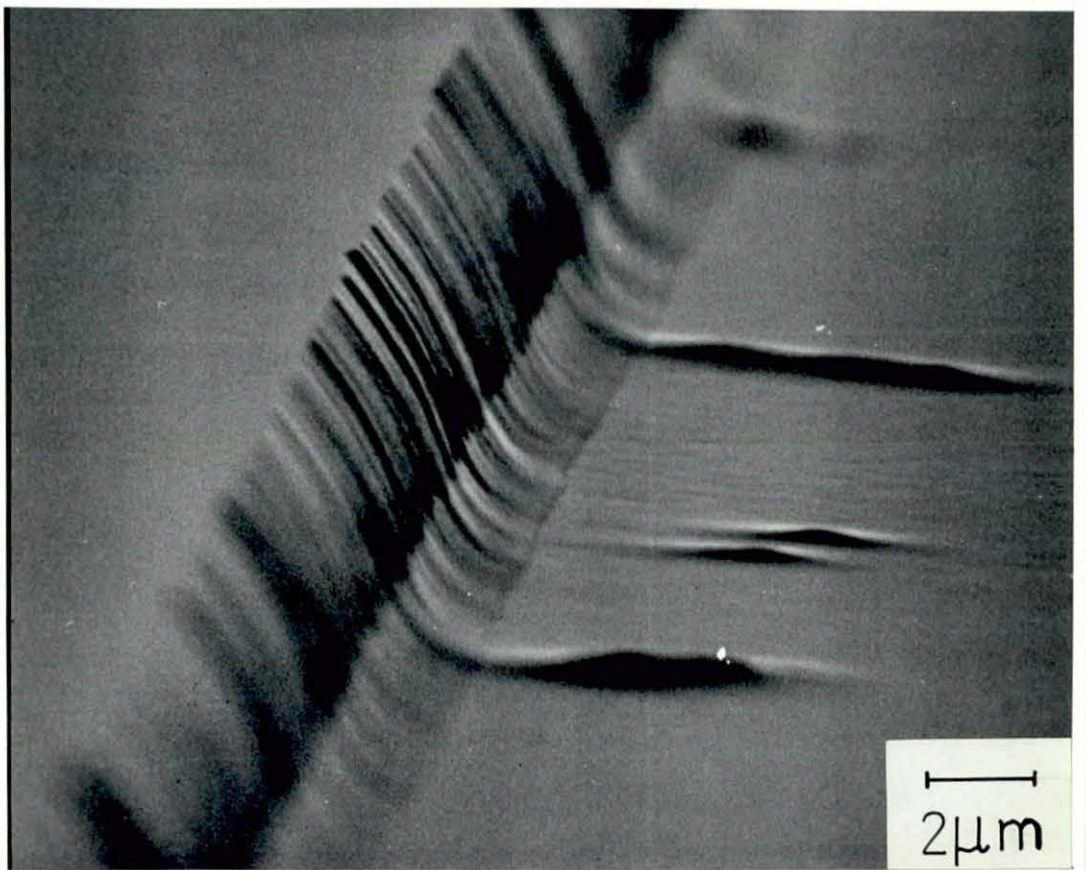
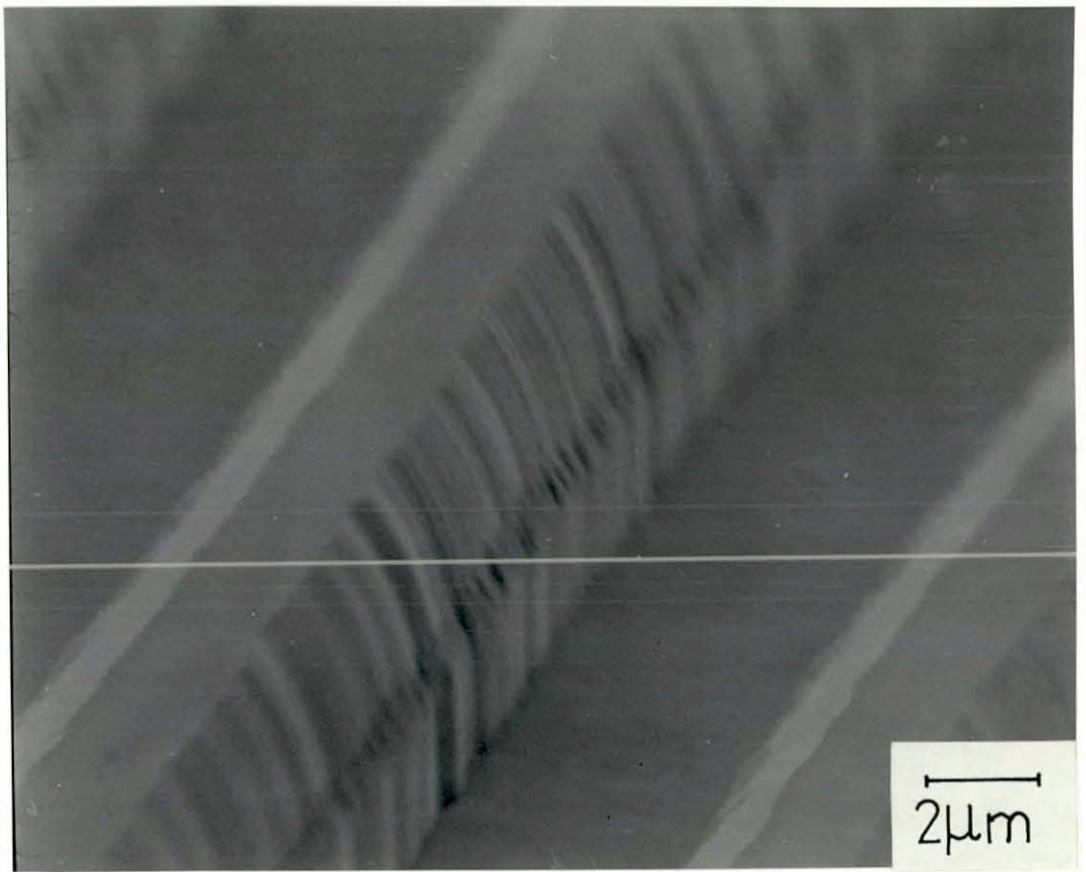
d

Fig. 3.11. Scanning electron micrograph illustrating the effects of redeposition and faceting after etching to a depth of  $6000\text{\AA}$  in a groove that was originally  $4\mu\text{m}$  by  $4\mu\text{m}$ . Bombardment was with  $600\text{eV Ar}^+$  ions with a current density of  $0.98\text{mA}\cdot\text{cm}^{-2}$  at normal incidence.

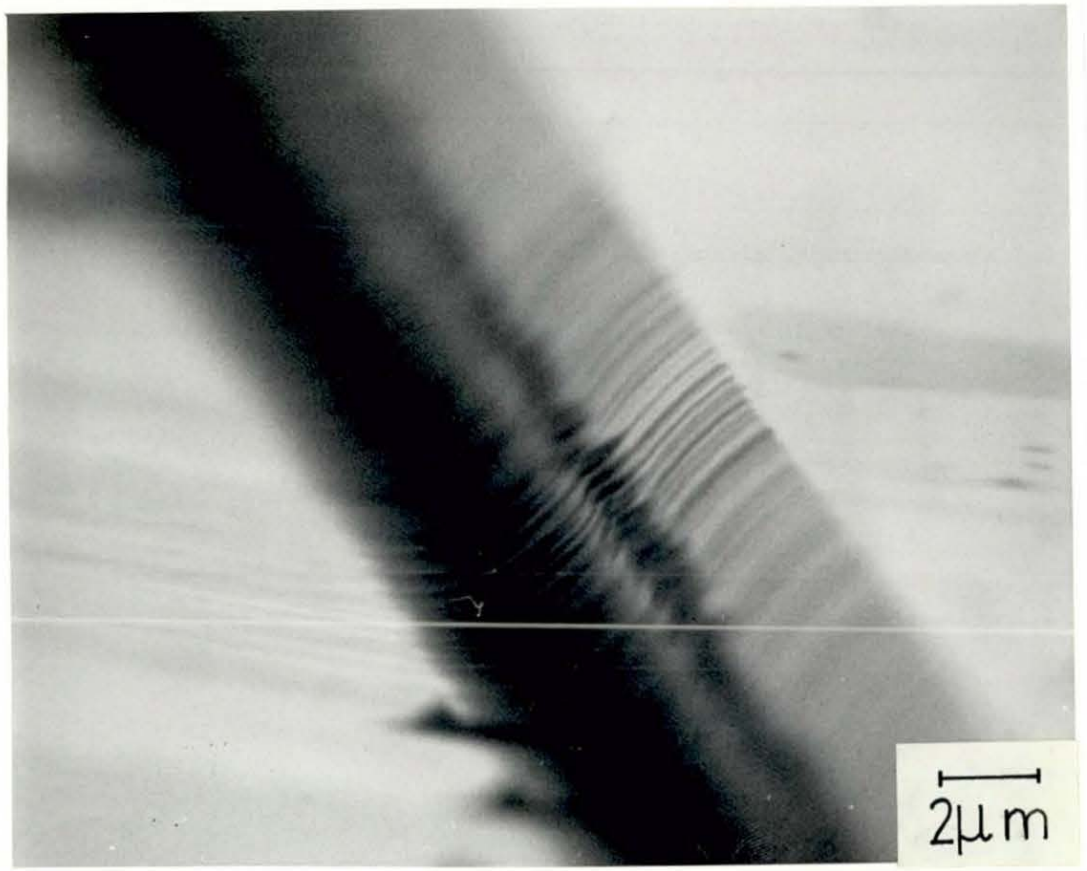
Fig. 3.12. Scanning electron micrographs illustrating the effects of redeposition and faceting in grooves for which the width is very much greater than the height (in each case the groove width is  $0.16\text{mm}$ ). Bombardment was with  $600\text{eV Ar}^+$  ions with a current density of  $0.98\text{mA}\cdot\text{cm}^{-2}$  at normal incidence.

- (a) Initial groove height =  $3.0\mu\text{m}$ ;  
Depth of erosion =  $9000\text{\AA}$ .
- (b) Initial groove height =  $4.0\mu\text{m}$ ;  
Depth of erosion =  $6000\text{\AA}$ .
- (c) Initial groove height =  $4.5\mu\text{m}$ ;  
Depth of erosion =  $4000\text{\AA}$ .

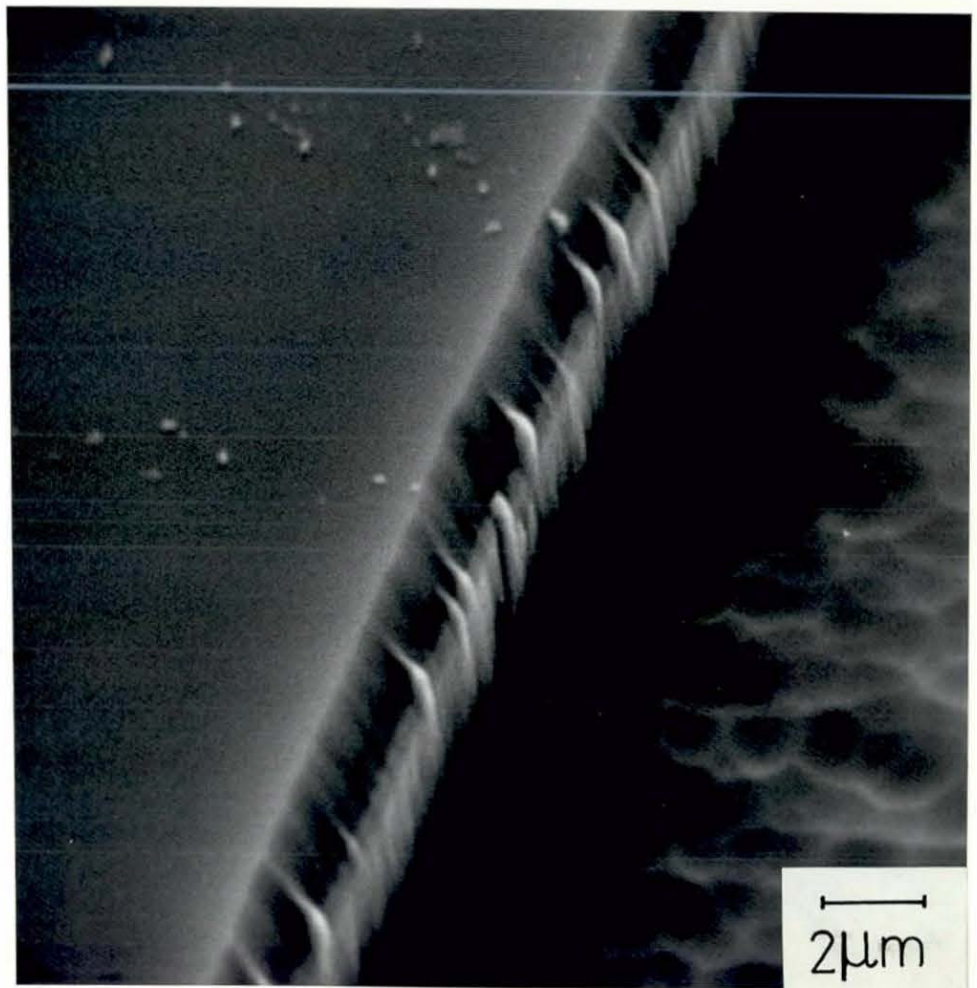




a



**b**



**c**

initial step heights were 3.0, 4.0 and 4.5 $\mu\text{m}$  respectively. The micrographs show the walls after etching through 9000, 6000 and 4000 $\text{\AA}$  respectively. Figures 3.13 and 3.14 show the effects of redeposition and faceting for grooves that were initially 4.0 $\mu\text{m}$  wide and 4.9 $\mu\text{m}$  high. In figure 3.13 the groove was etched to a depth of 2000 $\text{\AA}$  and in figure 3.14 to a depth of 3000 $\text{\AA}$ . The redeposited material is clearly visible on these micrographs. If the initially vertical grooves are bombarded for a long time the faceting (i.e. the erosion) will dominate the redeposition of sputtered material. This is illustrated in figure 3.15(a) and (b) which shows the grooves (figure 3.15(a)) and steps (figure 3.15(b)), both having an initial height of 4.0 $\mu\text{m}$ , after etching through 1.2 $\mu\text{m}$ . It can be seen that a triangular geometry has developed caused by the facet extending to the flat substrate.

### 3.3. Previous theories for the redeposition of sputtered material.

As mentioned in section 3.1 a number of attempts have been made to formulate a theoretical model for the redeposition of sputtered material. In this section the different models will be outlined and the advantages and disadvantages of each will be discussed.

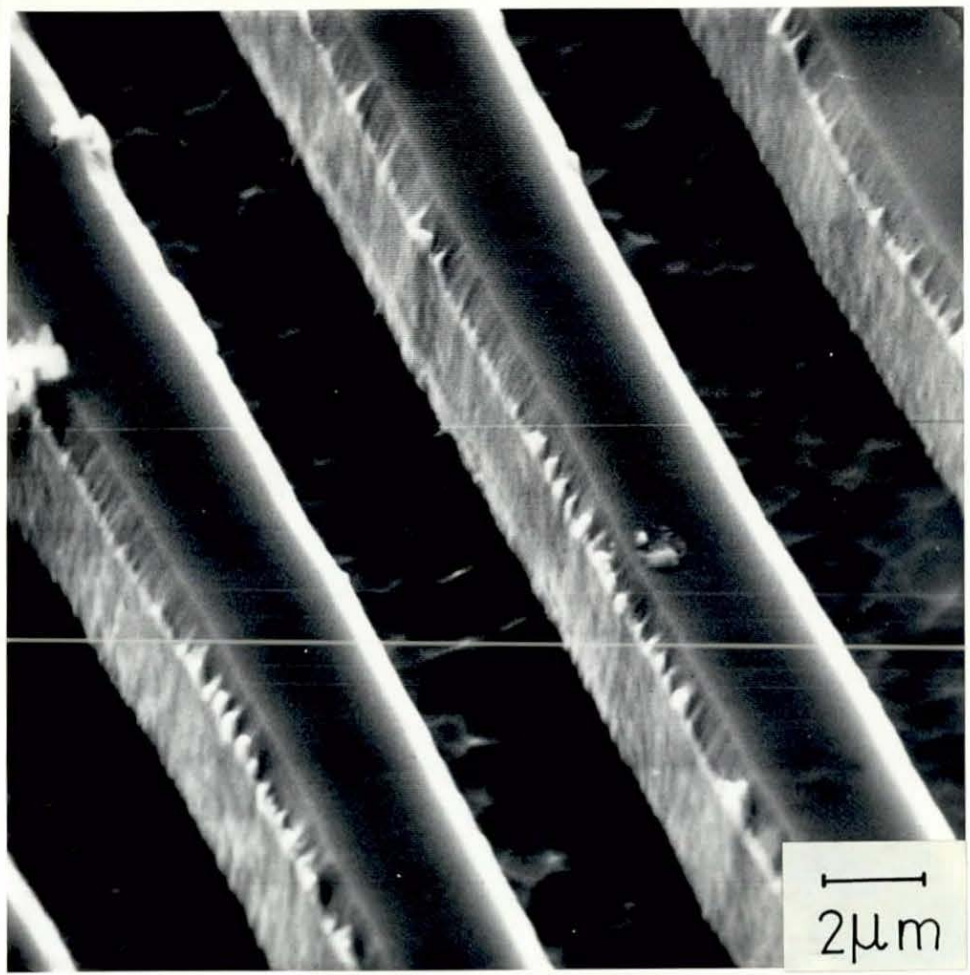
Bayly (1972) derived an expression for the redeposited flux of particles assuming a cosine emission distribution. He used this model to explain why flaws on non-etched surfaces did not develop. Following his argument, a point C emits particles according to  $\Phi = \phi_0 \cos \Omega$ , see figure 3.16. Then the total emitted flux from an area  $\delta x \cdot \delta y$ . at C is



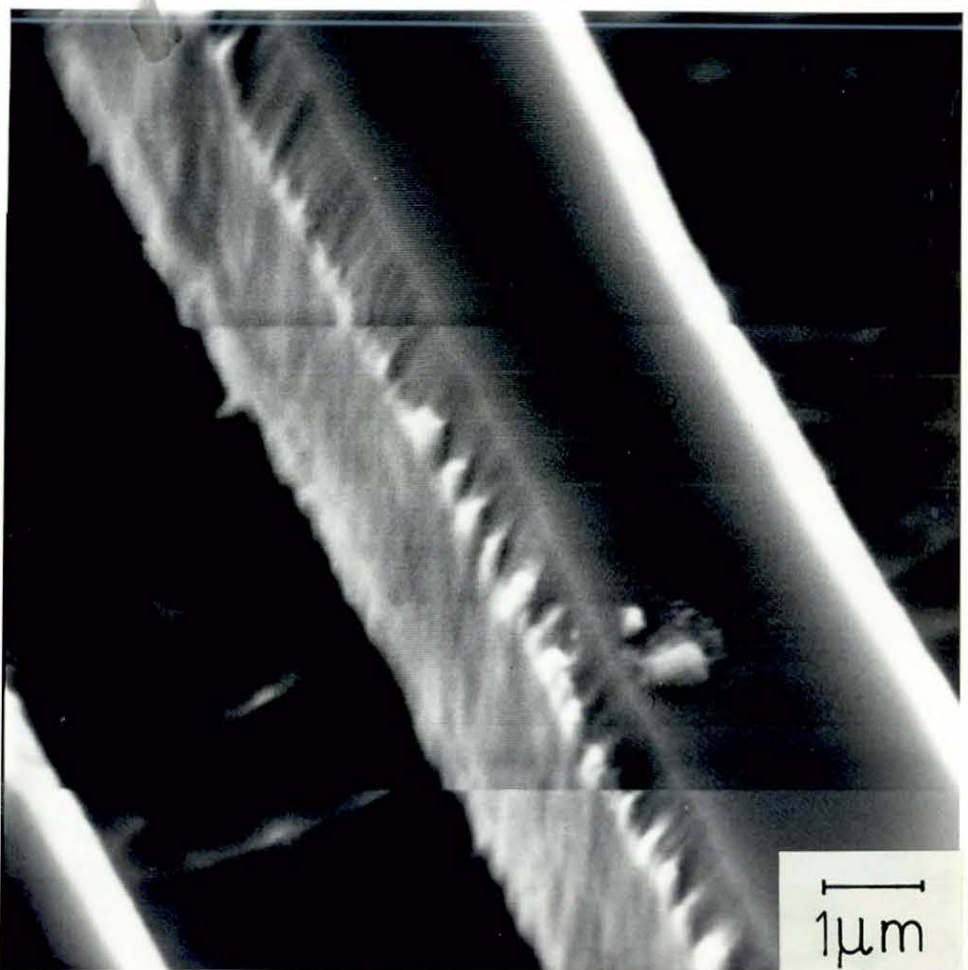


Fig. 3.13. Micrographs illustrating the effects of redeposition and faceting after etching to a depth of  $2000\text{\AA}$  in a groove that was originally  $4.9\mu\text{m}$  high. Bombardment was with  $600\text{eV Ar}^+$  ions with a current density of  $0.98\text{mA}\cdot\text{cm}^{-2}$  at normal incidence.

(a)  $\times 7000$   
(b)  $\times 14000$



**a**

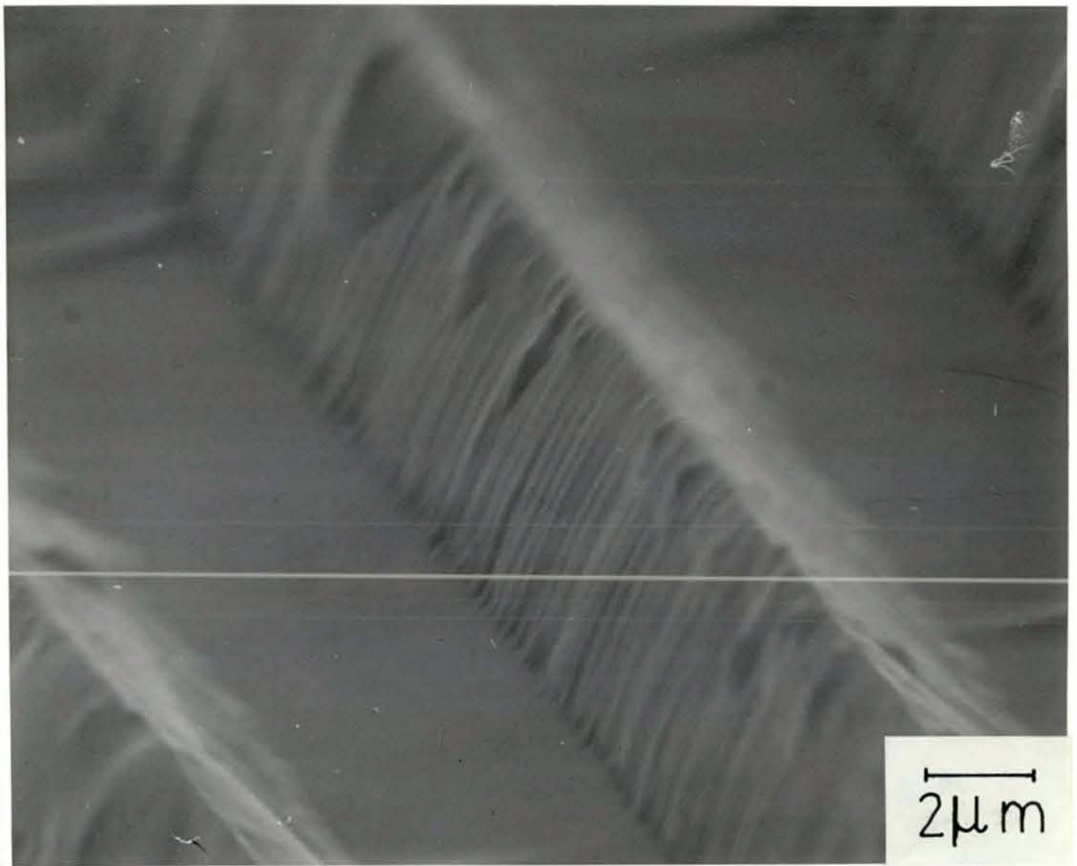


**b**

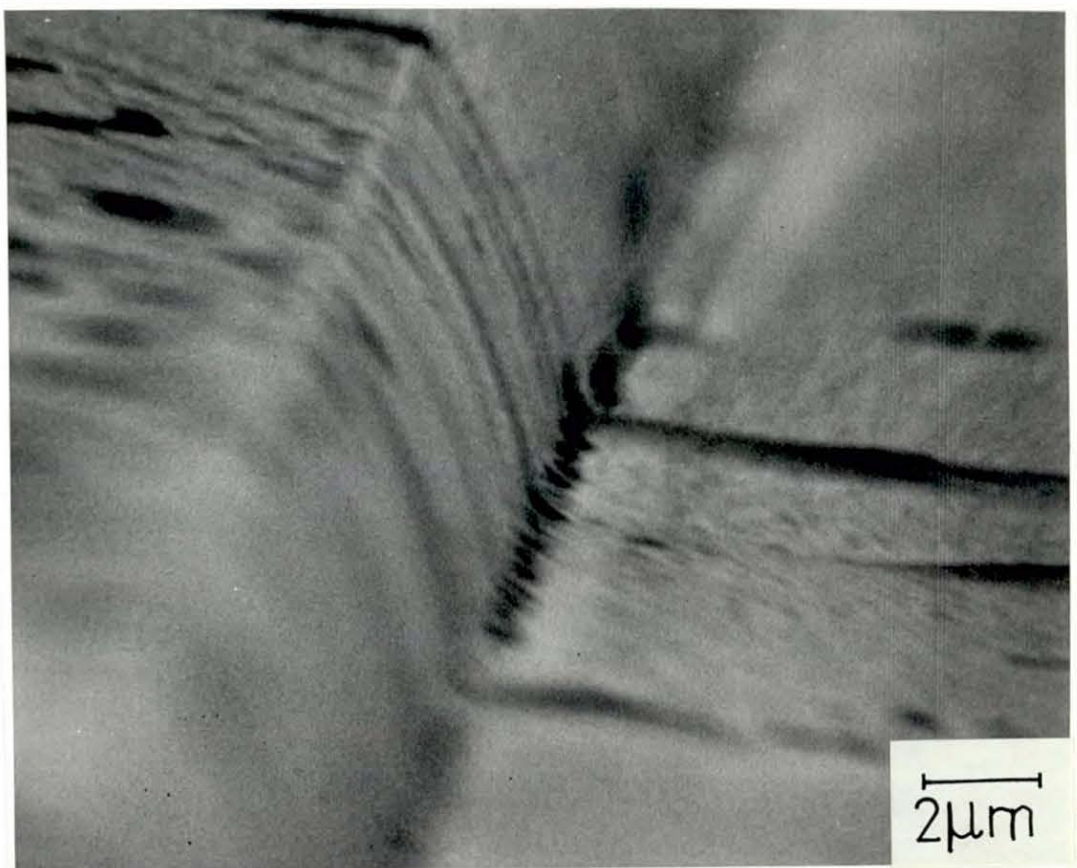
Fig. 3.14. Micrographs illustrating the effects of redeposition and faceting after etching to a depth of 3000Å in a groove that was originally 4.9 $\mu$ m high. Bombardment was with 600eV Ar<sup>+</sup> ions with a current density of 0.98mA.cm<sup>-2</sup> at normal incidence.

- (a) × 7000
- (b) × 14000

Fig. 3.15. Scanning electron micrographs illustrating the geometry obtained when the faceting (erosion) dominates the redeposition of sputtered material. Etching was to a depth of  $1.2\mu\text{m}$  using  $600\text{eV Ar}^+$  ions with a current density of  $0.98\text{mA}\cdot\text{cm}^{-2}$  at normal incidence. The micrographs illustrate the geometry obtained in grooves (a) and on a step (b) when the facet extends to the flat substrate.



**a**



**b**

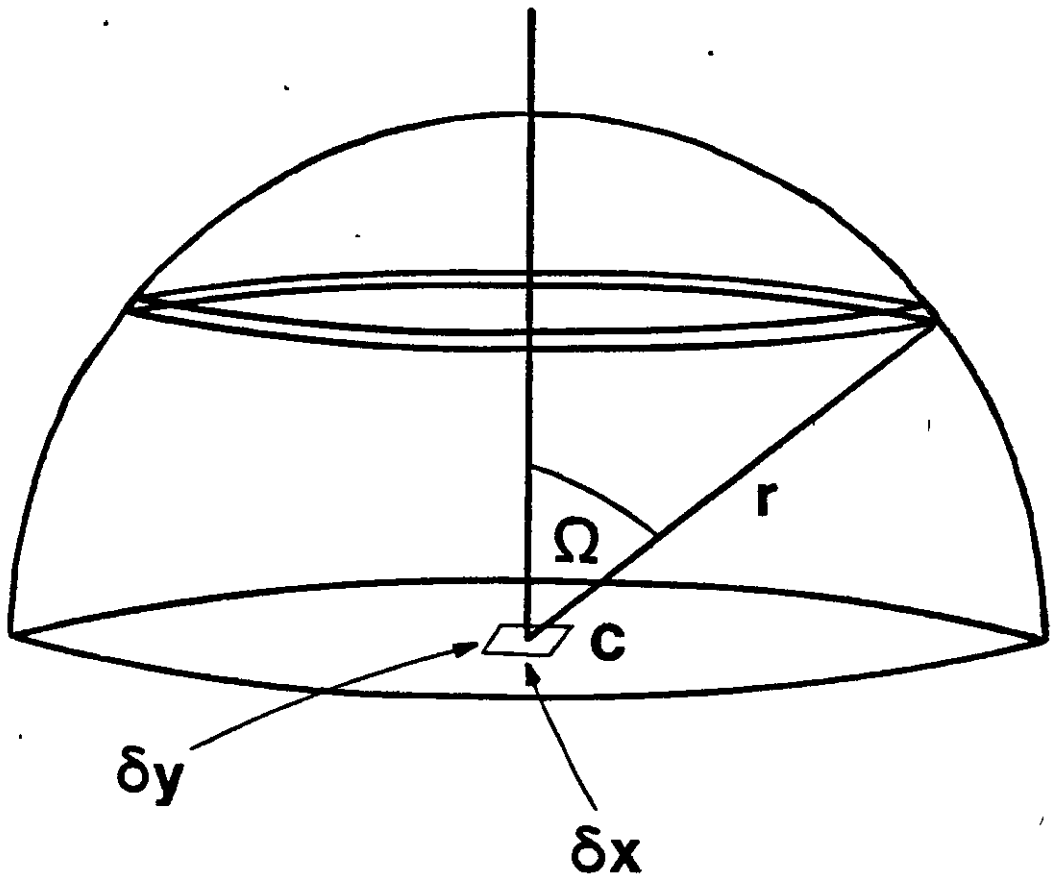


Fig. 3.16. Diagram for calculating the total number of particles emitted from a point C. See text for details.

$$\phi \cdot \cos\theta \cdot \delta x \delta y = \int_0^{\pi/2} 2\pi r \sin\Omega \cdot r d\Omega \cdot \phi_0 \cos\Omega = \pi r^2 \phi_0$$

$$\therefore \phi_0 = \frac{\phi \cos\theta \cdot S \cdot \delta x \cdot \delta y}{\pi r^2} \quad (3.1)$$

where  $\phi_0$  = peak emitted flux density,  $\phi$  = incident ion flux density,  $\theta$  = angle of incidence,  $\Omega$  = angle of emission and S is the sputtering coefficient. From figure 3.17, with the above assumptions the flux density of sputtered particles from C arriving at A is

$$\begin{aligned} \phi_1 &= \phi_0 \cdot \cos(\text{angle between normal at C and AC}) \\ &= \phi_0 \sin \widehat{ACD} \end{aligned}$$

The amount incident normally at A is the resulting flux density at A and is given by

$$\phi_1 \cos \widehat{ACE} = \phi_1 \sin \widehat{CAE}$$

Therefore the total flux density striking the plane at A from an infinite strip in the plane BCO parallel to the line of intersection is

$$\phi' = \int_{x_1}^{x_2} \int_{-\infty}^{\infty} \phi_1 \sin \widehat{CAE} = \int_{x_1}^{x_2} \int_{-\infty}^{\infty} \phi_0 \sin \widehat{ACD} \sin \widehat{CAE}$$

$$\phi' = \frac{1}{\pi} \int_{x_1}^{x_2} \int_{-\infty}^{\infty} \frac{\phi \cos\theta S}{(AC)^2} \frac{d \sin \psi}{AC} \frac{x \sin \psi}{AC} dy dx$$

Using  $AB^2 + y^2 = AC^2$  and  $AB = AC \cos \xi$  gives



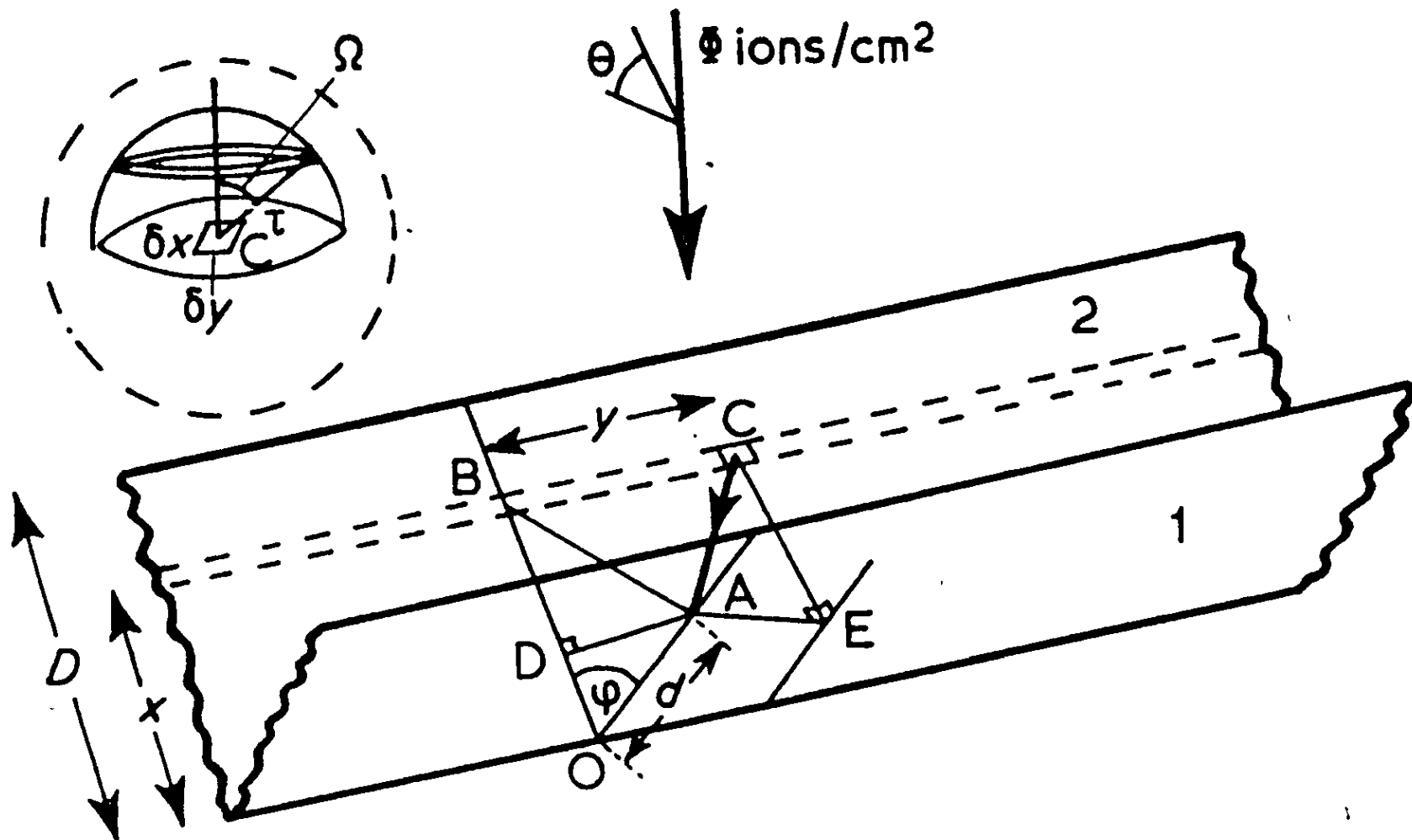


Fig. 3.17. Diagram for calculating the deposition rate of low energy sputtered particles from an infinite planar strip onto an adjacent plane. (After Bayly (1972)).

$$\phi' = \frac{\phi S d \cos \theta \sin^2 \psi}{\pi} \int_{x_1}^{x_2} \int_{-\pi/2}^{\pi/2} \frac{x \cos^2 \xi d\xi dx}{(AB)^3}$$

$$\phi' = \frac{\phi S d \cos \theta \sin^2 \psi}{2} \int_{x_1}^{x_2} \frac{x dx}{(AB)^3}$$

Now from triangle ABD

$$(AB)^2 = (AD)^2 + (BD)^2 = (d \sin \psi)^2 + (x-d \cos \psi)^2$$

$$\therefore \phi' = \frac{\phi S d \cos \theta \sin^2 \psi}{2} \int_{x_1}^{x_2} \frac{x dx}{\{(d \sin \psi)^2 + (x-d \cos \psi)^2\}^{3/2}}$$

Using the substitution  $x-d \cos \psi = t$  converts the integral to

$$\phi' = \frac{\phi S d \cos \theta \sin^2 \psi}{2} \int_{x_1-d \cos \psi}^{x_2-d \cos \psi} \frac{(t + d \cos \psi) dt}{\{(d \sin \psi)^2 + t^2\}^{3/2}}$$

Evaluating the above integral gives the final solution to be

$$\phi' = \frac{\phi S \cos \theta}{2} \left[ \frac{\cos \psi - (d/x)}{\{1-2(d/x)\cos \psi + (d/x)^2\}^{1/2}} \right]_{x_1}^{x_2} \quad (3.2)$$

Introducing a sticking coefficient  $\eta$  and considering the case of a V-shaped flaw of side D (i.e.  $x_1 = 0$ ,  $x_2 = D$ ) with  $\theta = \frac{\psi}{2}$  gives an effective sputtering rate  $S^*$  at A where  $S^* = \phi S \cos \theta - \phi' \eta$  is the net erosion rate. Thus

$$\frac{S^*}{S} = \phi \cos \frac{\psi}{2} \left[ 1 - \frac{\eta}{2} \left\{ 1 + \frac{\cos \psi - (d/D)}{\{1-2(d/D)\cos \psi + (d/D)^2\}^{1/2}} \right\} \right]$$

This is shown for  $\eta = 1$  as a function of  $\frac{d}{D}$  for various values of  $\psi$ , see figure 3.18.

Bayly (1972) used this model to explain why flaws in a non-etched surface did not develop. The deep, lightly-etched flaws would experience a variation in net sputtering yield due to redeposition which in the absence of secondary flux enhancement would cause a rapidly decreasing rate of separation with depth between points on opposite sides, see figure 3.19(a). The secondary flux enhancement superimposed on this variation in sputtering rate causes a sharp increase in yield which produces a 'wave' at the level where the incident secondary flux first appears, figure 3.19(b). This in turn affects the secondary flux distribution lower down on the opposite face, and so on until the faces are broken up into a series of waves, which develop more rapidly near the surface into sharply defined steps, and sequentially form the rectangular terraces as observed. These mechanisms are illustrated in figure 3.19.

The limitations of the model of Bayly (1972) are as follows: The author has only considered a cosine emission distribution for the sputtered particles. However this is not a good approximation for ion beams of low or high energies. The other drawback with the model is that it does not take into account the continuously changing geometry of the substrate due to redeposition and flux enhancement, although the author discusses these changes qualitatively. This means that no account is taken of the continuously changing geometry of, in this case, the V-shaped flaws.

Glöersen (1976) has also considered the problem of redeposition of sputtered material. This author has approached the problem with the needs of the electronics industry in mind. The requirement here

EFFECTIVE SPUTTERING RATIO,

$$S^* = S \left[ 1 - \frac{\eta}{2} \left\{ 1 + \frac{\cos \varphi - d/D}{(1 - 2d/D \cos \varphi + (d/D)^2)^{\frac{1}{2}}} \right\} \right]$$

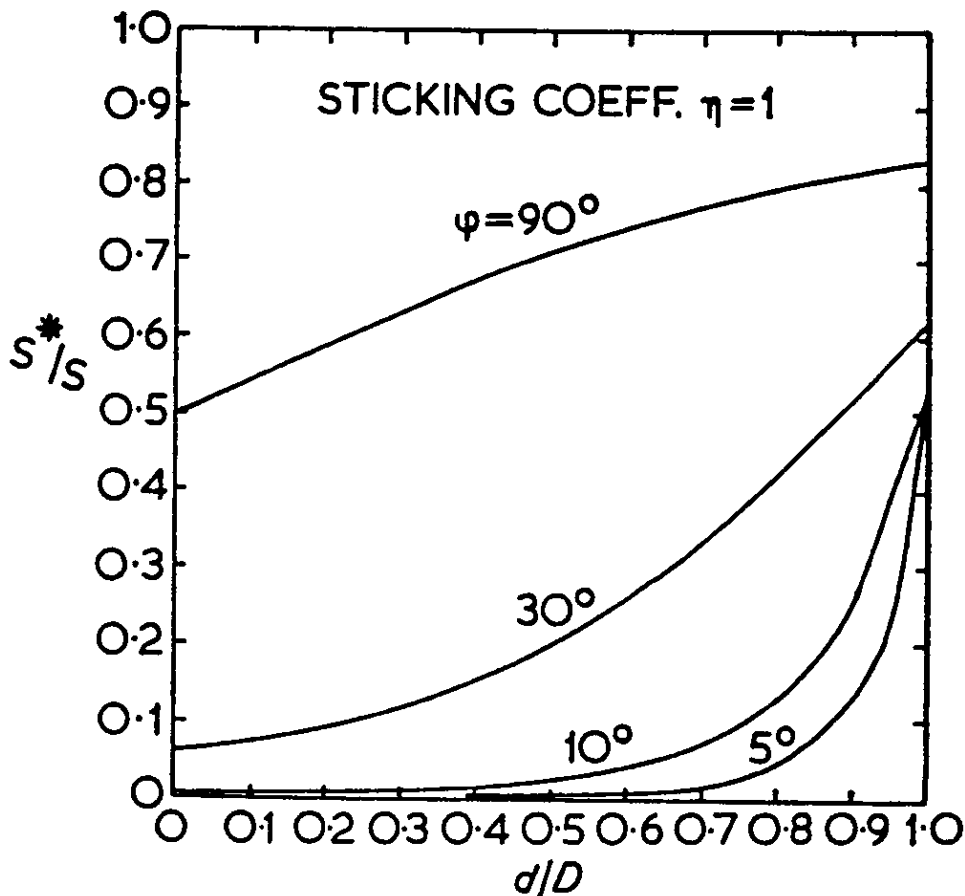


Fig. 3.18 The effective sputtering ratio,  $S^*$ , at a point A on a plane inclined symmetrically about the ion beam to a plane containing BCD, (see figure 3.17), when redeposition of the sputtered particles is taken into account, assuming a cosine spatial emission distribution. (After Bayly (1972)).

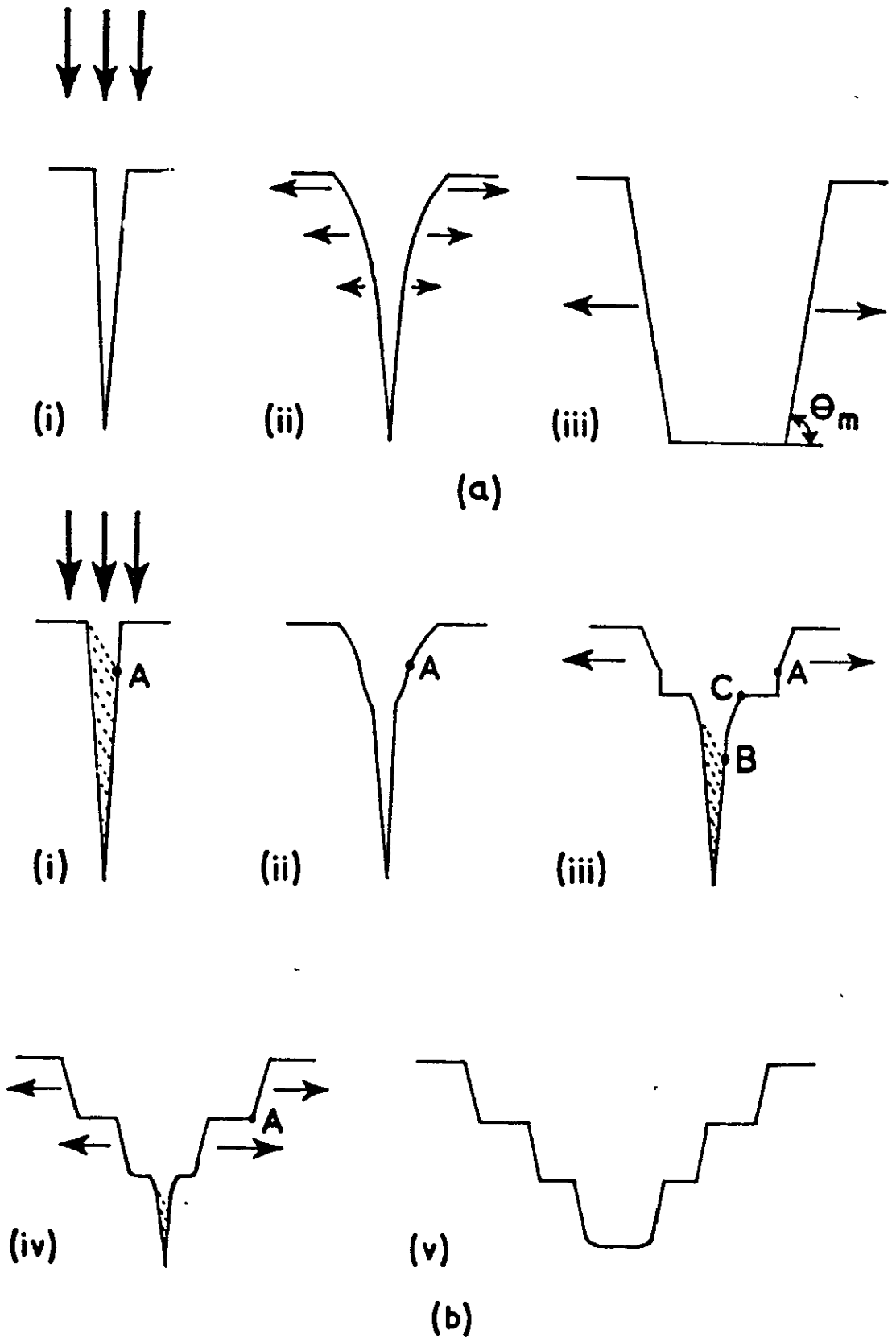


Fig. 3.19. (a) (i) A deep surface flaw expanding due to sputtering (ii) forms convex sides due to redeposition (iii) which eventually form  $\theta_m$  planes when deposition becomes negligible. (b) With the additional secondary high energy flux the erosion rate is proportionally increased below point A. This causes a series of steps to be formed as shown which sweep out as a fixed formation. (After Bayly (1972)).

is for structures with vertical walls standing proud of the substrate. He has thus developed a simple two-dimensional model for the flux of redeposited material incident on an initially vertical wall, see figure 3.20. Assuming that the material is ejected from each point according to a cosine distribution, then the total flux on the wall can be written as

$$F(y) = \int_0^d \frac{F_0 \cos \theta \cos \phi}{r} dx$$

where  $F_0$  is the flux density of ejected particles (per unit area and unit solid angle) in the direction  $\theta = 0$ , and the angles  $\theta$  and  $\phi$  are defined as in figure 3.20. The  $\frac{1}{r}$  dependence follows from the two-dimensional nature of the problem. From the diagram  $\cos \theta = \frac{y}{r}$ ,  $\cos \phi = \frac{x}{r}$  and  $r^2 = x^2 + y^2$ . Therefore the integral becomes

$$F(y) = F_0 y \int_0^d \frac{x dx}{(x^2 + y^2)^{3/2}}$$

By using the substitution  $x = y \tan \alpha$  the integral can be evaluated to give

$$F(y) = F_0 \left[ 1 - \frac{y}{(d^2 + y^2)^{1/2}} \right] \quad (3.3)$$

Equation (3.3) is the same as equation (3.2) except that (3.3) is less general. Therefore for a step of height much smaller than the distance to the neighboring protruding features, the flux density,  $F_0$ , is independent of  $y$ . This is half the flux density (integrated over all angles) emanating from each point exposed to the ion beam. Thus if a sticking coefficient of unity is assumed, then the sideways growth

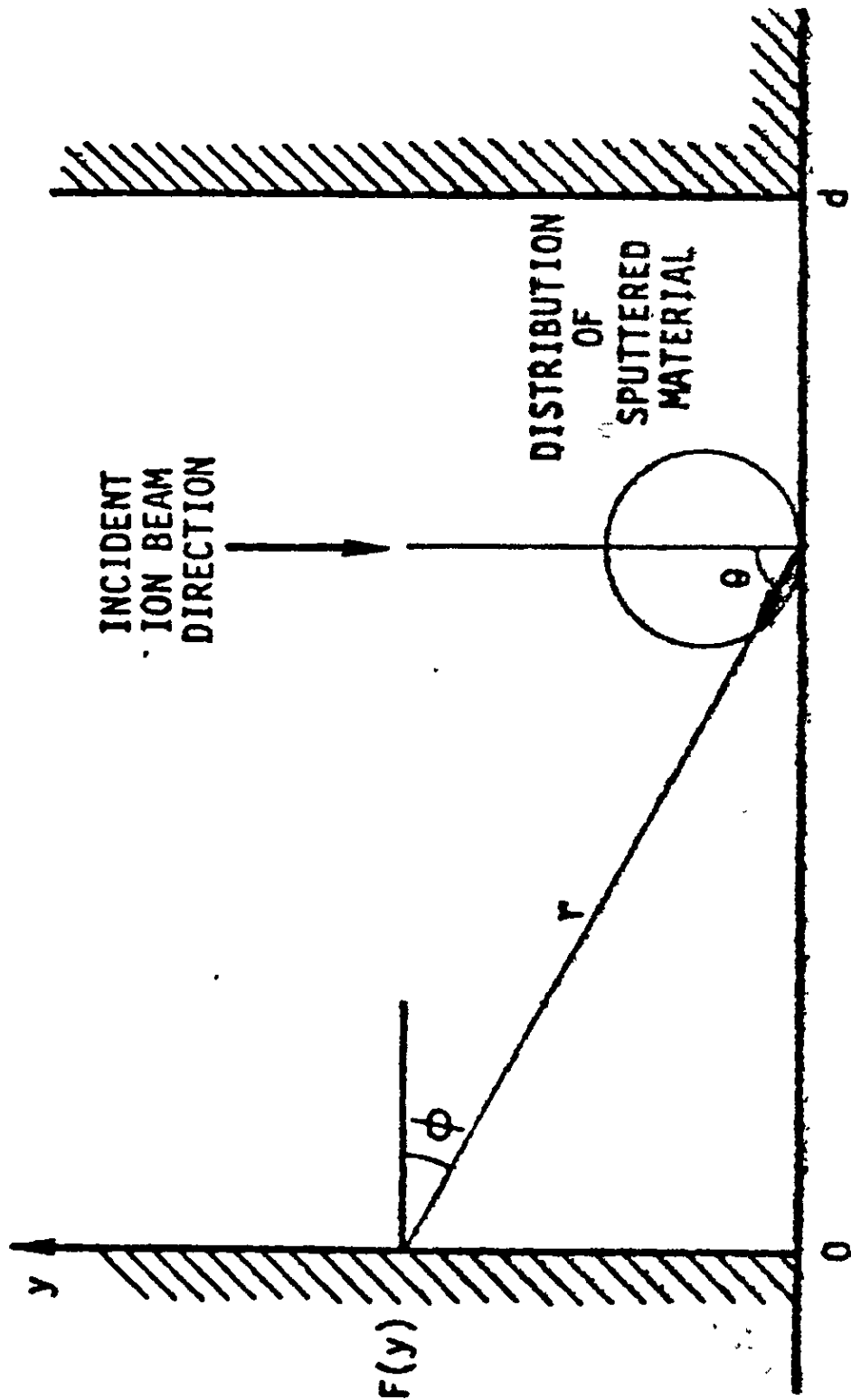


Fig. 3.20. Simple model for calculating the flux of sputtered material onto a vertical sidewall when etching at normal incidence. (After Gloersen (1976)).

rate of a low vertical wall is half the surface erosion rate. If the incoming beam is perfectly collimated, there will be no removal of material from a vertical wall, and the time evolution of a masked groove will be as shown in cross-section in figure 3.21. The facets which form at the corners are inclined at the angle of maximum sputtering rate with respect to the ion beam (Smith et al (1973)). When the photoresist is lifted after the etching is completed, the sidewalls may tear off or may remain, depending on how thin and brittle the walls are.

Glöersen also extended the simple model outlined above to include how the effects of non-vertical walls affect the redeposition of sputtered material. Consider a side wall which has a slope given by the angle  $\alpha$ , see figure 3.22. Now

$$F(y) = F_0 \int_a^d \frac{\cos\theta \cos\phi}{r} dx$$

Using the fact that  $\alpha + \phi + \theta = \pi$  and substituting  $\cos\theta = \frac{y}{r}$  the integral becomes

$$F(y) = yF_0 \int_a^d \frac{x \sin\alpha - y \cos\alpha}{(x^2 + y^2)^{3/2}} dx$$

The substitution  $x = y \tan\gamma$  reduces the integral to

$$F(y) = F_0 \int_{\tan^{-1}(\frac{a}{y})}^{\tan^{-1}(\frac{d}{y})} (\sin\gamma \sin\alpha - \cos\alpha \cos\gamma) d\gamma$$

After some manipulation this reduces to



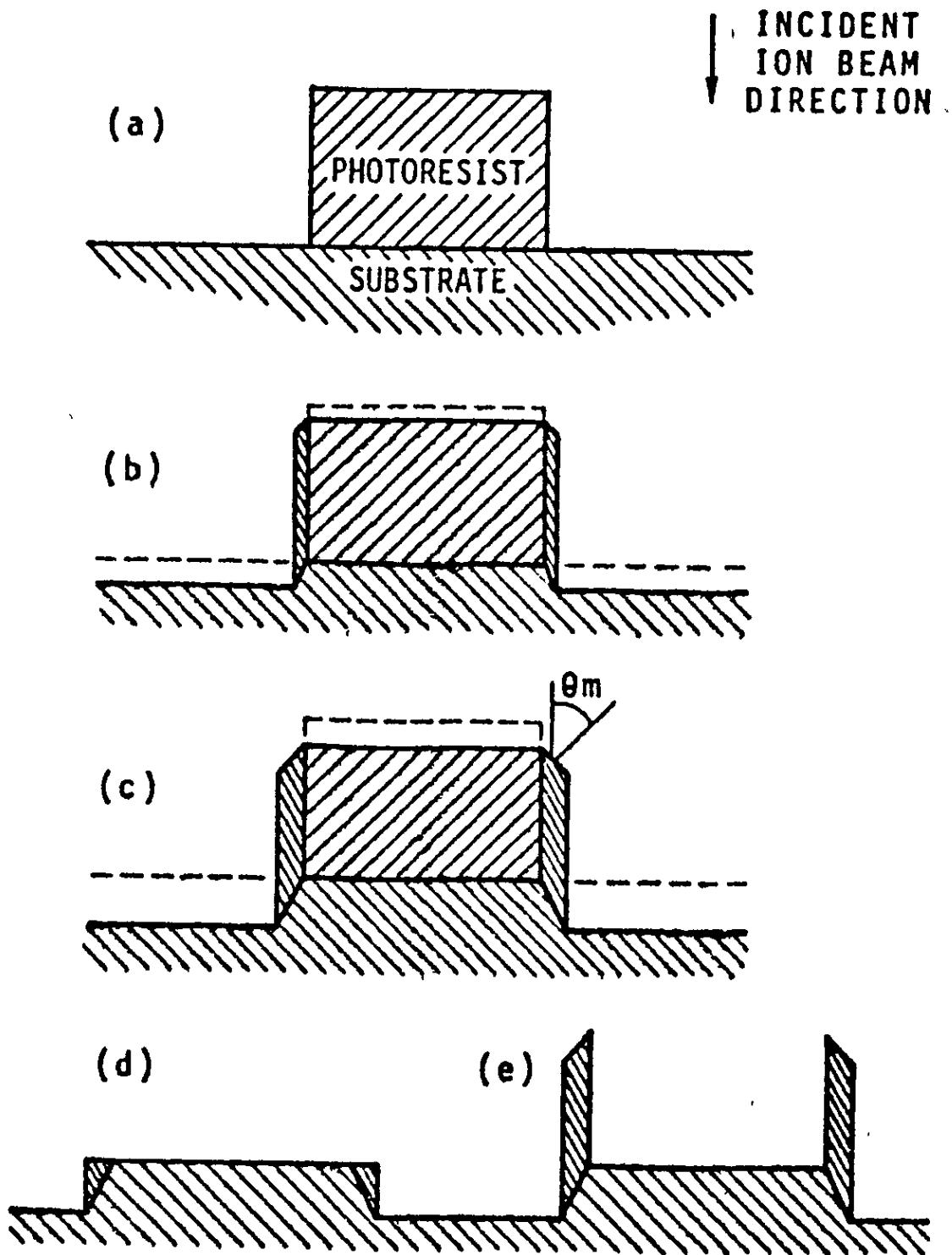


Fig. 3.21. A simple model depicting the stages in ion-beam etching of grooves using a photoresist mask (a) the photoresist cross-section before etching. As the etching proceeds, (b) and (c), facets are formed, and coating of the sidewalls takes place. When the remaining photoresist is lifted after etching is completed, the sidewalls may tear off (d) or may remain (e), depending on how thin and brittle the walls are (After Gloersen (1976)).

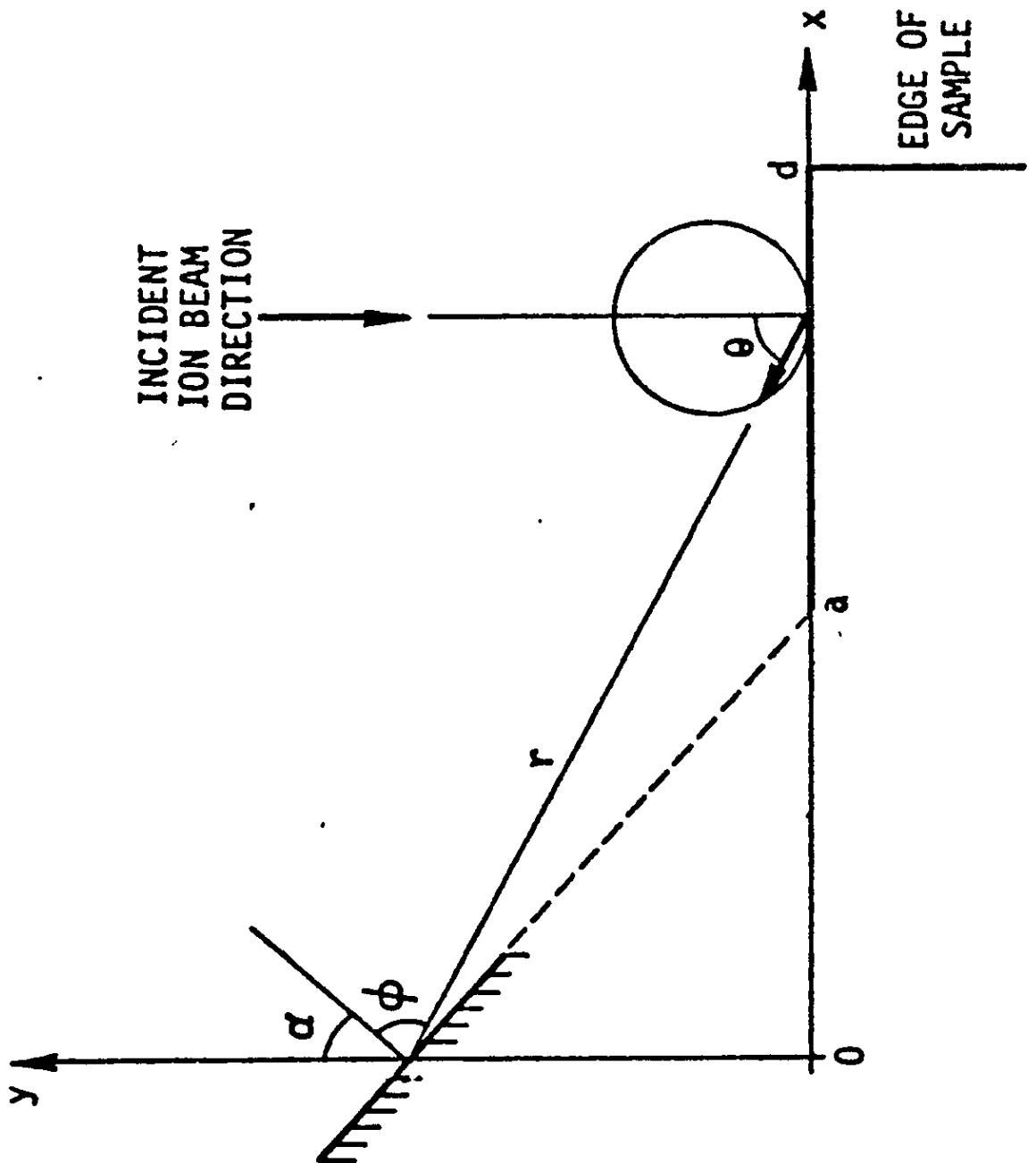


Fig. 3.22. Model used in calculating the flux of sputtered material onto a sloped sidewall. (After Gloersen (1976)).

$$F(y) = F_0 \left[ \frac{y \sin\alpha + a \cos\alpha}{\sqrt{a^2 + y^2}} - \frac{y \sin\alpha + d \cos\alpha}{\sqrt{d^2 + y^2}} \right]$$

But as  $\frac{y}{a} = \tan\alpha$  this reduces further to

$$F(y) = F_0 \left[ 1 - \frac{y \sin\alpha + d \cos\alpha}{\sqrt{d^2 + y^2}} \right] \quad (3.4)$$

The dependence of  $F$  on the angle of incidence and on the ratio between height above substrate surface and width of etched area is shown in figure 3.23.

The model outlined above suffers from the same limitations as that of Bayly (1972). First, a cosine emission distribution for the sputtered particles has been used. As pointed out earlier, this is not a good approximation for ion energies  $< 1\text{keV}$  or  $> 10\text{keV}$ . Secondly, although Glöersen has considered qualitatively the time evolution of a masked groove (figure 3.21), the model does not take into account the continuously changing geometry of the walls.

Belson and Wilson have considered the redeposition of sputtered material using an isotropic (1980a) and cosine (1980b) emission distribution. They considered a line  $OL$  which lies along the positive  $x$  axis such that  $0 \leq x \leq \ell$ , as shown in figure 3.24(a). For isotropic emission every point of  $OL$  emits particles at a constant rate  $n$  per unit length per unit time into the half plane above the  $x$ -axis and the trajectories of all emitted particles are assumed to be straight lines. They then defined and determined a flux density due to  $OL$  in some region such as the element  $PQ$  of arc on the profile  $y = f(\xi)$  in figure 3.24(a),

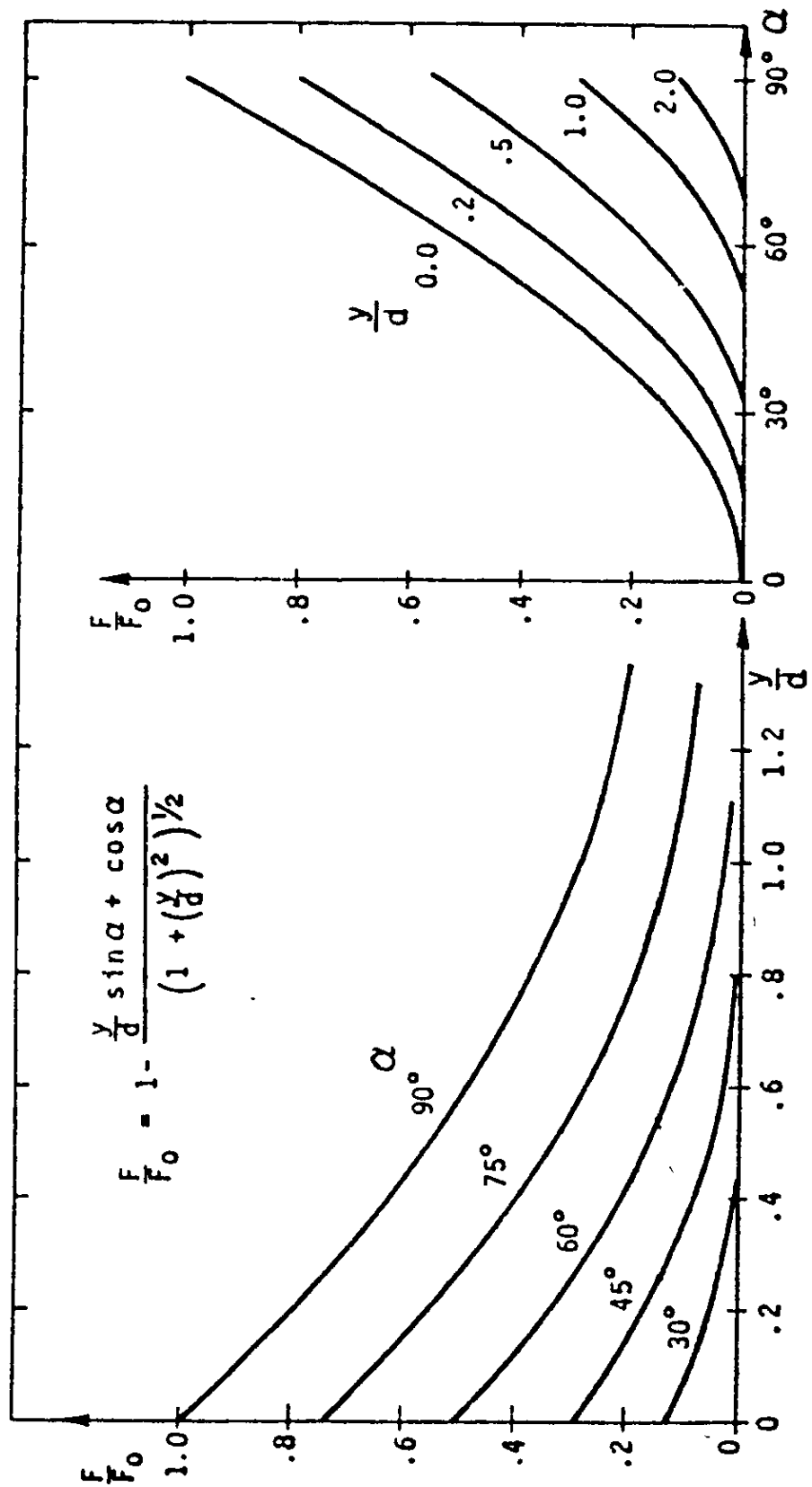


Fig. 3.23. Dependence of incoming flux on the angle of incidence and on the ratio between height above substrate surface and width of etched area. (After Gloersen (1976)).



where  $\xi \leq 0$  and  $f(0) = 0$ . The flux density in such a region is defined as

$$L_{t \text{ P} \rightarrow \text{Q}} \left( \frac{\text{number of particles traversing arc PQ per second}}{\text{length of arc PQ}} \right)$$

They assumed no a priori physical reason for the profile  $f$  and its disposition to be related to the configuration of the emitter. It is thus in order to describe emitter and profile by different variables. Figure 3.24(b) shows a linear slope whose foot is at 0, the origin of coordinates, and which is inclined at an angle  $\alpha$  to the negative  $\xi$  axis. Then Belson and Wilson (1980a) have shown that at a point on the slope where the height above the horizontal axis is  $H\ell$ , where  $H$  is dimensionless, the ratio of incident flux density to emitted flux per unit length of emitter (which they called the normalised flux density) is given by

$$\frac{F}{n} = \frac{1}{2\pi} \sin\alpha \ln \left[ \frac{(1+H\cot\alpha)^2 + H^2}{H^2 \operatorname{cosec}^2\alpha} \right] - \frac{\cos\alpha}{\pi} \left[ \tan^{-1} \left( \frac{1}{H} + \cot\alpha \right) - \left( \frac{\pi}{2} - \alpha \right) \right] \quad (3.5)$$

The variation of  $\frac{F}{n}$  with distance up the slope  $H/\sin\alpha$  is shown as a series of broken curves in figure 3.25 for values of  $\alpha$  between  $30^\circ$  and  $180^\circ$ . They went on to consider the deposition on to a sinusoidal asperity (figure 3.24(c)) which is adjacent to the linear emitter again assuming isotropic emission. The asperity has a fixed base dimension of  $\pi$  units and a parametrically variable amplitude  $a$ . In this way a range of asperity shapes between sharp convex surfaces ( $a \gg \pi$ ) and shallow convex surfaces ( $a \ll \pi$ ) may be configured for different emitter lengths  $\ell$ . They then showed that for this case the normalised flux density is given by

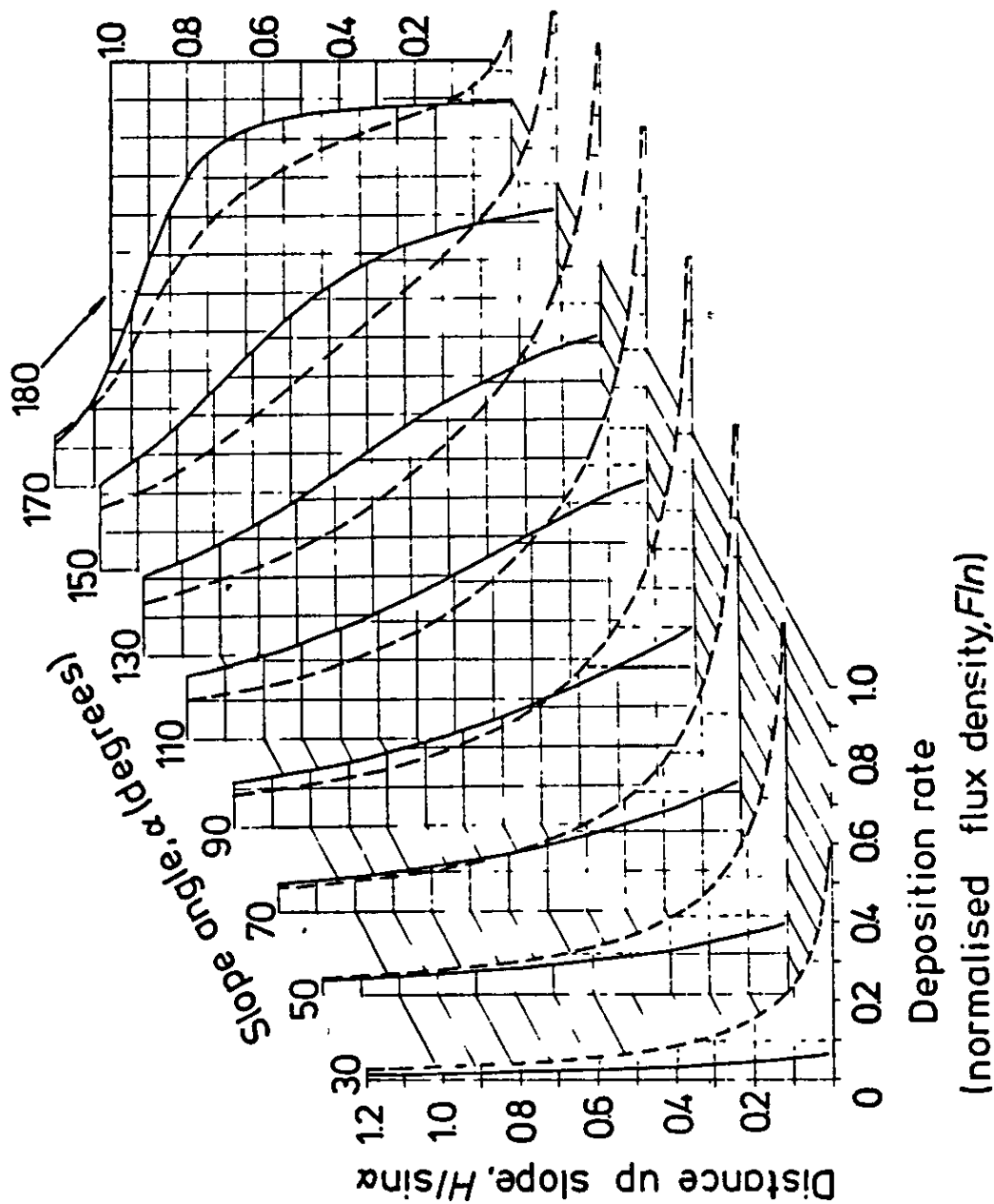


Fig. 3.25. Linear substrate; variation of flux density with distance up the slope and slope angle. Full curves, anisotropic emitter (cosine); broken curves, isotropic emitter. (After Belson and Wilson (1980b)).

$$\frac{F}{n} = \frac{A\ell \cos p}{2\pi(1+A^2\ell^2 \cos^2 p)^{\frac{1}{2}}} \ln \left[ \frac{(\ell+p)^2 + H^2\ell^2}{(d+p)^2 + H^2\ell^2} \right] - \frac{1}{\pi(1+A^2\ell^2 \cos^2 p)^{\frac{1}{2}}} \left[ \tan^{-1} \left( \frac{\ell+p}{H\ell} \right) - \tan^{-1} \left( \frac{d+p}{H\ell} \right) \right] \quad (3.6)$$

Belson and Wilson (1980b) next considered an emission distribution which is more physically realistic viz. a cosine distribution. Let emission from a point be independent of position on the emitter line OL (figure 3.24(a)) but dependent upon the direction  $\phi$ . They took the emission function  $v = v(\phi)$  as

$$v = n_0 \cos \left[ \frac{\pi}{2} - \phi \right] = n_0 \sin \phi$$

The emission rate is thus zero along the axis OL and a maximum ( $n_0$ ) normal to OL. Retaining the number of particles radiated per unit time per unit length as  $n$  the normalisation condition is

$$\int_{\phi=0}^{\pi} n_0 \sin \phi \, d\phi = n = 2n_0$$

Therefore the emitter function is

$$v = \frac{n}{2} \sin \phi$$

Consider the emission from the source OL on to the linear profile (figure 3.24(b)) which passes through the origin O and which has slope  $(-\tan\alpha)$  so that the profile function is  $f(\xi) = (-\tan\alpha)\xi$ . Since the entire length of OL contributes to the flux density at any point on the substrate line,  $F(x_1, x_2)$  is  $F(0, \ell)$  where



$$F(0, \ell) = - \int_0^{\ell} \frac{n}{2} \sin \phi \frac{1}{(1 + \tan^2 \alpha)^{\frac{1}{2}}} \left[ \frac{(-\tan \alpha) \xi + (x - \xi)(-\tan \alpha)}{(x - \xi)^2 + f^2} \right] dx$$

Upon integration, the ratio of incident flux density to emitted flux per unit length of source is

$$\frac{F}{n} = \frac{1}{2} \left[ 1 - \left\{ \frac{h \operatorname{cosec} \alpha + \ell \cos \alpha}{(h^2 \operatorname{cosec}^2 \alpha + 2 \ell h \cot \alpha + \ell)^{\frac{1}{2}}} \right\} \right]; \quad \frac{h}{\ell} \neq 0 \quad (3.7)$$

This equation is the same as equation (3.3) derived by Glöersen (1976). The variation of  $\frac{F}{n}$  with distance up the slope is shown as a series of full curves in figure 3.25 for values of  $\alpha$  between  $30^\circ$  and  $180^\circ$ . Belson and Wilson (1980(b)) then went on to consider the application of the cosine emitter function to a sinusoidal substrate of amplitude  $a$  described by  $f = -a \sin \xi$  for  $-\pi \leq \xi \leq 0$  as shown in figure 3.24(c). They were able to show that

$$\frac{F}{n} = \frac{1}{2(1 + A^2 \ell^2 \cos^2 p)^{\frac{1}{2}}} \left[ \frac{d + p + A^2 \ell^2 \sin p \cos p}{\{A^2 \ell^2 \sin^2 p + (d + p)^2\}^{\frac{1}{2}}} - \frac{\ell + p + A^2 \ell^2 \sin p \cos p}{\{A^2 \ell^2 \sin^2 p + (\ell + p)^2\}^{\frac{1}{2}}} \right] \quad (3.8)$$

Belson and Wilson (1980a, 1980b) refer to their model, outlined above, as the 'first burst' model. That is, they have found analytical solutions for the early evolution of linear and sinusoidal surface features in cases where the emitter radiates isotropically or anisotropically (cosine law) from each point of its length. This means that their model cannot predict the shape changes due to prolonged redeposition i.e. that the continuously changing geometry of the substrate is not taken into account.

Although they have modelled two different distributions for the sputtered particles, one of them (isotropic) is physically unrealistic. As pointed out earlier, Vossen (1979) has shown that the distribution is cosine, over-cosine or under-cosine depending on the incident ion energy, for normal incidence (see figure 3.1). But even these are simplified distributions for polycrystalline materials.

Thus it can be seen that the model of Belson and Wilson (1980a, 1980b) suffers from the same disadvantages as that of Bayly (1972) and Glöersen (1976). Recently a theoretical model for the redeposition of sputtered material has been presented which takes into account the continuously changing geometry of the walls (Makh et al (1980b)). In this paper a cosine emission distribution was used but the model can deal with any type of distribution for the sputtered particles. In the next section this model will be outlined and extended to include non-cosine distributions (Makh et al (1981b)).

#### 3.4. A model for redeposition using the method of characteristics.

The theory to be developed in this section is based on the kinematic wave approach and is similar to that used by Smith and Walls (1980) to predict the surface shape of ion-eroded surfaces. This approach is convenient for subsequent numerical calculations and these are used to illustrate the theory. In this section the build-up of material in initially rectangular grooves is investigated as a function of different groove widths, erosion times and different sputtered particle distributions. The simulated profiles are then compared with those obtained experimentally.

### 3.4.1. Modelling of different distributions for the sputtered particles.

As has been mentioned earlier, the distribution for the sputtered particles is dependent on the energy of the incident ions and on the angle of ion incidence (Vossen (1979), Oechsner (1975)). It has been shown that, for a beam incident normally on a surface, the angular distribution for the sputtered particles is a cosine one for ion energies in the range 1-10keV but under-cosine for energies < 1keV and over-cosine for energies > 10keV, see figure 3.1 (Vossen, (1979)). In this section the different distributions will be modelled analytically. Figure 3.1 shows the distributions for the three different energy regimes. For the distribution in the energy range 1-10keV it has been assumed that the radius vector is given by

$$r = \cos \gamma \quad (3.9)$$

where  $\gamma$  is the angle between the surface normal at P and the radius vector. This is the cosine distribution. In calculating the other distributions the area in the first quadrant has to be the same for all the distributions. On doing this it is found that the high energy distribution (> 10keV) can be modelled by

$$r = 1.265 \cos^3 \gamma \quad (3.10)$$

To model the low-energy distribution, the general curve  $r = a(b \cos \gamma + c \cos^2 \gamma + d \cos^3 \gamma)$  is numerically fitted to the experimental data subject to the following constraints

$$r = a \quad \text{for} \quad \gamma = 0 \quad (b + c + d = 1)$$

$$\frac{dr}{d\gamma} = 0 \quad \text{for} \quad \gamma = 60^\circ$$

$$\frac{d^2r}{d\gamma^2} \text{ is -ve for } \gamma = 60^\circ$$

and finally

$$\int_0^{\pi/2} \cos^2 \gamma \, d\gamma = \int_0^{\pi/2} a^2 (b \cos \gamma + c \cos^2 \gamma + d \cos^3 \gamma)^2 \, d\gamma$$

A computer programme was written to solve the above equations and it has been found that the low-energy distribution (< 1keV) can be modelled by

$$r = 0.594 (7.0 \cos \gamma - 10.0 \cos^2 \gamma + 4.0 \cos^3 \gamma) \quad (3.11)$$

The angular distributions described by equations (3.9)-(3.11) are shown in figure 3.26 and are used in the mathematical model to be developed in the next section to look at the effects of redeposition for different ion energies.

### 3.4.2. Derivation of equations describing the build-up due to redeposition.

#### 3.4.2.1. Intermediate Energy.

In the development of the model it is assumed that the flux  $\phi_1$  of the secondary particle emission from a surface is given by  $\phi_1 = \phi_0 \cos \Omega$  where  $\phi_0$  is the peak emitted flux density and  $\Omega$  the angle subtended by the sputtered particles with the surface normal. Consider the two surfaces shown in figure 3.27. The surface OX'' is being bombarded by a uniform beam and the point A on the surface OX' is receiving a flux  $\phi_1$  from B. Assuming that the point B emits particles according to a cosine distribution (equation (3.9)), then the secondary emitted flux  $\phi_1$  reaching the point A is given by

$$\phi_1 = \frac{\phi S \cos \theta \, dy_1 \, dS_1}{\pi N |\underline{AB}|^2} \frac{\underline{BA} \cdot \underline{n}_1}{|\underline{BA}|}$$

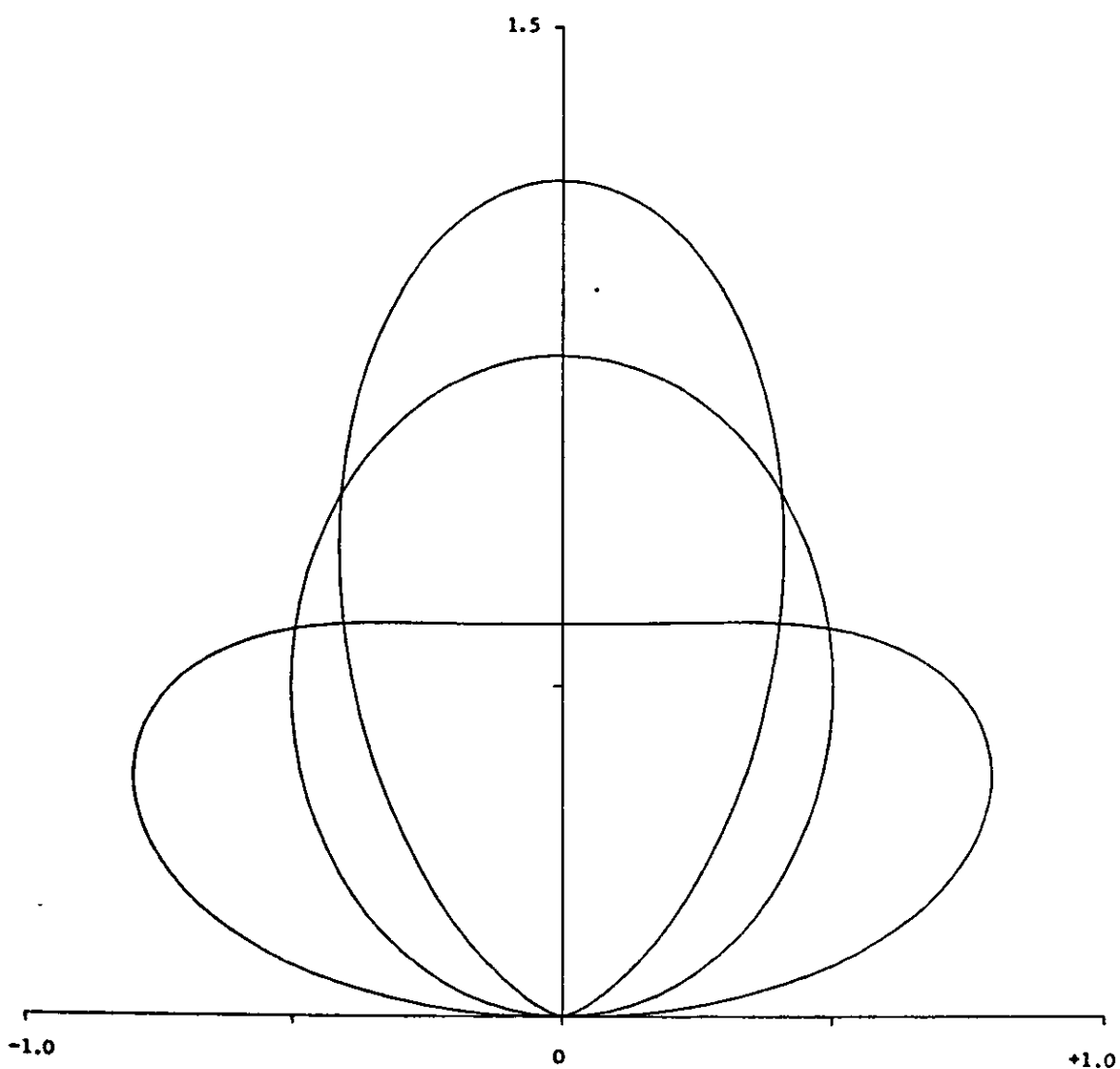


Fig. 3.26. Computer simulation of the different sputtered particle distributions for an ion beam incident normally on a surface.

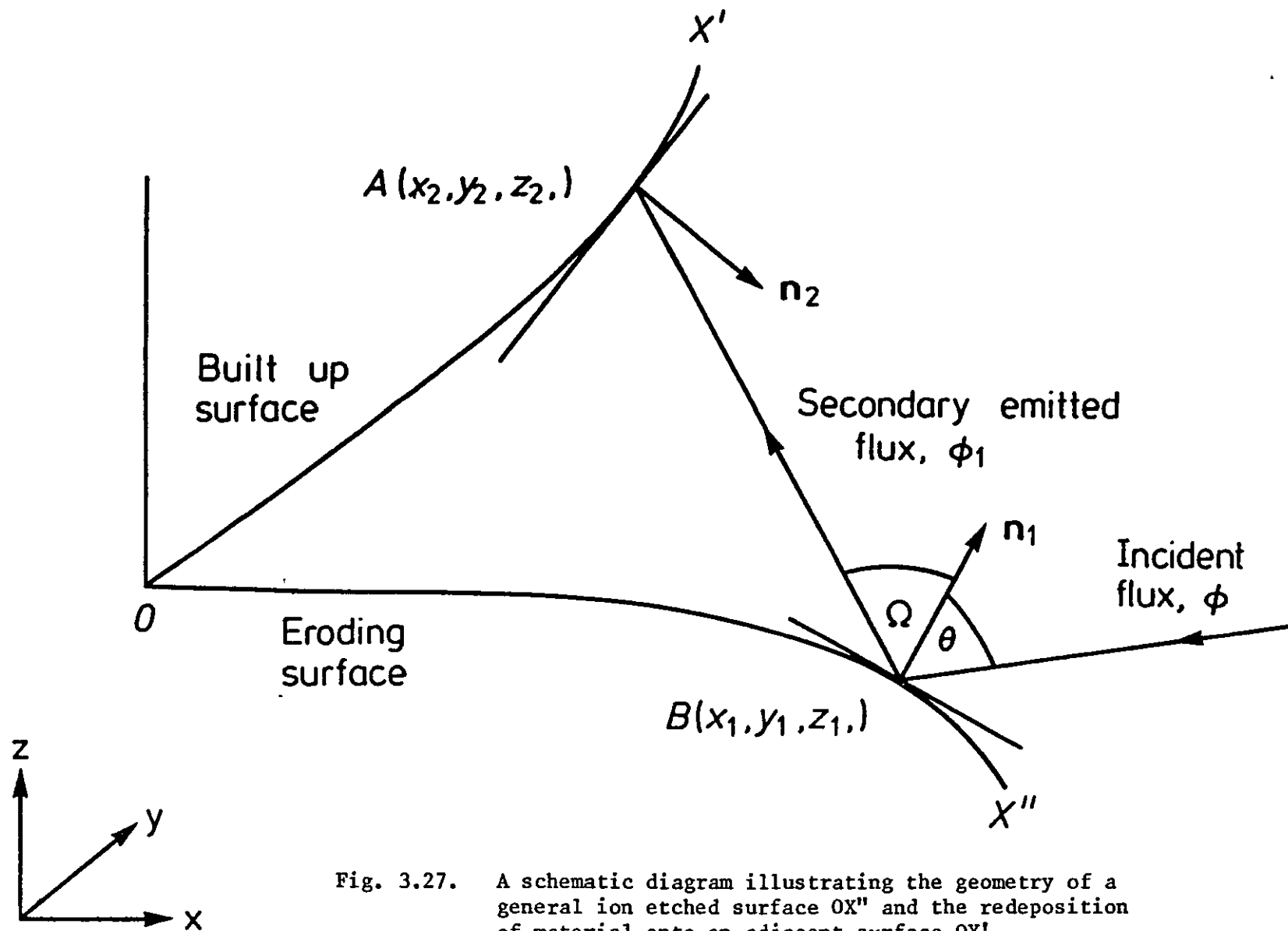


Fig. 3.27. A schematic diagram illustrating the geometry of a general ion etched surface  $OX''$  and the redeposition of material onto an adjacent surface  $OX'$ .

where  $\phi$  is the incident flux density,  $S$  the sputtering coefficient,  $N$  the atomic density,  $\theta$  the angle subtended by the incident ion beam with the surface normal,  $dS_1$  is the arc length in the ( $x$ - $z$ ) plane and  $\underline{n}_1$  is the unit normal at B. Therefore the flux density at A is  $\phi_2$  where

$$\phi_2 = \frac{\phi S \cos\theta \, dy_1 \, dS_1}{\pi N |\underline{AB}|^2} \frac{(\underline{BA} \cdot \underline{n}_1)}{|\underline{BA}|} \frac{(\underline{n}_2 \cdot \underline{AB})}{|\underline{AB}|}$$

and here  $\underline{n}_2$  is the unit normal at A. Thus the flux which originates from a sputtered two-dimensional surface (assumed infinite in the  $y_1$  direction) between the lines  $x_1 = x_1'$  and  $x_1 = x_1''$  is given by  $\phi'$  where

$$\phi' = \frac{\phi S \cos\theta}{\pi N} \int_{y_1=-\infty}^{y_1=+\infty} \int_{x_1=x_1'}^{x_1=x_1''} \frac{(\underline{n}_1 \cdot \underline{BA})(\underline{n}_2 \cdot \underline{AB})}{|\underline{AB}|^4} dy_1 dS_1$$

Now from figure 3.27

$$\underline{AB} = (x_1 - x_2) \hat{i} + (y_1 - y_2) \hat{j} + (z_1 - z_2) \hat{k}$$

$$dS_1 = (dz_1^2 + dx_1^2)^{\frac{1}{2}} = \left\{ 1 + \left( \frac{dz_1}{dx_1} \right)^2 \right\}^{\frac{1}{2}} dx_1$$

$$\underline{n}_1 = \left[ + \frac{dz_1}{dx_1} \left\{ 1 + \left( \frac{dz_1}{dx_1} \right)^2 \right\}^{-\frac{1}{2}}, 0, + \left\{ 1 + \left( \frac{dz_1}{dx_1} \right)^2 \right\}^{-\frac{1}{2}} \right] \quad (3.12)$$

$$\underline{n}_2 = \left[ + \frac{dz_2}{dx_2} \left\{ 1 + \left( \frac{dz_2}{dx_2} \right)^2 \right\}^{-\frac{1}{2}}, 0, - \left\{ 1 + \left( \frac{dz_2}{dx_2} \right)^2 \right\}^{-\frac{1}{2}} \right] \quad (3.13)$$

Thus the two scalar products in the above integral can be evaluated.

Therefore

$$\phi' = -\frac{\phi S \cos \theta}{\pi N} \int_{-\infty}^{\infty} \int_{x_1'}^{x_1''} \frac{\left\{1 + \left(\frac{dz_1}{dx_1}\right)^2\right\}^{-\frac{1}{2}} \left\{(z_1 - z_2) + \frac{dz_1}{dx_1}(x_1 - x_2)\right\} \left\{1 + \left(\frac{dz_2}{dx_2}\right)^2\right\}^{-\frac{1}{2}} \left\{\frac{dz_2}{dx_2}(x_1 - x_2) - (z_1 - z_2)\right\}}{\left\{(x_1 - x_2)^2 + (y_1 - y_2)^2 + (z_1 - z_2)^2\right\}^{\frac{3}{2}}} \times \left\{1 + \left(\frac{dz_1}{dx_1}\right)^2\right\}^{\frac{1}{2}} dx_1 dy_1$$

As the surface is assumed to be symmetrical in the  $y_1$  direction, the integration with respect to  $y_1$  can be carried out. Now consider the surface  $OX''$  in figure 3.27 to be a horizontal plane  $\left[\frac{dz_1}{dx_1} = 0\right]$  and  $OX'$  to be a vertical wall. Thus the integral reduces to

$$\phi' = -\frac{\phi S \cos \theta}{2N} \int_{x_1'}^{x_1''} \frac{A(x_1 - x_2) - B}{\left\{(x_1 - x_2)^2 + (z_1 - z_2)^2\right\}^{\frac{3}{2}}} dx_1$$

where

$$A = \frac{dz_2}{dx_2} (z_1 - z_2) \left\{1 + \left(\frac{dz_2}{dx_2}\right)^2\right\}^{-\frac{1}{2}} \quad \text{and} \quad B = (z_1 - z_2)^2 \left\{1 + \left(\frac{dz_2}{dx_2}\right)^2\right\}^{-\frac{1}{2}}$$

The above integral can now be evaluated exactly and the build-up at A in the normal direction in time  $\delta t$  can be determined as

$$\delta r_n = \frac{\eta \phi S \cos \theta \sin C}{N} \left\{1 + \left(\frac{dz_2}{dx_2}\right)^2\right\}^{-\frac{1}{2}} \left\{\frac{dz_2}{dx_2} \sin D - \cos D\right\} \delta t \quad (3.14)$$

where  $\eta$  is the sticking coefficient and

$$C = \frac{1}{2} \tan^{-1} \left[ \frac{(2x_0 - d)(z_1 - z_2)}{(z_1 - z_2)^2 + (x_0 - x_2)(d - x_0 - x_2)} \right];$$



$$D = \frac{1}{2} \tan^{-1} \left[ \frac{(d-2x_2)(z_1-z_2)}{(z_1-z_2)^2 - (x_0-x_2)(d-x_0-x_2)} \right];$$

Here  $d$  represents the initial width of the groove and  $x_0$  is a lower limit for integration which is initially zero. Equation (3.14) is the differential equation describing the build-up of the surface  $A(\underline{r}, t) = 0$  in the normal direction and this can be converted into a partial differential equation for  $A(\underline{r}, t)$  following the method of Smith and Walls (1980). This we will now proceed to do.

Consider a surface whose equation at time  $t$  is  $A(\underline{r}, t) = 0$  where  $\underline{r}$  is the position vector of a point on the surface. Suppose the point  $(\underline{r}, t)$  lies on the surface at time  $t$ , and let the point  $(\underline{r} + \delta \underline{r}, t + \delta t)$  on the normal from  $(\underline{r}, t)$  lie on the built-up surface at time  $t + \delta t$ . This point lies a distance  $\delta \underline{r}$  from  $(\underline{r}, t)$  in the direction of the surface normal  $\underline{n}_2 = \nabla A / |\nabla A|$ . Therefore equation (3.14) becomes

$$\delta \underline{r} = -M \delta t \frac{\nabla A}{|\nabla A|} \quad (3.15)$$

where

$$M = \frac{\eta \phi S \cos \theta \sin C}{N} \left\{ 1 + \left( \frac{dz_2}{dx_2} \right)^2 \right\}^{-\frac{1}{2}} \left[ \cos D - \frac{dz_2}{dx_2} \sin D \right]$$

After time  $\delta t$ , the equation of the surface is given by

$$A(\underline{r} + \delta \underline{r}, t + \delta t) = 0$$

and expanding using Taylor's theorem

$$A(\underline{r} + \delta \underline{r}, t + \delta t) = A(\underline{r}, t) + \frac{\partial A}{\partial t} \delta t + \nabla A \cdot \delta \underline{r} + \dots$$

Substituting in equation (3.15) and taking the limit as  $\delta t \rightarrow 0$  gives the following equation describing the motion of the surface.

$$\frac{\partial A}{\partial t} - M|\nabla A| = 0 \quad (3.16)$$

Using subscripts to denote partial derivatives then equation (3.16) can be written as

$$A_t^2 = M^2 |\nabla A|^2$$

$$\text{i.e.} \quad A_t^2 = M^2 (A_x^2 + A_y^2 + A_z^2) \quad (3.17)$$

where  $(x,y,z)$  are the rectangular cartesian coordinates. This is a non-linear first order partial differential equation of a type that occurs in geometrical optics and is sometimes known as the eikonal or Jacobi's equation (Whitham (1974), Smith and Walls (1980)). To solve equation (3.17) specify the surface  $A(\underline{r},t) = 0$  in a form where  $t$  is given explicitly as a function of  $\underline{r}$ , i.e.

$$A(\underline{r},t) = t - \sigma(\underline{r}) = 0 \quad (3.18)$$

The family of surfaces  $\sigma(\underline{r}) = \text{constant}$  gives the successive positions of the surface as it builds up with time in two dimensions. Thus (3.17) becomes

$$1 - M^2 (\sigma_x^2 + \sigma_z^2) = 0 \quad (3.19)$$

Also  $\nabla A$  and  $\underline{n}_2$  can be given in terms of  $\sigma$  and its derivatives and so from equation (3.18)

$$\nabla A = - (\sigma_x, 0, \sigma_z) \quad (3.20)$$

and thus

$$\underline{n}_2 = \frac{\nabla A}{|\nabla A|} = \frac{-(\sigma_x, 0, \sigma_z)}{(\sigma_x^2 + \sigma_z^2)^{\frac{1}{2}}}$$

Comparing this equation for  $\underline{n}_2$  with equation (3.13) gives

$$\frac{\sigma_x}{\sigma_z} = - \frac{dz_2}{dx_2} \quad (3.21)$$

Substituting for  $\frac{dz_2}{dx_2}$  in equation (3.19) enables us to write (3.19) in the standard form (Whitham (1974)) for which a standard method of analysis exists.

$$H(\underline{r}, \underline{p}, \sigma) = 1 - \frac{\eta^2 \phi^2 S^2 \cos^2 \theta \sin^2 C}{N^2} (\sigma_z \cos D + \sigma_x \sin D)^2 = 0 \quad (3.22)$$

where  $\underline{p} = (\sigma_x, 0, \sigma_z)$

The method of solution is to determine the characteristic lines of equation (3.22). Essentially, these are lines in space along which the partial differential equation (3.22) can be reduced to a set of ordinary differential 'characteristic' equations.

Let a characteristic curve be given in parametric form by  $\underline{r} = \underline{r}(\lambda)$  for some parameter  $\lambda$ . Then such curves are the lines defined by (Whitham (1974))

$$\frac{dx}{d\lambda} = \frac{\partial H}{\partial \sigma_x}; \quad \frac{dy}{d\lambda} = \frac{\partial H}{\partial \sigma_y}; \quad \frac{dz}{d\lambda} = \frac{\partial H}{\partial \sigma_z} \quad (3.23)$$

with corresponding characteristic equations

$$\left. \begin{aligned} \frac{d\sigma_x}{d\lambda} &= -\sigma_x \frac{\partial H}{\partial \sigma} - \frac{\partial H}{\partial x} \\ \frac{d\sigma_y}{d\lambda} &= -\sigma_y \frac{\partial H}{\partial \sigma} - \frac{\partial H}{\partial y} \\ \frac{d\sigma_z}{d\lambda} &= -\sigma_z \frac{\partial H}{\partial \sigma} - \frac{\partial H}{\partial z} \end{aligned} \right\} \quad (3.24)$$

and where  $t$  is related to  $\lambda$  by

$$\frac{dt}{d\lambda} = \sigma_x \frac{\partial H}{\partial \sigma_x} + \sigma_y \frac{\partial H}{\partial \sigma_y} + \sigma_z \frac{\partial H}{\partial \sigma_z} \quad (3.25)$$

Thus from equations (3.18), (3.22), (3.23) and (3.25) we determine the characteristic lines to be given by the following equations

$$\frac{dx_2}{dt} = \frac{\eta\phi S \cos\theta}{N} \sin C \sin D \quad (3.26)$$

$$\frac{dy_2}{dt} = 0 \quad (3.27)$$

$$\frac{dz_2}{dt} = \frac{\eta\phi S \cos\theta}{N} \sin C \cos D \quad (3.28)$$

where

$$\left. \begin{aligned} C &= \frac{1}{2} \tan^{-1} \left[ \frac{(2x_0 - d)(z_1 - z_2)}{(z_1 - z_2)^2 + (x_0 - x_2)(d - x_0 - x_2)} \right] \\ D &= \frac{1}{2} \tan^{-1} \left[ \frac{(d - 2x_2)(z_1 - z_2)}{(z_1 - z_2)^2 - (x_0 - x_2)(d - x_0 - x_2)} \right] \end{aligned} \right\} \quad (3.29)$$

### 3.4.2.2. High Energy.

To derive the characteristic equations for high energy, the procedure outlined in section 3.4.2.1 is carried out, but this time assuming the secondary particle emission from the surface is given by  $\phi_1 = 1.265\phi_0 \cos^3 \Omega$  where the notation is as before. Therefore in this case the secondary emitted flux reaching the point A in figure 3.27 is given by

$$\phi_1 = \frac{2\phi S \cos \theta}{\pi N |\underline{AB}|^2} \frac{(\underline{BA} \cdot \underline{n}_1)^3}{|\underline{BA}|^3} dy_1 dS_1$$

Therefore the flux density at A is  $\phi_2$  where

$$\phi_2 = \frac{2\phi S \cos \theta}{\pi N |\underline{AB}|^2} \frac{(\underline{BA} \cdot \underline{n}_1)^3}{|\underline{BA}|^3} \frac{(\underline{n}_2 \cdot \underline{AB})}{|\underline{AB}|} dy_1 dS_1$$

and hence the flux which originates from a sputtered two-dimensional surface (assumed infinite in the  $y_1$  direction) between the lines  $x_1 = x_1'$  and  $x_1 = x_1''$  is given by

$$\frac{2\phi S \cos \theta}{\pi N} \int_{y_1 = -\infty}^{y_1 = +\infty} \int_{x_1 = x_1'}^{x_1 = x_1''} \frac{(\underline{n}_1 \cdot \underline{BA})^3 (\underline{n}_2 \cdot \underline{AB})}{|\underline{AB}|^6} dy_1 dS_1$$

As before, for the case when the eroding surface  $OX''$  is a horizontal plane and redeposition is occurring on the side walls of an initially vertical groove, the above integral can be evaluated exactly. The build-up  $\delta r_n$  at A in the normal direction in time  $\delta t$  can be determined as

$$\delta r_n = \frac{3\eta\phi S \cos\theta D_2}{4N} \left[ -2\cos D \sin C + \frac{2}{3} \sin 2D \sin 2C \cos C (\sin D + \frac{dz_2}{dx_2} \cos D) \right. \\ \left. + \frac{1}{3} \sin C \cos 2D (\cos D - \frac{dz_2}{dx_2} \sin D) - \frac{1}{3} \sin C \cos 2C (\cos D + \frac{dz_2}{dx_2} \sin D) \right] \delta t \quad (3.30)$$

where

$$D_2 = \left\{ 1 + \left( \frac{dz_2}{dx_2} \right)^2 \right\}^{-\frac{1}{2}}$$

and C and D are given in equation (3.29).

Equation (3.30) can be solved in exactly the same way as equation (3.14) in the previous section. Thus it can be shown that the set of ordinary differential 'characteristic' equations describing the build-up due to a high energy distribution are

$$\frac{dx_2}{dt} = \frac{\eta\phi S \cos\theta}{4N} \left[ -\sin C \sin D (\cos 2D + \cos 2C) + 2\cos C \cos D \sin 2C \sin 2D \right] \quad (3.31)$$

$$\frac{dy_2}{dt} = 0 \quad (3.32)$$

$$\frac{dz_2}{dt} = \frac{\eta\phi S \cos\theta}{2N} \left[ 3\cos D \sin C - \sin 2D \sin 2C \cos C \sin D - \frac{1}{3} \sin C \cos D (\cos 2D - \cos 2C) \right] \quad (3.33)$$

and C and D are given in equation (3.29).

### 3.4.2.3. Low Energy.

To derive the characteristic equations for low energy, the procedure outlined in section 3.4.2.1 is carried out, but assuming the secondary particle emission from the surface is given by  $\phi_1 = 0.594\phi_0 (7.0\cos\Omega - 10.0\cos^2\Omega + 4.0\cos^3\Omega)$  where the notation is as before. Assuming that the point B in figure 3.27 emits particles according to the above law then the flux which originates from a sputtered two-dimensional surface (assumed infinite in the  $y_1$  direction) between the lines  $x_1 = x_1'$  and  $x_1 = x_1''$  can be easily worked out. As before, when the surface  $OX''$  in figure 3.27 is a horizontal plane and material is redepositing on the side walls of an initially vertical groove wall, the build-up at A in the normal direction in time  $\delta t$  can be determined as

$$\delta r_n = \eta D_2 \left[ \left\{ 2bC + b\sin 2C \cos 2D - a\sin C \cos D - 2e \cos D \sin C + \frac{2}{3} e \sin 2D \sin 2C \cos C \sin D + \frac{1}{3} e \sin C \cos 2D \cos D - \frac{1}{3} e \sin C \cos 2C \cos D \right\} + \frac{dz_2}{dx_2} \left\{ a \sin C \sin D - b \sin 2C \sin 2D + \frac{2}{3} e \sin 2D \sin 2C \cos C \cos D - \frac{1}{3} e \sin C \cos 2D \sin D - \frac{1}{3} e \sin C \cos 2C \sin D \right\} \right] \delta t \quad (3.34)$$

where  $a = 4.158\pi F'$ ;  $b = 3.96F'$ ;  $e = 0.891\pi F'$ ;  $F' = 0.2297\phi S \cos\theta/N$ ;

$$D_2 = \left\{ 1 + \left( \frac{dz_2}{dx_2} \right)^2 \right\}^{-\frac{1}{2}} ;$$

and C and D are given in equation (3.29).

Equation (3.34) can be solved in exactly the same way as equations (3.14) and (3.30). Thus it can be shown that the set of ordinary differential 'characteristic' equations describing the build-up due to a low energy distribution are

$$\frac{dx_2}{dt} = \frac{\eta\phi S \cos\theta}{N} \left[ 3.0005 \sin C \sin D - 0.9096 \sin 2C \sin 2D + 0.4287 \sin 2D \sin 2C \cos C \cos D \right. \\ \left. - 0.2143 \sin C \sin D (\cos 2D + \cos 2C) \right] \quad (3.35)$$

$$\frac{dy_2}{dt} = 0 \quad (3.36)$$

$$\frac{dz_2}{dt} = -\frac{\eta\phi S \cos\theta}{N} \left[ 1.8192C + 0.9096 \sin 2C \cos 2D + 0.4287 \sin 2D \sin C \cos C \sin D \right. \\ \left. - 4.2864 \sin C \cos D + 0.2143 \sin C \cos D (\cos 2D - \cos 2C) \right] \quad (3.37)$$

and C and D are given in equation (3.29).

### 3.5. Results of computer simulation.

The theory presented in section 3.4 can be used to carry out numerical calculations since the ordinary differential equations derived can be integrated so that a set of n points  $(x_i, y_i, z_i)$ ,  $i = 1, \dots, n$ , defining an initial surface can be transformed into  $(x'_i, y'_i, z'_i)$  defining the envelope of the built-up surface. For example the set of ordinary differential equations (3.26)-(3.28) can be integrated to give

$$x'_i = x_i + \int_0^t \left( \frac{\eta\phi S \cos\theta}{N} \right) \sin C \sin D \, dt$$

$$y'_i = y_i$$

$$z'_i = z_i + \int_0^t \left( \frac{\eta\phi S \cos\theta}{N} \right) \sin C \cos D \, dt$$



The factor  $\frac{\eta\phi S \cos\theta}{N}$  appearing in the above equations consists of two independent terms. The term  $\frac{\phi S \cos\theta}{N}$  is the amount eroded from a horizontal plane. The term  $\eta$  describes how much of the backspattered material sticks to the sidewalls i.e. how much is built-up. In the numerical calculations both factors have been normalised to 1. It should also be noted that the angles C and D (as given in equation (3.29)) are both functions of time as  $z_1 = z_1(t)$ . The numerical integration procedure has been carried out for the different distributions described in section 3.4. Thus the changes in the amount of material redeposited, brought about by using different ion energies, can be investigated as a function of erosion depth and groove width.

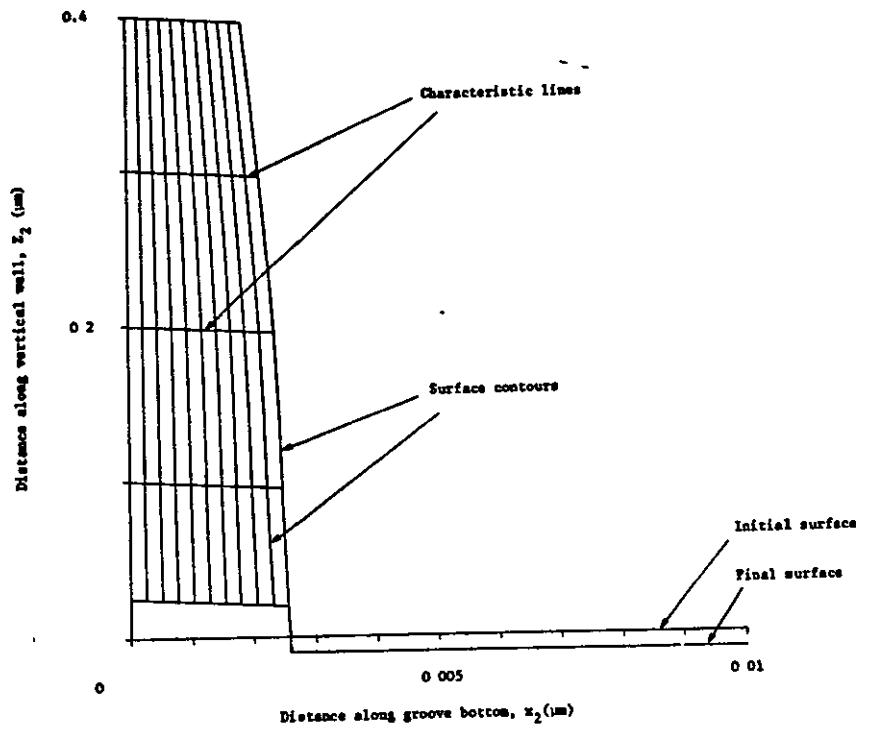
Figures 3.28-3.30 show the build-up due to redeposition for a rectangular groove in two dimensions assuming high, medium and low energy distributions respectively. For each energy regime a series of groove widths are used and the build-up determined in each case. In these diagrams the successive surface contours correspond to the development of surface shape over equal increments of erosion time. In all cases, the depth of erosion corresponding to each successive surface contour is 1nm.

Figures 3.31-3.33 again show the build-up due to redeposition for a rectangular groove in two dimensions assuming high, medium and low energy distributions. However in this case the depth of erosion corresponding to each successive contour is 10nm. For each energy regime a series of different groove widths are used in order to investigate fully, the changes in build-up that can occur.

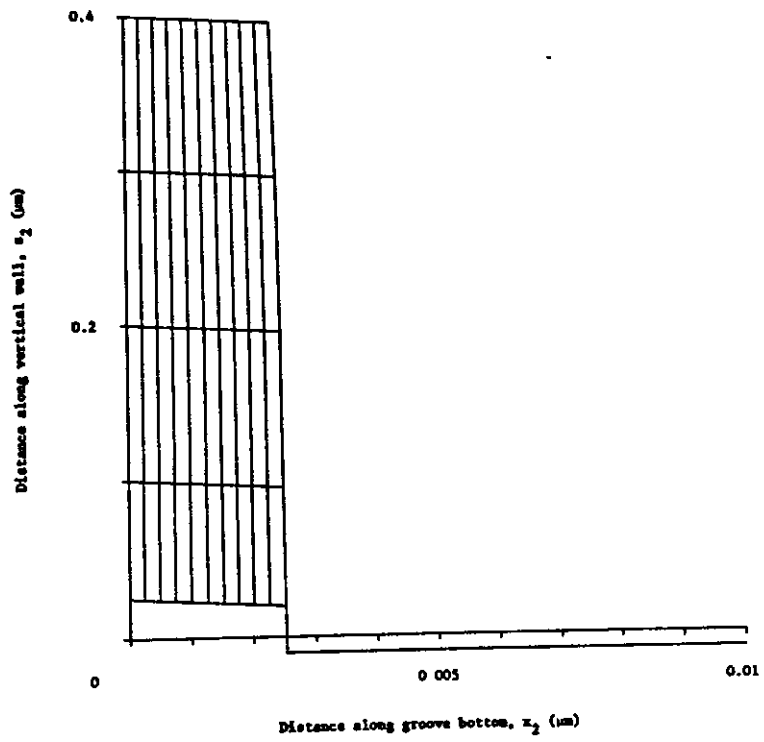
Figures 3.34-3.36 show the tenth surface contour of figures 3.28-3.30 plotted in three dimensions. The groove widths corresponding to each

Fig. 3.28. Theoretically calculated redeposition profiles for rectangular grooves of different widths and for different depths of erosion using the over-cosine distribution for the sputtered particles. The depth of erosion corresponding to each surface contour is 1nm and the groove height is 0.4 $\mu$ m.

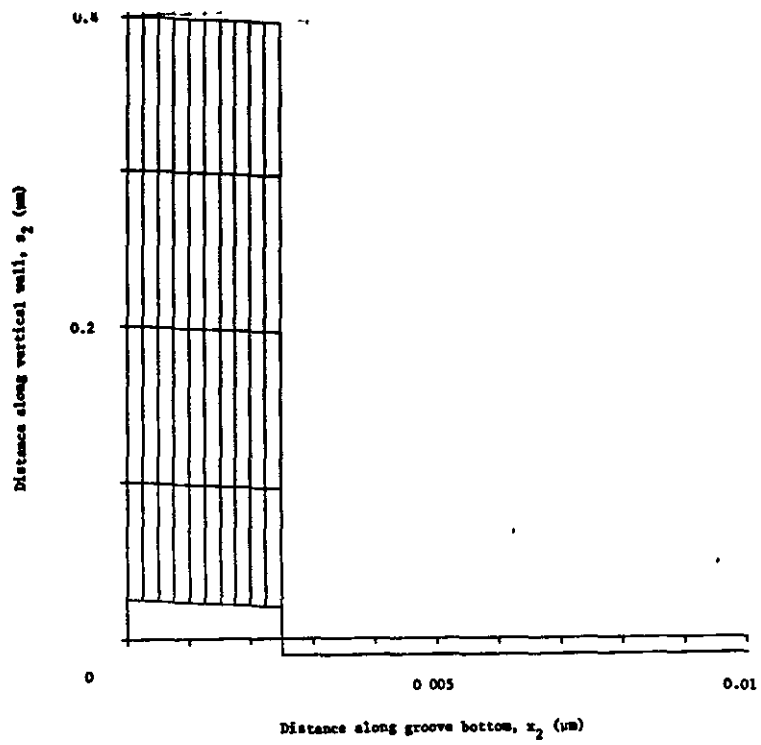
- (a) Groove width = 0.5 $\mu$ m
- (b) Groove width = 1.0 $\mu$ m
- (c) Groove width = 3.0 $\mu$ m
- (d) Groove width = 6.0 $\mu$ m.



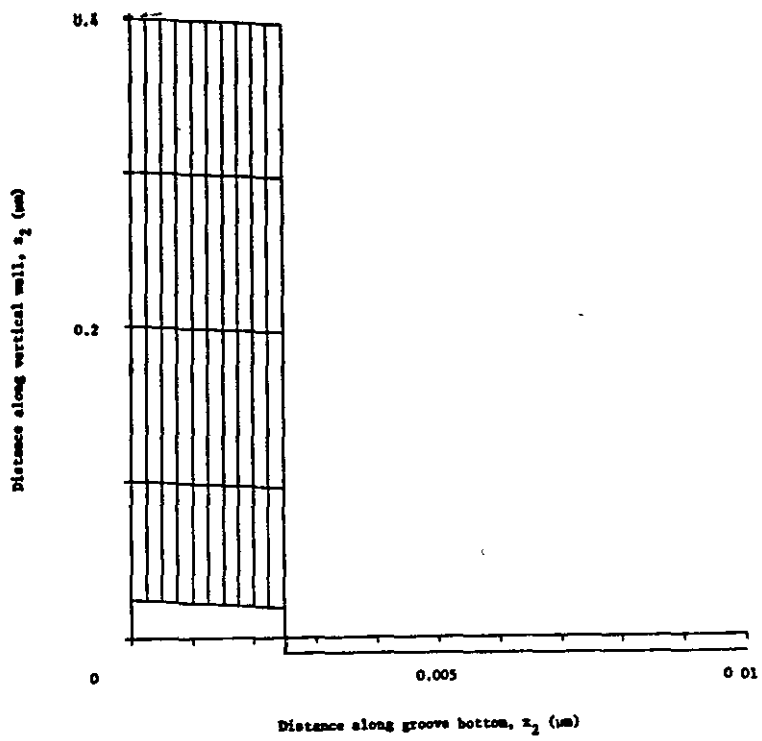
**a**



**b**



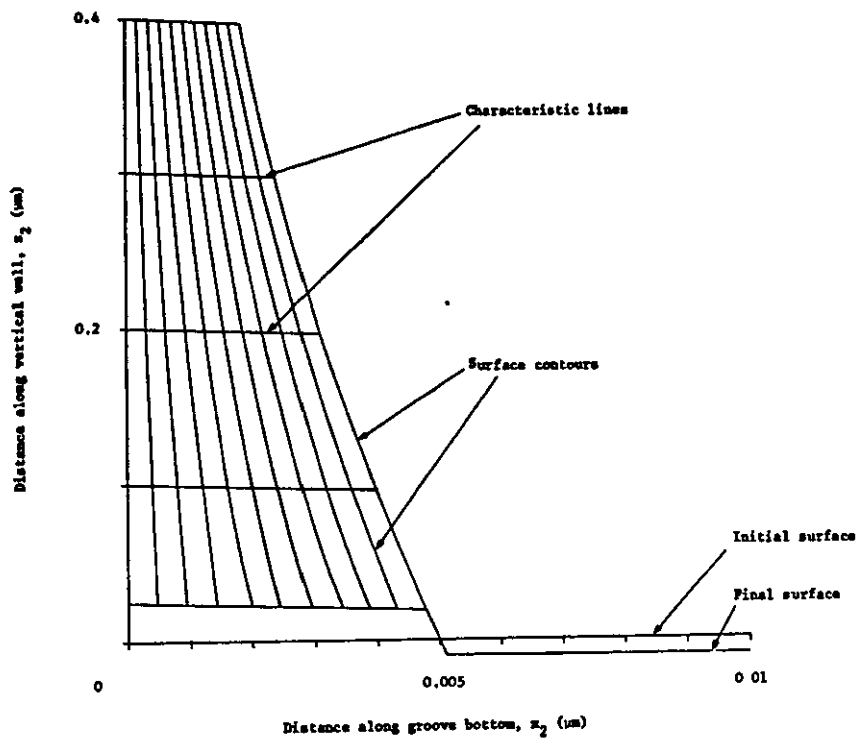
**C**



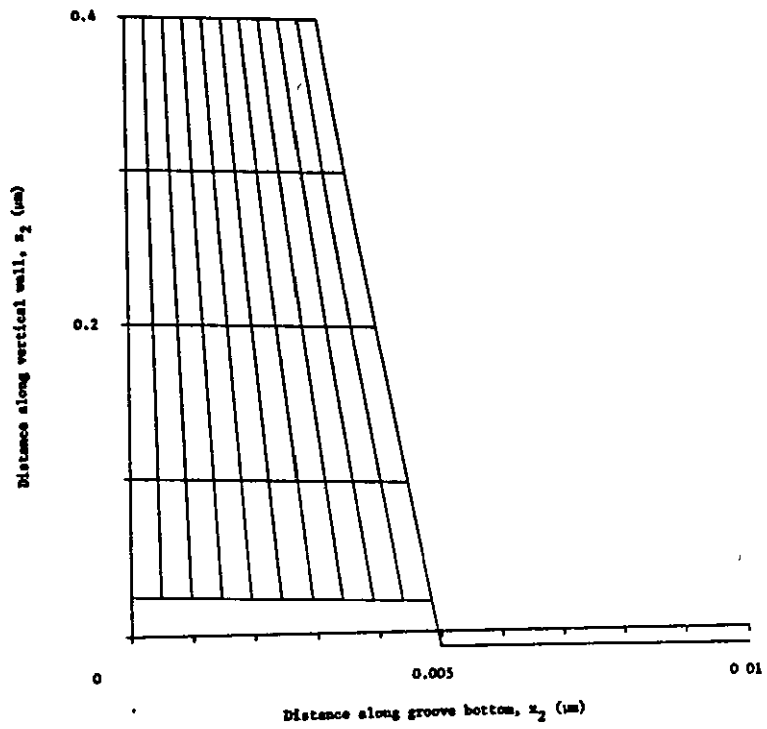
**d**

Fig. 3.29. Theoretically calculated redeposition profiles for rectangular grooves of different widths and for different depths of erosion using the cosine distribution for the sputtered particles. The depth of erosion corresponding to each surface contour is 1nm and the groove height is 0.4 $\mu$ m.

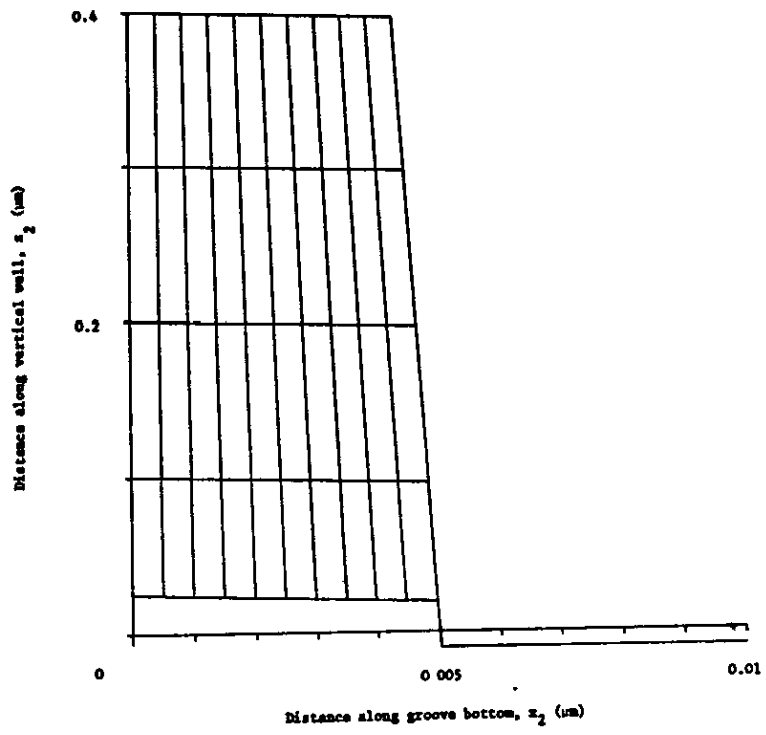
- (a) Groove width = 0.5 $\mu$ m
- (b) Groove width = 1.0 $\mu$ m
- (c) Groove width = 3.0 $\mu$ m
- (d) Groove width = 6.0 $\mu$ m.



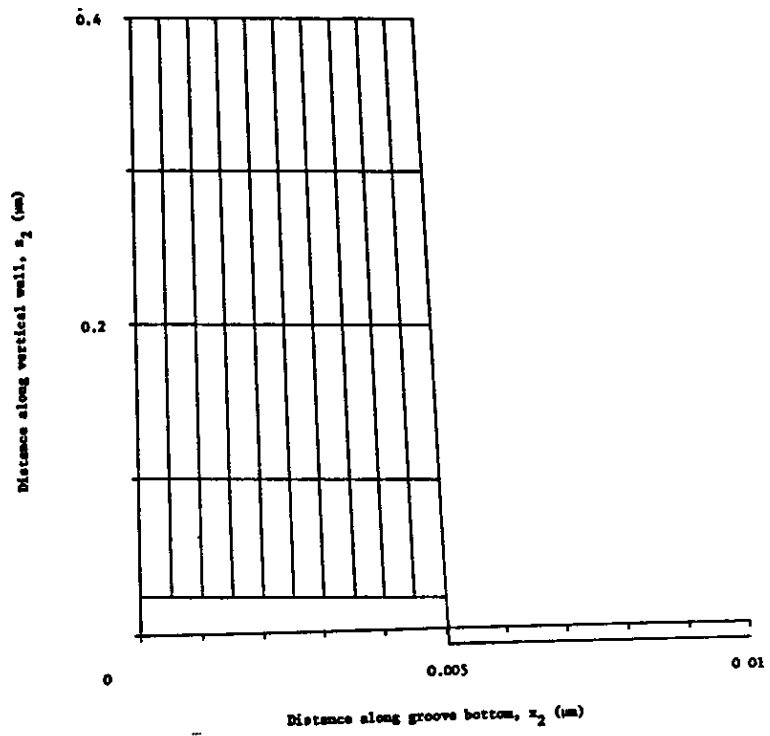
**a**



**b**



**C**

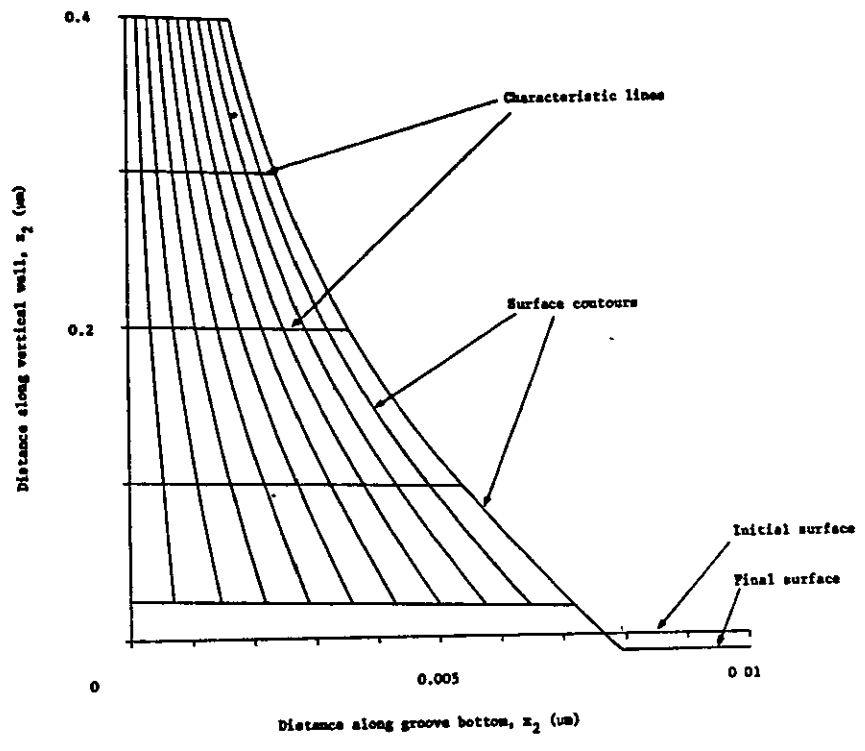


**d**

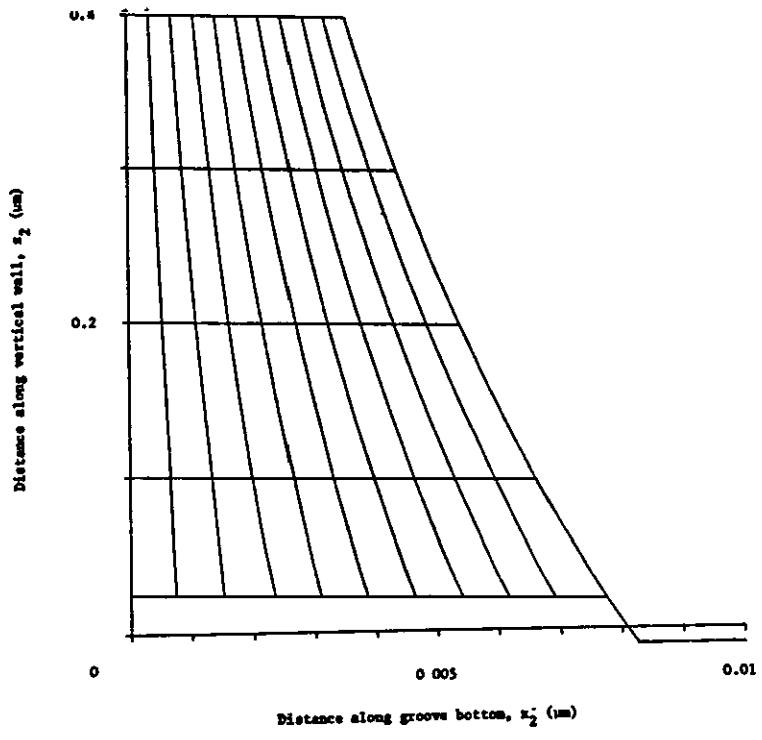
Fig. 3.30. Theoretically calculated redeposition profiles for rectangular grooves of different widths and for different depths of erosion using the under-cosine distribution for the sputtered particles. The depth of erosion corresponding to each surface contour is 1nm and the groove height is 0.4 $\mu$ m.

- (a) Groove width = 0.5 $\mu$ m
- (b) Groove width = 1.0 $\mu$ m
- (c) Groove width = 3.0 $\mu$ m
- (d) Groove width = 6.0 $\mu$ m.

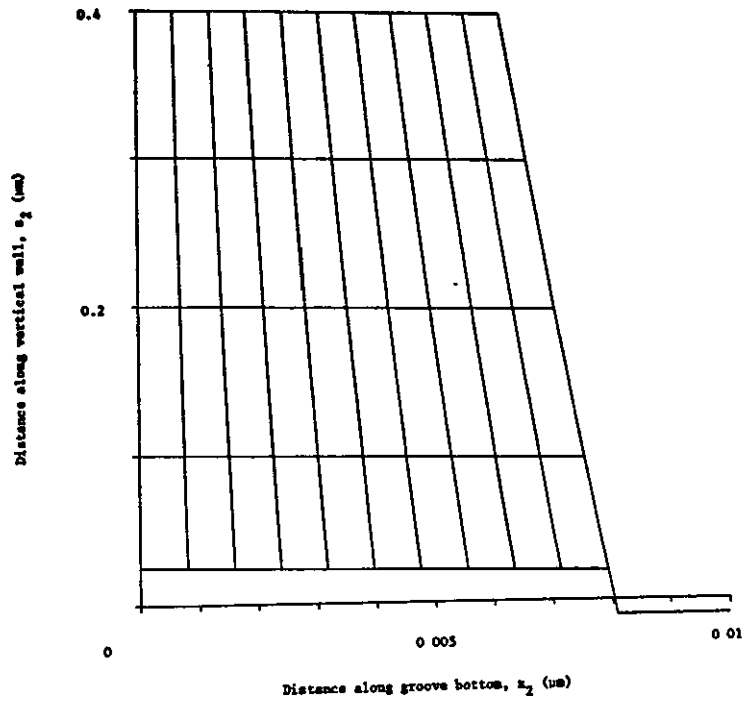




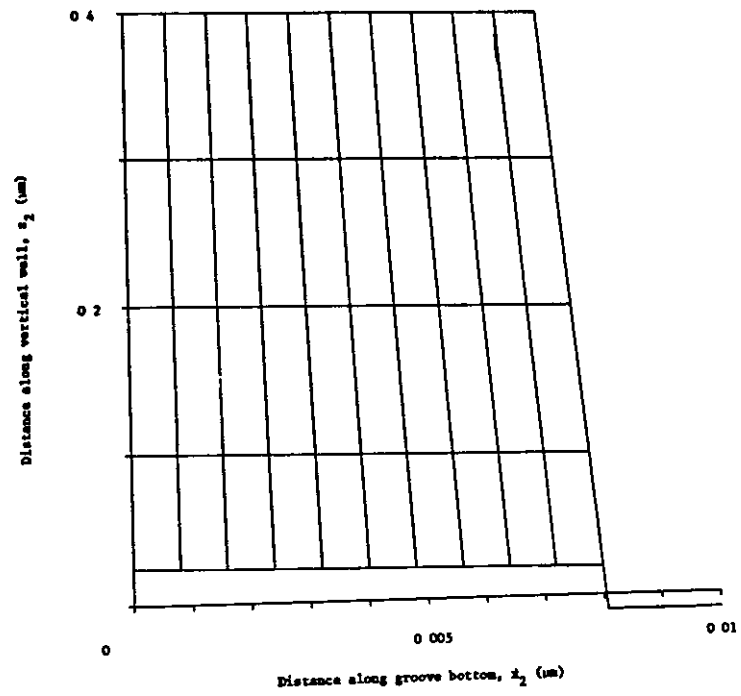
**a**



**b**



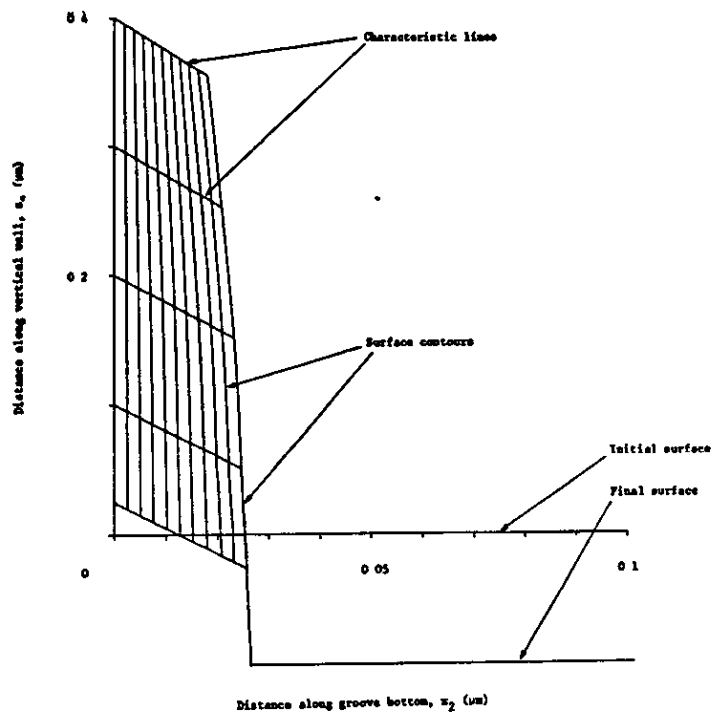
**c**



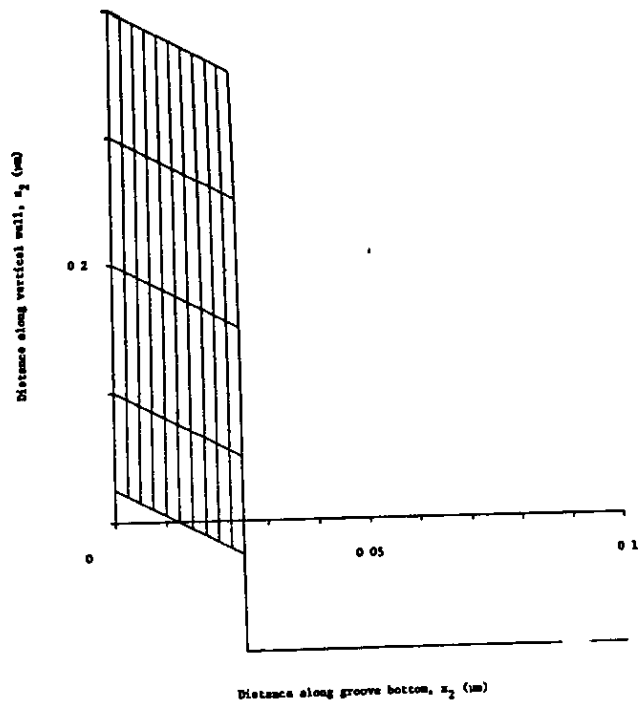
**d**

Fig. 3.31. Theoretically calculated redeposition profiles for rectangular grooves of different widths and for different depths of erosion using the over-cosine distribution for the sputtered particles. The depth of erosion corresponding to each surface contour is 10nm and the groove height is 0.4 $\mu$ m.

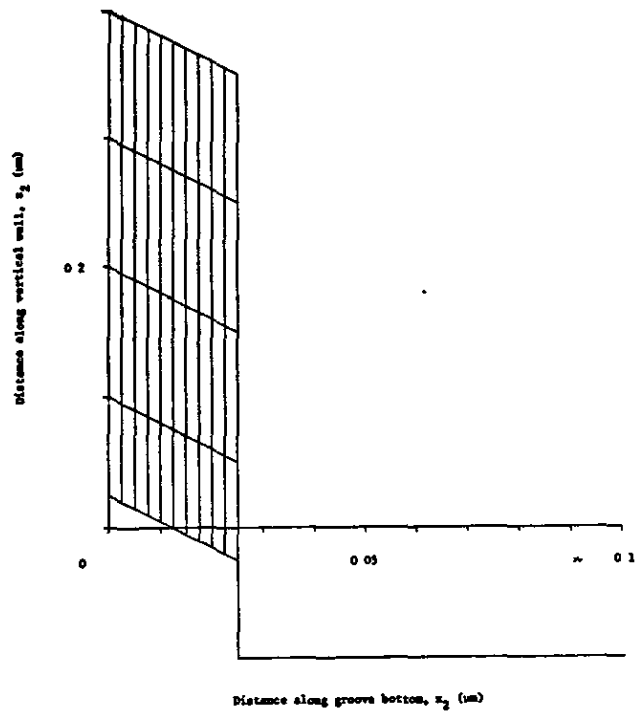
- (a) Groove width = 0.5 $\mu$ m
- (b) Groove width = 1.0 $\mu$ m
- (c) Groove width = 3.0 $\mu$ m
- (d) Groove width = 6.0 $\mu$ m.



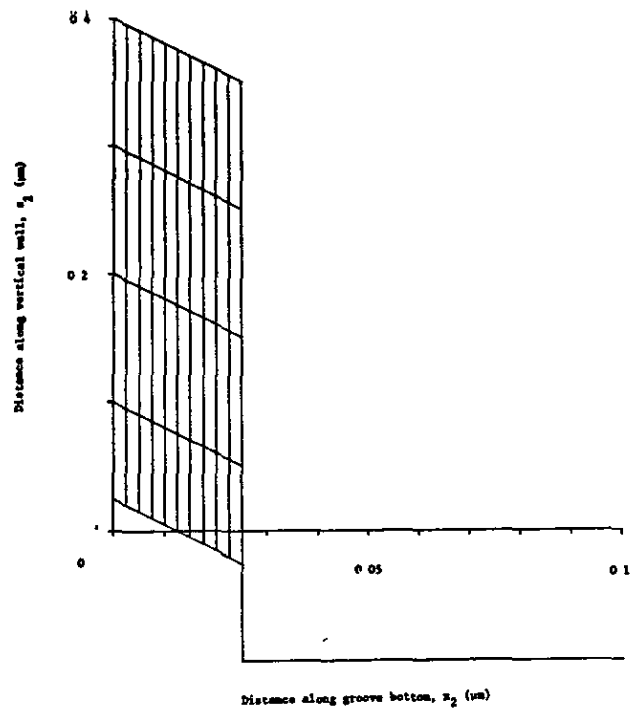
**a**



**b**



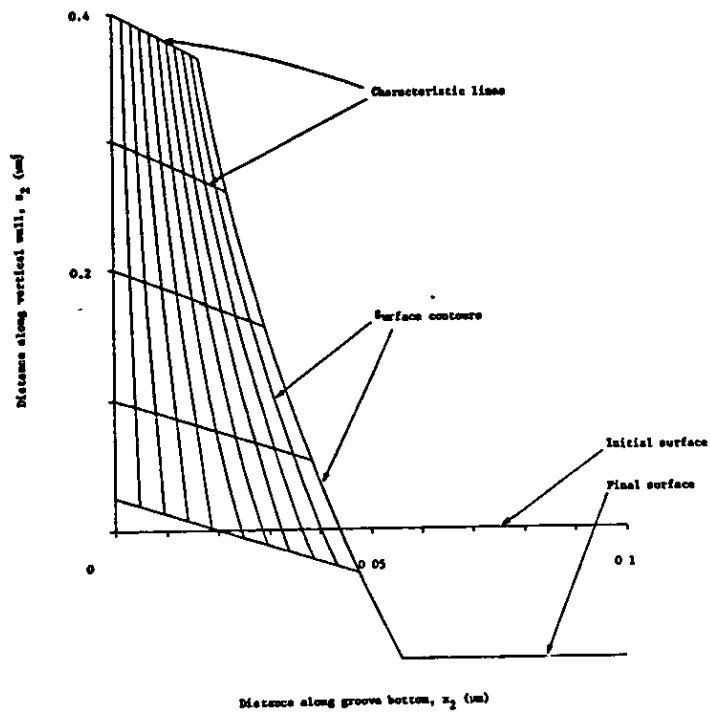
**c**



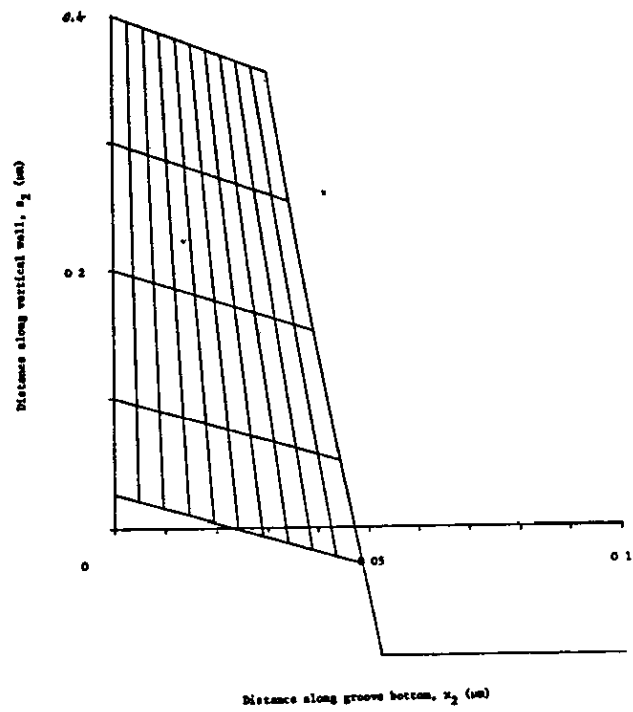
**d**

Fig. 3.32. Theoretically calculated redeposition profiles for rectangular grooves of different widths and for different depths of erosion using the cosine distribution for the sputtered particles. The depth of erosion corresponding to each surface contour is 10nm and the groove height is 0.4 $\mu$ m.

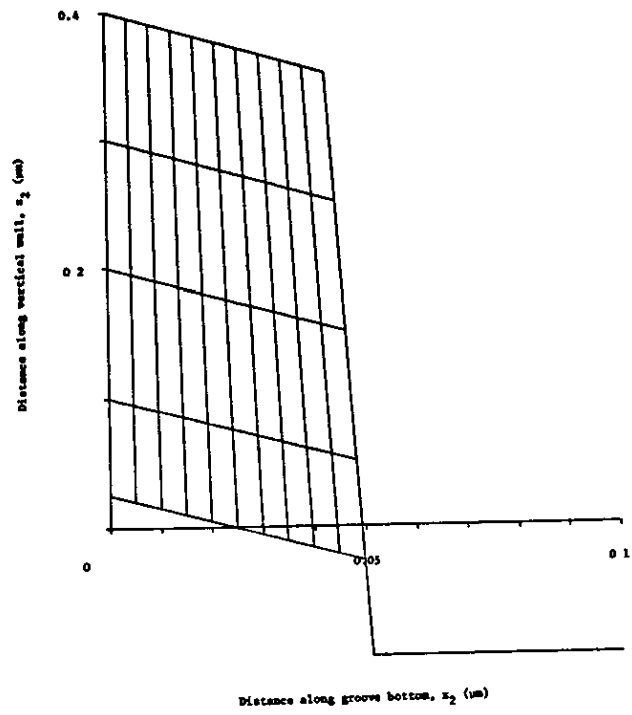
- (a) Groove width = 0.5 $\mu$ m
- (b) Groove width = 1.0 $\mu$ m
- (c) Groove width = 3.0 $\mu$ m
- (d) Groove width = 6.0 $\mu$ m.



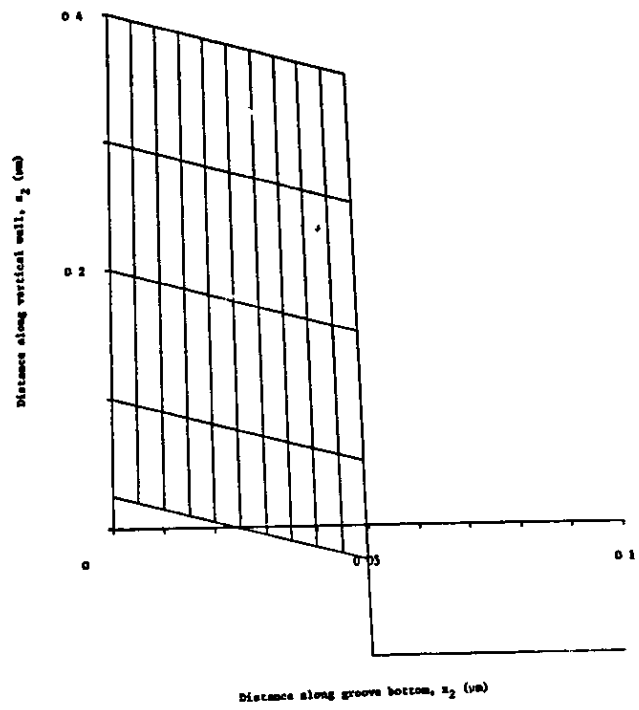
**a**



**b**



**C**

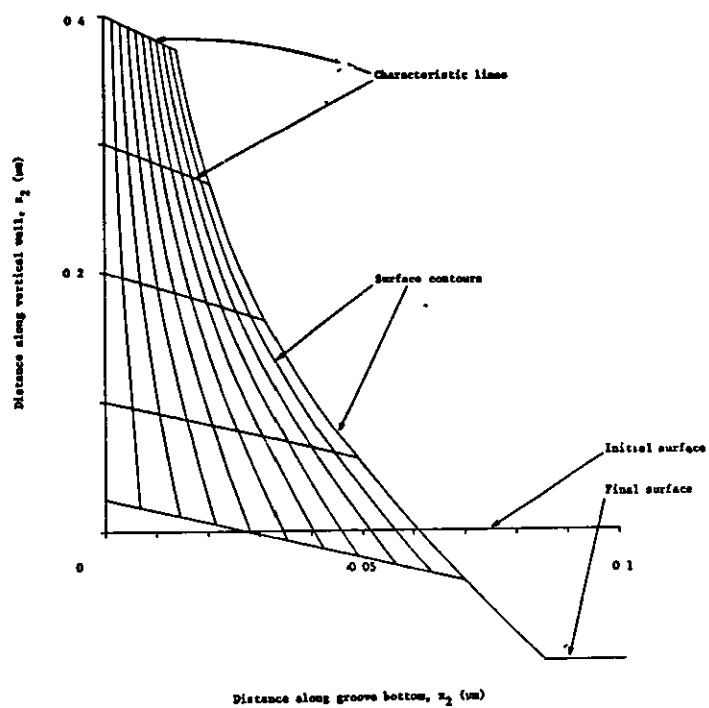


**D**

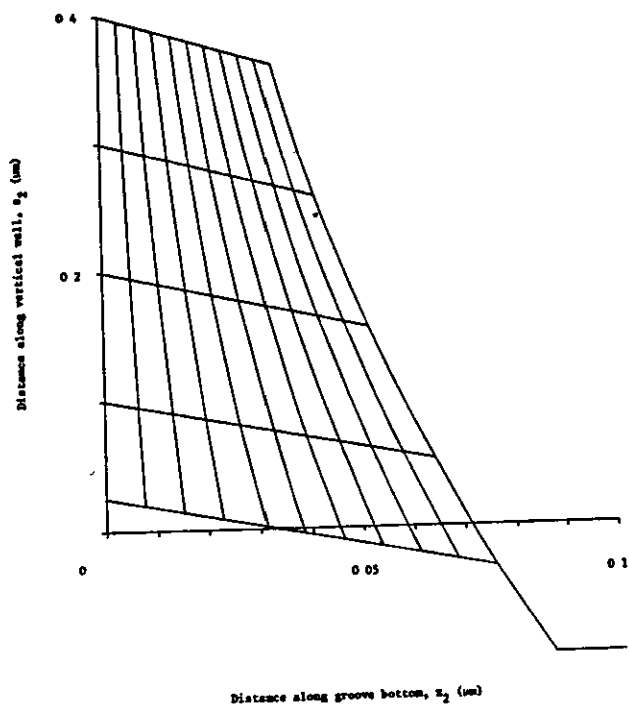


Fig. 3.33. Theoretically calculated redeposition profiles for rectangular grooves of different widths and for different depths of erosion using the under-cosine distribution for the sputtered particles. The depth of erosion corresponding to each surface contour is 10nm and the groove height is 0.4 $\mu$ m.

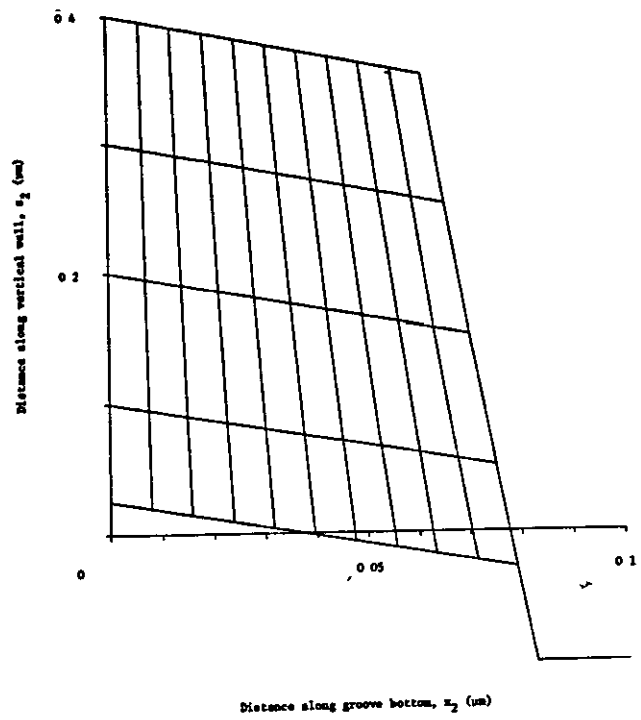
- (a) Groove width = 0.5 $\mu$ m
- (b) Groove width = 1.0 $\mu$ m
- (c) Groove width = 3.0 $\mu$ m
- (d) Groove width = 6.0 $\mu$ m.



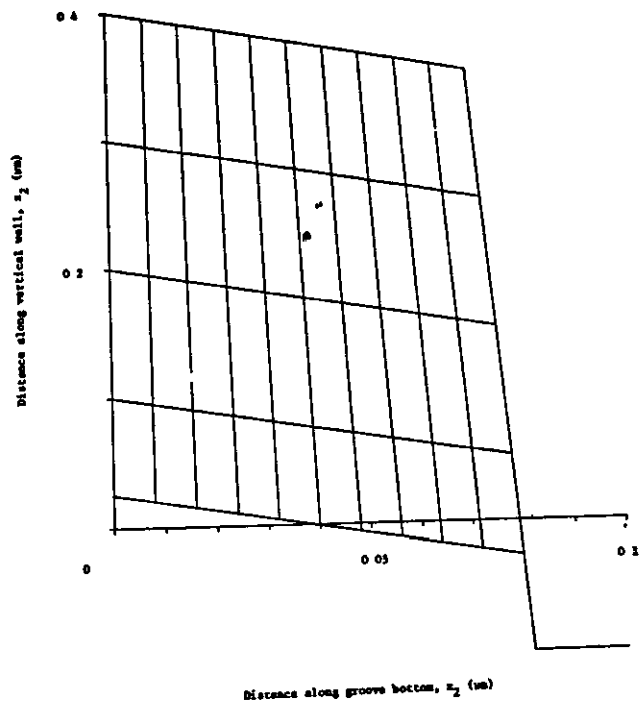
**a**



**b**



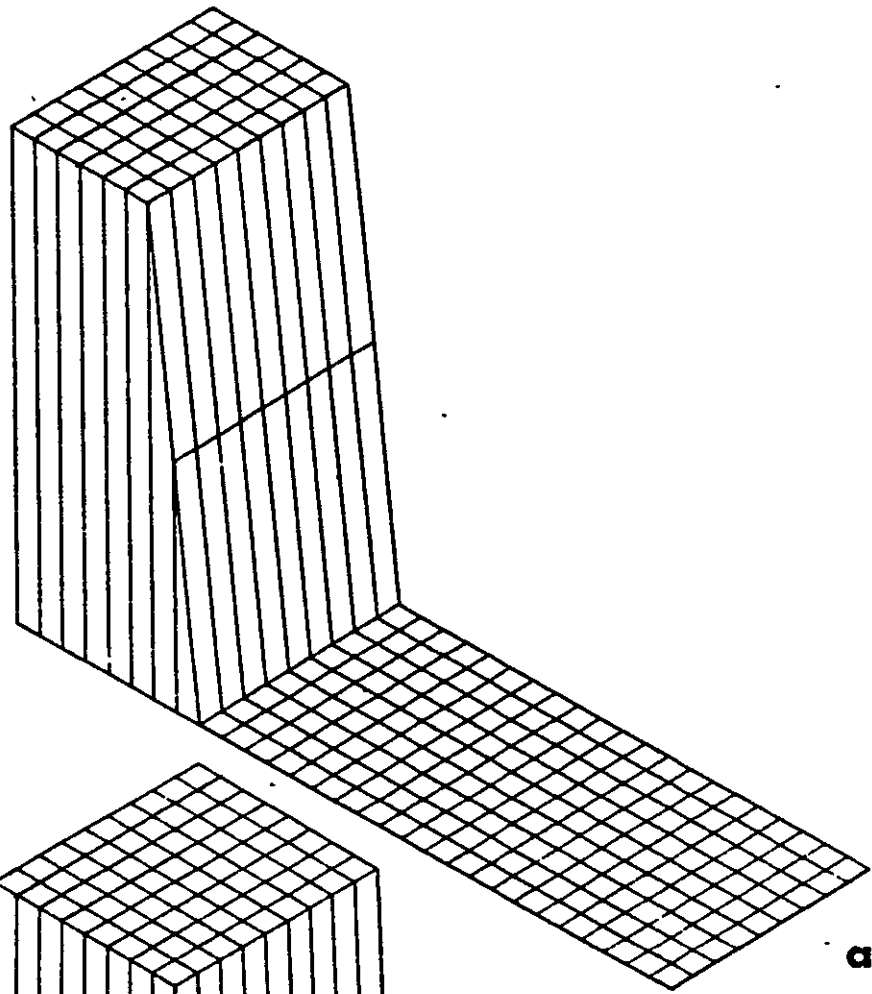
**c**



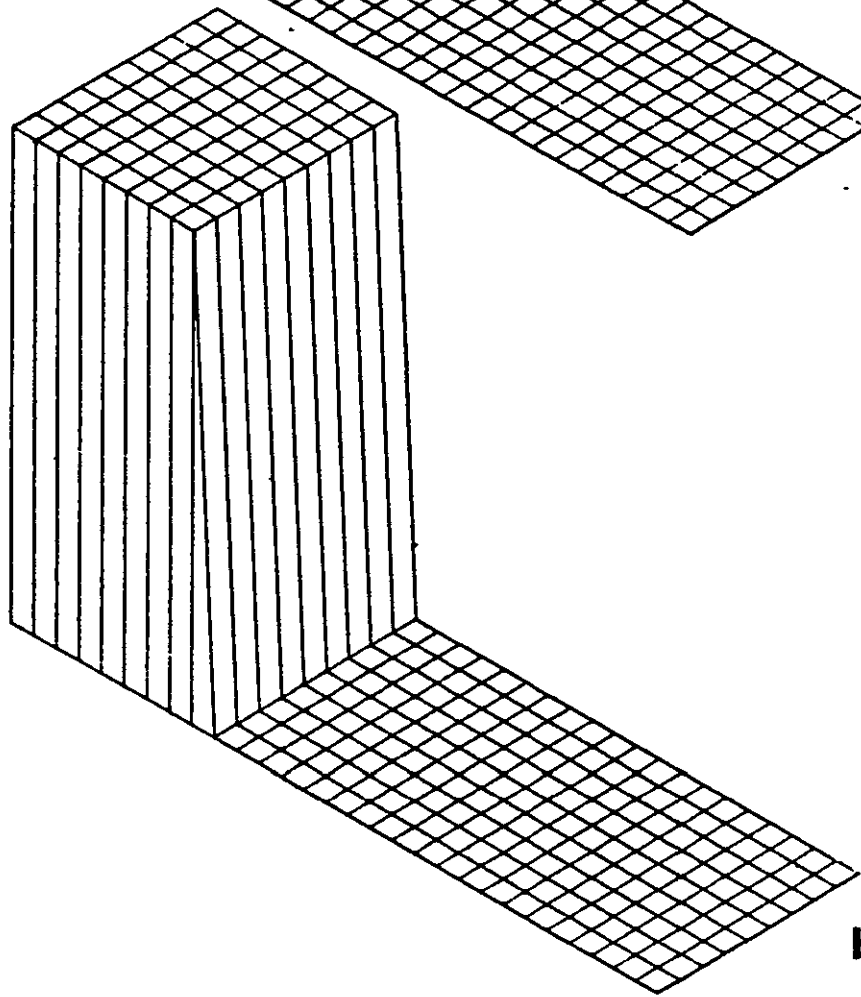
**d**

Fig. 3.34. Diagrams illustrating the build-up in three dimensions, for a rectangular groove, using an over-cosine distribution. The tenth surface contours of figs. 3.31(a) and (d) are shown.

- (a) Groove width =  $0.5\mu\text{m}$
- (b) Groove width =  $6.0\mu\text{m}$ .



**a**



**b**

Fig. 3.35. Diagrams illustrating the build-up in three dimensions, for a rectangular groove, using the cosine distribution. The tenth surface contour of figs. 3.32(a) and (d) are shown.

- (a) Groove width =  $0.5\mu\text{m}$
- (b) Groove width =  $6.0\mu\text{m}$ .

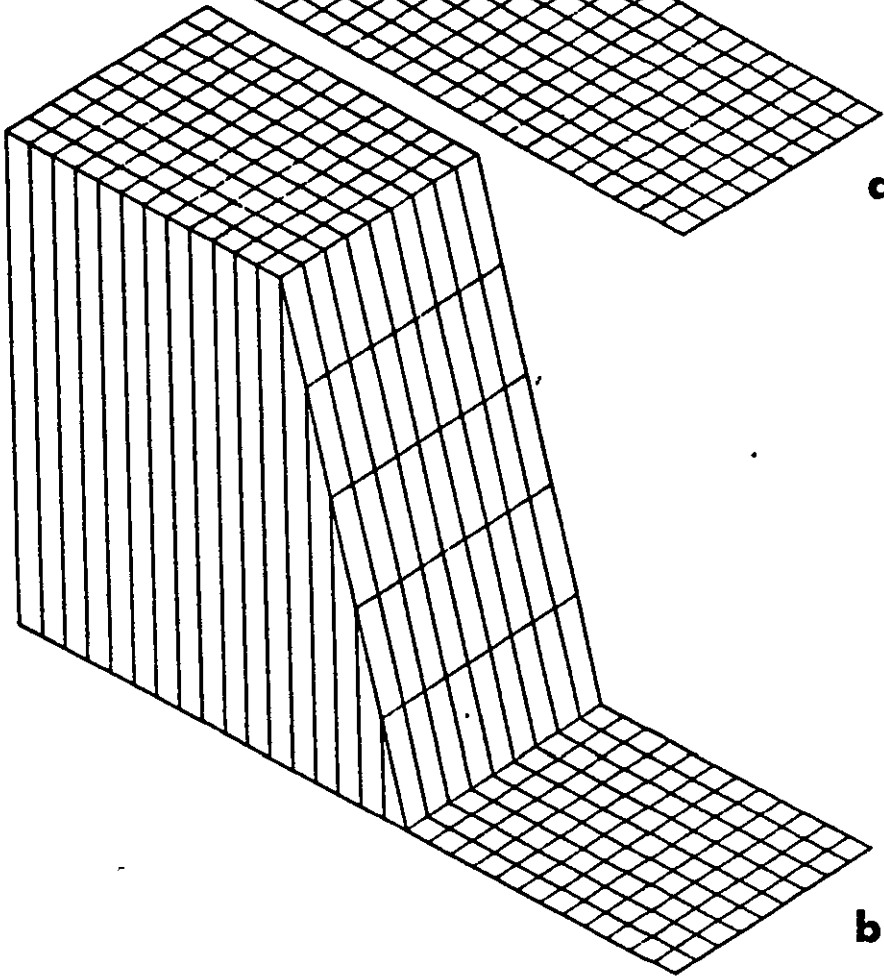
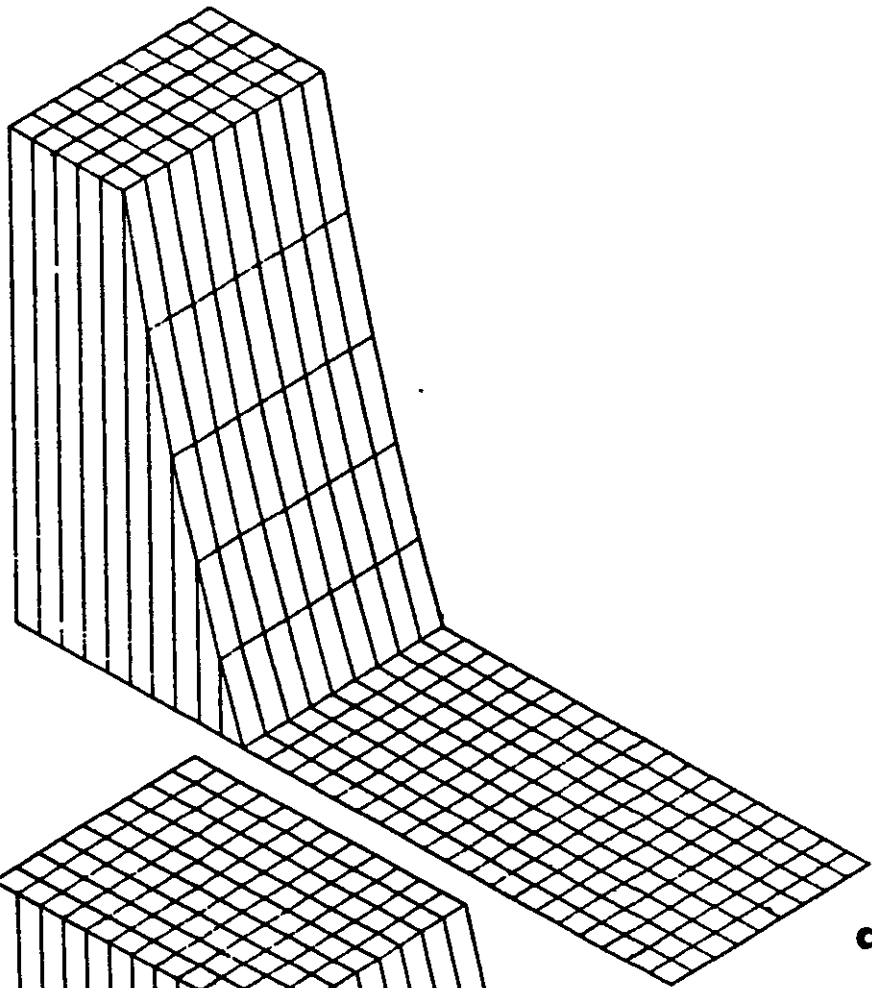


Fig.3.36. Diagrams illustrating the build-up in three dimensions, for a rectangular groove, using the under-cosine distribution. The tenth surface contour of figs. 3.33(a) and (d) are shown.

- (a) Groove width =  $0.5\mu\text{m}$
- (b) Groove width =  $6.0\mu\text{m}$ .



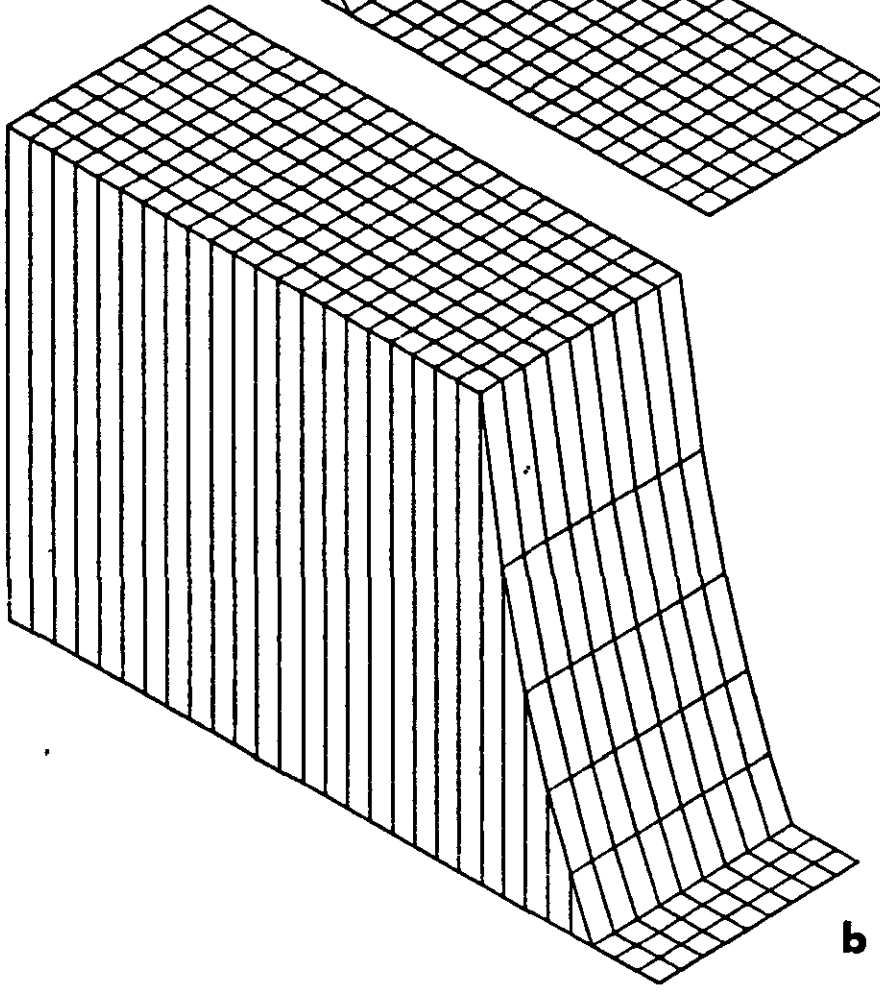
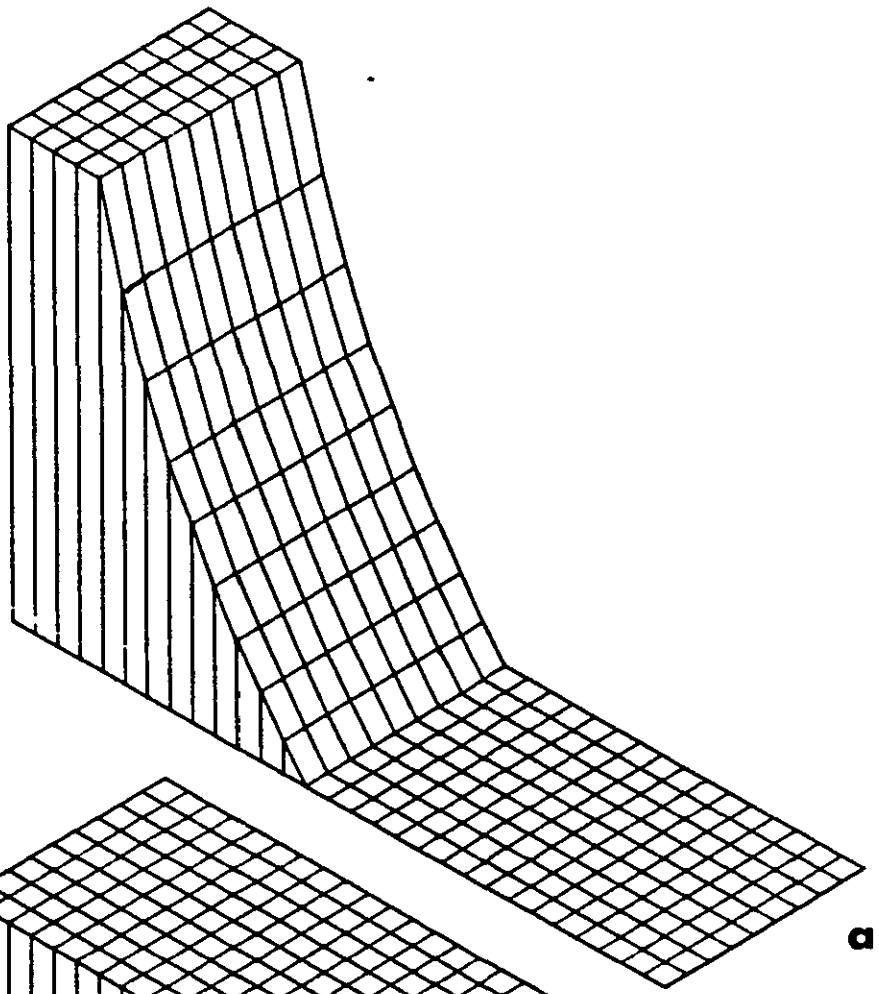


diagram are 0.5 and 6.0 $\mu$ m respectively. The diagrams show how the shape of the groove has changed due to redeposition for the different energy distributions. From these latter diagrams, it can be seen that for the same erosion time of the initial groove, the build-up increases and becomes more uniform with increasing groove width. For the same groove width but different distributions, the results show that redeposition increases with decreasing energy but consequently becomes less uniform.

### 3.6. Discussion.

A theoretical model has been presented which enables the geometrical changes due to redeposition to be predicted. The model can be used to calculate the build-up of redeposited material for any general two-dimensional surface. Its use has been illustrated using the rectangular groove geometry since this is important in many commercial devices. The model can also be used to find the redeposited build-up for different distributions of sputtered particles. The results show that the important parameter in defining the extent of the redeposited build-up is not, as is generally assumed, the aspect ratio of the groove. In fact the ratio of the groove width to the depth of ion etched material is more important. This is because the build-up of material at the bottom of the groove will be the same regardless of the groove height. However, it should be noted that ion reflection will become more important as the groove height increases and this will also affect the shape of the profile.

In general the build-up is more uniform for larger groove widths and this is illustrated in figures 3.28-3.30. In each figure the redeposited build-up has been calculated for groove widths of 0.5, 1.0,

3.0 and 6.0 $\mu\text{m}$ . The surface contours, although obtained after equal increments of erosion time, are not evenly spaced because as material is being redeposited, the groove width is continuously becoming smaller. Thus the area from which redeposition can occur is also becoming continuously smaller. This effect occurs in all the diagrams but is particularly noticeable in figure 3.33(a) where the initial groove width is 0.5 $\mu\text{m}$  and the final surface contour is obtained after etching through 0.1 $\mu\text{m}$  with a low energy distribution for the sputtered particles. The characteristic lines are shown on all the diagrams and they have been used in the construction of the surface contours. A characteristic line could not be drawn from the origin because the angles C and D, as defined in equation (3.29), become indeterminate at this point. Therefore a characteristic line was drawn near the origin and the final surface contour in each diagram has been extrapolated from this to the final horizontal surface.

The angle of inclination of the groove walls to the horizontal changes with the depth of material eroded. This angle,  $\delta$ , has been calculated for the last surface contour in each of the figures 3.28-3.33. The results are shown in Table 3.1. The results show that  $\delta$  tends to  $90^\circ$  for larger groove widths i.e. the build-up is more uniform for larger groove widths. Another important factor is the build-up at the bottom of the groove divided by the erosion depth. This ratio has been calculated for figures 3.28-3.33 and the results are presented in Table 3.1. The results show that this ratio is larger for smaller groove widths except for the low energy distribution where the maximum occurs around a groove width of 1.0 $\mu\text{m}$ .

TABLE 3.1. Table of data for the redeposited material using the different energy distributions.

$\delta$  = Angle between redeposited material and the horizontal

HIGH ENERGY DISTRIBUTION

Groove width	After erosion through 10nm				After erosion through 100nm			
	0.5 $\mu$ m	1.0 $\mu$ m	3.0 $\mu$ m	6.0 $\mu$ m	0.5 $\mu$ m	1.0 $\mu$ m	3.0 $\mu$ m	6.0 $\mu$ m
$\delta$	89.89 $^{\circ}$	89.98 $^{\circ}$	90.00 $^{\circ}$	90.00 $^{\circ}$	88.75 $^{\circ}$	89.73 $^{\circ}$	89.99 $^{\circ}$	90.00 $^{\circ}$
<u>Build-up at bottom</u> <u>Erosion time</u>	0.263	0.254	0.252	0.251	0.266	0.254	0.250	0.251

INTERMEDIATE ENERGY DISTRIBUTION

Groove width	After erosion through 10nm				After erosion through 100nm			
	0.5 $\mu$ m	1.0 $\mu$ m	3.0 $\mu$ m	6.0 $\mu$ m	0.5 $\mu$ m	1.0 $\mu$ m	3.0 $\mu$ m	6.0 $\mu$ m
$\delta$	89.59 $^{\circ}$	89.74 $^{\circ}$	89.91 $^{\circ}$	89.95 $^{\circ}$	86.06 $^{\circ}$	87.37 $^{\circ}$	89.04 $^{\circ}$	89.52 $^{\circ}$
<u>Build-up at bottom</u> <u>Erosion time</u>	0.513	0.500	0.502	0.505	0.558	0.522	0.509	0.503

TABLE 3.1 contd...

LOW ENERGY DISTRIBUTION

Groove width	After erosion through 10nm				After erosion through 100nm			
	0.5 $\mu$ m	1.0 $\mu$ m	3.0 $\mu$ m	6.0 $\mu$ m	0.5 $\mu$ m	1.0 $\mu$ m	3.0 $\mu$ m	6.0 $\mu$ m
$\delta$	89.29 $^{\circ}$	89.42 $^{\circ}$	89.74 $^{\circ}$	89.86 $^{\circ}$	83.73 $^{\circ}$	84.34 $^{\circ}$	87.41 $^{\circ}$	88.63 $^{\circ}$
<u>Build-up at bottom</u> Erosion time	0.794	0.826	0.809	0.808	0.853	0.873	0.826	0.816

In summary, the theoretical model presented here calculates the redeposited profiles taking into account for the first time the continuously changing geometry of the profile. The method can also account for different angular distributions of the sputtered particles due to different ion energies or different materials. The model does not currently include the effect of the simultaneous erosion of the redeposited material by ion etching or the effects of ion reflection. Nevertheless, the present theory should prove extremely valuable for defining the optimum conditions for developing well defined profiles on ion-etched surfaces.

CHAPTER 4TERTIARY EFFECTS4.1. Introduction.

When a surface is bombarded by an ion beam there are many mechanisms that contribute towards the formation of surface topography. Some of the mechanisms are sputtering yield versus angle of ion incidence effects, presence of impurities, redeposition of sputtered material, the effects of ion energy, the crystalline nature of the material, surface diffusion of atoms, volume diffusion and ion reflection. In the theoretical treatments to date it is assumed that, for an amorphous material, surface topography results only from a variation of sputtering yield with angle of ion incidence. This is not always the case and the effect of the presence of impurities on the depth resolution in composition-depth profiling has been dealt with (Makh et al (1981a)), the effects of redeposition (Makh et al (1980b)), the effects of ion energy (Makh et al (1981b)) and the effects of the crystalline nature of the material (Smith et al (1980),(1981)). However several authors have found substantial changes in the topography developed on polycrystalline iron as a function of the temperature of the iron. (Robinson and Southern (1968), Teodorescu and Vasiliu (1972), Vasiliu et al (1975)). These changes have been attributed to the greater influence of surface diffusion with increasing temperature. Thus in this chapter a theoretical model for surface diffusion and erosion of atoms on a surface will be developed. The effects of volume diffusion and ion reflection will be discussed qualitatively.

The effects of surface diffusion alone have been analysed by Mullins (1957), (1959), (1963) and Brailsford and Gjostein (1975). Mullins (1963) has shown that the effect of surface diffusion is to flatten bulges (convex surfaces) and fill out troughs (concave surfaces) so that an initially contoured surface would relax to a flat plane. The theory of Mullins will be outlined in section 4.2.1 and will be used as a starting point in developing a theoretical model for the surface diffusion and erosion of atoms on a surface. In the first study of the problem of surface diffusion and erosion, Carter (1976), derived differential equations describing the development of surface topography. Carter's analysis and its limitations will be presented in section 4.2.1.

The effects of volume diffusion have also been analysed by Mullins (1963) and by Collins and Carter (1981) and Carter et al (1981). Mullins (1963) derived expressions for the flux of material due to surface diffusion ( $J_s$ ) and volume diffusion ( $J_v$ ). The flux of material  $J_v$ , due to volume diffusion occurs at right angles to  $J_s$ . He assumed local equilibrium at the surface and free exchange of diffusing species between the volume and the surface. Mullins was able to derive equations to show how well defined shapes are modified due to the combined effects of surface and volume diffusion. This model will be outlined in section 4.3. Collins and Carter (1981) and Carter et al (1981) have considered the similar problem of volume diffusion/cascade mixing. In their model a semi-infinite solid of atomic species A has at a depth  $l$  a plane of impurity atoms B. Carter and colleagues have examined what happens when a flux density  $J$  of projectiles of any species, is directed at the surface of A. This model will be discussed in section 4.3. The work



of Anderson (1979), Hofer and Littmark (1979), Sigmund and Gras-Marti (1980) and Gras-Marti and Sigmund (1981) on recoil implantation and cascade mixing will also be discussed briefly in section 4.3.

The problem of ion reflection off steep profiles has received comparatively little attention. Bayly (1972) considered qualitatively the problem of ion reflection and showed how groove profiles can be modified. His treatment will be outlined in section 4.4. The spatial distribution of sputter-etch effects has been analysed theoretically under the assumption of random slowing-down of the bombarding ions (Sigmund (1973)). According to Sigmund, when a surface is bombarded at locally oblique incidence the most pronounced sputtering effect is likely to be observed not at the very point of impact, but further 'downstream'. This effect may cause a significant reduction of the local sputtering yield on top of a spike or a ridge, and an increase on the bottom of a groove or a crater. As a consequence, small irregularities on a relatively smooth surface may be enhanced during bombardment. Sigmund concluded that a microscopically flat surface is unstable under high-dose bombardment unless atom migration acts as a dominating smoothing effect. The model of Sigmund will also be outlined in section 4.4.

## 4.2. Development of surface topography due to surface diffusion and erosion.

### 4.2.1. Previous theories.

The first theory that will be outlined is one of pure surface diffusion and is due to Mullins (1957), (1959), (1963). The effects of the curvature of a surface on the chemical potential of the surface atoms

is given by the classical Gibbs-Thomson formula when the surface tension (or surface energy)  $\gamma$  is independent of orientation. A typical consequence is the dependence of the equilibrium vapour pressure of a liquid drop on its radius of curvature. Herring (1951) has generalised the formula to the case in which  $\gamma$  depends on orientation, as in a crystal, with no applied pressure. His result for the excess  $\mu$  of the chemical potential at a point P on a curved surface over and above that on a flat surface is

$$\mu(P) = \Omega \left[ \left( \gamma + \frac{d^2\gamma}{d\theta_1^2} \right) K_1 + \left( \gamma + \frac{d^2\gamma}{d\theta_2^2} \right) K_2 \right] \quad (4.1)$$

where all quantities are evaluated at the point P;  $K_1$  and  $K_2$  are the two principal curvatures of the surface at P ( $R_1$  and  $R_2$  are the corresponding radii of curvature),  $\theta_1$  is the angle between a general normal lying in the principal plane corresponding to  $K_1$  and the normal at P, and  $\theta_2$  is the corresponding quantity in the orthogonal principal plane corresponding to  $K_2$ .

If  $\gamma$  is isotropic, as in a liquid or an amorphous substrate, the angular derivatives are zero and equation (4.1) reduces to the classical Gibbs-Thomson formula, viz

$$\mu = \Omega \gamma (K_1 + K_2) = \Omega \gamma \left( \frac{1}{R_1} + \frac{1}{R_2} \right) \quad (4.2)$$

Mullins then considered a sinusoidal surface parallel to the z axis, whose cross-section is given by the equation

$$y = u(x,t) = a(t)\sin\omega x \quad (4.3)$$

where the amplitude,  $a(t)$ , depends on the time and satisfies the condition

$a\omega = 2\pi a/\lambda \ll 1$ , so that the slope referred to the mean surface is everywhere small. Using  $K = -\ddot{y}/(1+\dot{y}^2)^{3/2}$  and  $\left|\frac{du}{dx}\right| \ll \bar{\omega} \ll 1$  we obtain

$$\mu(x,t) = \Omega(\gamma+\gamma'')K = \Omega(\gamma_0+\gamma_0'')a(t)\omega^2 \sin\omega x \quad (4.4)$$

In this expression, the subscripts of  $\gamma$  and  $\gamma''$   $\left[ = \frac{d^2\gamma}{d\theta^2} \right]$  denote that they are to be evaluated at the orientation of the mean flat surface. This is justifiable because of the small slope approximation. Equation (4.4) shows that  $\mu$  depends on the position  $x$ ; there will be a tendency for material to move from positions of high  $\mu$  to those of low  $\mu$ . Thus, if  $\gamma_0 + \gamma_0'' > 0$ , material will move from the maximums to the minimums, causing the curve to decay. If  $\gamma_0 + \gamma_0'' < 0$ , material will move from the minimum to the maximums.

The transport mechanisms by which material may shift in response to the capillarity-induced differences of chemical potential are the same as those that can operate during sintering (Herring (1951)), namely transport by surface and volume diffusion, among others. In the case of surface diffusion, the flux of material moving along the surface is given in terms of the Einstein-Nernst relation (Mullins (1957)) for the drift velocity  $v$  by the expression

$$J_s = v \cdot v = - \frac{v D_s}{kT} \frac{\partial \mu}{\partial x} \quad (4.5)$$

where  $\frac{\partial}{\partial x}$  is used for the derivative along the surface because the slope is small, and where  $v$  is the number of atoms per square centimeter of surface participating in the diffusion. Substituting equation (4.4) into (4.5) gives

$$J_s = - \frac{v D_s \Omega}{kT} (\gamma_o + \gamma_o'') a \omega^3 \cos \omega x \quad (4.6)$$

This result is valid within the small slope approximation. The rate of motion of an element of profile, for surface diffusion alone, is given by the equation

$$\frac{\partial u}{\partial t} = - \Omega \frac{\partial J_s}{\partial x} \quad (4.7)$$

where again  $\frac{\partial}{\partial x}$  is used for the derivative along the surface. Substituting equations (4.3) and (4.6) into (4.7) gives

$$\frac{da}{dt} = - \left[ \frac{v D_s \Omega^2}{kT} (\gamma_o + \gamma_o'') \omega^4 \right] a(t)$$

Integrating the above equation to find  $a(t)$  and substituting back into equation (4.3), the final solution for the description of the sine wave is obtained as

$$y = u(x,t) = a_o \exp[-B\omega^4 t] \sin \omega x \quad (4.8)$$

where  $B = v D_s \Omega^2 (\gamma_o + \gamma_o'') / kT$ . Equation (4.8) shows an exponential growth or decay of the sine wave depending respectively on whether  $\gamma_o + \gamma_o''$  is negative or positive, the latter being the usual case. Thus the effects of surface diffusion alone is to flatten bulges on a surface and fill out troughs. The equations derived above can be easily modified to include the effects of volume diffusion and this will be done in a later section.

Carter (1976) was the first to study the simultaneous surface diffusion and erosion of an amorphous substrate. In this study equation (4.2) was re-written as

$$\mu = \Omega\gamma \left( \frac{1}{R_1} + \frac{1}{R_2} \right) = \frac{\Omega\gamma}{R} \quad (4.9)$$

where  $R$  refers to the radius of curvature of an element of the surface contour in the  $x$ - $y$  plane. Gradients of chemical potential along the surface will therefore be associated with gradients of curvature. Such gradients will produce a drift of surface atoms with an average velocity given by the Nernst-Einstein relation

$$v = - \frac{D}{kT} \frac{\partial \mu}{\partial z} = - \frac{D\gamma\Omega}{kT} \frac{\partial K}{\partial z}$$

where  $D$  is the coefficient of surface diffusion and  $z$  the arc length along the profile. The surface current  $J$  of atoms is the product of  $v$  by the number of atoms per unit area  $N_0$ .

$$J = - \frac{D\gamma\Omega N_0}{kT} \frac{\partial K}{\partial z} = - \frac{D\gamma\Omega N_0}{kT} \frac{\partial}{\partial z} \left( \frac{1}{R} \right)$$

If the divergence of  $J$  is taken, the increase in the number of atoms per unit area per unit time is obtained. This can be converted to the speed of movement  $r_n$  of the surface element along its normal by multiplying by  $\Omega$ . Thus

$$r_n = \frac{\partial n}{\partial t} = -\Omega \frac{\partial J}{\partial z} = \frac{D\gamma\Omega^2 N_0}{kT} \frac{\partial^2 K}{\partial z^2} \quad (4.10)$$

The sign  $\frac{\partial n}{\partial t}$  in equation (4.10) thus depends on the second derivative of  $K$  with respect to  $z$ . It is conventional to assign the local radius of curvature  $R$  between a solid and vacuum as a positive quantity towards the  $x$  axis for a convex bulge on a solid and a negative quantity for a concave trough (Mullins (1957)). If an ion beam is incident along the

negative y axis,  $\theta$  is the angle between the ion beam and the normal to the surface at a given point. Then with this convention  $R = -\frac{dz}{d\theta}$  and equation (4.10) can be rewritten as

$$\left(\frac{\partial n}{\partial t}\right)_{\text{Diffusion}} = -\frac{D\gamma N_o \Omega^2}{kT} \frac{\partial^3 \theta}{\partial z^3} \quad (4.11)$$

It has already been shown (see chapter 1) that the rate of erosion by sputtering, for both convex bulges and concave troughs, of a surface element along the normal direction is given by

$$\left(\frac{\partial n}{\partial t}\right)_{\text{Sputtering}} = -\frac{\phi}{N} S(\theta) \cos\theta \quad (4.12)$$

where  $\phi$  is ion beam flux and  $N$  the solid atomic density. Thus, if sputtering and surface diffusion are uncorrelated processes the total rate of erosion in the normal direction can be written as the sum of the contributions of equations (4.11) and (4.12). Thus

$$\left(\frac{\partial n}{\partial t}\right) = -\left[\frac{D\gamma N_o \Omega^2}{kT} \frac{\partial^3 \theta}{\partial z^3} + \frac{\phi}{N} S(\theta) \cos\theta\right] \quad (4.13)$$

Carter then went on to define, from equation (4.13), an effective sputtering coefficient  $S_e$ , which accommodates the effects of both ion erosion and surface diffusion. He thus defined

$$\frac{\phi}{N} S_e \cos\theta = \frac{\phi}{N} S(\theta) \cos\theta + \frac{DN_o \Omega^2 \gamma}{kT} \frac{\partial^3 \theta}{\partial z^3}$$

or

$$S_e = S(\theta) + \frac{N}{\phi} \frac{DN_o \Omega^2 \gamma}{kT \cos\theta} \frac{\partial^3 \theta}{\partial z^3} \quad (4.14)$$

Thus the differential equation to be solved is

$$\frac{\partial n}{\partial t} = - \frac{\phi}{N} S_e(\theta, z) \cos \theta \quad (4.15)$$

Carter (1976) solved equation (4.15) using the differential erosion theory derived earlier (Nobes et al (1969), Carter et al (1971), (1973)). In solving equation (4.15) the assumption that  $S_e$  is a function of  $\theta$  only, was made. However from equation (4.14) it can be seen that  $S_e$  is a function of  $\theta$  and  $z$  i.e.  $S_e = S_e(\theta, z)$ . Carter went on to derive differential equations describing how points move in x-y space with respect to time with the above assumption. An equation was also derived relating the radius of curvature to time from which the time required for edges to form could be deduced.

In the next section a theoretical model will be presented which incorporates surface diffusion and erosion. The starting point is the same as that used by Carter (1976) i.e. equation (4.13). However the method of solution is different. The solution enables numerical calculations to be performed for well defined small angle contours. The method is illustrated by examining how a Gaussian profile is modified due to surface diffusion and erosion.

#### 4.2.2. A new theoretical model.

As pointed out in section 4.2.1, the starting point is equation (4.13) viz.

$$\frac{\partial n}{\partial t} = - \left[ \frac{D \gamma N_o \Omega^2}{kT} \frac{\partial^3 \theta}{\partial z^3} + \frac{\phi}{N} S(\theta) \cos \theta \right]$$

Re-write this equation in terms of  $c$  the curvature where  $\frac{d\theta}{dz} = -\frac{1}{R} = -c$ .

Therefore the above equation becomes

$$\frac{\partial n}{\partial t} = \frac{D\gamma N_o \Omega^2}{kT} \frac{\partial^2 c}{\partial z^2} - \frac{\phi}{N} S(\theta) \cos \theta \quad (4.16)$$

where  $z$  is the arc length,  $c$  the curvature and the other symbols have the same meaning as before. Using the Frenet-Serret formula (Wardle (1965)) gives

$$\frac{\partial n}{\partial z} = -\frac{1}{R} b \quad (4.17)$$

Differentiate (4.16) with respect to  $z$

$$\therefore \frac{\partial}{\partial z} \left( \frac{\partial n}{\partial t} \right) = \frac{D\gamma N_o \Omega^2}{kT} \frac{\partial^3 c}{\partial z^3} - \frac{\phi}{N} \left\{ S'(\theta) \cos \theta - S(\theta) \sin \theta \right\} \frac{\partial \theta}{\partial z}$$

$$\text{but} \quad \frac{\partial}{\partial z} \left( \frac{\partial n}{\partial t} \right) = \frac{\partial}{\partial t} \left( \frac{\partial n}{\partial z} \right) = \frac{\partial}{\partial t} \left( -\frac{1}{R} \right)$$

Thus the above differential equation becomes

$$\frac{\partial c}{\partial t} = - \left[ \frac{D\gamma N_o \Omega^2}{kT} \frac{\partial^3 c}{\partial z^3} + \frac{\phi}{N} \left\{ S'(\theta) \cos \theta - S(\theta) \sin \theta \right\} c \right]$$

or

$$\frac{\partial c}{\partial t} = - S_1 \frac{\partial^3 c}{\partial z^3} - S_2 c \quad (4.18)$$

$$\text{where} \quad S_1 = D\gamma N_o \Omega^2 / kT \quad \text{and} \quad S_2 = \frac{\phi}{N} \left\{ S'(\theta) \cos \theta - S(\theta) \sin \theta \right\}$$

The approach used to solve parabolic differential equations by a numerical method is to replace the partial derivatives by finite



difference approximations. One of the most simple techniques used is the Explicit Method (Gerald (1970)). This uses central difference approximations for the derivatives and solves by a "marching" process in time. For example for  $n$  odd we have

$$f^{(n)}(x)|_{x=x_0} = \frac{\Delta^n f_{(-n+1)/2} + \Delta^n f_{(-n-1)/2}}{2h^n} + O(h^2)$$

which is the  $n$ th derivative evaluated at the point  $x = x_0$  and the fixed step length is  $h$ , see fig.4.1. Therefore

$$f^{(3)}(x)|_{x=x_0} = \frac{\partial^3}{\partial x^3} = \frac{\Delta^3 f_{-1} + \Delta^3 f_{-2}}{2h^3} + O(h^2) \quad (4.19)$$

From figure 4.1

$$\Delta f_1 = f_2 - f_1; \quad \Delta f_0 = f_1 - f_0; \quad \Delta f_{-1} = f_0 - f_{-1}; \quad \Delta f_{-2} = f_{-1} - f_{-2};$$

Therefore

$$\Delta^3 f_{-1} = \Delta^2(\Delta f_{-1}) = \Delta^2(f_0 - f_{-1}) = \Delta(\Delta f_0 - \Delta f_{-1})$$

Thus it can be shown that

$$\Delta^3 f_{-1} = f_2 - 3f_1 + 3f_0 - f_{-1}$$

and similarly

$$\Delta^3 f_{-2} = f_1 - 3f_0 + 3f_{-1} - f_{-2}$$

Substituting for  $\Delta^3 f_{-1}$  and  $\Delta^3 f_{-2}$  in equation (4.19) gives

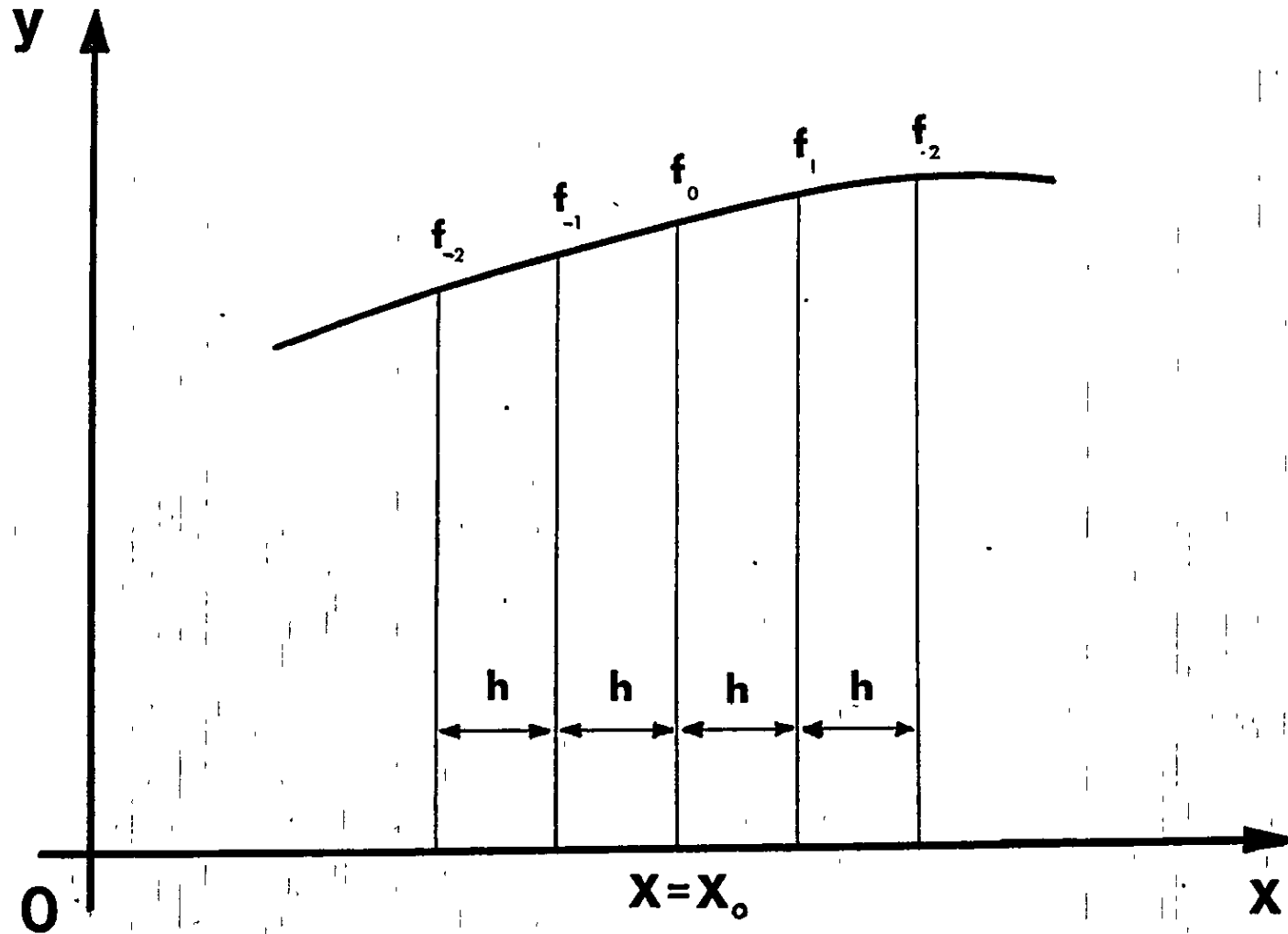


Fig.4.1. Schematic diagram for calculating the third differential.

$$f^{(3)}(x) = \frac{f_2 - 2f_1 + 2f_{-1} - f_{-2}}{2h^3} + O(h^2)$$

Now let

$$h \equiv \Delta z; \text{ and } f_2 = c_{i+2}^j; f_1 = c_{i+1}^j; f_{-1} = c_{i-1}^j; f_{-2} = c_{i-2}^j;$$

Here the subscripts are used to denote position and superscripts time. Therefore

$$\frac{\partial^3 c}{\partial z^3} = \frac{c_{i+2}^j - 2c_{i+1}^j + 2c_{i-1}^j - c_{i-2}^j}{2(\Delta z)^3} + O(\Delta z^2) \quad (4.20)$$

In a similar way approximate  $\frac{\partial c}{\partial t}$  by a forward difference approximation.

Thus

$$\frac{\partial c}{\partial t} = \frac{c_i^{j+1} - c_i^j}{\Delta t} \quad (4.21)$$

Therefore equation (4.18) becomes

$$\frac{c_i^{j+1} - c_i^j}{\Delta t} = - \left[ \frac{S_1 (c_{i+2}^j - 2c_{i+1}^j + 2c_{i-1}^j - c_{i-2}^j)}{2(\Delta z)^3} + S_2 c_i^j \right]$$

or

$$c_i^{j+1} = (1 - S_2 \Delta t) c_i^j - \frac{S_1 \Delta t}{2(\Delta z)^3} \left\{ c_{i+2}^j - 2c_{i+1}^j + 2c_{i-1}^j - c_{i-2}^j \right\} \quad (4.22)$$

Equation (4.22) describes how to calculate the curvature at an arbitrary point on a profile which has been modified by sputtering and surface diffusion. In the next section it will be shown how the coordinates on the new profile can be calculated.

#### 4.2.3. Computer simulation.

To illustrate the effects of equation (4.18) on the development of surface shape, a Gaussian profile ( $y = e^{-0.01 x^2}$ ) was chosen which would be subsequently modified by surface diffusion and erosion. The first step is to calculate the arc length AB in figure 4.2, by solving the differential equation

$$\frac{dz}{dx} = \sqrt{1 + \left(\frac{dy}{dx}\right)^2} \quad (4.23)$$

Having worked out the arc length AB, a constant increment  $\Delta z$  along the profile is defined viz  $\Delta z = \frac{\text{length AB}}{N}$  where  $(N+1)$  is the number of points along the profile. Starting from the point A, increment  $\Delta z$  along the profile and then calculate the  $x$  coordinate corresponding to this increment by solving the differential equation

$$\frac{dx}{dz} = \frac{1}{\sqrt{1 + \left(\frac{dy}{dx}\right)^2}} \quad (4.24)$$

Increment  $\Delta z$  again and calculate the  $x$ -coordinate of the next point and so on for all  $(N+1)$  points. At each of these points the curvature is calculated. For the initial Gaussian profile the curvature is given simply by

$$c = -\frac{d^2y}{dx^2} / \left\{1 + \left(\frac{dy}{dx}\right)^2\right\}^{3/2}$$

Then at each point the angle  $\theta$  between the ion beam (incident along the negative  $y$ -axis) and the normal at each point is calculated by solving the differential equation

$$\frac{d\theta}{dz} = -c \quad (4.25)$$

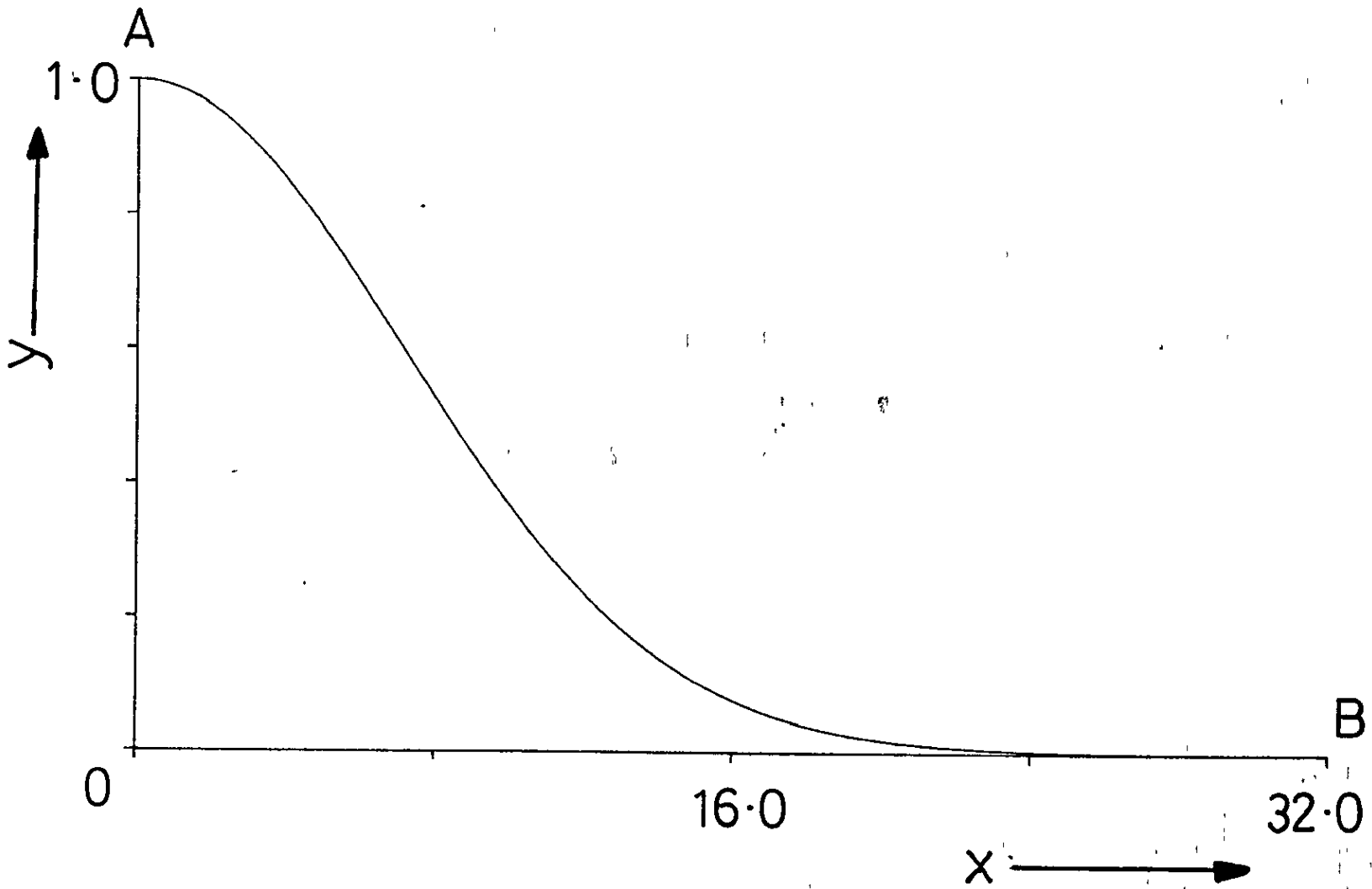


Fig.4.2. The Gaussian profile used to model the development of surface shape. ( $y = e^{-0.01x^2}$ ).

The solution is commenced at the point A as before. Knowing  $\theta$  at all the points, the x and y coordinates of the (N+1) points can be calculated by solving the following differential equations

$$\frac{dx}{dz} = \cos\theta \quad (4.26)$$

$$\frac{dy}{dz} = \sin\theta \quad (4.27)$$

Having carried out the above procedure for the initial profile i.e. at  $t = 0$ , the next step is to calculate a new profile, obtained from the previous one by surface diffusion and erosion of atoms, after a time  $\Delta t$ . This is done by solving the diffusion-erosion equation, (equation (4.22)) and calculating the curvatures on the new profile at the (N+1) points. Knowing the curvatures, equation (4.25) is solved to find  $\theta$  at the (N+1) points and then equations (4.26) and (4.27) are solved to find the x and y coordinates. This procedure is carried out iteratively for the length of time required. It should be noted that although  $\theta$  is zero at A for  $t = 0$  it does not necessarily remain so when diffusion and erosion are modifying the profile.

#### 4.2.4. Results.

The theory presented in the previous sections is a linearised theory of surface diffusion and erosion. Thus the theory is valid for small angles  $\theta$  (the angle between the ion beam and the surface normal) and cannot be used to describe the formation of edges and cones which is a non linear effect. The relative magnitudes of the erosion and diffusion process can be evaluated by comparing the values of  $S_1$  and  $S_2$  in equation (4.18), that is

$$S_2 = \frac{\phi}{N} \left[ S'(\theta) \cos \theta - S(\theta) \sin \theta \right]$$

and

$$S_1 = D\gamma N_0 \Omega^2 / kT$$

The equation for  $S_2$  can be re-written

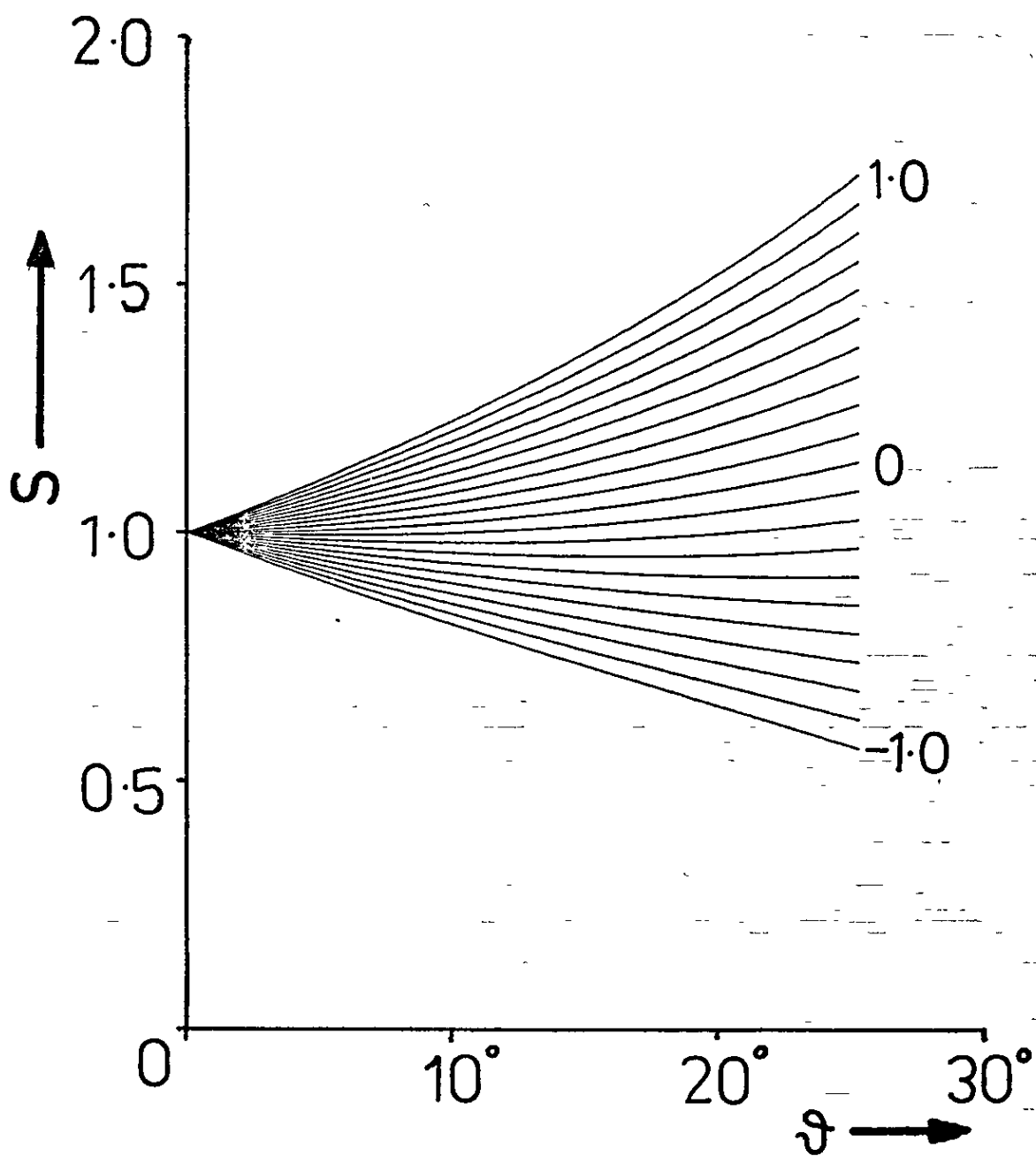
$$\frac{d}{d\theta} \left[ S(\theta) \cos \theta \right] = \frac{NS_2}{\phi} = \alpha$$

i.e. 
$$S(\theta) = \beta \left( \frac{\alpha}{\beta} \theta + 1 \right) \sec \theta \quad (4.28)$$

where  $\alpha$  and  $\beta$  are constants. Figure 4.3 shows the modified sputtering yield as a function of  $\theta$  (small values only) for different values of  $\alpha$  (i.e.  $S_2$ ). The value of  $S_1$  has been evaluated by Mullins (1957) for a metal near its melting point. The following values are for Ag near its melting point:  $D = 10^{-3} \text{ cm}^2 \cdot \text{sec}^{-1}$ ;  $\gamma = 10^3 \text{ dynes} \cdot \text{cm}^{-1}$ ;  $N_0 = 1.5 \times 10^{15} \text{ cm}^{-2}$ ;  $\Omega = 1.7 \times 10^{-23} \text{ cm}^3$  and  $kT = 10^{-13} \text{ ergs}$  ( $T = 452^\circ \text{C}$ ). With these values  $S_1 = 4.34 \times 10^{-18} \text{ cm}^4 \cdot \text{sec}^{-1}$ . It should be noted that  $S_1$  as evaluated by Mullins is for the case of pure surface diffusion only. In the present case of sputtering and diffusion modifying a profile, the sputtering might enhance the surface diffusion by collisional effects. However, it is expected that the value of  $S_1$  will still be relatively small.

Thus the important parameter in the computer simulations to be presented is the ratio  $S_2/S_1$ . This ratio has been chosen in order to make the diffusion effects large. The following range of values for  $S_2/S_1$  has been used:-  $S_2 = 1.0$ ;  $S_2/S_1 = 10^{-2}, 10^{-1}, 1, \infty$ ;  $S_2 = 0.5$ ;  $S_2/S_1 = 5 \times 10^{-3}, 5 \times 10^{-2}, 5 \times 10^{-1}, \infty$ . The case of  $S_2/S_1 = \infty$  corresponds to no diffusion i.e. the profile is modified by erosion only.

Fig.4.3. Modified sputtering yield curves for small values of  $\theta$ .





The way in which a Gaussian profile ( $y = e^{-0.01 x^2}$ ) is modified by surface diffusion and erosion for  $S_2/S_1 = 10^{-2}$ ,  $10^{-1}$  and 1 is shown in figure 4.4(a), (b) and (c) respectively. The same profile modified by surface diffusion and erosion for  $S_2/S_1 = 5 \times 10^{-3}$ ,  $5 \times 10^{-2}$   $5 \times 10^{-1}$  is shown in figure 4.5(a), (b) and (c) respectively. Finally in figure 4.6 the Gaussian profile is shown modified by erosion only ( $S_2/S_1 = \infty$ ) for  $S_2 = 1.0$  (figure 4.6(a)) and  $S_2 = 0.5$  (figure 4.6(b)). By comparing the profiles obtained by pure erosion only (figure 4.6) with these obtained by surface diffusion and erosion, (figures 4.4 and 4.5), it can be seen that the effect of surface diffusion is to flatten the profile. This result is to be expected as Mullins (1963) has shown that the effect of surface diffusion alone is to flatten bulges and fill out troughs.

#### 4.3. Volume diffusion/mixing.

As temperature is increased, surface and volume diffusion processes occur at an increasing rate, (Mullins (1959)), and are the result of both atomic and defect migration. Since bombardment can produce defects, diffusion can be radiation enhanced in addition to thermally stimulated. In this section we are interested in the near surface effects of diffusion, particularly in any resultant effects on surface topography and we are therefore interested in diffusion controlled atomic or defect fluxes which can lead to local material accretion or removal.

In section 4.2.1 it was shown how a sinusoidal profile,  $y = u(x,t) = a(t)\sin\omega x$ , is modified due to the effects of surface diffusion alone (Mullins (1963)). An expression was derived for the flux of material

Fig.4.4. The initial Gaussian profile and the subsequent development in surface shape when modified by surface diffusion and erosion for  $S_2 = 1.0$  (a)  $S_2/S_1 = 10^{-2}$  (b)  $S_2/S_1 = 10^{-1}$  (c)  $S_2/S_1 = 1.0$ . Each profile corresponds to the development of surface shape after a time  $\Delta t = 1.0 \times 10^{-2}$ .

Fig.4.4(a)

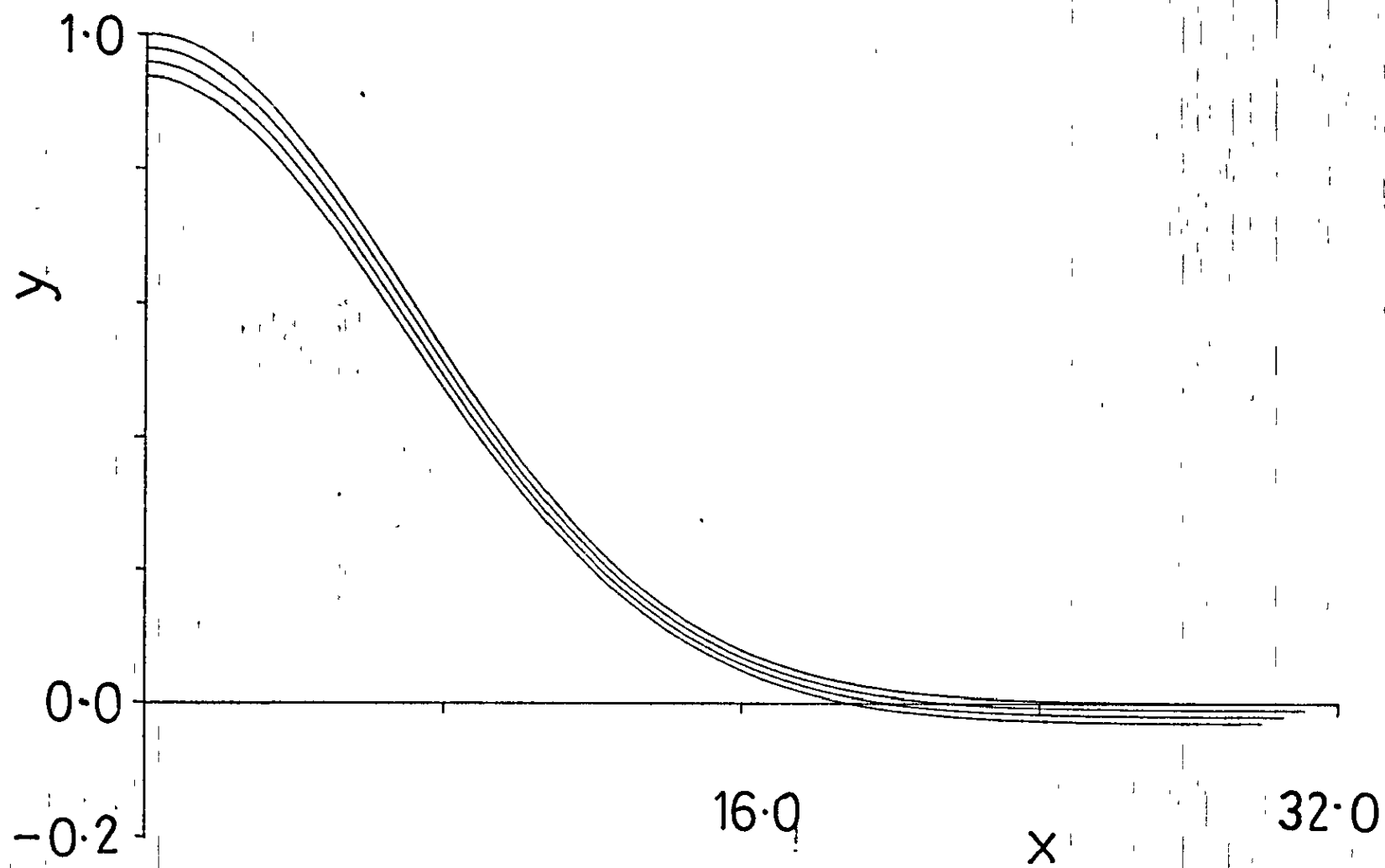


Fig.4.4(b)

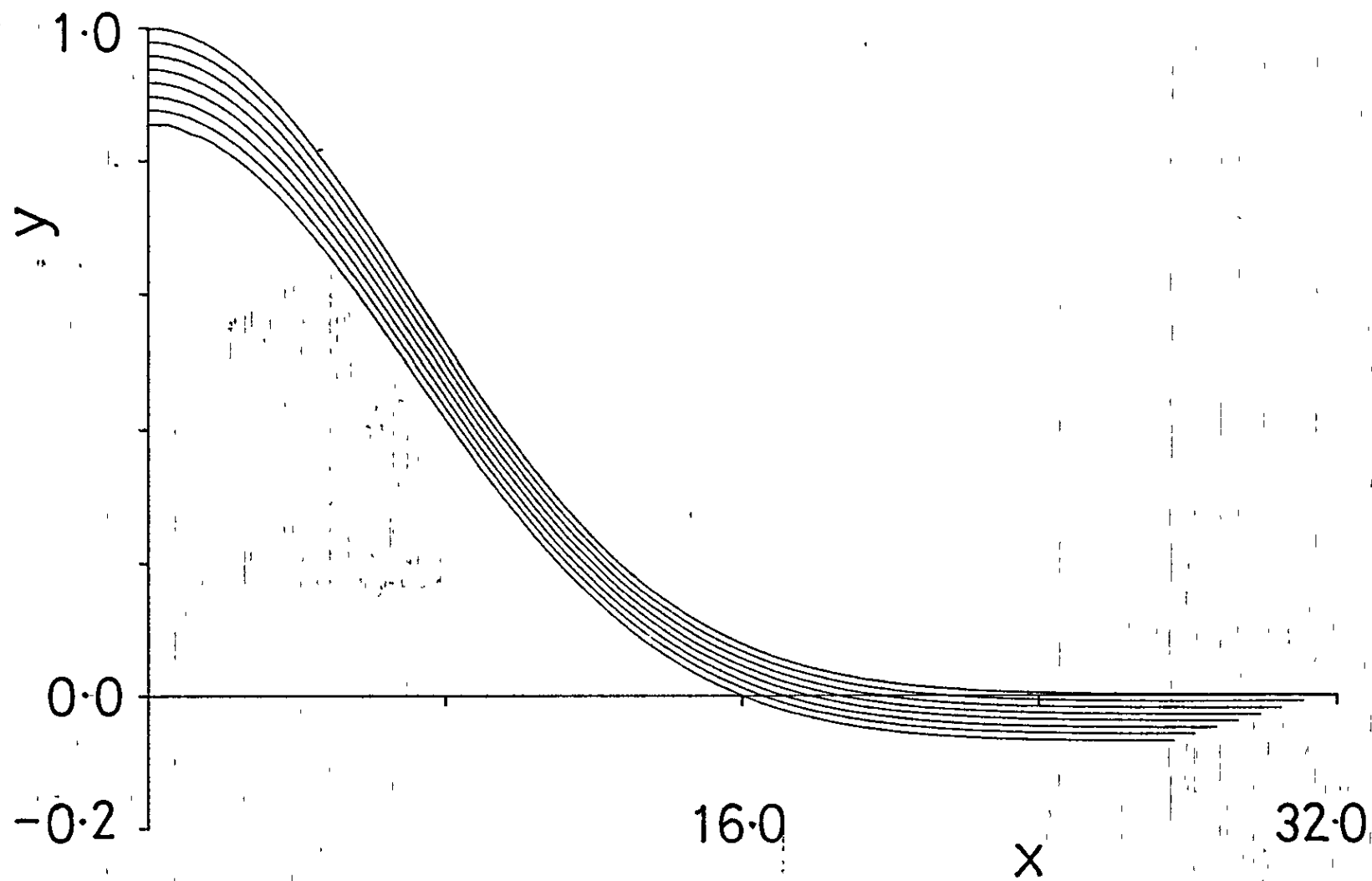


Fig.4.4(c)

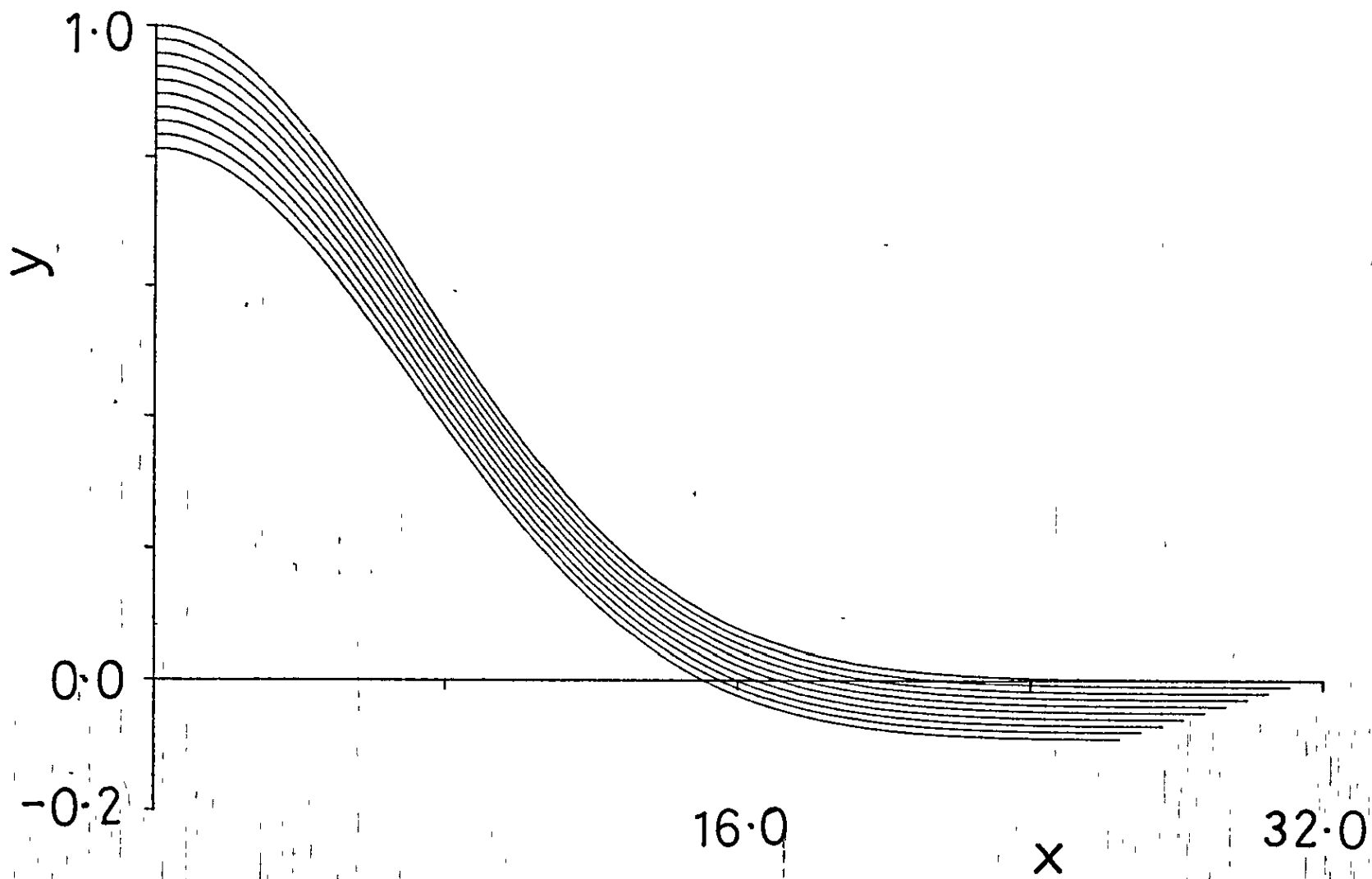


Fig.4.5. The initial Gaussian profile and the subsequent development in surface shape when modified by surface diffusion and erosion for  $S_2 = 0.5$  (a)  $S_2/S_1 = 5.0 \times 10^{-3}$  (b)  $S_2/S_1 = 5.0 \times 10^{-2}$  (c)  $S_2/S_1 = 5.0 \times 10^{-1}$ . Each profile corresponds to the development of surface shape after a time  $\Delta t = 1.0 \times 10^{-2}$ .

4.5(a)

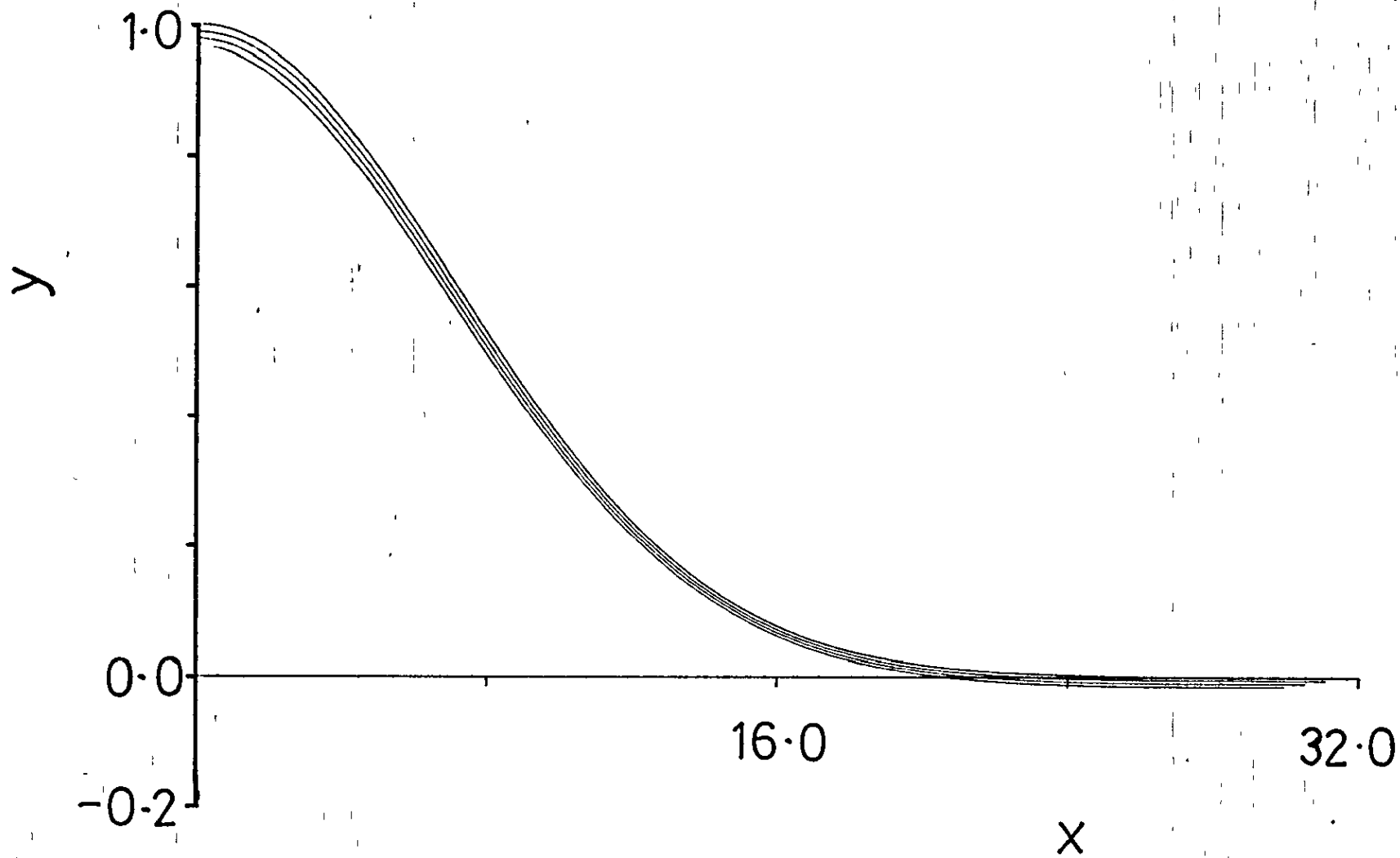


Fig.4.5(b)

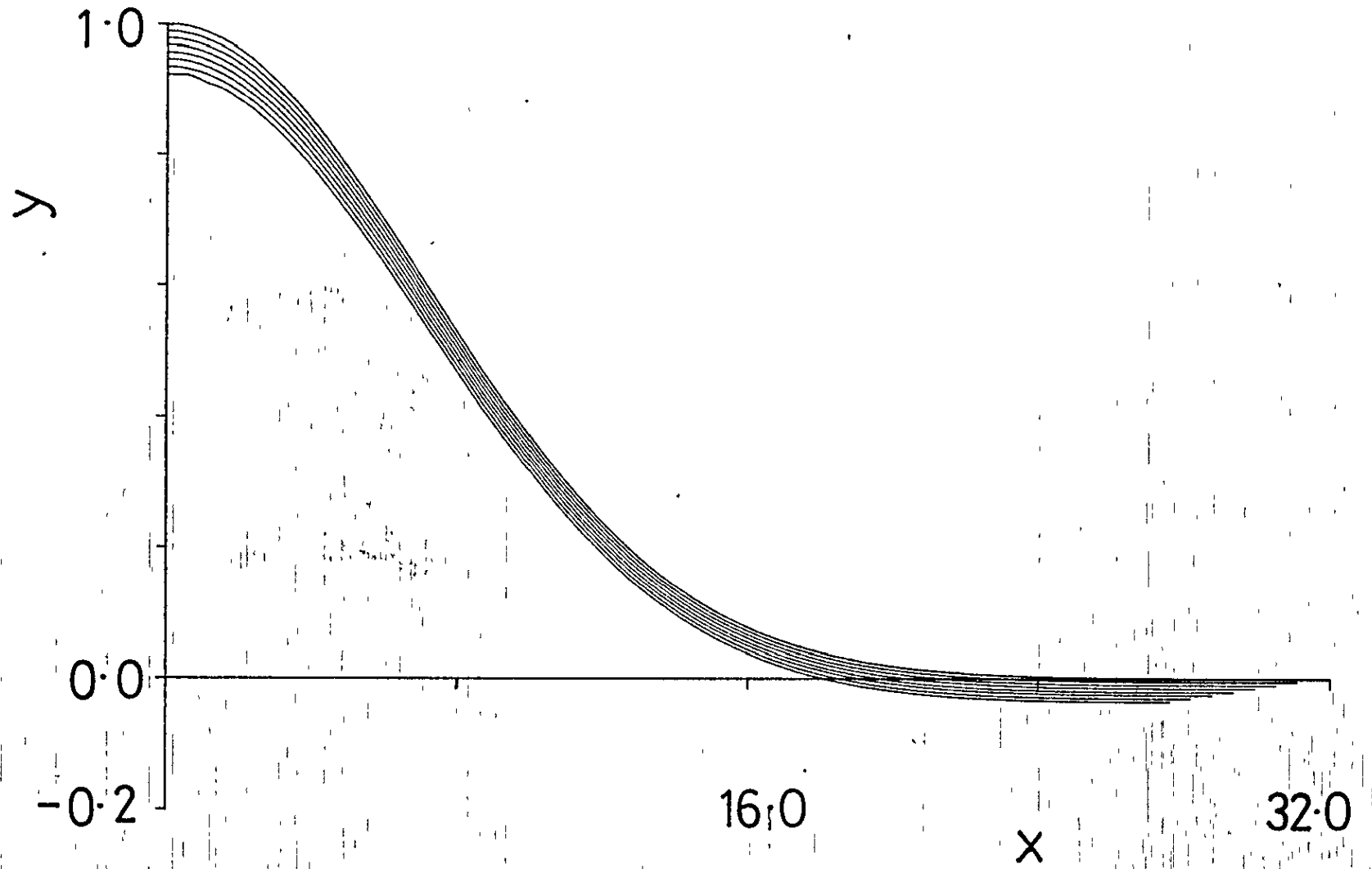




Fig.4.5(c)

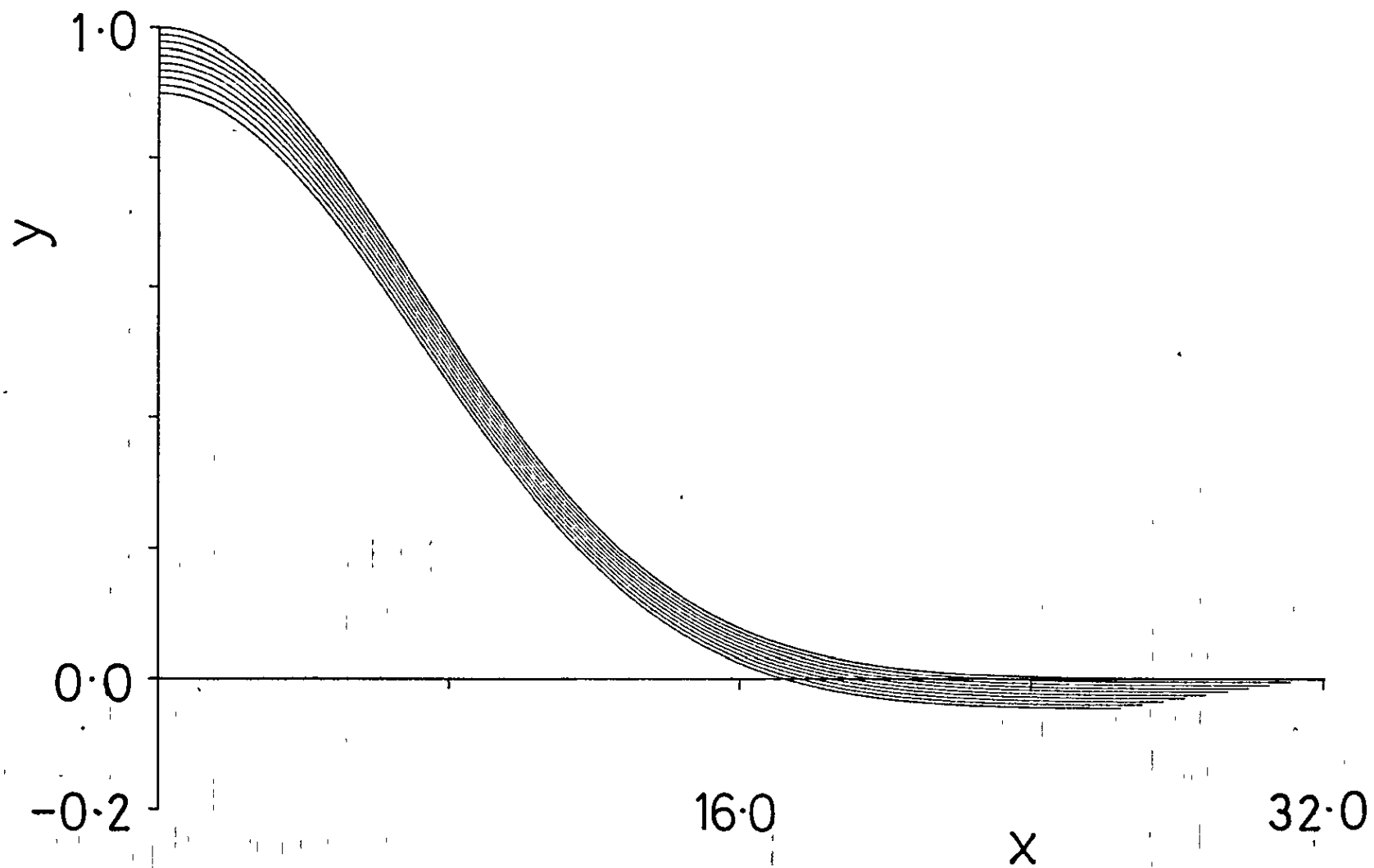


Fig.4.6. The initial Gaussian profile and the subsequent development in surface shape when modified by erosion only (a)  $S_2 = 1.0$  (b)  $S_2 = 0.5$ . Each profile corresponds to the development of surface shape after a time  $\Delta t = 1.0 \times 10^{-2}$ .

Fig.4.6(a)

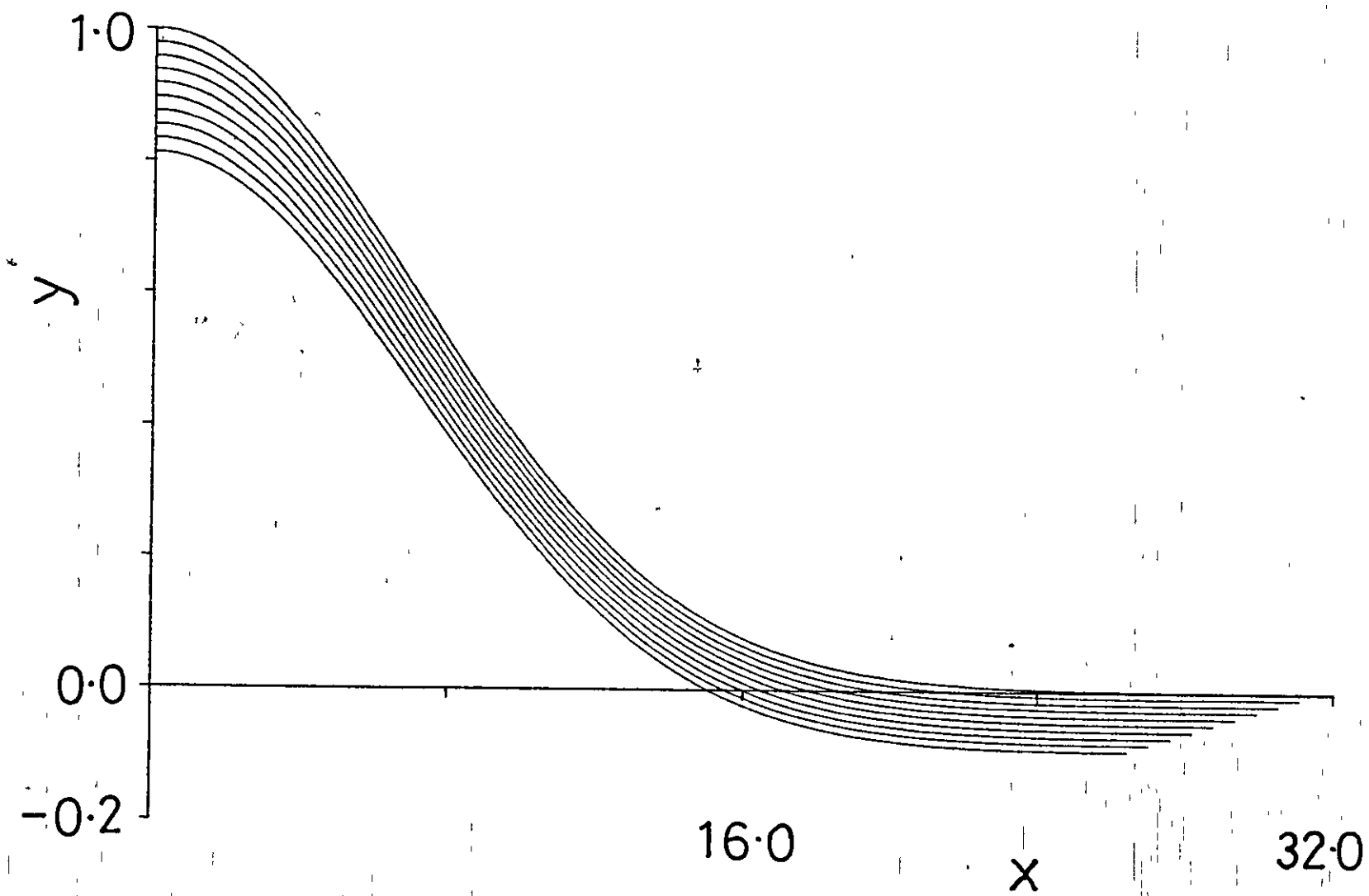
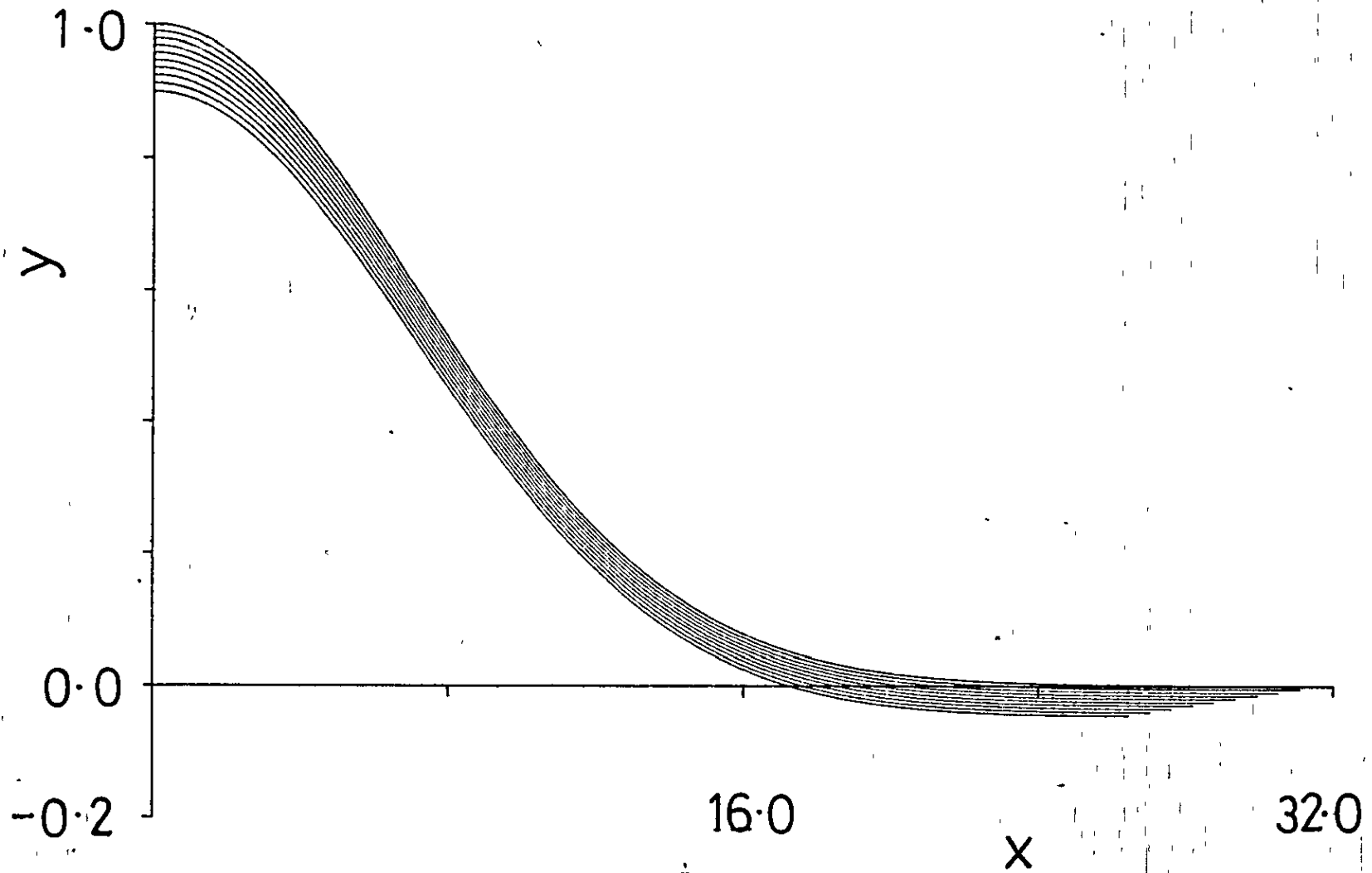


Fig.4.6(b)



( $J_s$ ) moving along the surface (equation (4.6)). Using this equation an expression was derived for how the sinusoidal profile is modified by the effects of surface diffusion (equations (4.8)). Mullins (1963) also included the effects of volume diffusion in his work and this will now be outlined briefly.

As before the sinusoidal profile of equation (4.3) is used and we will now analyse how it is modified by surface and volume diffusion. The flux of material,  $J_v$ , due to volume diffusion occurs at right angles to  $J_s$ . Assuming local equilibrium at the surface and free exchange of diffusing species between the volume and the surface,  $J_v$  is found by taking the normal gradient on the surface  $y = u(x,t)$  of the concentration  $c(x,y)$  of the diffusing species which is assumed to obey Laplace's equation (Mullins (1963)). The concentration  $c$  reduces to the value  $c_s$  required by capillarity on the interface i.e.

$$c_s = c_o + c_o \Omega \left( \frac{\gamma_o + \gamma_o''}{kT} \right) K \quad (4.29)$$

where  $c_o$  is the concentration in equilibrium with a flat surface. The solution for the current  $J_v$  leaving a surface element, to first order in  $a\omega$ , is given by

$$J_v = -D_v \frac{\partial}{\partial y} \left[ c_o + \frac{c_o (\gamma_o + \gamma_o'') \Omega \omega^2}{kT} a \sin \omega x e^{-\omega y} \right]_{y=0}$$

i.e.

$$J_v = \frac{D_v c_o (\gamma_o + \gamma_o'') \Omega}{kT} \omega^3 a \sin \omega x \quad (4.30)$$

where the expression in square brackets satisfies Laplace's equation under the stated conditions, and where the normal gradient has been

approximated by  $\frac{\partial}{\partial y}$  and evaluated on  $y = 0$ , because of the small slope. Equation (4.30) shows that material flows away from the maximums and into the minimums if  $\gamma_o + \gamma_o'' > 0$ , and the other way if  $\gamma_o + \gamma_o'' < 0$ . The rate of motion of an element of profile is given by the equation

$$\frac{\partial u}{\partial t} = -\Omega \frac{\partial^J s}{\partial x} - \Omega J_v \quad (4.31)$$

where again  $\frac{\partial}{\partial x}$  is used for the derivative along the surface. Substituting equations (4.3), (4.6) and (4.30) into (4.31), using the abbreviations

$$C = \frac{c_o D_v (\gamma_o + \gamma_o'') \Omega^2}{kT} \quad \text{and} \quad B = \frac{v (\gamma_o + \gamma_o'') D_s \Omega^2}{kT}$$

and cancelling  $\sin \omega x$ , gives

$$\frac{da}{dt} = - [B\omega^4 + C\omega^3] a \quad (4.32)$$

Integrating equation (4.32) to find  $a(t)$  and substituting into equation (4.3), the final solution for the description of the sine wave (with surface and volume diffusion) is obtained viz

$$y = u(x,t) = a_o \exp [-(B\omega^4 + C\omega^3)t] \sin \omega x \quad (4.33)$$

Equations (4.32) and (4.33) show an exponential growth or decay of the sine wave depending respectively on whether  $\gamma_o + \gamma_o''$  is negative or positive, the latter being the usual case. Surface diffusion should dominate on a sufficiently large scale. The wavelength at which the two transport processes contribute equally to the decay corresponds to  $B\omega^4 = C\omega^3$ .

Collins and Carter (1981) have considered a diffusion approximation to the ion bombardment induced 'mixing' of tracer atoms, initially located as a delta function of depth, in a host matrix of like atoms, with simultaneous erosion of the surface. These authors assumed diffusion enhancement to operate over an infinite range but in a later publication a better model was developed by assuming the diffusion to be limited to a fixed depth from the instantaneous surface (Carter et al (1981)). The model of Collins and Carter will be outlined briefly.

It is assumed, initially, that a semi-infinite solid of atomic species A occupies the region  $0 < x < \infty$ . The atomic density of this solid is  $C_A(0)$ . At a depth  $l$  from the initial surface ( $x = 0$ ) a plane of impurity atoms B, of concentration  $C_B(0)$  is located. At time  $t = 0$ , a flux density  $J$  of projectiles of any species, is directed at the surface of A. Thus the species A and B are caused to interdiffuse. In any accurate simulation of mixing processes the diffusivities for both species A and B must be expected to be depth and time dependant. However this makes the analysis much more difficult and therefore the authors assumed  $D_A$  and  $D_B$  (the diffusivities of atoms A and B respectively) to be spatially and temporally constant. At the instant of commencing irradiation, the incident particle flux is considered to cause uniform surface erosion in the positive  $x$  direction at a speed  $U(x,t)$ . This erosion speed is given by

$$U(x,t) = J \cdot \frac{\text{Surface Sputtering Yield}}{\text{Surface Atomic Density}} \quad (4.34)$$

and may be variable. The authors also assumed a constant atomic density. With these assumptions and assuming one dimensional diffusion only, the authors set up the transport equations for species A and B. These were then solved using the method of Laplace transforms to find

the surface atomic concentration as a function of time. On analysing the solutions it was found that there is a depth shift of the mean value of the surface concentration and broadening of the initial profile. It was clear from the results that depth independent constant diffusivity approximations to linear cascade mixing processes are not totally appropriate since, although predicting the correct signs for shifts and broadenings they do not fully predict the correct depth parametric dependence. The authors concluded that infinite range diffusion should be applied cautiously to simulate atomic redistribution effects and finite range, depth variable diffusion and drift processes should represent an improvement. Carter et al (1981) used a finite range approximation for the diffusion process. Their theory will not be outlined here but, they found that the finite range diffusion approximation could be employed to more adequately simulate detailed linear cascade atomic redistribution processes under radiation perturbation. In particular, depth shifts of the mean of the surface concentration-sputtered depth profile were found to be positive or zero and the variance was found to decrease. Various other authors have considered the distortion of depth profiles during sputtering (Anderson (1979), Hofer and Littmark (1979), Sigmund and Gras-Marti (1980), Gras-Marti and Sigmund (1981)). These authors were concerned with collisional mixing which is one of the factors limiting the depth resolution of sputter depth profiles. The primary disordering mechanism is collisional mixing which can be sub-divided into recoil implantation and cascade mixing (Sigmund and Gras-Marti (1980)). These authors called the direct displacement of a target atom by a bombarding ion, recoil implantation, while indirect processes involving other target atoms was called cascade mixing. Within this classification, recoil implantation produces a shift and a broadening of a given initial profile while cascade



mixing produces primarily a broadening. Sigmund and Gras-Marti (1980) went on to develop a theory for collisional mixing and a general treatment comprising the effects of recoil implantation and cascade mixing on the distortion of an impurity profile in a bulk matrix was presented. The statistics of the distorting events was shown to be a close analogue to that of the stopping of charged particles in random matter, and describable in terms of the Bothe-Landau theory of energy loss. A general expression was given for the Green's function transforming a given impurity profile into an apparent (or distorted) profile. In the diffusion approximation, the theory yielded a well defined shift and smearing (broadening) of an impurity profile. Sigmund and Gras-Marti (1980) also showed that, with appropriate modifications, their theory reduced to the theories of previous authors (Anderson (1979), Hofer and Littmark (1979)). The advantage of their model was that it offered a simple and general scheme to treat the combined effects of recoil implantation and cascade mixing.

#### 4.4. Ion reflection.

Very little work has been done on the effects of ion reflection. Wilson (1973) has examined in detail, cones produced by ion bombardment and found a number of features which cannot be explained by the erosion theories outlined in chapter 1. It has been shown, for example, that at the base of cones a trough or ridge frequently occurs. Figure 4.7 shows a good example of a trough formed around the base of a cone. It has been suggested that these effects are due to the bombardment of the base of the cone by ions reflected and atoms sputtered from its sides. Wilson (1973) has analysed these processes qualitatively, and concluded

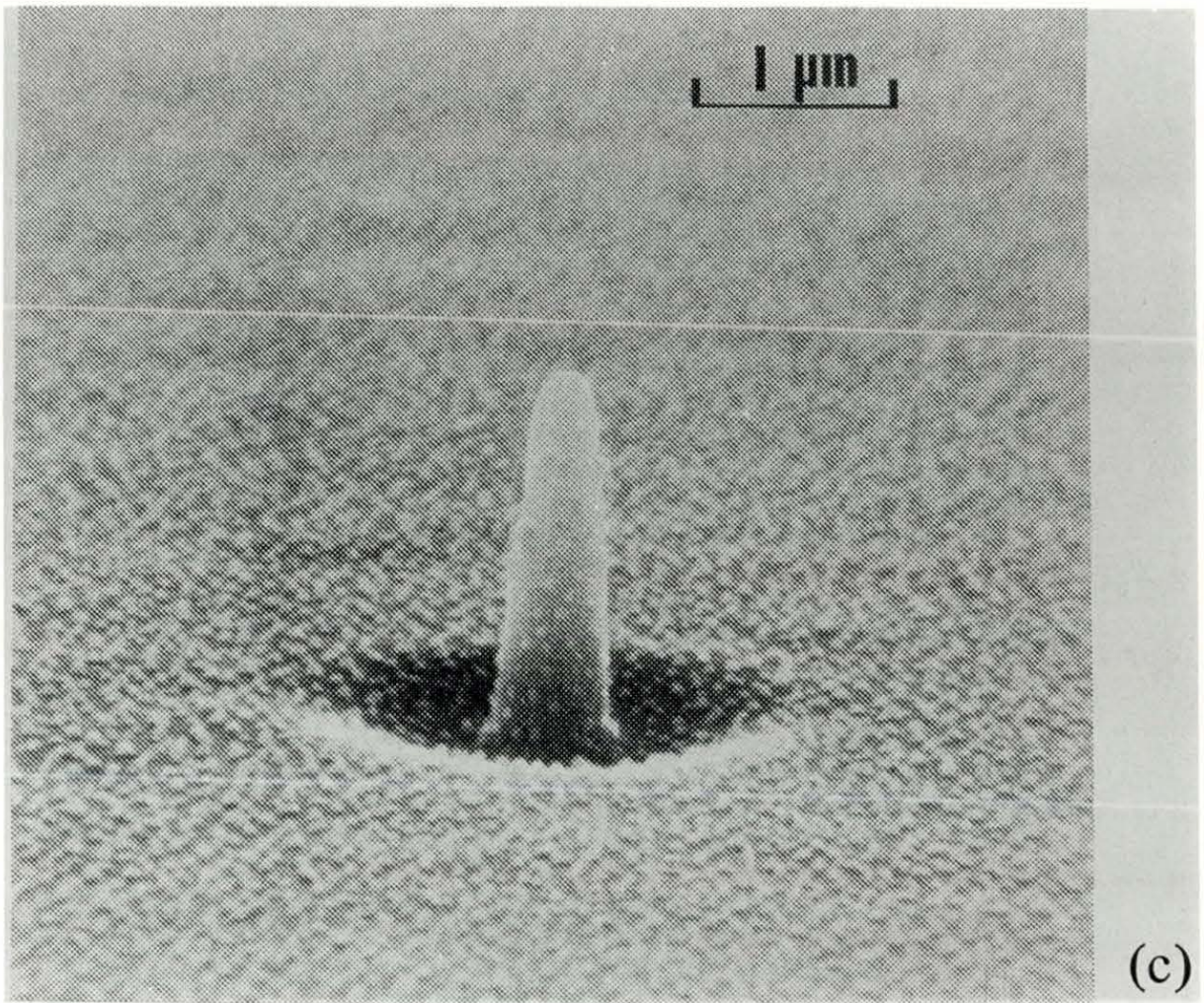


Fig.4.7. A cone formed on the surface of InP after bombardment by 40keV Ar<sup>+</sup> ions to a dose of  $2 \times 10^{18}$  ions cm<sup>-2</sup> (After Wilson (1973)).

that reflected ions are probably dominant for the conditions  $90^\circ > \theta > \hat{\theta}$ , where  $\theta$  is the angle between the incident ion beam and the surface normal and  $\hat{\theta}$  is the angle at which maximum sputtering occurs. Whether deposition or erosion takes place is predicted to depend on the sputtering yield.

It has been suggested, (Stewart and Thompson (1969)), that the peak in sputtering yield versus angle occurs because as  $\theta$  increases, the incident ion has an increasing probability of being reflected without traversing the effective surface layer. Hence the energy deposited eventually falls with increasing  $\theta$ . Stewart and Thompson (1969) applied a physical criterion to determine  $\hat{\theta}$ , the angle at which  $S(\theta)$  reaches its maximum value. When  $\theta = \hat{\theta}$ , reflection of the ion from the potential barrier associated with the surface plane of atoms prevents penetration. Lindhard (1965) has shown that the critical angle for such reflection is given by

$$\frac{\pi}{2} - \hat{\theta} = \left\{ \frac{5\pi a_0^2 n^{2/3} Z_1 Z_2 E_R}{(Z_1^{2/3} + Z_2^{2/3}) E_1} \right\}^{1/2} \quad (4.35)$$

where  $a_0$  = hydrogen Bohr radius,  $Z_1$  = ion atomic number,  $Z_2$  = target species atomic number,  $E_R$  = Rydberg energy,  $E_1$  = incident ion energy and  $n$  = density of atoms per unit volume. Thus when  $\theta > \hat{\theta}$ , penetration is not possible. Therefore it can be seen that ion reflection could be used to explain the pit or trough which sometimes appears around the base of cone structures. The reflected ion flux, retaining most of the incident energy, adds to the primary flux around the cone base, causing a localised flux enhancement and the development of the pit. Bayly (1972) applied these ideas to flaws and deep grooves, where the sides present a high angle for the incident ion flux, see figure 4.8.

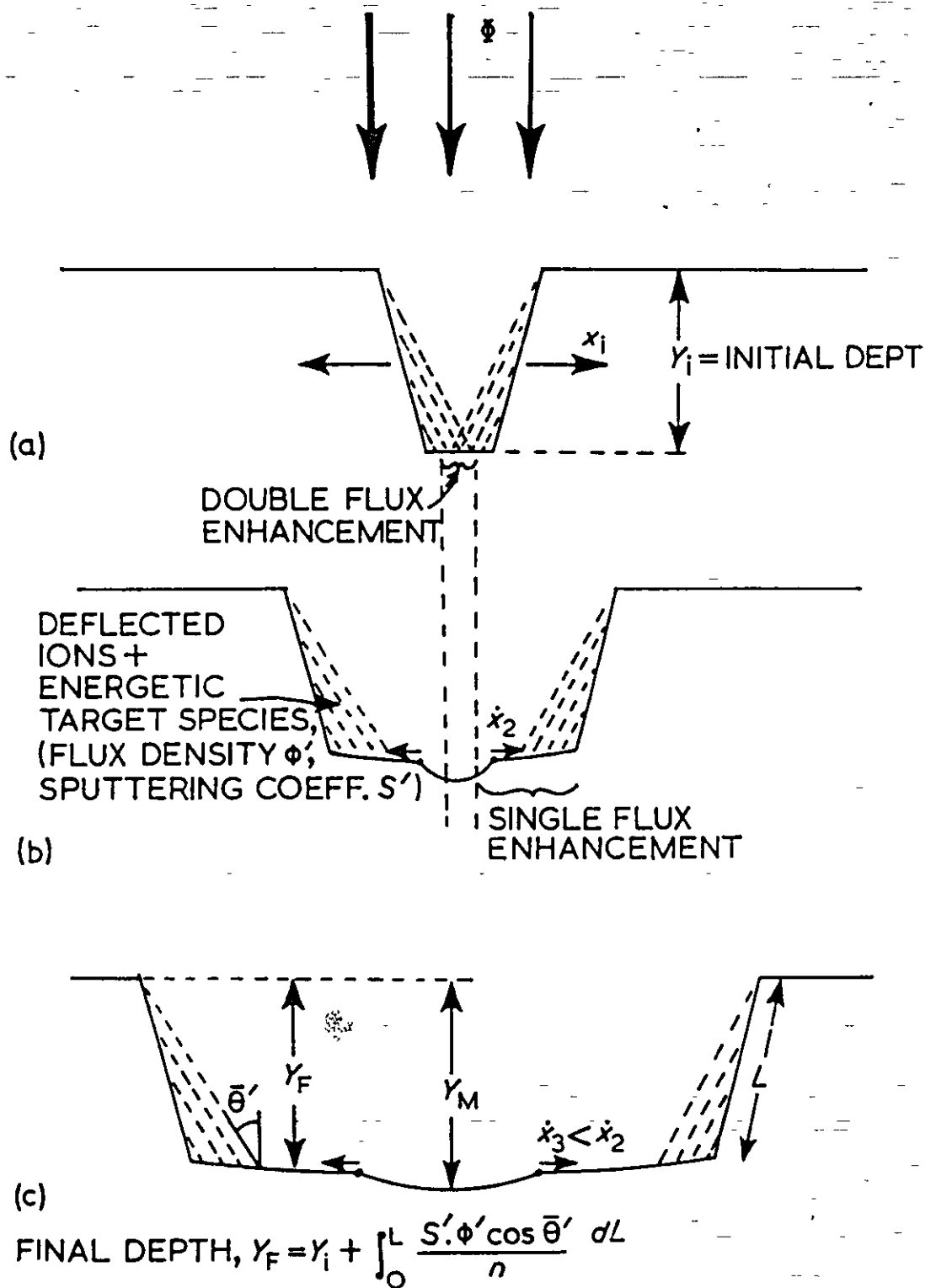


Fig.4.8. Schematic diagram showing a shallow surface flaw which experiences an additional energetic particle flux at the base due to quasi-specular reflection or re-emission of ions from both faces and how it is subsequently modified. See text for details (After Bayly (1972)).

The base of the shallow flaws must initially receive a doubly enhanced flux as the reflected beams from opposite sides overlap. As the sides separate, the reflected beams cease to overlap, leaving a smooth depression in the centre of the base, after which the expanding base formed by the separation of the sides is swept by a singly enhanced flux and finally eroded by the primary flux only. The central depression, being a shallow pit, and now eroded by the primary flux, will expand outwards as its radius of curvature increases, to the equilibrium  $0^\circ$  plane.

An alternative explanation for the formation of the trough around the base of cones has been formulated by Sigmund (1969), (1973), who analysed theoretically the spatial distribution of sputter-etch effects under the assumption of random slowing-down of the bombarding ions. This model will now be briefly outlined. When an energetic ion strikes a solid surface, a dynamic cascade of moving atoms is created in the zone where the ion deposits its energy. If these atoms are mobilized at and near the surface, then sputtering will occur provided that the kinetic energy of mobile atoms is greater than the surface binding energy. Since the energy deposition is spatially distributed about the point of impact of any individual ion, so also the sputtered atoms will be radially distributed in their ejection points about the point of ion impact. The majority of sputtered atoms will be ejected within a radius of the order of the depth of ion penetration from the point of ion impact. Sigmund (1969), (1973) gave analytical form to these local sputtering effects, by suggesting that the local sputtering yield at a point a vector distance  $\underline{r}$  from the point of ion impact was given by

$$S(\underline{r}) = \Lambda \cdot F_D(\underline{r}) \quad (4.36)$$

where  $\Lambda$  was a derivable constant for any ion energy-target combination and  $F_D(\underline{r})$  was the fraction of the ion energy deposited at the vector distance  $\underline{r}$ . The energy deposition function  $F_D(\underline{r})$  has been studied in detail under the assumption of random slowing-down of the ion, (Sigmund and Sanders (1967), Winterbon et al (1970), Sigmund et al (1971)).

Figure 4.9 illustrates the form of variation of this function in the x-y plane for an ion incident normally to a surface in the x direction. The energy deposition function is cylindrically symmetric about the x axis in this figure, which gives contour plots of mean deposited energy, and the sputtering yield at any surface point will be proportional to the fractional energy deposition at that point, as represented by the energy-contour surface intersection. In this case the sputtering yield will be distributed with azimuthal symmetry about the point of ion incidence, but will vary with distance from the point of impact. If, however, the ion is incident non-normally to a surface e.g. at an angle  $\theta$  as depicted in figure 4.10, then the deposited energy distribution function intersects the surface asymmetrically as shown in the figure. It is seen that the maximum of the deposited-energy function along the surface plane is not at the point of impact, but at a point C further 'downstream'. One implication of such a sputtering yield distribution would be that, for a uniform flux of ions incident upon a conical structure protruding from a plane, there would be a reduced yield of sputtered atoms near the apex of the cone and an enhanced yield at the cone-plane intersection. Thus a cone (triangle)-plane geometry could develop a more steeply angled apex, since sputtering is retarded there, and a trough can form around the cone foot. Sigmund (1973) assumed

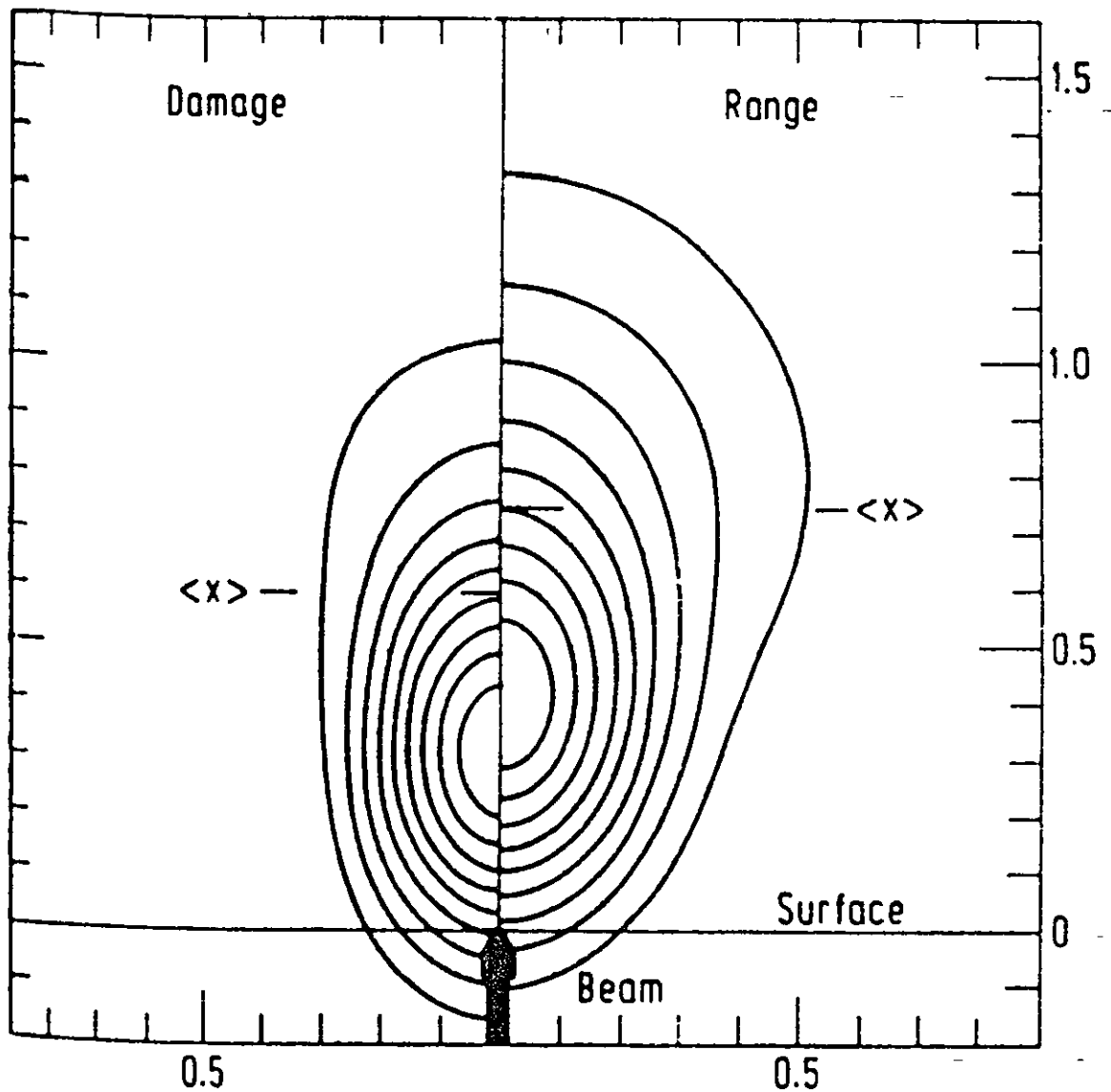


Fig.4.9. Contour plot of average deposited energy (left) and ion range profile (right) calculated for equal masses of bombarding ion and target. Both profiles show cylindrical symmetry around the ion beam direction (After Winterbon et al (1970)).

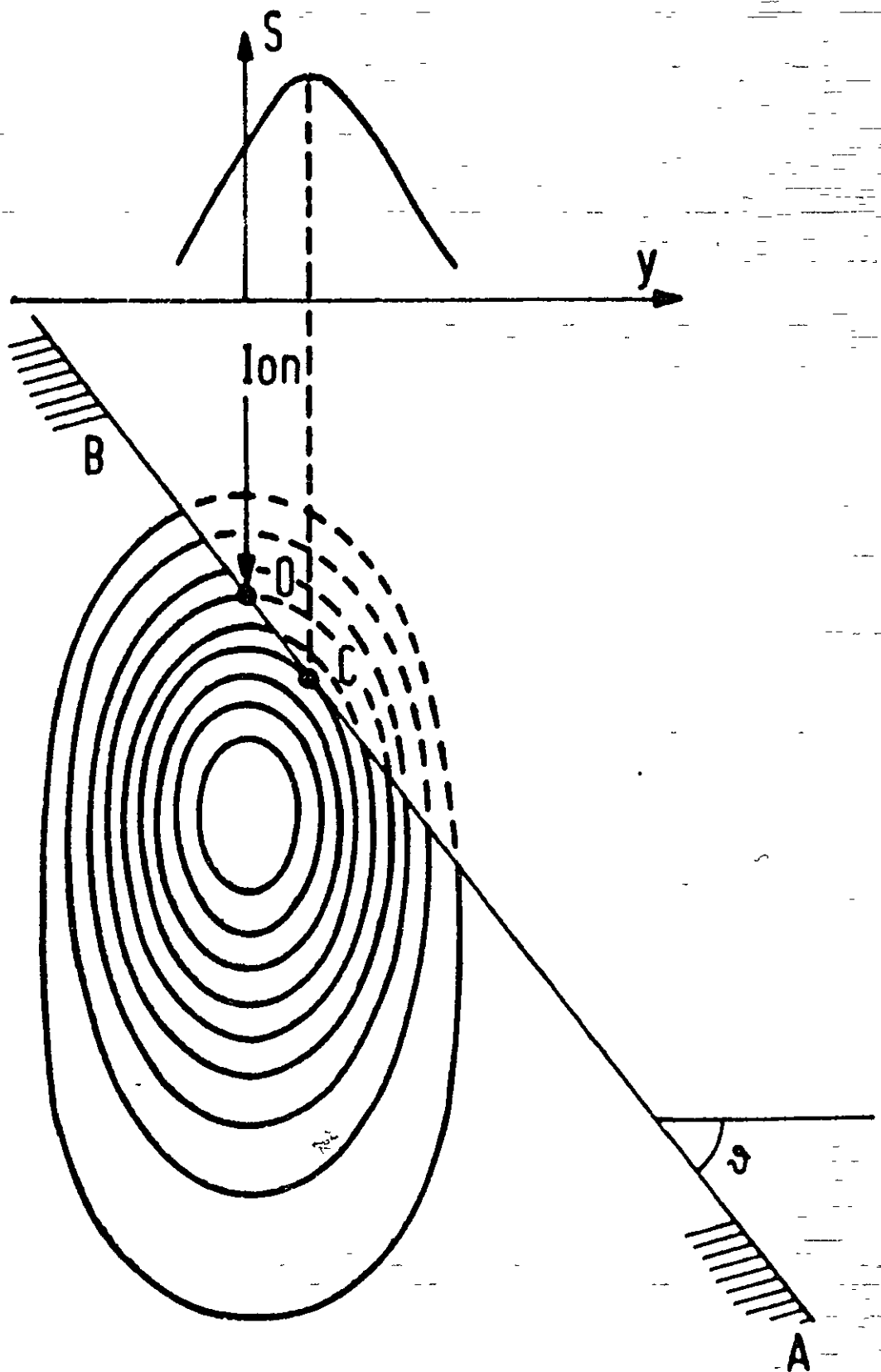


Fig.4.10. Contour plot of deposited energy as in fig.4.9. Target surface AB, angle of incidence is  $\theta$ , point of ion impact O and point of maximum sputtering yield C. Upper graph: Distribution of sputtering yield along surface for ion incident at O (After Sigmund (1973)).



that the energy deposition  $F_D(\underline{r})$  could be approximated by a Gaussian form with scaling parameters of mean depth of energy deposition and mean width of the deposition function in the x and y directions. Using this function, the total sputtering yield at any surface point due to a uniform distribution of impacts over any surface can be evaluated by integration of equation (4.36). Sigmund evaluated local sputtering yields for particular contours of two dimensional triangular protuberances and pits and line intersections and for the three dimensional cone-plane configuration. Figure 4.11 shows schematically the sputtering of a ridge using Sigmund's model. It was found that for this configuration, the regression rate of the cone top was found to be orders of magnitude lower than the surrounding plane. However, Sigmund was careful to emphasize that these differential erosion effects are operational on a scale where the linear dimensions of a feature are of similar order to the ion penetration depth.

It was mentioned previously that troughs are often observed around the bottom of a cone on an otherwise comparatively flat surface area. The occurrence of these grooves may be explained by the mechanism sketched in figure 4.11, provided that the characteristic dimensions are reasonably close to the ion range. An alternative explanation, (Wilson and Kidd (1971), Bayly (1972)), involves sputtering by scattered ions and high-energy sputtered atoms. Within the framework of collision cascade theory in an infinite medium, the two mechanisms appear to be very similar aspects of one basic mechanism. Analytic calculations including target surface effects at very oblique incidence should give further insight.

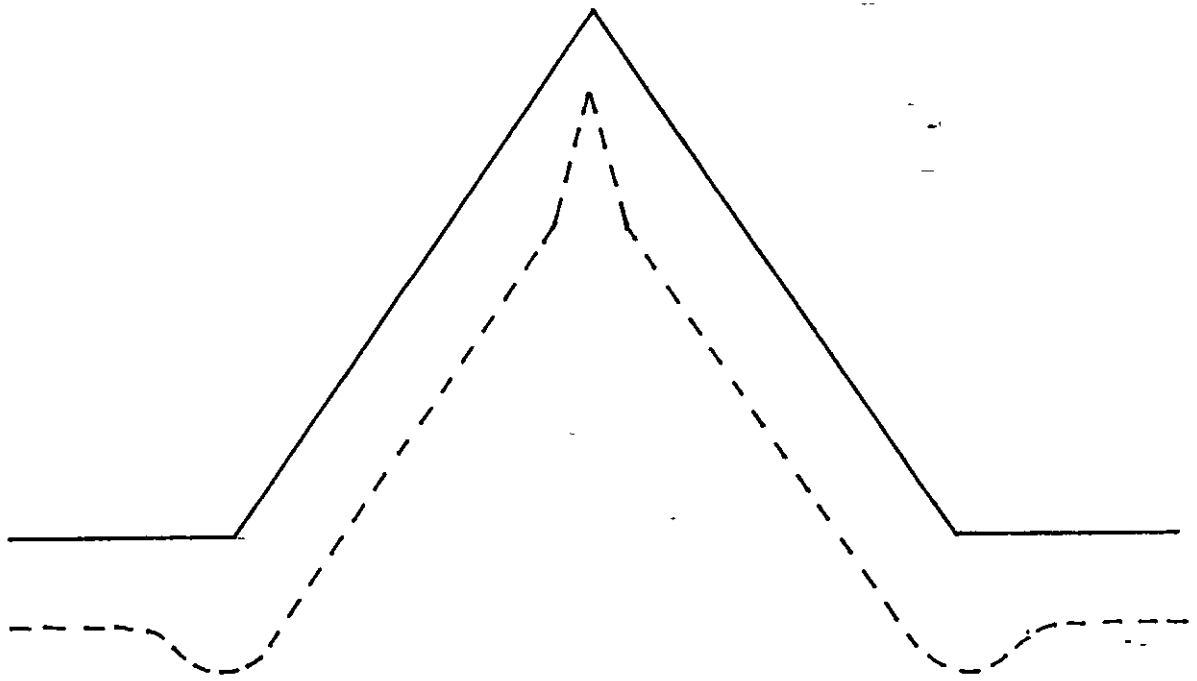


Fig.4.11. Schematic diagram illustrating the sputtering of a ridge. The regression speed is greatest at the lower edge, slightly smaller on the slope, considerably smaller on the horizontal plane and smallest near the top (After Sigmund (1973)).

#### 4.5. Discussion.

A linearised theory of surface diffusion and erosion has been developed. The theory enables calculations to be made concerning the development of surface shape due to the presence of surface diffusion and erosion. The computer simulations have shown that the effect of surface diffusion is to flatten the initial Gaussian profile. The linearised theory developed in this chapter is only valid for small values of  $\theta$ , the angle between the ion beam and the surface normal. Thus the theory would not be applicable to profiles for which  $\theta$  is large.

There are two cases to consider in the theory presented and these are related to the ratio  $\alpha/\beta$  in equation (4.28). If  $\alpha/\beta$  is positive then the curvatures on the new calculated profile will tend towards zero i.e. the profile becomes flatter. In the computer simulations presented (see figs. 4.4 and 4.5) the ratio  $\alpha/\beta$  is positive and the results show that the profile is becoming flatter. The final equilibrium shape will be a flat plane. However, if  $\alpha/\beta$  is negative, the curvatures on the new calculated profile will become larger and the shape will become sharper. As the profile sharpens,  $\theta$  increases, and the linearised theory no longer applies. The shape of the profile will then be determined by the non-linear theory (Carter et al (1977), Smith and Walls (1980)). However the effect of the non-linear theory is to flatten the profile and then the present theory will again apply and will make the shape flatter. Again the final equilibrium shape will be a flat plane.

Due to the fact that surface diffusion is a relatively small effect compared with erosion, the diffusion effects have been magnified to make them noticeable in the simulations. However this leads to

problems with the numerical technique being used if the bombardment time is increased. The problem is that although the angle  $\theta$  is zero at  $x = 0$  on the Gaussian profile at  $t = 0$ , it does not remain so when the profile is being modified by diffusion and erosion. Thus if the diffusion effect is increased, the angle at  $x = 0$  becomes large and this leads to instabilities in the numerical technique. For this reason only a few calculated profiles have been presented in figs. 4.4(a) and 4.5(a) where the diffusion effect is large.

A fully comprehensive theory of the modification of surfaces by tertiary effects would have to include the effects of volume diffusion and ion reflection. At present a complete theoretical description of this problem is not possible. In this chapter the effects of volume diffusion alone and ion reflection alone have been discussed qualitatively. The effect of volume diffusion is to flatten bulges and fill out troughs (Mullins (1963)). The effects of ion reflection become important in the vicinity of very steep profiles (large  $\theta$ ). The general effect is to develop a trough at the base of these steep structures.

In conclusion, for the first time computer simulations have been presented for the development of surface shape due to a profile being modified by surface diffusion and erosion. The simulations show that surface diffusion contributes towards the more rapid attainment of equilibrium end forms. There are still a number of deficiencies in the numerical technique being used, which leads to instabilities in the calculation of the modified profiles, and thus there is scope for more work on this aspect of the problem. Nevertheless, the theory presented here should contribute towards the attainment of a greater understanding of the processes involved during ion bombardment.

CHAPTER 5CONCLUSIONS AND SUGGESTIONS FOR FUTURE WORK5.1. Surface analysis.

Two separate but related problems have been considered. These were as follows 1) the development of surface topography on the macroscopic and the microscopic scale, 2) the influence of the development of surface topography on the degradation of composition-depth profiles.

In section 2.3 the development of surface shape on the macroscopic scale was investigated using methods previously developed for predicting the two dimensional evolution of surfaces during ion bombardment. The computer simulations were used to predict the changes in shape of non-flat samples which might occur in surface analysis. These predictions were then used to determine the effective depth resolution of such profiles as a function of both sample and electron and ion beam geometry.

The results show that the initial surface shape is never preserved during ion bombardment because the erosion rate is a sensitive function of ion-incidence angle. In general, concave surfaces tend to become shallower during ion etching while surfaces which are convex in the direction of the bombarding ion beam erode to form a conical shape. The eventual equilibrium profile in both cases is a flat plane.

In surface analysis, the non-uniform erosion leads to a deterioration in the depth-resolution of composition-depth profiles of samples with curved surfaces such as rods, wires and fibres. Thus an attempt has been made, using a model system, to estimate the extent of the problem. From the results it was possible to make some general

conclusions:

1. The depth resolution is a sensitive function of  $a/R$  ( $a$  = electron beam radius,  $R$  = radius of initial profile) and for this reason the electron beam diameter should be as fine as possible consistent with any beam damage effects which may occur on the surface under investigation.
2. The depth resolution ( $|\Delta d|/d$ ) is optimised at a point on the surface where the ion beam is incident along the surface normal. For some samples this geometry may not be feasible and a local minimum in  $|\Delta d|/d$  occurs when the angle between the surface normal and the incident ion beam corresponds to the angle at which maximum sputtering occurs.

Section 2.4 dealt with the development of surface topography using two ion beams and the effects of this on the composition-depth profiling of surfaces. Recently, it has been reported that the depth resolution of composition-depth profiles using AES can be improved when two ion guns are employed each aligned symmetrically about the sample normal and both delivering the same ion current. It has been interpreted that the effect of using two ion guns is to suppress the formation of ion induced surface topography. Thus in section 2.4 a theoretical model has been developed which supports this view and which allows the mechanisms involved to be more fully understood.

The results show that the type of topography developed varies significantly with  $\epsilon$ , the angle between the ion beams and the vertical. For  $\epsilon = 0$  (the one ion beam case) a two dimensional wedge is formed pointing in the direction of the ion beams. For  $0 \leq \epsilon < 45^\circ$  the end form is still wedge shaped. However for  $45^\circ \leq \epsilon \leq 70^\circ$  a flat topped structure results. Also, as the angle  $\epsilon$  increases the lateral erosion of the hummocks decreases.

One of the most important applications of ion etching is in surface analysis and the erosion of such surfaces during depth profiling is a complex process with the constant inception of surface protrusions and pits due to impurities or intrinsic or ion-beam induced defects. Such topography is subsequently modified due to the variation of sputtering yield with ion-incidence angle. In order to determine the effects of this latter mechanism during depth-profiling a model consisting of two semi-circular protrusions above a flat plane was chosen as an initial contour and the effects of bombardment by one and two beams analysed. The results show that shielding can effect the type of topography developed. If the distance between the structures is large, a stepped surface results due to erosion by one and two ion beams. However, if the distance is small, then the surface between the structures is shielded and hence uneroded.

The erosion of a surface by one ion beam, for non-normal incidence, has also been considered. The results show that for erosion by one ion beam a wedge is always formed which points in the direction of the incident ion beam. An attempt was also made to quantify the surface roughness obtained after bombardment of the model system by one and two beams. It has been assumed that the depth resolution can be related to the maximum deviation about the average surface height. The results show that the deviation is less in the case of bombardment by two ion beams which is in agreement with the experimental results obtained by Sykes et al (1980).

## 5.2. Redeposition of sputtered material.

The current trend in the microelectronics industry is towards circuits with greater density and devices with smaller feature sizes. This trend has aroused interest in several new process technologies for pattern replication. Ion beam etching is one such technology which offers higher resolution, greater dimensional control and higher yield than conventional wet chemical etching (Lee (1979)). However the nature of ion etching is such that several unique problems are encountered when directly applying the technique. One of the most important of these is the redeposition of back-sputtered material around the edges of steep surface features. The redeposited material is undesirable because it could interconnect isolated regions or it might prevent complete coverage by a subsequently deposited layer.

Due to the importance of the redeposition phenomena a theoretical model has been developed for the redeposition of back sputtered material. The theoretical model developed uses the concept of characteristic lines. These are lines in space along which the partial differential equation describing the erosion or build-up of a surface can be reduced to a set of ordinary 'characteristic' differential equations. In principle, the solution in a whole region can be obtained by integrating these characteristic differential equations along the characteristics covering the region.

The theory has been used to model the build-up of redeposited material in initially rectangular grooves. The results show that the important parameter in defining the extent of the redeposited build-up is the ratio of groove width to the depth of ion etched material. This is because the build-up of material at the bottom of the groove will be the same regardless of the groove height. However it should be noted



that ion reflection will become more important as the groove height increases and this will also affect the shape of the profile. In general, the results show that the build-up is more uniform for larger groove widths. However, for the same groove width but using different distributions for the sputtered particles, the results show that redeposition increases with decreasing energy but consequently becomes less uniform.

In summary, the theoretical model developed here calculates the redeposited profiles taking into account for the first time the continuously changing geometry of the profile. The method can account for different angular distributions of the sputtered particles due to different ion energies or different materials.

### 5.3. Surface diffusion and erosion.

Many authors have found substantial changes in the topography developed on polycrystalline materials as a function of the temperature of material (see for example Robinson and Southern (1968), Teodorescu and Vasiliu (1972)). These changes have been attributed to the greater influence of surface diffusion with increasing temperature. Thus a theoretical model for surface diffusion and erosion of atoms on a surface has been developed. The theory developed is a linearised theory of surface diffusion and erosion. Thus it is valid only for small angles  $\theta$  (the angle between the ion beam and the surface normal) and cannot be used to describe the formation of edges and cones which is a non-linear effect. The results show that the effect of surface diffusion is to flatten the initial Gaussian profile used in the computer simulations.

Thus surface diffusion contributes towards the more rapid attainment of equilibrium end forms. Due to the fact that surface diffusion is a relatively small effect compared with erosion, the diffusion effects have been emphasized to make them visible in the simulations. However this leads to problems with the numerical technique being used if the bombardment time is increased. The problem is that although the angle  $\theta$  is zero at  $x = 0$  on the Gaussian profile at  $t = 0$ , it does not remain so when the profile is being modified by diffusion and erosion. Thus if the diffusion effect is increased the angle at  $x = 0$  becomes large and the linearised theory developed here breaks down. Nevertheless, the theory developed in this thesis for diffusion and erosion provides a tentative step towards the attainment of a greater understanding of the processes involved during ion bombardment.

#### 5.4. Future work.

The bombardment of surfaces by low energy ion beams leads to a number of problems due to the non-uniform erosion of surfaces. A number of theories have been developed to try to account for the changes in surface topography observed to occur. These theories and their limitations have been outlined in this thesis. Recently Smith and Walls (1979), (1980) and Smith et al (1981) have developed a three-dimensional theory of surface erosion using the method of characteristics. In this thesis the theory has been modified and applied to a number of problems that arise during bombardment of surfaces. However, although a number of problems have been solved there are still many remaining.

The theory developed by Smith and Walls (1980) has been modified to look at the build-up of surfaces due to the redeposition of sputtered material in two dimensions (Makh et al (1980b), (1981b)). A computational method has been developed to show how initially rectangular grooves deform due to redeposition. One suggestion for further work is to extend the theory and apply it non-rectangular geometries.

Further research is needed to develop a three-dimensional theory of redeposition for amorphous materials, based on the method of characteristics. It is further proposed to extend this theory to include the effects of the crystalline structure of the material.

As yet, no attempt has been made to solve the problem of the simultaneous erosion and build-up of a surface. The primary ion beam erodes the vertical edge of a groove and this eroded edge has material redepositing on it. Thus another suggestion for further work is the developing of a mathematical model for the simultaneous erosion and build-up of a surface.

A major cause of cone formation during ion bombardment of surfaces is the presence of impurities having a different sputtering yield than that of the bulk solid. Once a cone is formed it is further developed due to the  $S(\theta)$  dependence. Thus cones have been observed on surfaces surrounded by pits. The formation of this pit is explained, qualitatively, by ion reflection off the cone walls causing a locally enhanced flux at the bottom of the groove. Developing a mathematical model for the formation of this pit constitutes another avenue for research.

Finally, a theoretical model has been developed for the migration of surface atoms away from the bombardment zone due to local heating

effects of the incident ion beam. However there are still a number of problems with the numerical technique being used which leads to instabilities in the calculation of modified profiles. Thus another suggestion for future work is to investigate the instabilities in the numerical technique. This should enable the calculation of modified profiles due to surface diffusion and erosion for much longer periods of time.

REFERENCES

- ALMÉN, O. and BRUCE, G. (1961) Nucl. Instrum. Methods 11 257.
- ANDERSON, H.H. (1979) Appl. Phys. 18 131.
- AUCIELLO, O. and KELLY, R. (1980) Proc. Symposium on Sputtering, Eds. P. Varga, G. Betz and F.P. Viehbock (Inst. f. Allgem. Phys. Tech. Univ. Wien) p.594.
- AUCIELLO, O. and KELLY, R (1981) To be published.
- BACH, H. (1970) J. Non-Crystalline Solids 3 1.
- BARBER, D.J., FRANK, F.C., MOSS, M., STEEDS, J.W. and TSONG, I.S.T. (1973) J. Mater. Sci. 8 1030.
- BAYLY, A.R. (1972) J. Mater. Sci. 7 404.
- BELSON, J. and WILSON, I.H. (1980a) Rad. Eff. 51 27.
- BELSON, J. and WILSON, I.H. (1980b) 'Low-Energy Ion Beams-2', Eds. I.H. Wilson and K.G. Stephens (Institute of Physics, London) p.252.
- BENNINGHOVEN, A. (1970) Z. Phys. 230 403.
- BENNINGHOVEN, A. (1975) Surf. Sci. 53 596.
- BETZ, G., DOBROZEMSKY, R. and VIEHBÖCK, F.P. (1970) Niederl. Tijdschr. Vacuumtechn. 8 203.
- BRAILS FORD, A.D. and GJOSTEIN, N.A. (1975) J. Appl. Phys. 46 2390.
- BRAMBLEY, D. (1981) Private communication.
- BRIGGS, D. (ed.) (1977) 'Handbook of X-ray and Ultraviolet Photoelectron Spectroscopy', Heydon, London.

- BUSH, V. and SMITH, G.C. (1922) Trans. American Inst. Elec. Eng. 41 627.
- CARTER, G. and COLLIGON, J.S. (1969) 'Ion Bombardment of Solids',  
(Elsevier Publishing Co., Inc., New York).
- CARTER, G., COLLIGON, J.S. and NOBES, M.J. (1971) J. Mater. Sci. 6 115.
- CARTER, G., COLLIGON, J.S. and NOBES, M.J. (1973) J. Mater. Sci. 8 1473.
- CARTER, G. (1976) J. Mater. Sci. 11 1091.
- CARTER, G., COLLIGON, J.S. and NOBES, M.J. (1977) Rad. Eff. 31 65.
- CARTER, G., NOBES, M.J., ARSHAK, K.I., WEBB, R.P., EVANSON, D.,  
EGHAWARY, B.D.L. and WILLIAMSON, J.H. (1979)  
J. Mater. Sci. 14 728.
- CARTER, G., COLLINS, R. and THOMPSON, D.A. (1981) Rad. Eff. 55 99.
- CASTAING, R. and SLODZIAN, G. (1962) J. Microscopy 1 395.
- CASTELLANO, R.N. (1980) Proc. 8th International Vacuum Congress, Cannes,  
France, Vol.1 74. (Thin Films).
- CATANA, G., COLLIGON, J.S. and CARTER, G. (1972) J. Mater. Sci. 7 467.
- CHAPMAN, R.E. (1977) J. Mater. Sci. 12 1125.
- CHUANG, T.J. and WANDELT, K. (1978) IBM J. Res. Dev. 22 277.
- COBURN, J.W. and KAY, E. (1974) 'CRC Critical Reviews in Solid State Sciences',  
p.562.
- COBURN, J.W. and WINTERS, H.F. (1979) J. Vac. Sci. Technol. 16 391.

- COLLINS, R. and CARTER, G. (1981) Rad. Eff. 54 235.
- CZANDERNA, A.W. (ed.) (1975) 'Methods of Surface Analysis', Elsevier, Amsterdam.
- DARGENT, B. and SIBUET, H. (1980) Proc. 8th International Vacuum Congress, Cannes, France Vol.1 78 (Thin Films).
- DIMIGEN, H. and LUTHJE, H. (1975) Philips. Tech. Rev. 35 199.
- DUCOMMUN, J.P., CANTAGREL, M. and MARCHAL, M. (1974) J. Mater. Sci. 9 725.
- DUCOMMUN, J.P., CANTAGREL, M. and MOULIN, M. (1975) J. Mater. Sci. 10 52.
- ERENTS, S.K. and McCracken, G.M. (1973) Rad. Eff. 18 191.
- FORMANN, E., VIEHBOCK, F.P. and WOTKE, H. (1966) Phys. Letters 23 558.
- FRANK, F.C. (1958) Growth and perfection of crystals (Conference report) J. Wiley, p.411.
- FRANK, F.C. and IVES, M.B. (1960) J. Appl. Phys. 31 1966.
- FRANK, F.C. (1972) Z. für Phys. Chemie. Neue. Folge. 77 84.
- GERALD, C.F. (1970) 'Applied Numerical Analysis' (Addison-Wesley Publishing Company, Inc.) p.219.
- GLOERSEN, P.G. (1975) J. Vac. Sci. Technol. 12 28.
- GLOERSEN, P.G. (1976) Solid State Technology 4 68.
- GRAS-MARTI, A. and SIGMUND, P. (1981) Nucl. Inst. and Meth. 180 211.
- GURMIN, B.M., RYZHOV, Y.A. and SKHARBAN, I.I. (1969) Bull. Acad. Sci. USSR, Phys. Ser. (USA) 33 752.

HARRIS, L.A. (1968) J. Appl. Phys. 39 1419.

HARRISON, D.E., LEVY, N.S., JOHNSON, J.P. and EFFRON, H.M. (1966)  
Appl. Phys. Lett. 8 33.

HERMANNE, N. and ART, A. (1970) Fizika 2 Suppl. 1 72.

HERMANNE, N. (1973) Rad. Eff. 19 161.

HERRING, C. (1951) 'The Physics of Powder Metalurgy', Ed. W.E. Kingston,  
McGraw-Hill Book Co., New York.

HIPPEL, A.V. (1926) Ann. Physik 81 1043.

HOFER, W.O. and LITTMARK, U. (1979) Phys. Lett. 71A 457.

HOFKER, W.K., WERNER, H.W., OOSTHOEK, D.P. and DE GREFFE, H.A.M. (1973)  
Rad. Eff. 17 83.

HOFMANN, S. (1976) Appl. Phys. 9 59.

HOFMANN, S. (1977) Appl. Phys. 13 205.

HOFMANN, S., ERLEWEIN, J. and ZALAR, A. (1977) 43 275.

IRVING, S.M., LEMONS, K.E. and BOBOS, G.E. (1969) U.S. Patent No.3,615,956  
(Filed (1969)).

ISHITANI, T., KATO, M. and SHIMIZU, R. (1974) J. Mater. Sci. 9 505.

IVES, M.B. (1961) J. Appl. Phys. 32 1534.

JOHNSON, L.F. (1979) Appl. Opt. 18 2559.

JOSHI, A., DAVIS, L.E. and PALMBERG, P.W. (1975) in 'Methods of Surface  
Analysis', Ed. A.W. Czanderna (Elsevier, Amsterdam) p.159.

KAMINSKY, M. (1964) Adv. Mass. Spectrom. 3 69.



- KAMINSKY, M. (1966) 'Advances in Mass Spectrometry 3, Paper No.4, Paris, (Institute of Petroleum, London).
- KEYWELL, F. (1952) Phys. Rev. Lett. 87 160.
- LAEGREID, N. and WEHNER, G.K. (1961) J. Appl. Phys. 32 365.
- LAMAR, E.S. and COMPTON, K.T. (1934) Science 80 541.
- LEE, R.E. (1979) J. Vac. Sci. Technol. 16 164.
- LEWIS, G.W., NOBES, M.J. and CARTER, G. (1980) Symposium on Sputtering, Vienna. Unpublished poster presentation.
- LEWIS, G.W., CARTER, G., NOBES, M.J. and CRUZ, S.A. (1981) To be published.
- LIEBL, H.J. and HERZOG, R.F.K. (1963) J. Appl. Phys. 34 2893.
- LIGHTHILL, M.J. and WHITHAM, G.B. (1955) Proc. Roy. Soc. 229A 281.
- LINDHARD, J. (1965) Math. Fys. Medd. Dan. Vid. Selsk 34 14.
- MAKH, S.S., SMITH, R. and WALLS, J.M. (1980a) Surface and Interface Analysis 2 115.
- MAKH, S.S., SMITH, R. and WALLS, J.M. (1980b) 'Low Energy Ion Beams - 2', Eds. I.H. Wilson and K.G. Stephens (Institute of Physics, London) p.246.
- MAKH, S.S., SMITH, R. and WALLS, J.M. (1981a) J. Mater. Sci., To be published.
- MAKH, S.S., SMITH, R. and WALLS, J.M. (1981b) To be submitted to Phil. Mag.
- MAUL, J., SCHULZ, F. and WITTMACK, K. (1972) Phys. Lett A41 177.

- MAZEY, D.J., NELSON, R.S. and THACKERAY, P.A. (1968) *J. Mater. Sci.* 3 26.
- McCRACKEN, G.M. (1975) *Rep. Prog. Phys.* 38 241.
- McHUGH, J.A. (1975) in 'Methods of Surface Analysis', Ed. A.W. Czanderna (Elsevier, Amsterdam) p.223.
- MECKEL, B.B., NENADOVIC, T., PEROVIC, B. and VLAHOV, A. (1975) *J. Mater. Sci.* 10 1188.
- MORRISON, G.H. and SLODZIAN, G. (1975) *Anal. Chem.* 47 932A.
- MULLINS, W.W. (1957) *J. Appl. Phys.* 28 333.
- MULLINS, W.W. (1959) *J. Appl. Phys.* 30 77.
- MULLINS, W.W. (1963) in 'Metal Surfaces', Eds. N.A. Gjostein and W.D. Robertson (American Society for Metals) p.17.
- MURRAY, R.J., NORRIS, B. and RICHARDS, B.P. (1978) *J. Mater. Sci.* 13 2105.
- NELSON, R.S. and THOMPSON, M.W. (1962) *Phys. Lett.* 2 124.
- NOBES, M.J., COLLIGON, J.S. and CARTER, G. (1969) *J. Mater. Sci.* 4 730.
- OECHSNER, H. (1975) *Appl. Phys.* 8 185.
- OLSON, N.T. and SMITH, H.P. (1967) *Phys. Rev.* 157 241.
- ONDERDELINDEN, D. (1966) *Appl. Phys. Lett.* 8 189.
- PALMBERG, P.W. (1972) *J. Vac. Sci. Technol.* 9 160.
- PATTERSON, H. and TOMLIN, D.H. (1962) *Proc. Roy. Soc.* 265 474.
- PRIMAK, W. (1963) *J. Appl. Phys.* 34 3630.

ROBINSON, M.T. and SOUTHERN, A.L. (1968) J. Appl. Phys. 39 3470.

RODELSPERGER, K., KRUGER, W. and SCHARMANN, A. (1974) Z. Physik 269 83.

ROSENBERG, D. and WEHNER, G.K. (1962) J. Appl. Phys. 33 1842.

SIGMUND, P. and SANDERS, J.B. (1967) in Proc. International Conf. on Application of Ion Beams to Semiconductor Technology, Editions Ophrys, Paris, p.215.

SIGMUND, P. (1969) Phys. Rev. 184 383.

SIGMUND, P., MATTHIES, M.T. and PHILLIPS, D.L. (1971) Rad. Eff. 11 34.

SIGMUND, P. (1973) J. Mater. Sci. 8 1545.

SIGMUND, P. and GRAS-MARTI, A. (1980) Nucl. Inst. and Meth. 168 389.

SMITH, H.I., MELNGAILIS, J., WILLIAMSON, R.C. and BROGAN, W.T. (1973) in 'Proc. IEEE Ultrasonics Symposium', Monterey, California, p.558.

SMITH, H.I. (1976) Proc. of the Symposium on 'Etching for Pattern Definition', Eds. H.G. Hughes and M.J. Rand, p.133.

SMITH, R. and WALLS, J.M. (1979) Surf. Sci. 80 557.

SMITH, R. and WALLS, J.M. (1980) Phil. Mag. 42 235.

SMITH, R., MAKH, S.S. and WALLS, J.M. (1980) Proc. 4th International Conference on Solid Surfaces and ECOSS III, Cannes, France, Vol.2 1209.

SMITH, R., VALKERING, T.P. and WALLS, J.M. (1981) Phil. Mag. 44 879.

SPENCER, E.G., SCHMIDT, P.H. and FISHER, R.F. (1970) Appl. Phys. Lett. 17 328.

STEWART, A.D.G. and THOMPSON, M.W. (1969) J. Mater. Sci. 4 56.

- SYKES, D.E., HALL, D.D., THURSTANS, R.E. and WALLS, J.M. (1980) *Applns. Surf. Sci.* 5 103.
- TEODORESCU, A. and VASILIU, F. (1972) *Rad. Eff.* 15 101.
- THOMPSON, M.W. (1961) *Proc. 5th Int. Conf. Ionization Phenomena in Gases, Munich (North-Holland Publishing Co., Amsterdam, 1962)* p.85.
- THOMPSON, J.J. (1921) 'Rays of Positive Electricity', (Longmans Green, New York).
- VASILIU F., TEODORESCU, A. and GLODEANU, F. (1975) *J. Mater. Sci.* 10 399.
- VOSSSEN, J.L. (1979) *J. Phys. E: Sci. Instrum.* 12 159
- WALLS, J.M. (1981) *Thin Solid Films* 80 213.
- WARDLE, K.L. (1965) 'Differential Geometry', (Routledge and Kegan Paul Ltd., London) p.20.
- WEBB, R., CARTER, G. and COLLINS, R. (1978) *Rad. Eff.* 39 129.
- WEBBER, R.D. and WALLS, J.M. (1979) *Thin Solid Films* 57 201.
- WEHNER, G.K. (1957) *Phys. Rev.* 108 35.
- WEHNER, G.K. (1959) *J. Appl. Phys.* 30 1762.
- WEHNER, G.K. and HAJICEK, D.J. (1971) *J. Appl. Phys.* 42 1145.
- WHITHAM, G.B. (1974) 'Linear and Nonlinear Waves', (Wiley: New York).
- WHITTON, J.L., TANOVIC, L. and WILLIAMS, J.S. (1978) *Applns. Surf. Sci.* 1 408.
- WILLIAMS, P. (1979) *IEEE Trans. Nucl. Sci.* NS-26 1807.

WILLIAMSON, R.C. and SMITH, H.I. (1973) IEEE Trans. MTT-21 195.

WILSON, I.H. and KIDD, M.W. (1971) J. Mater. Sci. 6 1362.

WILSON, I.H. (1973) Rad. Eff. 18 95.

WINTERBON, K.B., SIGMUND, P. and SANDERS, J.B. (1970) Mat. Fys. Medd. Dan. Vid. Selsk. 37 14.

WITCOMB, M.J. (1975) J. Mater. Sci. 10 669.

WITTMACK, K. and SCHULZ, F. (1978) Thin Solid Films 52 259.

WITTMACK, K. (1979) Surf. Sci. 85 69..

WITTMACK, K. (1980) Nuc. Inst. Meth. 168 343.

APPENDIX 1

Let  $A(t)$  define the surface at time  $t$  and  $A(t + \delta t)$  define the surface at time  $(t + \delta t)$ , see figure A.1. Erosion of the surface is by a variable flux  $\phi = \phi(x)$ . By definition

$$\frac{\partial y}{\partial t} = - \frac{\phi(x)}{N} S(\theta) \quad (\text{A.1})$$

Also

$$\frac{\partial y}{\partial x} = \tan \theta \quad (\text{A.2})$$

Using equations (A.1) and (A.2) we have

$$\frac{\partial}{\partial x} \left( \frac{\partial y}{\partial t} \right) = \frac{\partial}{\partial t} \left( \frac{\partial y}{\partial x} \right) = \sec^2 \theta \frac{\partial \theta}{\partial t}$$

and

$$\frac{\partial}{\partial x} \left[ - \frac{\phi(x)}{N} S(\theta) \right] = - \frac{1}{N} \left[ \frac{\partial \phi}{\partial x} S(\theta) + \phi(x) S'(\theta) \frac{\partial \theta}{\partial x} \right]$$

Equating gives

$$\frac{\partial \theta}{\partial t} + \frac{\phi(x)}{N} S'(\theta) \cos^2 \theta \frac{\partial \theta}{\partial x} = - \frac{1}{N} \frac{\partial \phi}{\partial x} S(\theta) \cos^2 \theta \quad (\text{A.3})$$

From figure A.1

$$\frac{\delta y}{\delta x} = \tan \theta$$

and using equation (A.1) gives

$$\delta x = \delta y \cot \theta = - \frac{\phi(x)}{N} S(\theta) \cot \theta \delta t$$

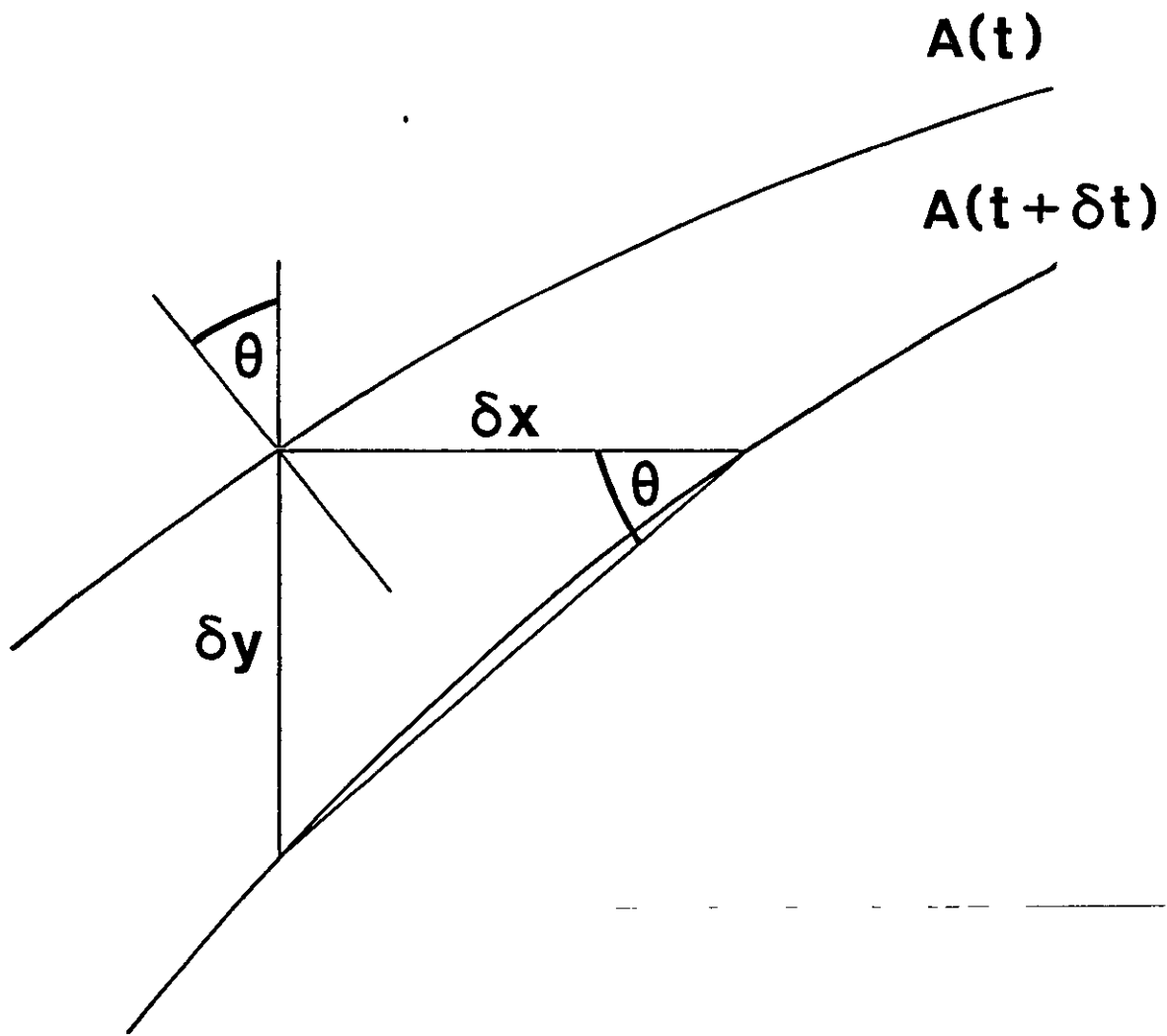


Fig. A.1. Diagram for calculating the relationship between  $\delta x$  and  $\delta y$ .

which can be rewritten as

$$\frac{\partial x}{\partial t} = -\frac{\phi(x)}{N} S(\theta) \cot \theta \quad (\text{A.4})$$

Using equations (A.2) and (A.4) we have

$$\frac{\partial}{\partial y} \left( \frac{\partial x}{\partial t} \right) = \frac{\partial}{\partial t} \left( \frac{\partial x}{\partial y} \right) = -\operatorname{cosec}^2 \theta \frac{\partial \theta}{\partial t}$$

and

$$\frac{\partial}{\partial y} \left[ -\frac{\phi(x)}{N} S(\theta) \cot \theta \right] = -\frac{\phi(x)}{N} \left[ S'(\theta) \cot \theta - \operatorname{cosec}^2 \theta S(\theta) \right] \frac{\partial \theta}{\partial y}$$

Equating gives

$$\frac{\partial \theta}{\partial t} - \frac{\phi(x)}{N} \left[ S'(\theta) \sin \theta \cos \theta - S(\theta) \right] \frac{\partial \theta}{\partial y} = 0 \quad (\text{A.5})$$

Equations (A.3) and (A.5) are standard partial differential equations which are solved by writing down their auxiliary equations. Thus the auxiliary equations of (A.3) are

$$\frac{dt}{1} = \frac{dx}{\frac{\phi(x)}{N} S'(\theta) \cos^2 \theta} = \frac{d\theta}{-\frac{1}{N} \frac{\partial \phi}{\partial x} S(\theta) \cos^2 \theta}$$

which gives

$$\left. \begin{aligned} \frac{dx}{dt} &= -\frac{\phi(x)}{N} S'(\theta) \cos^2 \theta \\ \frac{d\theta}{dt} &= -\frac{1}{N} S(\theta) \cos^2 \theta \frac{\partial \phi}{\partial x} \\ \frac{d\theta}{dx} &= -\frac{S(\theta)}{\phi(x) S'(\theta)} \frac{\partial \phi}{\partial x} \end{aligned} \right\} (\text{A.6})$$



Similarly the auxiliary equations of (A.5) are

$$\frac{dt}{1} = \frac{dy}{-\frac{\phi(x)}{N} [S'(\theta)\cos\theta\sin\theta - S(\theta)]} = \frac{d\theta}{0}$$

This gives

$$\frac{dy}{dt} = -\frac{\phi(x)}{N} [S'(\theta)\sin\theta\cos\theta - S(\theta)] \quad (\text{A.7})$$

Thus equations (A.6) and (A.7) define the characteristic lines in x-y space. It should be noted that the right hand sides of these equations are not constant as in the case of a uniform beam and the trajectories are no longer those of constant surface orientation. The invariant relation holding along these characteristics is determined by integration of the last equation of (A.6) viz

$$\frac{d\theta}{dx} = -\frac{S(\theta)}{\phi(x)S'(\theta)} \frac{\partial\phi}{\partial x}$$

As  $\phi = \phi(x)$  only, the above equation can be re-written

$$\frac{S'(\theta)}{S(\theta)} d\theta = -\frac{1}{\phi(x)} \frac{d\phi}{dx} dx$$

which integrates to

$$\phi(x) \cdot S(\theta) = \text{constant} \quad (\text{A.8})$$

Carter et al (1979) have considered the influence of a non-uniform flux upon the surface erosion process in two dimensions. However these authors appear to have missed the significance of the characteristic lines and in particular the importance of the invariant relation (equation (A.8)) holding along these lines.

## ACKNOWLEDGEMENTS

I would like to thank Dr. D. Brambley, Dr. R.N. Castellano, Dr. B. Dargent, Dr. H.I. Smith and Professor G.K. Wehner for providing micrographs of their work.

It is a great pleasure to thank Mr. D.D. Hall and Dr. D.E. Sykes for their help and for many useful discussions. I would also like to express my gratitude to Dr. D. Brambley and Mr. R.E. Chapman for their advice and assistance during the time spent at the Allen Clark Research Centre, Caswell. In particular I am indebted to Mr. R.E. Chapman for carrying out the reactive ion beam etching. My thanks are also due to Miss. D. Patel for helping with the diagrams.

I would also like to thank Professor J.F. Raffle and Professor C. Storey for the provision of research facilities in the Departments of Physics and Mathematics respectively.

My thanks are also due to the Science Research Council and the Plessey Company Ltd. for a CASE award during the tenure of which this work was undertaken.

Finally I would like to thank Dr. R. Smith and Dr. J.M. Walls for their different contributions and for their advice and encouragement during the period of research which culminated in the completion of this thesis.

